

The background features a dark blue gradient with numerous thin, glowing lines in shades of white, orange, and red. These lines radiate from a central point, creating a starburst or network-like effect. Small, bright dots are scattered along these lines, some appearing as nodes in a network. The overall aesthetic is scientific and modern.

Ph.D. Thesis

Measurement of the top quark coupling to the Z boson, and applications to searches for physics

Beyond the Standard Model

Baptiste Ravina



THE UNIVERSITY OF SHEFFIELD
DEPARTMENT OF PHYSICS & ASTRONOMY

*Ph.D. thesis submitted in partial fulfillment of the requirements
for the degree of*
Doctor of Philosophy
in the subject of Physics

Measurement of the top quark coupling to the Z boson, and applications to searches for physics Beyond the Standard Model

Supervisors:
Prof. Dan Tovey
Prof. Davide Costanzo

Candidate:
Baptiste Ravina
April 2020

À Jacques.

Toute l'écriture est de la cochonnerie.
Les gens qui sortent du vague pour essayer
de préciser quoi que ce soit de ce qui se
passe dans leur pensée, sont des cochons.

Antonin Artaud

Abstract

This thesis presents results using data collected by the [ATLAS](#) experiment in the 2015–2016 and 2015–2018 periods, corresponding to integrated luminosities at a centre-of-mass energy $\sqrt{s} = 13$ TeV of 36.1 fb^{-1} and 139 fb^{-1} respectively. It explores a connection between the top quark sector of the Standard Model and searches for supersymmetry in the all-hadronic final state.

In Part [II](#), a measurement of the inclusive cross section of the $t\bar{t}Z$ process in multi-lepton events results in $\sigma_{t\bar{t}Z} = 0.95 \pm 0.13 \text{ pb}$ with 36.1 fb^{-1} of data, and $\sigma_{t\bar{t}Z} = 1.09 \pm 0.10 \text{ pb}$ with the full [LHC](#) Run 2 dataset. Both results are compatible with the Standard Model prediction of $\sigma_{t\bar{t}Z}^{\text{theory}} = 0.863_{-0.10}^{+0.09}(\text{scale}) \pm 0.03(\text{PDF}+\alpha_s) \text{ pb}$. In the former analysis, exclusion limits are set on relevant dimension-6 effective field theory operators, while in the latter, the very first measurement of the differential $t\bar{t}Z$ cross section at ATLAS is presented.

In Part [III](#), a search for the supersymmetric partner to the top quark in the all-hadronic final state, characterised by six or more jets and large $E_{\text{T}}^{\text{miss}}$, is described. No significant excess over the expected Standard Model background is observed, using 36.1 fb^{-1} of ATLAS data. Assuming a 100% branching ratio of $\tilde{t}_1 \rightarrow t + \tilde{\chi}_1^0$, stop masses are excluded up to 1 TeV for neutralino masses smaller than 350 GeV. The estimation of the irreducible $t\bar{t}Z(\rightarrow \nu\bar{\nu})$ through a boson replacement technique is described in detail. Following the results obtained in Part [II](#), the use of a multi-lepton $t\bar{t}Z$ control sample is instead proposed and shown to significantly improve modelling uncertainties in a subsequent analysis using the full LHC Run 2 dataset.

Author's contributions

This thesis presents results from four ATLAS analyses, either published or in preparation. The author's contributions to each are listed below:

- **Measurement of the inclusive $t\bar{t}Z$ cross section (36.1 fb^{-1}):** lead analyser in the trilepton $t\bar{t}Z$ channel, fit results in the trilepton and tetralepton channels (Chapter 5, published in Ref. [1]);
- **Measurement of the inclusive and differential $t\bar{t}Z$ cross sections (139 fb^{-1}):** lead analyser for the differential measurement, development of unfolding tools and strategy, optimisation of trilepton signal regions and physics objects (Chapters 6 and 7, made public in [2]);
- **Search for all-hadronic supersymmetry (36.1 fb^{-1}):** validation of results in signal regions SRA and SRB, optimisation of top categories, estimation of $t\bar{t}Z$ background from $t\bar{t}\gamma$ (Chapters 8 to 10, published in Ref. [3]);
- **Search for all-hadronic supersymmetry (139 fb^{-1}):** estimation of $t\bar{t}Z$ background from a dedicated multi-lepton control region (Chapter 9, published in Ref. [4]).

The author further contributed to the development of the **ATLAS Fast Monte Carlo Chain** (FastChain), as part of the ATLAS authorship qualification: development of on-the-fly out-of-time pile-up fast simulation, performance monitoring and physics validation of generated Monte Carlo events against references from full simulation and data.

Acknowledgments

The research presented in this thesis spans four years of intense work, which wouldn't have been possible without the encouragements of my family, colleagues and close friends. Having patiently listened through my more or less coherent ramblings about physics these past few years, they know I am deeply grateful for their support, but also that I am just getting started.

Thanks first to my family, for standing by my side as I made the peculiar decision to spend eight years at university and for understanding my passion for physics. To Jacques, to whom I dedicate these pages; it's not medicine, but I might yet get a doctorate out of it. And to Indy, for being a constant reminder that life without worries is an achievable goal; your (largely unwanted) contributions to video meetings rightfully earned you an honorific position within our research group.

Thanks to my supervisors, Dan and Davide, who guided me through my Ph.D., helped me successfully navigate the world of ATLAS and were always a source of inspiration with their insightful comments and sharp intellects. To Alvaro, Calum, Fabio and Silvia, who offered me advice and mentoring in Sheffield; to Matt, Theo, Tom and the whole D44 crowd for the lively discussions and rants about everything and anything from pileup reweighting to my pronunciation of the letter "k".

Thanks to all the lovely people I met in Sheffield; in no particular order other than alphabetical: Armanda, Armando, Audrey, Caterina, Claudio, David, Giuseppe, Irene, Jasminder, Kyriakos, Léa, Luca, Luke, Maya, Pete, Rahul, Riccardo, Rosie, Valentina and Viktor. You made the grey skies of northern England that much more colourful. To Maxime, Yasmine, Ali, Gabrielle and the cohort of *lecteurs* for helping represent Francophony, our home abroad. And to Italy and Italians in general.

Thanks to all my friends at CERN and for the countless hours spent in R1, drinking coffee or otherwise. To Gedas-sensei and the wonderful Wife Person for the dubious philosophy debates, to Xavier for your fantastic exuberance, to Nico for all the pen-based stories and to Dan for being an island of sanity in the whole LTA madness. To Alessia, Ana, Antonio, Christina, Daniele, Fabrizio, Lukas and Rosanna for the wonderful times in Maratea and all the drama. To Sarah, Lily and Kate for being strong role models all around.

Thanks to Jay for his patience in teaching me unfolding, and for enlightening me about top dynamics; may our future collaboration be long and fruitful. To Mohamed-Ali, Salvish and Edoardo for our friendship at King's and beyond; and to Alex for our much-awaited yearly encounters. To Jean, Mairi, Malcolm, Nick, John, Angelo, Marco, Heinrich and Jan; I wouldn't be where I am today without your inspiring example and unwavering support.



Contents

Motivation and outline	13
------------------------------	----

I Introduction

1	Theoretical background	15
1.1	The Standard Model	15
1.1.1	The top quark	17
1.1.2	The Z boson	18
1.1.3	Coupling of the top quark to the Z boson	19
1.2	Limitations of the Standard Model	22
1.2.1	Dark Matter	22
1.2.2	The hierarchy problem	23
1.3	Supersymmetry	23
1.3.1	Superalgebras, superspaces and superfields	24
1.3.2	Elements of phenomenology	26
1.3.3	R-parity	28
1.3.4	Third generation and naturalness	29
1.3.5	Searches for light stops at the LHC	31
2	The ATLAS experiment	33
2.1	The Large Hadron Collider	33
2.1.1	Hadron collisions	34
2.1.2	Structure of an event	35
2.1.3	Luminosity	36

2.2	The ATLAS detector	37
2.2.1	Coordinate system	37
2.2.2	Magnet system	38
2.2.3	Inner detector	38
2.2.4	Calorimeters	40
2.2.5	Muon spectrometer	42
2.2.6	Trigger system	43
2.3	Monte Carlo simulation	44
2.3.1	Generation	44
2.3.2	Simulating the ATLAS detector	45
2.3.3	Towards a fast MC simulation	46
3	Analysis tools	51
3.1	The 2015–2018 ATLAS dataset	51
3.2	Reconstruction of physics objects	53
3.2.1	Tracks and vertices	53
3.2.2	Electrons	54
3.2.3	Muons	55
3.2.4	Photons	56
3.2.5	Jets	57
3.2.6	Jet flavour tagging	59
3.2.7	Missing transverse energy	60
3.3	Particle- and parton-level definitions	66
3.4	Aspects of top quark reconstruction	66
3.4.1	Semi-leptonic $t\bar{t}$ case	66
3.4.2	Di-leptonic $t\bar{t}$ case	68
4	Statistical techniques	71
4.1	Around profile likelihoods	71
4.1.1	Extended likelihood and maximal likelihood estimators	71
4.1.2	Extended likelihood with background components	72
4.1.3	Maximisation of a binned likelihood	72
4.1.4	Nuisance parameters	73
4.1.5	Hypothesis testing	74
4.1.6	Discovery and exclusion	75
4.2	An unfolding primer	76
4.2.1	The response matrix	76
4.2.2	Inverting the response matrix	77
4.2.3	Bin-by-bin unfolding	78
4.2.4	An iterative approach to regularised unfolding	79
4.2.5	Implementation in an ATLAS analysis	80
II Top quark pair production in association with a Z boson		
5	Inclusive cross section with the 2015–2016 dataset	85
5.1	Analysis strategy	85
5.1.1	Signal processes	86

5.2	Object definitions	86
5.3	Event selection	87
5.3.1	Triggers	87
5.3.2	Event cleaning	87
5.4	Signal regions	87
5.5	Prediction of the Standard Model backgrounds	89
5.5.1	Three-lepton control region	90
5.5.2	Four-lepton control region	90
5.5.3	Fake lepton estimation	91
5.6	Systematic uncertainties	94
5.6.1	Experimental uncertainties	94
5.6.2	Theoretical uncertainties	95
5.7	Results	96
5.7.1	Fit strategy	96
5.7.2	Results in the 3L channel	97
5.7.3	Results in the 4L channel	97
5.7.4	Results of the combined $t\bar{t}Z$ fit	98
5.7.5	Results of the two-dimensional fit	99
5.8	EFT interpretation	105
6	Inclusive cross section with the full Run 2 dataset	107
6.1	Analysis strategy	107
6.2	Object definitions	108
6.3	Event selection	108
6.3.1	Triggers	108
6.3.2	Event cleaning	108
6.4	Signal regions	109
6.5	Prediction of the Standard Model backgrounds	110
6.5.1	Three-lepton control region	110
6.5.2	Four-lepton control region	111
6.6	Systematic uncertainties	113
6.6.1	Experimental uncertainties	113
6.6.2	Theoretical uncertainties	113
6.7	Results	114
6.7.1	Fit strategy	114
6.7.2	Results in the 3L channel	115
6.7.3	Results in the 4L channel	115
6.7.4	Results of the combined $t\bar{t}Z$ fit	116
7	Differential cross section with the full Run 2 dataset	123
7.1	Event reconstruction and differential variables	123
7.1.1	Fiducial volumes in the 3L channel	123
7.1.2	Top reconstruction in the 3L channel	124
7.1.3	Fiducial volumes in the 4L channel	125
7.1.4	$t\bar{t}$ reconstruction in the 4L channel	125
7.1.5	Definition of differential variables	125

7.2	Unfolding tests	126
7.2.1	Binning optimisation	127
7.2.2	Number of iterations	127
7.2.3	Closure tests	129
7.2.4	Impact of limited MC statistics	132
7.2.5	Stress tests	133
7.2.6	Alternative unfolding methods	135
7.3	Results	141
7.3.1	Compatibility between observation and prediction	141

III

All-hadronic supersymmetry

8	Analysis strategy	151
8.1	Signal processes	151
8.2	Object definitions	152
8.3	Event selection	153
8.3.1	Triggers	153
8.3.2	Event cleaning	154
8.3.3	Discriminating variables	154
8.3.4	Top quark reconstruction	155
8.4	Signal regions	156
8.5	Prediction of the Standard Model backgrounds	159
8.5.1	One-lepton control regions	159
8.5.2	Two-lepton control regions	161
8.5.3	Jet Smearing	162
9	Estimation of the irreducible $t\bar{t}Z$ background	165
9.1	Boson replacement	165
9.1.1	Description of the method	165
9.1.2	Results	167
9.1.3	Limitations	167
9.2	Multi-lepton approach	172
9.2.1	Three-lepton control region	172
9.2.2	Results	173
10	Statistical analysis and search results	175
10.1	Systematic uncertainties	175
10.1.1	Experimental uncertainties	175
10.1.2	Theoretical uncertainties	176
10.2	Results	179
10.2.1	Description of fits	179
10.2.2	Background-only fit	179
10.2.3	Discovery fit	182
10.2.4	Exclusion fit	182
	Conclusion	189

Abbreviations	191
List of tables	193
List of figures	195
References	199

Appendices

A	Further $t\bar{t}Z$ differential results with the full Run 2 dataset	223
A.1	Results in the 3L channel	223
A.2	Results in the 4L channel	236

Motivation and outline

At the time of writing of this thesis, the [Large Hadron Collider \(LHC\)](#) [5] has come to a temporary halt and construction work is well under way to upgrade the network of experiments it serves, before proton-proton collisions start again in 2021. One of these experiments, [ATLAS \(A Toroidal LHC ApparatuS\)](#) [6], is a general-purpose detector built to be as efficient in measuring the properties of particles predicted by the historically successful [Standard Model \(SM\)](#) of particle physics, famously enabling the discovery of the Higgs boson in 2012 [7, 8], as in providing a wide range of signatures to reveal potential new physics [Beyond the Standard Model \(BSM\)](#). The impressive dataset collected by the ATLAS experiment over the 2015–2018 period therefore serves a dual purpose that we intend to fully exploit in this thesis.

One of the most abundantly produced particles during these proton collisions is the top quark, the heaviest fundamental particle known to date. Enjoying a strong coupling to the Higgs boson, which gives rise to its large mass, the precise measurement of its properties is of central importance to our knowledge of the SM. It is also one of the most promising gateways through which new physics could manifest itself, with a rich phenomenology and striking detector signatures. One class of such new models is [Supersymmetry \(SUSY\)](#), which predicts a heavy partner to the top quark as well as a Dark Matter candidate, expected to escape the detection of the ATLAS detector in the same way the SM neutrino does. The pair production of such SUSY top quark partners can hence result in the observation of two top quarks and neutrino-like missing particles at high energies, a very specific and particular production mode that is a direct test of the realisation of SUSY models in Nature.

In 2014 [9], it was however noted that a rare yet remarkable SM process would become relevant as the energy of particle colliders increased and would effectively act as an irreducible background to this SUSY signature, mimicking its properties almost exactly – a prophecy that Run 2 of the LHC realised. The pair production of top quarks in association with a Z boson, and the subsequent decay of the latter into a pair of neutrinos, is indeed today one of the leading backgrounds in direct searches for the SUSY partner to the top quark in events with no leptons at the LHC.

The goal of this thesis is therefore twofold: to provide the world’s most precise measurement to date of the SM $t\bar{t}Z$ process, and assess its impact on the latest searches for SUSY top partners at the LHC.

In what follows, we will briefly review in Chapter 1 the theoretical status and limitations of the SM, drawing particular attention to the top quark and Z boson, before exploring the phenomenology of SUSY models. The LHC complex and ATLAS experiment will be clearly presented in Chapter 2, while data analysis and statistical concepts of relevance will be laid out in Chapters 3 and 4. In Part II, we will present the outcome of successive measurements of the $t\bar{t}Z$ process in ATLAS, detailing new techniques employed. Finally, in Part III we will describe a particular search for SUSY partners to the top quark, focusing on the estimation of the irreducible $t\bar{t}Z$ background and showing explicitly the improvements made by better constraining this process.



Introduction

1 Theoretical background

- 1.1 The Standard Model
- 1.2 Limitations of the Standard Model
- 1.3 Supersymmetry

2 The ATLAS experiment

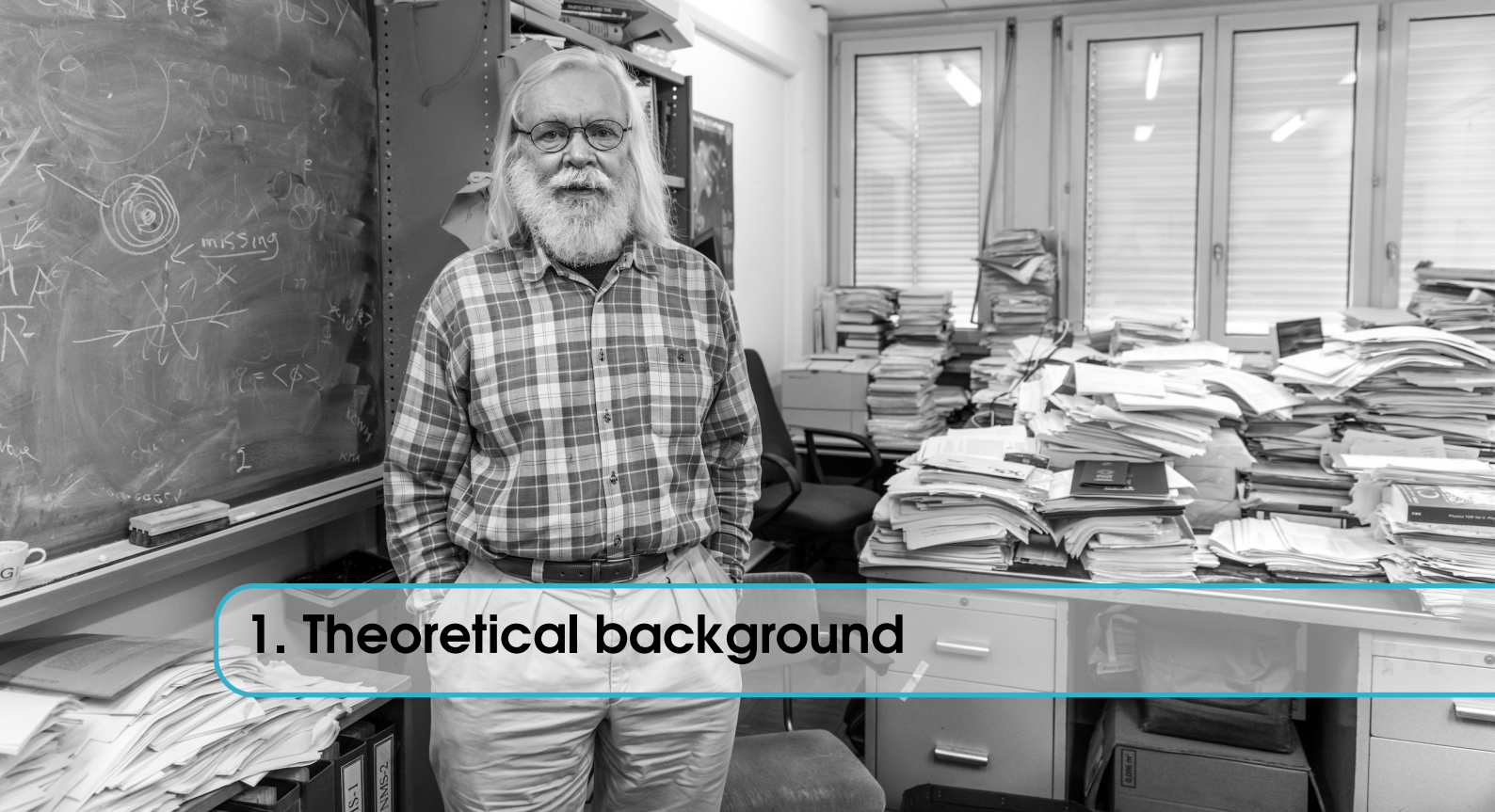
- 2.1 The Large Hadron Collider
- 2.2 The ATLAS detector
- 2.3 Monte Carlo simulation

3 Analysis tools

- 3.1 The 2015–2018 ATLAS dataset
- 3.2 Reconstruction of physics objects
- 3.3 Particle- and parton-level definitions
- 3.4 Aspects of top quark reconstruction

4 Statistical techniques

- 4.1 Around profile likelihoods
- 4.2 An unfolding primer



1. Theoretical background

Elements of theoretical and phenomenological high energy particle physics are reviewed in this chapter. In Section 1.1, we present the [Standard Model \(SM\)](#) as a [Quantum Field Theory \(QFT\)](#) and describe its gauge, bosonic and fermionic contents, focusing on two particles of interest: the top quark and the Z boson. Limitations of the SM are outlined in Section 1.2, paying particular attention to the problems of Dark Matter and the Higgs mass. [Supersymmetry \(SUSY\)](#) is mathematically introduced in Section 1.3 and shown to provide a solution to these problems. The experimental status of top quark and Z boson precision measurements, as well as searches for SUSY, is briefly surveyed throughout the chapter.

1.1 The Standard Model

The [Standard Model \(SM\)](#) of particle physics is a four-dimensional gauge quantum field theory first formulated in the 1960's by Glashow [10], Weinberg [11] and Salam [12] to describe the unified electroweak interaction, and later extended by Gell-Mann [13], Gross [14], Politzer [15] and Wilczek [16] in the 1970's to incorporate the strong force of quantum chromodynamics, such that the interactions of elementary fields can be represented by the internal Lie group

$$G_{SM} = SU(3) \times SU(2) \times U(1). \tag{1.1}$$

The matter content of the SM, the result of decades of collaboration between experimental and theoretical high energy physics, is described by spin- $\frac{1}{2}$ fields known as fermions; their properties are listed in Table 1.1. The first generation of these fields provides the building blocks of ordinary matter: the electron and its neutrino, and the up and down quarks aggregating into protons and neutrons. The further generations of leptons and quarks are unstable and accessible only through energetic events, whether astrophysical or generated in particle accelerators. Integer spin particles, referred to as bosons, are responsible for mediating interactions between fermions: the photon

¹“In Theory: John Ellis”. Photo credits: Sophia Elizabeth Bennett. © 2016 CERN.

associated to electromagnetism, the W^\pm and Z bosons to the weak nuclear force, and the gluons to the strong nuclear force. Their quantum numbers are further described in Table 1.2.

The crucial role of the Higgs field in spontaneously breaking [17–19] the electroweak symmetry $SU(2)_L \times U(1)_Y$ down to the electromagnetic component $U(1)_{EM}$, thereby enabling the generation of masses in a gauge-invariant way for leptons, quarks and the weak force carriers, was confirmed by the joint discovery of its eponymous boson in 2012 by the ATLAS [7] and CMS [8] collaborations at CERN. The SM, and the Higgs sector in particular, however still leave a number of questions open. We will describe some of these limitations in Section 1.2.

Table 1.1: Fermion (spin- $\frac{1}{2}$) content of the SM and their quantum numbers Q , T_3 and Y_W , corresponding to electric charge, weak isospin and weak hypercharge respectively, as well as their representation under colour $SU(3)$. All masses and mass limits are taken from [20].

		Particle	Q	T_3	Y_W	Colour	Mass	
Leptons	I	electron	e	-1	-1/2	-1	1	511 keV
		electron neutrino	ν_e	0	+1/2	-1	1	< 0.28 eV
	II	muon	μ	-1	-1/2	-1	1	106 MeV
		muon neutrino	ν_μ	0	+1/2	-1	1	< 0.28 eV
	III	tau	τ	-1	-1/2	-1	1	1.78 GeV
		tau neutrino	ν_τ	0	+1/2	-1	1	< 0.28 eV
Quarks	I	up	u	+2/3	+1/2	+1/3	3	2.2 MeV
		down	d	-1/3	-1/2	+1/3	3	4.7 MeV
	II	charm	c	+2/3	+1/2	+1/3	3	1.3 GeV
		strange	s	-1/3	-1/2	+1/3	3	93 MeV
	III	top	t	+2/3	+1/2	+1/3	3	172.9 GeV
		bottom	b	-1/3	-1/2	+1/3	3	4.2 GeV

Table 1.2: Boson (integer spin) content of the SM and their quantum numbers Q , T_3 and Y_W , corresponding to electric charge, weak isospin and weak hypercharge respectively, as well as their spin and representation under colour $SU(3)$. All masses are taken from [20].

	Particle	Q	T_3	Y_W	Colour	Spin	Mass	
	photon	γ	0	0	0	1	1	—
	W^\pm	± 1	± 1	0	1	1	80.4 GeV	
	Z	0	0	0	1	1	91.2 GeV	
	gluon	g	0	0	0	8	1	—
	Higgs	h	0	-1/2	+1	1	0	125.1 GeV

1.1.1 The top quark

The top quark is the heaviest fundamental particle in the SM. Discovered at the Tevatron (Fermilab) by the CDF [21] and D0 [22] experiments in 1995, it boasts a mass of $172.9 \pm 0.4 \text{ GeV}$ [20]. With a decay width $\Gamma = 1.42^{+0.19}_{-0.15} \text{ GeV}$, the top quark is highly unstable and decays within 10^{-25} s of production [23] – an order of magnitude below the mean hadronisation time of QCD, $\sim 10^{-24} \text{ s}$. The top quark is thus unique in that it can be studied, from careful reconstruction of its decay products, as a bare quark.

Production of top-antitop quark pairs is the most abundant generation mechanism, proceeding via the strong interaction either from quark-antiquark or gluon-gluon initial states. In pp collisions at the LHC at a centre-of-mass energy of $\sqrt{s} = 13 \text{ TeV}$, the latter process dominates $\simeq 90\%$ of the time. The corresponding $pp \rightarrow t\bar{t}$ cross section is predicted in the SM, at NNLO+NNLL precision, to be $832^{+40}_{-46} \text{ pb}$ [24]. Since the various combined Tevatron, ATLAS and CMS measurements rely on different centre-of-mass energies through the years, it is possible to compare SM predictions to experimental observation in the dependence of the $t\bar{t}$ cross section on \sqrt{s} ; as is shown in Figure 1.1, good agreement is found.

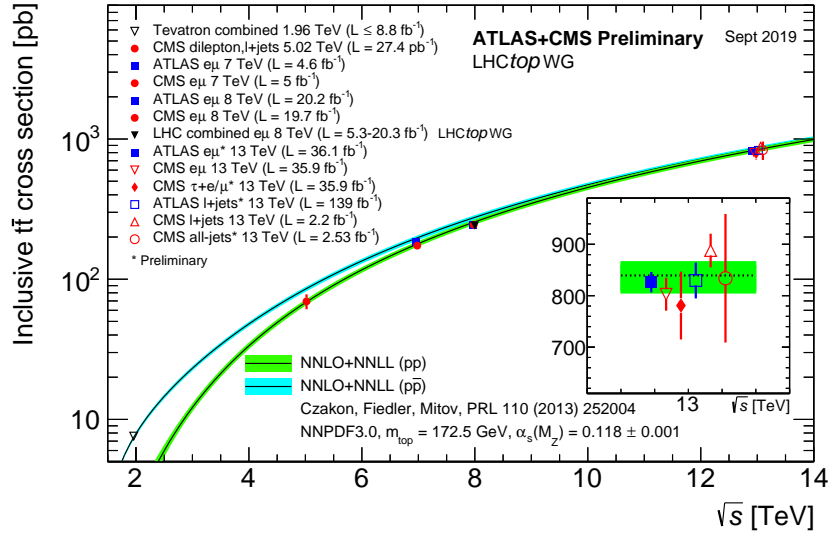


Figure 1.1: Summary of the LHC and Tevatron measurements of the top quark pair production cross section as a function of the centre-of-mass energy compared to the NNLO QCD calculation complemented with NNLL resummation. The theory band represents uncertainties due to renormalisation and factorisation scales, parton density functions and the strong coupling. The measurements and the theory calculation are quoted at $m_t = 172.5 \text{ GeV}$. Measurements made at the same centre-of-mass energy are slightly offset for clarity. From [25].

The top quark almost always decays into its weak isospin partner, the b -quark, and a W boson, providing an independent measurement of the CKM element $|V_{tb}|$, $\approx 99.8\%$ [20]. In the remaining 0.2% of cases, the top quark may decay into a d - or s -quark and a W boson. These rare decays are the object of specific searches by the ATLAS [26–28] and CMS [29, 30] collaborations; in all other analyses, they are simply ignored.

The final state of a $t\bar{t}$ event therefore depends on the decay channels of the W boson itself. These can be hadronic or leptonic, and are reported in Table 1.3. A full $t\bar{t}$ system can then be reconstructed with four light-flavour jets (all-hadronic), two light-flavour jets and a lepton (semi-leptonic) or two leptons (di-leptonic), and always two b -jets (see Section 3.2). The corresponding branching ratios are given in Table 1.4.

Table 1.3: Branching ratios (in percent) of the main W decay channels. Numbers taken from [20].

Process	Branching ratio
$W \rightarrow q\bar{q}'$	67.41 ± 0.27
$W \rightarrow e\nu_e$	10.71 ± 0.16
$W \rightarrow \mu\nu_\mu$	10.63 ± 0.15
$W \rightarrow \tau\nu_\tau$	11.38 ± 0.21

The τ leptons being themselves unstable particles with a short lifetime ($\tau_\tau \approx 10^{-13}$ s [20]), they are not directly measured in the ATLAS detector and also need to be reconstructed from their decay products, which can be either a mixture of charged and neutral hadrons, or any of the lighter two charged leptons and a τ -neutrino. The branching ratio of this latter process is about 17.39% in the electron channel and 17.82% in the muon channel [20]. The reconstruction of hadronic taus is particularly challenging, while leptonic taus approximately mimic the direct decay of a W boson into an electron or muon. In the SM analyses presented in the next part of this document, tau reconstruction is not considered, and cross sections are corrected for leptonic taus where appropriate.

Table 1.4: Branching ratios (in percent) of the main $t\bar{t}$ decay channels.

Channel	Branching ratio
all-hadronic	45.4
semi-leptonic	
... without τ decays	28.8
... with leptonic τ decays	34.2
... with leptonic+hadronic τ decays	44.1
di-leptonic	
... without τ decays	4.6
... with leptonic τ decays	6.4
... with leptonic+hadronic τ decays	10.7

1.1.2 The Z boson

The direct discovery of the Z boson at the UA1 [31] and UA2 [32] experiments of the Super Proton Synchrotron in 1983 was an early major success for CERN. Neutral current interactions, leaving the interacting particles unaffected up to a transfer of spin and/or momentum (as opposed to charged current interactions, mediated by the W boson), were first observed ten years prior in the Gargamelle bubble chamber at CERN [33, 34] as the scattering of electrons and electron-neutrinos.

The neutral spin-1 mediator of the weak nuclear force, its mass is currently estimated at 91.1876 ± 0.0021 GeV [20], with a decay width $\Gamma = 2.4952 \pm 0.0023$ GeV [20] corresponding to a mean lifetime of $\approx 10^{-25}$ s making its reconstruction from decay products necessary. The main decay channels of the Z boson are summarised in Table 1.5. The Z boson couples to all SM particles except the photon and the gluon, and because of the chiral- and electric-charge-dependence of the

weak interaction, more strongly to down-type quarks than to up-type quarks.

Table 1.5: Branching ratios (in percent) of the main Z decay channels.

Channel	Branching ratio
neutrinos (all)	20.00 ± 0.06
charged leptons (all)	10.097 ± 0.003
... e^+e^-	3.363 ± 0.004
... $\mu^+\mu^-$	3.366 ± 0.007
... $\tau^+\tau^-$	3.367 ± 0.008
hadrons	69.91 ± 0.06
... down-type quarks	15.6 ± 0.4
... up-type quarks	11.6 ± 0.6

1.1.3 Coupling of the top quark to the Z boson

In the SM, the cross section of the generic $t\bar{t} + X$ ($X = Z, W, H, \gamma$) process depends on the particular coupling of the top quark to the additional particle X . Beyond providing an estimation of these important backgrounds to **SUSY** searches, as will be motivated throughout this document, they also offer a unique test of the top quark properties in the SM. The associated production of a $t\bar{t}$ pair and a Z boson is a rare enough process that its cross section falls three orders of magnitude below that of pure $t\bar{t}$ production, with the latest theoretical prediction with NLO+NNLL QCD and NLO **EWK** precision suggesting a pp initiated cross section at $\sqrt{s} = 13$ TeV of [35]

$$\sigma_{t\bar{t}Z}^{\text{theory}} = 0.863_{-0.10}^{+0.09}(\text{scale}) \pm 0.03(\text{PDF}+\alpha_s) \text{ pb.} \quad (1.2)$$

Various decay channels can be utilised when studying the $t\bar{t}Z$ process; the corresponding branching ratios are straightforward multiplications of the numbers previously listed in Tables 1.4 and 1.5. Thinking ahead to our brief survey of the experimental literature, we note that the invisible and hadronic decays of the Z boson make the problem of $t\bar{t}Z$ reconstruction particularly difficult and thus have not been used in any analysis so far. The leptonic channels, usually to electrons and muons to avoid the additional complication of tau identification and reconstruction, are preferred, while the $t\bar{t}$ system is allowed to decay in any of the three modes described in the previous subsection, relying on validated top quark reconstruction techniques. An example of a $t\bar{t}Z$ production Feynman diagram is shown in Figure 1.2.

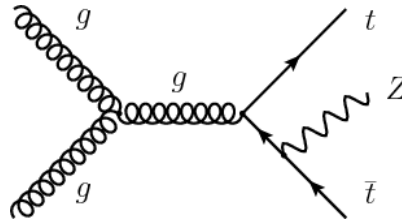


Figure 1.2: Example leading-order Feynman diagram for $t\bar{t}Z$ production, via gluon fusion and splitting into a $t\bar{t}$ pair, before emission of a Z boson via a tZ coupling.

Towards a description of anomalous couplings

In a $t\bar{t}Z$ event, the Z boson can be radiated either from an initial parton (in the case of quark-antiquark initiated $t\bar{t}$ production) or from the final state (anti-)top quark itself (as in Figure 1.2). In the latter case, the coupling of the Z boson and the top quark is directly probed. In the SM, one can write schematically the following Lagrangian describing the interaction in question [36]:

$$\mathcal{L}_{t\bar{t}Z} = e\bar{u}(p_t) \left[\gamma^\mu \left(C_V^{SM} + \gamma_5 C_A^{SM} \right) \right] v(p_{\bar{t}}) Z_\mu \quad (1.3)$$

where e is the electron charge and we've introduced the vector and axial couplings

$$C_V^{SM} = \frac{T_t^3 - 2Q_t \sin^2 \theta_W}{2 \sin \theta_W \cos \theta_W}, \quad (1.4)$$

$$C_A^{SM} = \frac{-T_t^3}{2 \sin \theta_W \cos \theta_W}. \quad (1.5)$$

with Q_t the electric charge of the top quark, T_t^3 its weak isospin and θ_W the Weinberg angle. From previous measurements of these parameters, the following numerical values are obtained [37]:

$$C_V^{SM} \simeq 0.244, \quad (1.6)$$

$$C_A^{SM} \simeq -0.601. \quad (1.7)$$

A number of **Beyond the Standard Model (BSM)** scenarios could influence the interactions between the top quark and the Z boson [38, 39]: extra dimensions, supersymmetry and Little Higgs models, to name but a few. It is useful to turn to a model-independent **Effective Field Theory (EFT)** formulation, where higher-dimensional operators are allowed in the theory, giving rise to new types of interactions of strength quantified by a corresponding Wilson coefficient. The Lagrangian (1.3) can then be rewritten rather compactly as [40]

$$\mathcal{L}_{t\bar{t}Z}^{\text{eff}} = e\bar{u}(p_t) \left[\gamma^\mu \left(C_{1,V} + \gamma_5 C_{1,A} \right) + \frac{i\sigma_{\mu\nu} q_\nu}{M_Z} \left(C_{2,V} + i\gamma_5 C_{2,A} \right) \right] v(p_{\bar{t}}) Z_\mu, \quad (1.8)$$

with $\sigma_{\mu\nu}$ a suitably normalised commutator of Dirac matrices and q_ν the momentum transfer between the top and antitop quarks. The effective couplings $C_{1,V/A}$ correspond to the sum of their SM counterparts plus the contributions of higher-dimensional operators (such as those listed in Table 5.11). The object $\Delta C_i = \frac{C_i}{C_i^{SM}} - 1$ is often found in the literature [41], as any deviation from zero would indicate new physics. We note further that the C_2 couplings are expected to vanish at tree-level in the SM, and receive negligible one-loop corrections. However, these so-called anomalous weak magnetic and electric dipole moments are often enhanced in BSM theories, and the latter term sources **CP**-violation.

Experimental status

The search for $t\bar{t}Z$ production was initiated by the **CMS** collaboration at CERN, which first determined its cross section using 5 fb^{-1} of data at $\sqrt{s} = 7 \text{ TeV}$ to be [42]:

$$\sigma_{t\bar{t}Z} = 0.28_{-0.11}^{+0.15} \text{ pb}, \quad (1.9)$$

in good agreement with the corresponding SM prediction at NLO precision of $0.137_{-0.016}^{+0.012} \text{ pb}$ [43]. The analysis used only events with three leptons and reached a signal significance (over the background-only hypothesis) of 3.3σ , classifying it as “evidence” for $t\bar{t}Z$ production.

Using the 19.5 fb^{-1} dataset at $\sqrt{s} = 8 \text{ TeV}$ and an additional channel with four leptons, the CMS collaboration measured [44]:

$$\sigma_{t\bar{t}Z} = 0.200_{-0.076}^{+0.089} \text{ pb}, \quad (1.10)$$

with a significance of 3.1σ , again agreeing within uncertainties with the theoretical prediction of $0.206_{-0.024}^{+0.019}$ [43]. Only when repeating this last measurement with the inclusion of a dilepton channel and full event reconstruction, using the kinematics of the leptons and top quarks as inputs for a multivariate analysis, was the CMS collaboration able to claim discovery, reaching a significance of 6.4σ and an updated cross section of [45]:

$$\sigma_{t\bar{t}Z} = 0.242_{-0.055}^{+0.065} \text{ pb}. \quad (1.11)$$

This measurement also included a first set of experimental limits on the vector and axial anomalous couplings $C_{1,V}$ and $C_{1,A}$ (discussed in the previous subsection) and reported in Figure 1.3. No deviation from the SM prediction is observed in either component of the t - Z coupling.

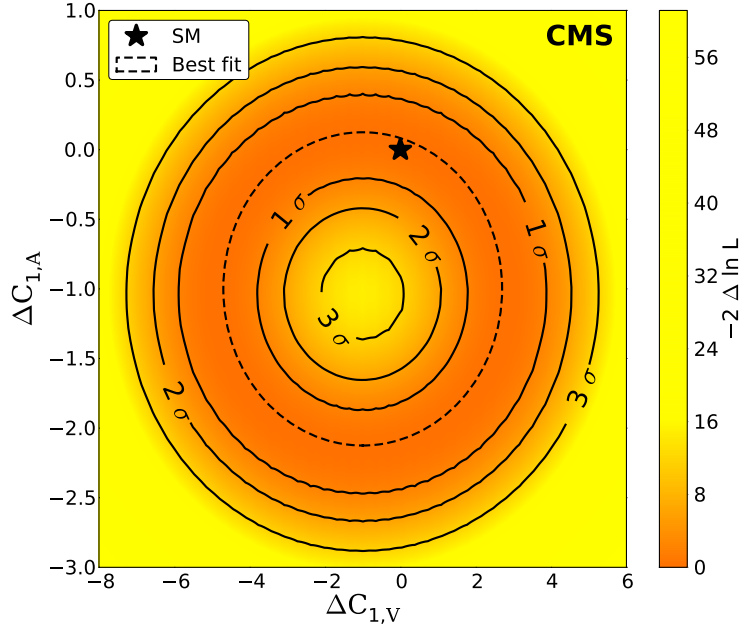


Figure 1.3: Difference between the profile likelihood and the best fit profile likelihood functions for the relative vector and axial components of the t - Z coupling. Contours corresponding to the best fit and the 1, 2, and 3 standard deviation (σ) CLs are shown in lines. From [45].

The ATLAS collaboration only performed a single measurement using 20.3 fb^{-1} of pp collisions at $\sqrt{s} = 8 \text{ TeV}$, reporting an observation with a significance of 4.2σ in final states with at least two leptons and a cross section [46]:

$$\sigma_{t\bar{t}Z} = 0.176_{-0.052}^{+0.058} \text{ pb}. \quad (1.12)$$

Using only the final states with three or four leptons, the ATLAS collaboration finally provided the first measurement at $\sqrt{s} = 13 \text{ TeV}$, using a preliminary 3.2 fb^{-1} dataset [47]:

$$\sigma_{t\bar{t}Z} = 0.9 \pm 0.3 \text{ pb}, \quad (1.13)$$

with a signal significance of 3.9σ . We conclude this review of previous experimental measurements of the inclusive $t\bar{t}Z$ cross section by noting that, although displaying generally good agreement with the corresponding SM predictions, they are still limited by systematic uncertainties (above the $\sim 15\%$ level) and even more strongly so by statistics ($\sim 30\%$).

1.2 Limitations of the Standard Model

The SM contains 19 free parameters, which need to be determined experimentally: the masses of the three charged leptons and six quarks, three flavour-mixing parameters and one CP-violating phase in the quark sector, the three gauge couplings of G_{SM} , the Higgs mass and vacuum expectation value, and the QCD vacuum angle. Note that the putative masses of the neutrinos are not part of the current description of the SM, even though upper bounds are indicated in Table 1.1: this is a direct consequence of both the experimental observation of neutrino flavour oscillation and the experimental absence of right-handed neutrinos. These two facts combined preclude the addition of a Yukawa (i.e. Higgs-fermion) coupling for the neutrinos, which remain theoretically massless; an extension of the SM is therefore motivated.

The lack of experimental evidence for CP-violation in the strong sector, and the correspondingly small values allowed for the QCD vacuum angle θ_{CP} , provides another tension with the SM, in the form of a fine-tuning problem [48]. A possible solution, the Peccei-Quinn mechanism [49, 50], requires the addition of a new light pseudo-Goldstone boson, the axion. Gravity, the fourth fundamental force of physics, has also not yet been given a quantum mechanical description (quantum gravity) and its graviton therefore remains purely hypothetical. Moreover, numerous attempts at merging the strong and electroweak forces under one common gauge theory at high enough energies (grand unification), a common approach to building models of particle physics beyond the Standard Model (BSM), remain invalidated by experimental tests of their phenomenological predictions or simply beyond the reach of current technology [51–54].

1.2.1 Dark Matter

One of the most significant changes of paradigm in astroparticle physics within the last century is the realisation that ordinary, baryonic, luminous matter (the first generation of quarks and leptons) cannot provide a sufficient description of the matter content of the Universe [55, 56]. The early studies in the 1930’s of the motions of galaxies by Oort [57] and Zwicky [58], later systematised by Rubin in the 1970’s [59–61], led to the observation that the rotational velocities of stars within these galaxies, expected to follow the classical Keplerian law $v(r) \propto r^{-1/2}$ as a function of the radius r of their orbit, instead exhibited “flat” rotation curves with a constant velocity after some distance from the centre of the galaxy. Since this is where most of the luminous mass is concentrated, if one wishes to preserve the rule of classical gravity “the conclusion is inescapable” [62]: there must be an abundant form of non-luminous, massive matter component distributed in and around galaxies. This new matter component is **Dark Matter (DM)**.

The observation in 1979 by Walsh et al. [63] of gravitational lensing from “invisible” sources further lent credence to the Dark Matter hypothesis [64], and prompted common efforts across the astrophysical and cosmological community to explore its consequences. It is now clearly established that no particle in the SM can play the role of DM, as the latter must be stable, electrically neutral, non-relativistic and only weakly interacting. Its inclusion in standard cosmology led to the development of the so-called “Lambda-CDM” model [65, 66] (combining a cosmological constant Λ for dark energy, and “cold” Dark Matter) and the measurement of the DM density parameter $\Omega_c = 0.2589 \pm 0.0057$ [67]; in other words, DM represents roughly 26% of the energy content of the Universe and accounts for 84% of all matter.

The application of simple thermodynamics principles to the early Universe in the presence of a

DM candidate, and the attempt to match its mass and self-annihilation cross section to the current observed cosmological parameters produces a fortuitous coincidence: the candidate in question must resemble a ~ 100 GeV particle interacting with the same strength as the electroweak force. This surprising result promises a [Weakly Interacting Massive Particle \(WIMP\)](#) that could be within reach of modern particle colliders; this is the “WIMP miracle” [68].

1.2.2 The hierarchy problem

The Higgs sector of the SM Lagrangian yields another major phenomenological issue [69–71]. It contains self-coupling and kinematic terms, while the effective mass of the Higgs boson receives corrections from the coupling of the Higgs to all other massive particles. At the one-loop level, these are proportional both to the Yukawa couplings and to the cutoff scale of the theory, which from the quantum gravity argument alluded to in the previous paragraph is understood to be around the Planck mass ($\sim 10^{19}$ GeV). From the running of the SM gauge couplings, it can also be argued that grand unification, if it is indeed realised in Nature, could take place at energies of order 10^{16} GeV [72, 73]. It remains that a large gap (“desert”) is likely to exist between the physics of the SM, around the electroweak scale of $\sim 10^2$ GeV, and any theoretical completion of the SM, which is in turn understood to act only as an [EFT](#). The top quark has the largest Yukawa coupling, $y_t \simeq 1$ [20], and is therefore responsible for the main contribution to the effective Higgs mass.

The Higgs potential can be schematically written as

$$V = \mu^2 |\phi|^2 + \lambda |\phi|^4, \quad (1.14)$$

where $\mu^2 < 0$ is a requirement for the spontaneous symmetry breaking of $SU(2)_L \times U(1)_Y$ to $U(1)_{EM}$, leading to the massive electroweak W^\pm and Z gauge bosons and the massless photon. However, μ itself isn’t predicted by the SM: it is a renormalisable coupling that receives radiative corrections from Yukawa couplings of particles up to the upper scale Λ of validity of the SM as an EFT. Taking the bare Higgs mass to be some μ_0 and considering only the top quark Yukawa as the largest contribution, we have

$$\mu^2 = \mu_0^2 + \frac{3\Lambda^2}{8\pi^2} \left(\lambda - y_t^2 + \mathcal{O}\left(m_t^2 \ln \frac{\Lambda}{m_t}\right) \right). \quad (1.15)$$

The first term in the bracket corresponds to the Higgs self-interaction, the second to the top quark loop. In order to maintain an experimentally consistent mass term $\sqrt{2}|\mu| \approx m_h^{\text{exp}}$, the bare parameter μ_0 needs to be extremely finely tuned (to the level of one part in 10^{34}); this is the hierarchy problem.

Broadly speaking, two approaches can be taken in solving the hierarchy problem: setting $\Lambda \lesssim 1$ TeV and postulating a non-elementary Higgs boson (e.g. technicolor, composite Higgs models), or setting $\Lambda \sim \mathcal{O}(10^{16})$ TeV with an additional symmetry forbidding the mass term in the Higgs potential at high energies (the Higgs mass becomes “protected”). Within the second approach, three types of symmetry can be considered, depending on their action on the Higgs field: scalar, gauge or fermionic. These lead, respectively, to so-called “little Higgs” models, extra dimensions and supersymmetry.

1.3 Supersymmetry

The term “supersymmetry” ([SUSY](#)) [74–80] refers to a paradigm (rather than a single theory) under which new space-time symmetries are allowed, with direct phenomenological consequences. We want to stress here a point of major conceptual importance: SUSY was first developed as a

generalisation of space-time symmetries in [Quantum Field Theory \(QFT\)](#), before the realisation that it provides solutions to a number of limitations of the SM. In this context, it is indeed possible to stabilise the Higgs mass, providing a natural evasion of fine-tuning in its quantum corrections, predict various Dark Matter candidates, provide a framework for sterile neutrinos (and hence neutrino masses) and axions (solving the strong CP problem), unify the electroweak and strong interactions, as well as provide a strong basis for string theory to yield a possible description of quantum gravity. Crucially, we maintain that these are phenomenological consequences, indisputably of great interest, of a more fundamental question in mathematical physics.

1.3.1 Superalgebras, superspaces and superfields

The Poincaré group contains the isometries of the Minkowski spacetime (with metric $\eta_{\mu\nu}$ mostly negative), understood in physics as the symmetries of special relativity; namely: rotations, translations and boosts. In that sense it contains both the translation and Lorentz groups as subgroups, and can be written as the semidirect product $\mathbf{R}^{1,3} \rtimes \text{SL}(2, \mathbb{C})$. The corresponding generators are denoted P_μ and $M_{\mu\nu}$ and satisfy [\[81, 82\]](#):

$$[P_\mu, P_\nu] = 0 \quad (1.16)$$

$$[M_{\mu\nu}, P_\rho] = i(\eta_{\mu\rho}P_\nu - \eta_{\nu\rho}P_\mu) \quad (1.17)$$

$$[M_{\mu\nu}, M_{\rho\sigma}] = i(\eta_{\mu\rho}M_{\nu\sigma} - \eta_{\mu\sigma}M_{\nu\rho} - \eta_{\nu\rho}M_{\mu\sigma} + \eta_{\nu\sigma}M_{\mu\rho}) \quad (1.18)$$

The Coleman-Mandula theorem [\[81\]](#) states that any QFT with a finite particle content that describes non-trivial interactions and scattering, can only have the direct product $\mathbf{R}^{1,3} \rtimes \text{SL}(2, \mathbb{C}) \times G$ (with G an appropriate internal group) as the Lie group. This statement is the basis of traditional model-building for [BSM](#) theories: only the gauge group G can be extended and it never mixes with the Poincaré group.

The “no-go” conclusions of the Coleman-Mandula theorem can be circumvented by non-trivially extending the Poincaré algebra itself [\[75, 76\]](#), to contain a spinor structure that anticommutes to connect with the usual “bosonic” part. One introduces two Weyl fermions, the SUSY charges, which combine to form the only allowed 4-vector conserved charge, namely P_μ ; the SUSY charges can be seen as “taking the square root of momentum” (as in the case of the Dirac and Klein-Gordon equations), and must connect fermionic dimensions with the Minkowski spacetime.

$$\{Q_\alpha, \bar{Q}_\beta\} = 2(\sigma^\mu)_{\alpha\beta} P_\mu \quad (1.19)$$

$$[Q_\alpha, P^\mu] = 0 \quad (1.20)$$

$$[M^{\mu\nu}, Q_\alpha] = \frac{1}{2}(\sigma^{\mu\nu})_\alpha^\beta Q_\beta \quad (1.21)$$

The dotted and undotted Greek indices are spinor indices, used to distinguish the representations of the Lorentz group with opposite chirality (essentially, although not exactly, $SU(2) \times SU(2)$). Haag, Lopuszański and Sohnius demonstrated, in a theorem [\[83\]](#) that bears their name, that the generators of the most general symmetry group enjoyed by the S-matrix must reside within the direct sum of the super-Poincaré Lie algebra and another internal Lie algebra.

Extending Minkowski spacetime to accommodate four fermion-like dimensions [\[83\]](#), labeled by the Grassmann numbers θ^α and $\theta_{\dot{\alpha}}^\dagger$, we can define a superspace, which allows for two elegant simplifications of the typical SUSY treatment: i) the various fields that belong in a same supermultiplet can be expressed as a single object, superfield; ii) SUSY field transformations become translations on this space. Indeed, the SUSY central charges can be written as differential operators

of the superspace coordinates, as:

$$Q_\alpha = i \frac{\partial}{\partial \theta^\alpha} - (\sigma^\mu \theta^\dagger)_\alpha \partial_\mu \quad (1.22)$$

$$Q_\beta^\dagger = -i \frac{\partial}{\partial \theta^{\beta\dagger}} + (\theta \sigma^\mu)_\beta \partial_\mu \quad (1.23)$$

from which Equation (1.19) can be recovered.

It's precisely because the supercharges are functions of the triplet $(x, \theta, \bar{\theta})$ and that they mix the three coordinates that the resulting commutators of infinitesimal transformations don't commute, and a non-trivial S-matrix is achievable overall. Under the action of the SUSY charges, the superspace coordinates transform as:

$$x^\mu \rightarrow x^\mu + i \epsilon \sigma^\mu \theta^\dagger + i \epsilon^\dagger \bar{\sigma}^\mu \theta \quad (1.24)$$

$$\theta \rightarrow \theta + \epsilon \quad (1.25)$$

$$\theta^\dagger \rightarrow \theta^\dagger + \epsilon^\dagger \quad (1.26)$$

Having set up general coordinates, one can naturally start building functions out of them; these are the superfields $S(x, \theta, \bar{\theta})$, ultimately the building blocks of any SUSY Lagrangian. They transform locally under the action of the SUSY charges:

$$\sqrt{2} \delta_\epsilon S = -i (\epsilon Q + \epsilon^\dagger Q^\dagger) S = S(z') - S(z). \quad (1.27)$$

Because we need to extract the x^μ component, we expand S in the most general possible way as:

$$S = a + \theta \xi + \theta^\dagger \chi^\dagger + \theta \theta b + \theta^\dagger \theta^\dagger c + \theta^\dagger \bar{\sigma}^\mu \theta v_\mu + \theta^\dagger \theta^\dagger \theta \eta + \theta \theta \theta^\dagger \zeta^\dagger + \theta \theta \theta^\dagger \theta^\dagger d, \quad (1.28)$$

where (a, b, c, d) are scalar fields, (ξ, χ, η, ζ) are 2-component Weyl spinors and v_μ is a vector field. Since the Grassmann variables (θ, θ^\dagger) anticommute with any combination of indices, we are assured that the above expansion contains only repeated indices and any term built out of three or more such Grassmann variables vanishes identically; in other words, Equation (1.28) is finite and complete.

However, being the most general superfield expansion, S transforms in a reducible representation of the superalgebra. In order to form correct supermultiplets, one needs to impose covariant constraints, using the SUSY covariant derivative:

$$D^{\dagger\dot{\alpha}} = \frac{\partial}{\partial \theta^{\dot{\alpha}}} - i (\bar{\sigma}^\mu \theta)^{\dot{\alpha}} \partial_\mu. \quad (1.29)$$

For example, a chiral superfield Φ is obtained by setting

$$D^{\dagger\dot{\alpha}} \Phi = 0, \quad (1.30)$$

which reduces the expansion in Equation (1.28) to

$$\Phi(x, \theta, \bar{\theta}) = \phi(x) + \sqrt{2} \theta \psi(x) + \theta^2 F(x) + \text{spacetime derivatives}, \quad (1.31)$$

where ϕ is a complex scalar, ψ a 2-component left-handed Weyl spinor and F a non-propagating complex scalar (the so-called auxiliary field, which plays a role in SUSY breaking). A general SUSY Lagrangian can be built out of Φ and its complex conjugate only as

$$\mathcal{L} = \Re(\Phi, \Phi^\dagger) + \Im(\Phi) + \Im^\dagger(\Phi^\dagger), \quad (1.32)$$

where \mathfrak{K} is the Kähler potential and \mathfrak{W} the superpotential. A specific example is the Wess-Zumino model [77, 78] (renormalizable), defined by choosing the potentials

$$\mathfrak{K} = \Phi^\dagger \Phi, \quad \mathfrak{W} = \frac{m}{2} \Phi^2 + \frac{\lambda}{3} \Phi^3, \quad (1.33)$$

which, plugging in the expansion of Φ , leads to the Wess-Zumino Lagrangian

$$\mathcal{L}_{WZ} = -\partial_\mu \phi \partial^\mu \bar{\phi} + i \bar{\psi} \sigma^\mu \partial_\mu \psi - \frac{m}{2} (\phi^2 + \bar{\phi}^2) - \lambda \phi \psi^2 - \lambda \bar{\phi} \bar{\psi}^2 - |m\phi - \lambda\phi^2|^2. \quad (1.34)$$

One can understand \mathcal{L}_{WZ} as a ϕ^4 theory for a massive complex scalar ϕ , with a Yukawa coupling to a left-handed Weyl spinor ψ with the same mass.

An important conceptual point has been reached: by the properties of superspace itself, scalars (bosons) and spinors (fermions) are necessarily packaged in the same superfield (chiral supermultiplet), which is then used to build SUSY Lagrangians. A similar argument links vector bosons to fermions in so-called gauge supermultiplets). Supersymmetry is finally understood as an “exchange symmetry” between bosonic and fermionic degrees of freedom.

1.3.2 Elements of phenomenology

Out of the wide variety of phenomenological models built according to the basic description of SUSY we’ve outlined so far, the minimal supersymmetric extension to the Standard Model (MSSM) stands out [84, 85]. While bringing out a new set of 120 free parameters (reducible to 19 by requesting no new source of CP-violation, no flavour-changing neutral currents and a degeneracy of the first and second generations of squark and slepton mass eigenstates, in the so-called phenomenological MSSM or pMSSM [86, 87]), the MSSM was originally constructed to address directly the hierarchy problem presented in Section 1.2.2. We will now briefly explore its phenomenology and simply note that similar arguments can be carefully extended to other models, such that not one but various SUSY-flavoured solutions to the limitations of the SM can be considered [88].

The superfield content of the MSSM is made explicit in Tables 1.6 and 1.7 below. While most SM fields receive a relative $\pm \frac{1}{2}$ -spin supersymmetric partner, we note the special case of the Higgs sector, where two Higgs supermultiplets are introduced. This apparent complication serves in fact a dual purpose: avoiding gauge anomalies arising from the triangle diagrams of a single Higgsino, and generating mass terms for the up- and down-type quarks separately.

Table 1.6: Chiral supermultiplets in the MSSM and their representation under the $SU(3)$, $SU(2)$ and $U(1)$ gauge groups.

Particles	Spin-0	Spin-1/2	Representation	
Quarks, squarks	Q	$(\tilde{u}_L \tilde{d}_L)$	$(u_L d_L)$	$(\mathbf{3}, \mathbf{2}, +1/6)$
	\bar{u}	\tilde{u}_R^*	u_R^\dagger	$(\bar{\mathbf{3}}, \mathbf{1}, -2/3)$
	\bar{d}	\tilde{d}_R^*	d_R^\dagger	$(\bar{\mathbf{3}}, \mathbf{1}, +1/3)$
Leptons, sleptons	L	$(\tilde{\nu} \tilde{e}_L)$	(νe_L)	$(\mathbf{1}, \mathbf{2}, -1/2)$
	\bar{e}	\tilde{e}_R^*	e_R^\dagger	$(\mathbf{1}, \mathbf{1}, +1)$
Higgs, higgsinos	H_u	$(H_u^+ H_u^0)$	$(\tilde{H}_u^+ \tilde{H}_u^0)$	$(\mathbf{1}, \mathbf{2}, +1/2)$
	H_d	$(H_d^+ H_d^0)$	$(\tilde{H}_d^+ \tilde{H}_d^0)$	$(\mathbf{1}, \mathbf{2}, -1/2)$

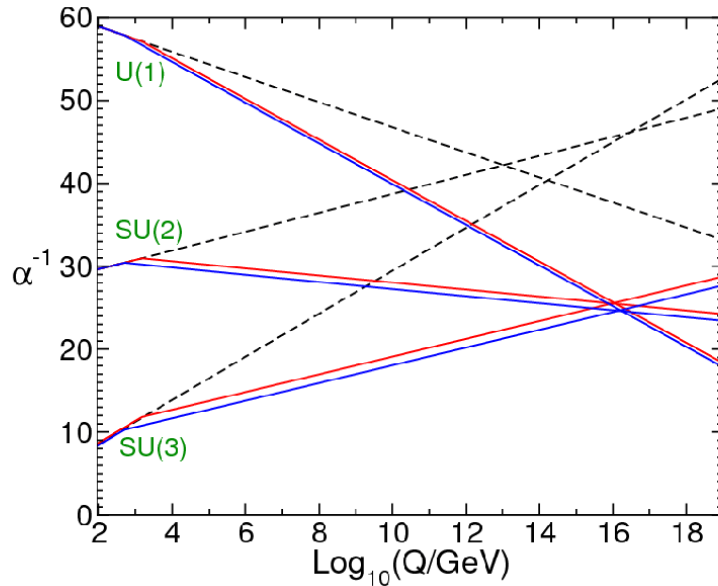
Table 1.7: Gauge supermultiplets in the MSSM and their representation under the $SU(3)$, $SU(2)$ and $U(1)$ gauge groups.

Particles	Spin-1/2	Spin-1	Representation
Gluon, gluino	\tilde{g}	g	$(\mathbf{8}, \mathbf{1}, 0)$
W bosons, winos	$\tilde{W}^\pm, \tilde{W}^0$	W^\pm, W^0	$(\mathbf{1}, \mathbf{3}, 0)$
B boson, binos	\tilde{B}^0	B^0	$(\mathbf{1}, \mathbf{1}, 0)$

Up until this point, we have assumed the masses of the new superpartners to be exactly that of their SM counterparts. This formulation of unbroken SUSY is particularly attractive since it solves, by construction, the hierarchy problem: the fermionic contribution of the top quark to the effective Higgs mass is exactly balanced by that of its scalar superpartner (which introduces an opposite-sign term of the same magnitude). The lack of experimental evidence for equally massive superpartners of different spin points to the realisation of broken SUSY. The so-called “soft” breaking of SUSY [89–91] yields corrections to the bare Higgs mass proportional to the corresponding scale m_{soft}^2 , such that a natural solution to the hierarchy problem is preserved if m_{soft} is not too large ($\lesssim 1$ TeV).

After symmetry breaking, the superpartners described so far mix to produce a variety of mass eigenstates. The neutral bosinos (bino, wino and Higgsino) end up forming four neutral particles, the neutralinos $\tilde{\chi}_i^0$ (where the index i runs from 1 to 4 in ascending order of mass). Likewise, the two charginos $\tilde{\chi}_i^\pm$ arise from the mixing of the charged winos and Higgsinos. In the squark and slepton sectors, the mixing is proportional to the mass of the SM partner particle, such that it is only non-negligible in the third generations, yielding two top squarks (“stop”) \tilde{t}_1 and \tilde{t}_2 from the original \tilde{t}_L and \tilde{t}_R , and similarly for the bottom squarks (“sbottom”) and the stau leptons.

This extended particle content turns out to be enough to change the running of the gauge coupling constants such that grand unification can take place at $\sim \mathcal{O}(10^{16})$ GeV [69–71, 92]. Figure 1.4 clearly shows the difference in convergence between the running predicted from the particles of the SM alone and the full MSSM.

Figure 1.4: Running of the gauge couplings in the SM (dashed lines) and the MSSM (solid lines), showing unification at a scale $\mathcal{O}(10^{16})$ GeV.

1.3.3 R-parity

Within the MSSM, and in general within grand unified theories incorporating $SU(5)$, processes exist that allow for proton decay. In its simplest form, the superpotential of the MSSM can be expressed as

$$\mathfrak{W}_{\text{MSSM}} = \bar{u}_i \mathbf{y}_u Q_i H_u - \bar{d}_j \mathbf{y}_d Q_j H_d - \bar{e}_k \mathbf{y}_e L_k H_d + \mu H_u H_d, \quad (1.35)$$

in terms of the chiral supermultiplets listed in Table 1.6 and of the 3×3 (in family-space) Yukawa matrices \mathbf{y} . These are the supersymmetric equivalents of the usual quark and lepton Higgs terms in the SM, with μ the Higgsino mass parameter. One could however add the following terms to the superpotential, which violate lepton (L) and baryon (B) number conservation by one unit, respectively:

$$\mathfrak{W}_{\Delta L=1} = \frac{1}{2} \lambda^{ijk} L_i L_j \bar{e}_k + \lambda'^{ijk} L_i Q_j \bar{d}_k + \mu'^i L_i H_u, \quad (1.36)$$

$$\mathfrak{W}_{\Delta B=1} = \frac{1}{2} \lambda''^{ijk} \bar{u}_i \bar{d}_j \bar{d}_k, \quad (1.37)$$

where the index i runs over the three generations of (s)fermions. The baryon number B is $+1/3$ for Q_i and $-1/3$ for \bar{u}_i and \bar{d}_i (and zero otherwise), while the lepton number L is $+1$ for L_i and -1 for \bar{e}_i (and zero otherwise), such that the two expressions above indeed lead to B - and L -violation. Proton decay requires $\Delta B = 1$ and $\Delta L = 1$, and therefore unsuppressed λ' and λ'' couplings. A possible decay diagram is given in Figure 1.5 for the \tilde{s} -mediated $p^+ \rightarrow e^+ \pi^0$ channel; other final states, such as $\mu^+ \pi^0$, $\bar{\nu} \pi^+$ or $\bar{\nu} K^+$ are also possible. From dimensional analysis, the corresponding decay width can be formulated as

$$\Gamma_{p^+ \rightarrow e^+ \pi^0} \sim m_{\text{proton}}^5 \sum_i \frac{|\lambda'^{11i} \lambda''^{11i}|^2}{m_{\tilde{d}_i}^4}, \quad (1.38)$$

giving rise to a proton half-life much smaller than a second for $\lambda'^{11i} \sim \lambda''^{11i} \sim 1$ and squark masses at the TeV scale.

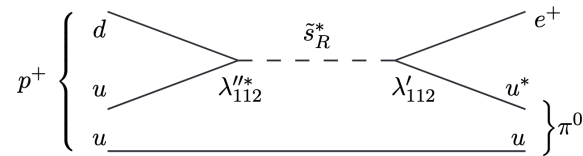


Figure 1.5: B - and L -violating proton decay to a positron and neutral pion, via an internal strange squark line.

The experimental non-observation of such a phenomenon, most notably by the Super-Kamiokande experiment [93], sets lower bounds on the lifetime of the proton $\sim \mathcal{O}(10^{34}$ yrs.). To avoid having to suppress these processes by moving the SUSY scale to much larger values (and losing the natural solution to the hierarchy problem [94, 95]), it is possible to invoke an ad-hoc \mathbb{Z}_2 symmetry to forbid baryon and lepton number violating couplings, still permitting such violations in tiny amount via non-perturbative effects but eventually preventing proton decay. This R -parity is defined [96], for a particle with baryon and lepton numbers B and L , and spin S , as

$$P_R = (-1)^{3(B-L)+2S}. \quad (1.39)$$

R -odd particles are defined to be the SUSY partners, while R -even particles are the SM counterparts, and R -parity itself is conserved multiplicatively.

A number of important conclusions can be drawn from the conservation of this symmetry: i) sparticles can only decay to an odd number of daughter sparticles (leading to so-called cascade decays); ii) in pp collisions at the LHC, sparticles can only be produced in pairs; iii) the [Lightest Supersymmetric Particle \(LSP\)](#) is a stable massive state (hence, if uncharged, a natural candidate for Dark Matter) [97, 98].

In Part III of this document, we will refer to MSSM-inspired R -parity-conserving models, whereby the supersymmetric partner to the top quark is the lightest squark and the neutralino, taken to be the LSP, is a suitable Dark Matter candidate.

1.3.4 Third generation and naturalness

The left- and right-handed squarks can undergo mixing to produce a new set of mass eigenstates. This mixing is proportional to the Yukawa couplings of their SM counterparts (and so to their masses), such that it is only relevant in the third generation. This suppressed mixing of the first and second generations of squarks (and similarly, sleptons) results in a mass degeneracy at much higher values than the stop and sbottom masses. Schematically, the MSSM Lagrangian contains a term:

$$\mathcal{L}_{\text{stop masses}} = - \begin{pmatrix} \tilde{t}_L^* & \tilde{t}_R^* \end{pmatrix} \mathbf{m}_{\tilde{t}}^2 \begin{pmatrix} \tilde{t}_L \\ \tilde{t}_R \end{pmatrix}, \quad (1.40)$$

where

$$\mathbf{m}_{\tilde{t}}^2 = \begin{pmatrix} m(\tilde{t}_L)^2 & m_t (A_t - \mu \cot \beta) \\ m_t (A_t - \mu \cot \beta) & m(\tilde{t}_R)^2 \end{pmatrix}, \quad (1.41)$$

with

$$m(\tilde{t}_L)^2 = m_{Q_3}^2 + m_t^2 + \left(\frac{1}{2} - \frac{2}{3} \sin^2 \theta_W \right) \cos(2\beta) m_Z^2 \quad (1.42)$$

$$m(\tilde{t}_R)^2 = m_{u_3}^2 + m_t^2 + \frac{2}{3} \sin^2 \theta_W \cos(2\beta) m_Z^2. \quad (1.43)$$

Here, A_t is the top squark trilinear coupling (a soft SUSY breaking term), μ is the Higgsino mass parameter, $\tan \beta$ is the ratio of the two Higgs vacuum expectation values and $m_{Q_3}^2$ and $m_{u_3}^2$ are the scalar squared masses. By diagonalising the matrix $\mathbf{m}_{\tilde{t}}^2$ above, one obtains the stop mass eigenstates through mixing of the left- and right-handed components:

$$\begin{pmatrix} \tilde{t}_1 \\ \tilde{t}_2 \end{pmatrix} = \begin{pmatrix} \cos \theta_{\tilde{t}} & -\sin \theta_{\tilde{t}} \\ \sin \theta_{\tilde{t}} & \cos \theta_{\tilde{t}} \end{pmatrix} \begin{pmatrix} \tilde{t}_L \\ \tilde{t}_R \end{pmatrix} \quad (1.44)$$

with the angle $\theta_{\tilde{t}}$ parameterising the mixing. The off-diagonal entries of $\mathbf{m}_{\tilde{t}}^2$, proportional to the large mass of the SM top quark, introduce significant mixing which always leads to $m_{\tilde{t}_1}^2 < m_{\tilde{t}_2}^2$ and in general to a large gap between the third generation squark masses and those of the previous two generations. A common prediction of MSSM-inspired models is the \tilde{t}_1 state as the lightest

squark [99, 100], with a large right-handed component (which in turn can influence its favoured decay channels).

For the purpose of driving the analysis of ATLAS data, simplified models [101–103] are used in the optimisation of the searches, whereby only a few massive states of interest are considered, while the rest of the MSSM spectrum is taken to be decoupled and out of the energy reach of the LHC. This approach usually leads to clear signal signatures, whose kinematics however differ depending on the choice of masses. A range of such simplified models can then be combined to re-interpret either an excess in data or an exclusion limit, in terms of more realistic and complex SUSY models.

Assuming a Yukawa coupling for the top squark of equal magnitude, but crucially of opposite sign, to that of the SM top quark, the radiative correction to the Higgs mass induced by the sfermion loop cancels that of the top quark. We can write the physical Higgs mass, m_h , in terms of the bare parameter $m_{h,0}$ and the corrections from the extended top quark sector:

$$m_h^2 = m_{h,0}^2 + \Delta m_{h,t,\tilde{t}}^2, \quad (1.45)$$

with

$$\Delta m_{h,t,\tilde{t}} = \Delta m_t^2 + \Delta m_{\tilde{t}}^2 = \frac{y_t^2}{16\pi^2} |m_{\tilde{t}_1}^2 - m_t^2|. \quad (1.46)$$

Following [104], a quantitative measure of the amount of fine-tuning needed in order to restore $m_h = m_{h,\text{exp}}$ is

$$\Delta \equiv \frac{2\Delta m_{h,t,\tilde{t}}^2}{m_{h,0}^2}, \quad (1.47)$$

such that small values of $\Delta \lesssim 1$ are said to *naturally* solve the hierarchy problem. Requiring such a natural solution and enforcing the experimental constraint $m_{h,0}^2 = m_{h,\text{exp}}^2 - \Delta m_{h,t,\tilde{t}}^2$, we get

$$\Delta = \frac{2}{\frac{m_{h,\text{exp}}^2}{\Delta m_{h,t,\tilde{t}}^2} - 1} \lesssim 1 \iff \frac{16\pi^2 m_{h,\text{exp}}^2}{3y_t^2} \gtrsim |m_{\tilde{t}_1}^2 - m_t^2| \quad (1.48)$$

which, using the approximate values $m_{h,\text{exp}}^2 = (125 \text{ GeV})^2$ and $y_t = 0.94$, yields a naturalness condition on the stop mass

$$|m_{\tilde{t}_1}^2 - m_t^2| \lesssim 1 \text{ TeV}^2. \quad (1.49)$$

A similar argument can be made for the bottom and sbottom corrections to the Higgs mass, and one ends up with a reduced particle spectrum when dealing with natural SUSY: top and bottom squarks at around 1 TeV [104], light Higgsinos generating a WIMP-like Dark Matter candidate (the neutralino) and possibly a heavy gluino (leading to a more rich topology of the ensuing cascade decay). All other superpartners can be taken to be decoupled, at a much larger mass scale, without spoiling the SUSY solution to the hierarchy problem.

1.3.5 Searches for light stops at the LHC

The earliest recorded search for the direct pair production of the supersymmetric partner to the top quark in the all-hadronic final state at the LHC was performed [105] by the ATLAS collaboration, using 4.7 fb^{-1} of pp collisions at $\sqrt{s} = 7 \text{ TeV}$. Stop masses in the range $370 < m_{\tilde{t}_1} < 465 \text{ GeV}$ were excluded for $m_{\tilde{\chi}_1^0} \approx 0 \text{ GeV}$, while $m_{\tilde{t}_1} = 445 \text{ GeV}$ was excluded for $m_{\tilde{\chi}_1^0} < 50 \text{ GeV}$. A further search [106] using 20.1 fb^{-1} of data at $\sqrt{s} = 8 \text{ TeV}$ yielded stronger exclusion bounds of $270 < m_{\tilde{t}_1} < 645 \text{ GeV}$ for $m_{\tilde{\chi}_1^0} < 30 \text{ GeV}$. The corresponding excluded region in the $(m_{\tilde{t}_1}, m_{\tilde{\chi}_1^0})$ plane is shown fully in Figure 1.6 and compared to that of the previous result at $\sqrt{s} = 7 \text{ TeV}$.

Using the complete 18.9 fb^{-1} dataset at $\sqrt{s} = 8 \text{ TeV}$, the CMS collaboration [107] produced extended limits, excluding $m_{\tilde{t}_1} < 775 \text{ GeV}$ for $m_{\tilde{\chi}_1^0} < 200 \text{ GeV}$. In an early Run 2 search [108], with only 2.3 fb^{-1} of data at $\sqrt{s} = 13 \text{ TeV}$, a similar result of $m_{\tilde{t}_1} < 740 \text{ GeV}$ for $m_{\tilde{\chi}_1^0} < 240 \text{ GeV}$ was obtained. The corresponding full exclusion limits are shown in Figure 1.7.

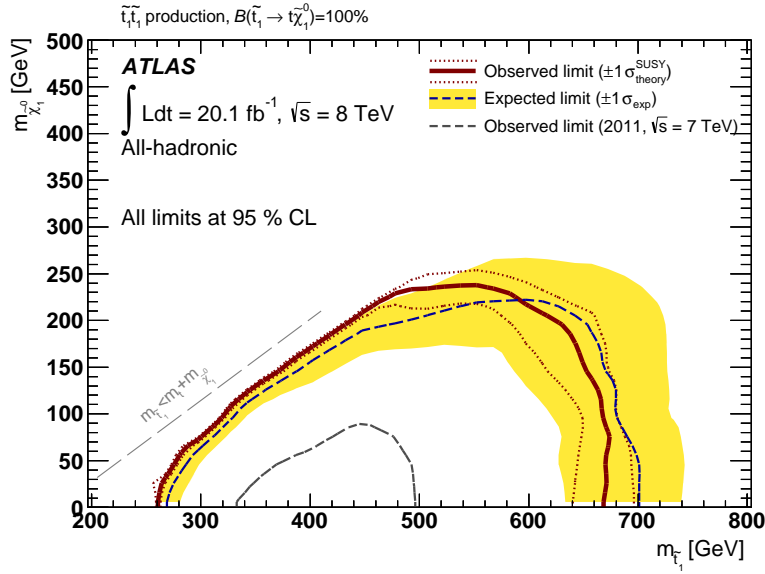


Figure 1.6: Exclusion contours at 95% CL in the scenario where both top squarks decay exclusively via $\tilde{t}_1 \rightarrow t + \tilde{\chi}_1^0$ and the top quark decays hadronically. The blue dashed line indicates the expected limit, and the yellow band indicates the $\pm 1\sigma$ uncertainties, which include all uncertainties except the theoretical uncertainties in the signal. The red solid line indicates the observed limit, and the red dotted lines indicate the sensitivity to $\pm 1\sigma$ variations of the signal theoretical uncertainties. The observed limit from the all-hadronic $\sqrt{s} = 7 \text{ TeV}$ is overlaid for comparison. From [106].

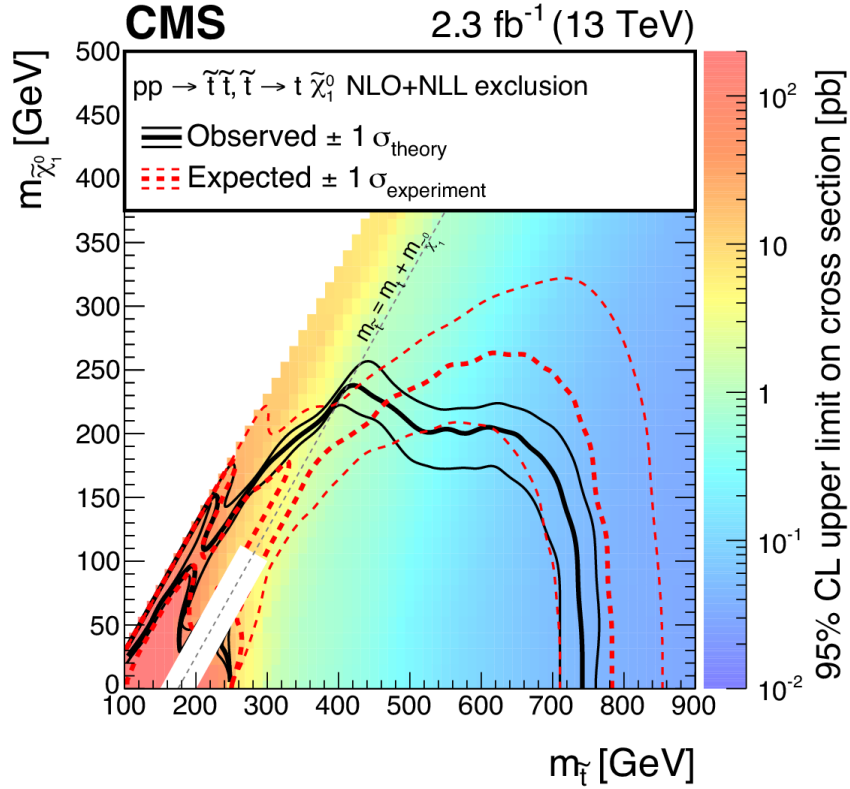


Figure 1.7: Exclusion limits at 95% CL for simplified models of top squark pair production in the exclusive $\tilde{t}_1 \rightarrow t + \tilde{\chi}_1^0$ scenario. The solid black curves represent the observed exclusion contour with respect to NLO+NLL cross section calculations and the corresponding $\pm 1\sigma$ uncertainties. The dashed red curves indicate the expected exclusion contour and the $\pm 1\sigma$ uncertainties including experimental uncertainties. No interpretation is provided for signal models for which $|m_{\tilde{t}_1} - m_{\tilde{\chi}_1^0} - m_t| \leq 25 \text{ GeV}$ and $m_{\tilde{t}_1} \leq 275 \text{ GeV}$ because of significant differences between the fast simulation and the GEANT4-based simulation for these low- E_T^{miss} scenarios. From [108].



2. The ATLAS experiment

This chapter provides in Section 2.1 a brief description of the [Large Hadron Collider \(LHC\)](#) [5] complex at the European Centre for Nuclear Research ([CERN](#)), near Geneva, Switzerland. One of its main experiments, the [ATLAS](#) detector [6], is presented and details are given about its various components in Section 2.2. Chapter 3 will highlight how information from these detector subsystems is used to reconstruct physics objects for analysis of collision data. Finally, Section 2.3 outlines the main steps and principles in generating [Monte Carlo \(MC\)](#) samples for data analysis and modelling. The performance and accuracy of a range of simulation algorithms are discussed, resulting in a proposal for a future ATLAS Fast Monte Carlo Chain [109].

2.1 The Large Hadron Collider

The LHC [5] is a circular proton accelerator and collider, and the largest addition to the experimental complex at CERN. The construction and operation of this gargantuan machine, a 27 km underground synchrotron crossing the French-Swiss border, relied on an already well-established suite of particle accelerators and facilities developed since the 1960's and schematically represented in Figure 2.1, most notably its predecessor the [Large Electron Positron collider \(LEP\)](#) collider [110], which was the previous occupier of the tunnel.

By stripping hydrogen from its electrons, bare protons are obtained and sent through to a series of accelerators that gradually build up their energies: first to 50 MeV thanks to the [LINear ACcelerator 2 \(LINAC2\)](#) [111, 112], then to 1.4 GeV within the [Proton Synchrotron Booster \(PSB\)](#) [113, 114] and 25 GeV within the [Proton Synchrotron \(PS\)](#) [115], before reaching a final energy of 450 GeV in the [Super Proton Synchrotron \(SPS\)](#) [116]. The final acceleration takes place in the LHC ring itself, by means of 9593 superconducting dipole and quadrupole electromagnets (kept at an operational temperature of 1.9 K), so the protons finally reach a staggering centre-of-mass energy $\sqrt{s} = 13$ TeV in the 2015–2018 (Run 2) period. The two beams (split at the exit of the SPS) are squeezed by further electromagnets at four designated interaction points around the LHC, where

“Inside the ATLAS detector”. Photo credits: ATLAS Experiment. © 2012 CERN.

the ALICE [117], ATLAS [6], CMS [118] and LHCb [119] detectors are located. The ATLAS and CMS experiments are multi-purpose detectors and cover a rich range of physics programs, while the ALICE and LHCb experiments are tailored for heavy ion and forward b-physics respectively.

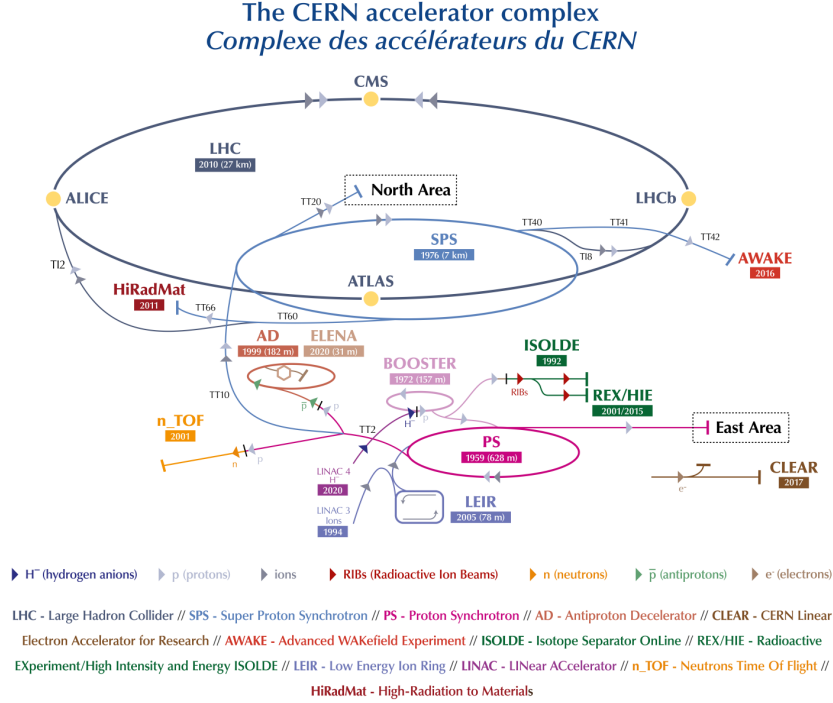


Figure 2.1: The LHC is the last ring (dark blue line) in a complex chain of particle accelerators. The smaller machines are used in a chain to help boost the particles to their final energies and provide beams to a whole set of smaller experiments, which also aim to uncover the mysteries of the Universe. From [120].

2.1.1 Hadron collisions

Protons are heavy hadrons (with a mass $m_p \simeq 938.27 \text{ MeV}$ [20]) composed of three valence quarks: two u -quarks and one d -quark. Since it is not possible to know which of these initial partons will take part in any given collision event, they enter in the computation of the cross section for some pp -initiated process X as parton distribution functions (PDF) [121], representing the probability of a parton to carry some Bjorken fraction x of the incoming proton. These PDFs are dependent on the transfer of momentum Q^2 ; at large values of Q^2 , the impact of so-called “sea” quarks, virtual pairs of quarks and antiquarks, and gluons becomes important. This effect is clearly visible in Figure 2.2.

The production cross section for the process X , $\sigma_{pp \rightarrow X}$, can therefore be factorised into a “hard” part $\hat{\sigma}$ and the PDFs f_i associated to initial state partons as [123]

$$\sigma_{pp \rightarrow X} = \int dx_1 f_1(x_1, Q^2) \int dx_2 f_2(x_2, Q^2) \hat{\sigma}(x_1, x_2, Q^2), \quad (2.1)$$

for a squared centre-of-mass energy $\hat{s} = x_1 x_2 s$ (where \sqrt{s} is the centre-of-mass energy of the two protons). Since such proton interactions effectively probe the substructure of the proton itself and produce a final state with different partons, they are referred to as “deep inelastic scattering” (DIS) processes. The cross sections of various SM processes are illustrated in Figure 2.3, comparing their measurements by the ATLAS experiment to theoretical predictions.

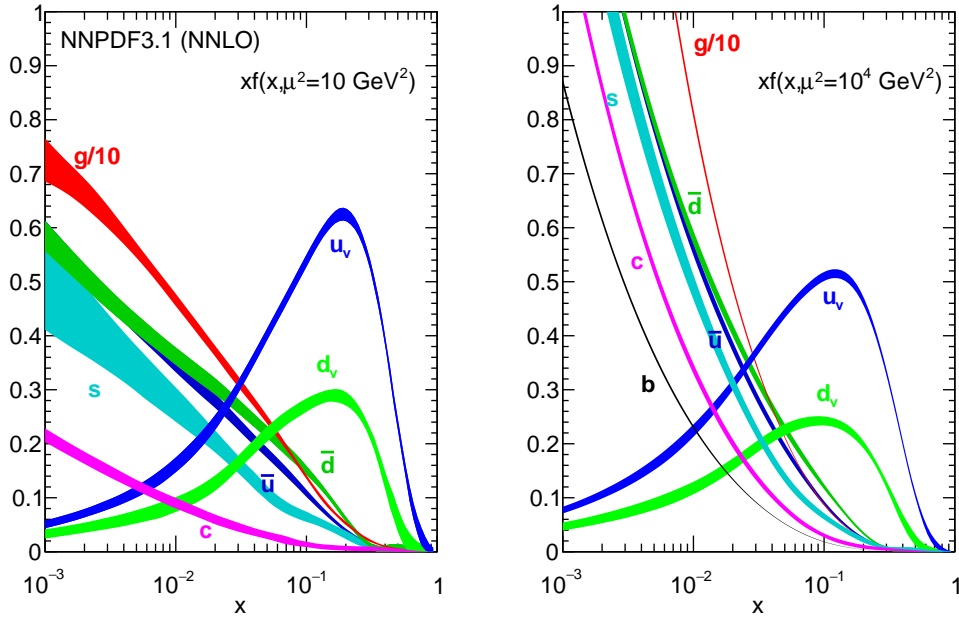


Figure 2.2: Parton distribution functions for the valence quarks (u and d), sea quarks and gluons of the proton, at a momentum transfer $Q^2 = 10 \text{ GeV}^2$ (left) and $Q^2 = 10^4 \text{ GeV}^2$ (right). From [122].

2.1.2 Structure of an event

The main purpose of conducting particle collisions at each of the four interaction points of the LHC is to study hard-scatter (HS) processes, where a large transfer of momentum occurs between partons of the incoming protons and usually results in the creation of new massive particles. At the LHC, the beamline is filled in bunches, containing about 10^{11} protons each; it is therefore possible for additional soft interactions to take place during a collision event [125]. These are referred to as “in-time pile-up” and are a common large background of soft hadronic activity in hard-scatter events. As we will see in Section 3.2.1, it is possible to reduce the contamination of those background events when performing their reconstruction. When bunch crossings happen at a similar or faster rate than the operation cycle (e.g. dissipation of electric signal) of a given hardware component of a detector, the previous or next bunch crossing can affect the readout of the current one; this “out-of-time pile-up” is however usually much less significant. A further source of background, the “underlying event” (UE) consists of the interaction of the partons not involved in the hard process, while multi-parton interactions (MPI), where several partons from the same proton enter in the main event, are the subject of dedicated physics analyses.

The hard-scatter event itself, described by perturbation theory, can be accompanied by additional “soft” radiation. This is the result of non-perturbative QCD effects and translates into the emission of gluons as initial state (ISR) or final state radiation (FSR). Any gluon in the final state will undergo parton showering, producing further quarks and decreasing the value of Q^2 until it reaches $\sim \mathcal{O}(1 \text{ GeV}^2)$, at which scale the hadronisation process, whereby charged particles bound into colourless hadrons, is likely to take place.

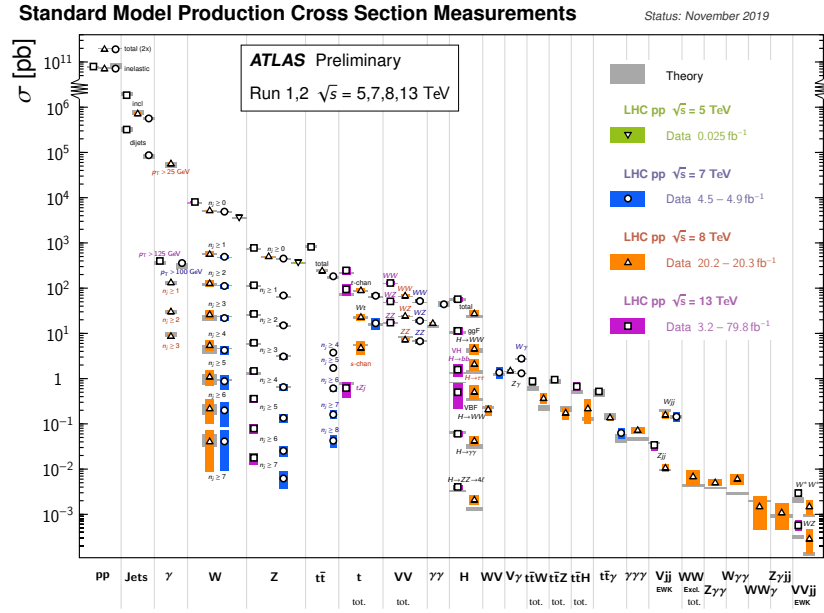


Figure 2.3: Summary of several Standard Model total and fiducial production cross section measurements at the ATLAS detector, corrected for branching fractions, compared to the corresponding theoretical expectations. Where relevant, selections based on the number of jets are indicated by n_j . From [124].

2.1.3 Luminosity

For a given process with cross section σ , the expected number of events to be produced via hard collisions is given by the integrated luminosity L (in units of inverse barns, b^{-1}) [126]:

$$N_{\text{events}} = \sigma L = \sigma \int \mathcal{L} dt, \quad (2.2)$$

where the instantaneous luminosity \mathcal{L} depends directly on various parameters of the LHC:

$$\mathcal{L} = \frac{N_b^2 n_b f_{\text{rev}} \gamma_r}{4\pi \epsilon_n \beta^*} F, \quad (2.3)$$

namely: the number of protons per bunch N_b , the number of bunches per beam n_b , the revolution frequency f_r , the relativistic gamma factor γ_r , the normalised transverse beam emittance ϵ_n ¹, the beta function at the collision point β^* and the geometric luminosity reduction factor (due to a crossing angle at the interaction point) F . The nominal and Run 2 values for these beam parameters are given in Table 2.1 below.

¹The beam emittance can be thought of as the area of the beam in its position-momentum phase space and is a conserved quantity as the beam travels around the LHC. Normalising the emittance removes its dependency on the beam energy. Note that a beam with low emittance can be thought of as more focused, and hence the likelihood of particle collisions (and the luminosity) is greater.

Table 2.1: LHC beam parameters in Run 2 (2015–2018), compared to nominal design values. From [127].

Parameter	Nominal	Run 2	Units
Beam energy	7.0	6.5	TeV
Bunch population (N_b)	1.15	1.15	10^{11} protons
Bunch spacing	25	25	ns
Bunch multiplicity (n_b)	2808	2556	
Revolution frequency (f_r)	11.2	11.2	kHz
Normalised emittance (ϵ_n)	3.75	2.2	μm
Beta function (β^*)	55	25	cm
Crossing angle (θ_c)	285	260	μrad
Geometric reduction (F)	0.836	0.858	
Peak luminosity (\mathcal{L})	1.0	2.0	$10^{34} \text{ cm}^{-2}\text{s}^{-1}$

2.2 The ATLAS detector

The *ATLAS* detector [6] is a 25 m wide, 46 m long, 7000 ton cylindrical general-purpose experiment, situated 100 m underground at one of the 4 main interaction points of the LHC. The detector is composed of a variety of layered subsystems, each specialised in the identification and processing of various types of experimental signals, and arranged in concentric forward-backward symmetric cylindrical layers, so as to cover almost all the solid angle around the centre of particle collisions.

An inner detector is dedicated to measuring particle tracks, through their interaction with a 2 T solenoid magnetic field. An electromagnetic and a hadronic calorimeter then use scintillation techniques to measure energy deposits, surrounded by a toroidal magnet system and a final array of muon spectrometers.

2.2.1 Coordinate system

A right-handed Cartesian coordinate system (x, y, z) is used, such that the origin coincides with the interaction point and the z -axis is taken to be parallel to the beam pipe. The positive x -direction points towards the centre of the LHC ring and the positive y , upwards. Since the LHC is a pp collider and the relative momentum fraction carried by partons is described by a PDF, the centre-of-mass frame can undergo a Lorentz boost in the z -direction. It is therefore useful to introduce the transverse $x - y$ plane, where conservation of momentum is more readily imposed. Given the cylindrical nature of the detector, it is natural to transform to polar coordinates (r, θ, ϕ) , where the azimuthal angle ϕ ranges from $-\pi$ to π around the beam axis, and to introduce the pseudorapidity

$$\eta = -\ln \tan\left(\frac{\theta}{2}\right). \quad (2.4)$$

The pseudorapidity is a useful approximation of the rapidity, $y = \frac{1}{2} \ln \frac{E+p_z}{E-p_z}$, for massless particles (equivalently, in the limit of vanishing mass-to-momentum ratio). Differences in rapidity are Lorentz invariant under boosts along the longitudinal axis and hence the (pseudo-)rapidity is preferred to θ . We note that $\eta = 0$ defines the plane transverse to the beam and $\eta \rightarrow \infty$ the direction parallel to the beam axis, with the terms ‘‘central’’ and ‘‘forward’’ (or ‘‘backward’’ where relevant)

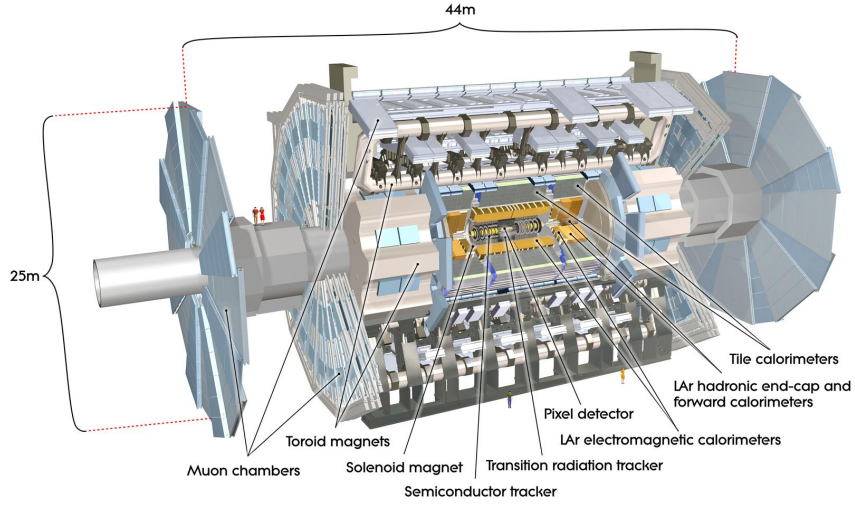


Figure 2.4: Computer generated image of the whole ATLAS detector, indicating the major components. Length and radius measurements are indicated, and a couple of average particle physicists are shown for comparison. From [128].

referring to values of η close to each of these two limits, respectively. Distances in the $\eta - \phi$ plane are parameterised by

$$\Delta R = \sqrt{(\Delta\eta)^2 + (\Delta\phi)^2}, \quad (2.5)$$

which is also a quantity invariant under longitudinal Lorentz boosts.

2.2.2 Magnet system

ATLAS uses a combination of a central superconducting solenoid and three outer superconducting toroid magnets to enable a precise measurement of the momenta of charged particles [129]. The layout is shown schematically in Figure 2.5. The central solenoid surrounds the inner detector and permeates it with a 2 T field parallel to the beam axis, such that charged particles follow a bent trajectory in the azimuthal plane. Two toroids are placed on either end of the detector, providing a 1 T field for the muon systems in the end-cap regions, and a central 0.5 T field in the central barrel.

2.2.3 Inner detector

The **Inner Detector (ID)** is the innermost layer of the ATLAS detector [131, 132]. Charged particles coming out of the collision points are reconstructed from hits in the ID and referred to as tracks. With the high luminosity of the LHC and the corresponding large track density, high resolution measurements of track kinematics and positions of vertices is essential to the reconstruction of several physics objects. The ID is composed of three distinct subsystems, depicted in Figure 2.6 and described in what follows. By combining information from the entire ID, an overall momentum resolution of

$$\frac{\sigma_{p_T}}{p_T} = 0.05\% \cdot \frac{p_T}{\text{GeV}} \oplus 1\% \quad (2.6)$$

is achieved, where the symbol \oplus represents a sum in quadrature.

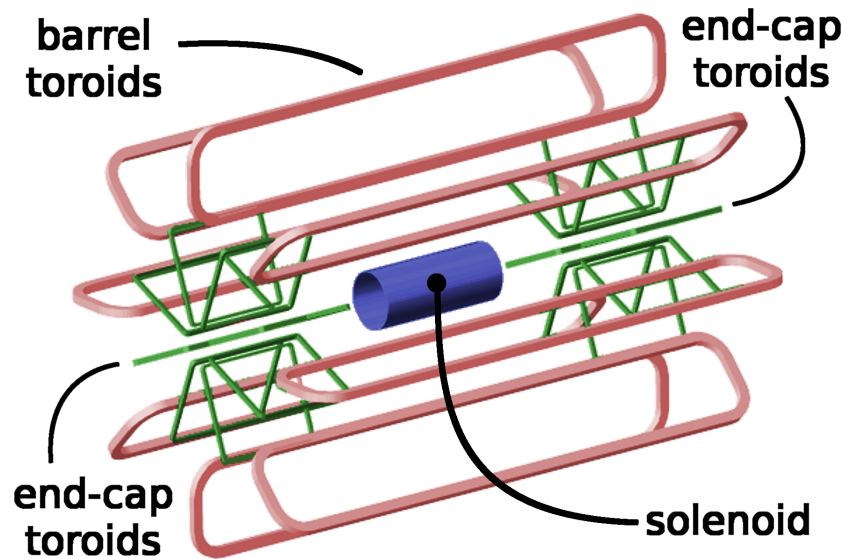


Figure 2.5: Schematic representation of the magnet system in ATLAS. From [130].

Pixel detector

The pixel detector [134, 135] is the very first layer of the ID, situated between 33.25 mm and 122.5 mm to the beamline. The part closest to the beamline is the **Insertable B-Layer (IBL)** [136–138], an important component in the identification of secondary vertices associated to the decays of B-hadrons. The pixel detector as a whole boasts an impressive 87.2 million $50 \times 400 \mu\text{m}$ pixels, arranged in 3 barrel layers and 2×3 endcap disks, and grouped in 1744 silicon modules. Charged particles going through the silicon modules generate electron–hole pairs in amounts related to the energy of the incoming particle. A bias voltage is applied to force the drift of these electron–hole pairs and the charge separation is ultimately picked up and processed to form the recorded signal. This finely granulated structure results in an intrinsic resolution of $10 \mu\text{m}$ in the $R - \phi$ direction (orthogonal to the beamline) and $115 \mu\text{m}$ in the z -direction, with a full coverage in azimuthal angle and up to $|\eta| < 3$.

Semi-conductor tracker

The **Semi-Conductor Tracker (SCT)** is located right outside the pixel detector and is of a similar modular design, with long strips of silicon rather than individual pixels. The SCT consists of 4088 modules, arranged in four layers of silicon micro-strip modules in the barrel ($|\eta| < 1.4$) and nine discs on either end-caps ($1.4 < |\eta| < 2.5$). An average particle will have three measurements provided by the pixel detector, and eight by the SCT. Measurements in the SCT have a precision of $17 \mu\text{m}$ in the $R - \phi$ ($z - \phi$) direction and $580 \mu\text{m}$ in the z -(R -)direction in the barrel (endcaps).

Transition radiation tracker

The **Transition Radiation Tracker (TRT)** [139–141] is the final and outermost layer of the ID, and is built from straw detectors (4 mm tubes) filled with a mixture of (mostly) xenon and carbon dioxide gas, such that charged particles passing through the TRT emit transition radiation in the form of photons and a trail of ionisation electrons. The intensity of the transition radiation being proportional to the Lorentz factor $\gamma = E/m$, the combination of this information with the energy measurements in the previous layers is a first step towards particle identification.

The nearly 400,000 straw detectors are arranged in 73 barrel layers (parallel to the beamline) and 2×122 end-cap layers (orientated radially). The lower spatial resolution of $130 \mu\text{m}$ in the $R - \phi$ direction is compensated for the large number of hits expected (around 36 per track) and the greater

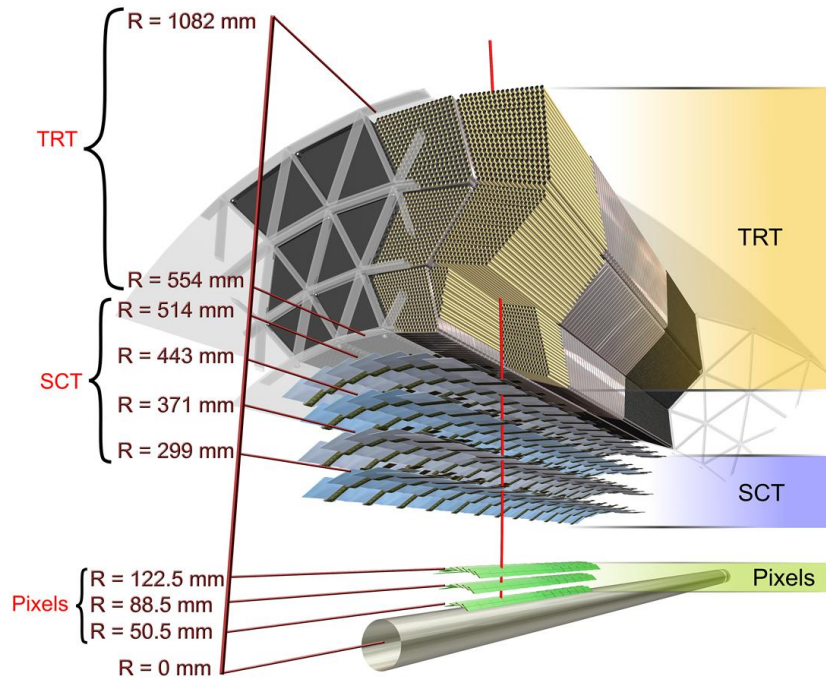


Figure 2.6: Computer generated image of the ATLAS inner detector, showing its various subsystems. From [133].

track length.

2.2.4 Calorimeters

Outside the inner detector lies the ATLAS calorimetry system [142], composed of an electromagnetic (ECAL) [143] and hadronic calorimeter (HCAL) [144]. These are so-called “sampling” detectors, i.e. they use an alternate layout of active detecting medium and dense absorbing material, such that the energy of particles is progressively (and fully) absorbed while measurements are taken. The energy $E(x)$ of a particle after it has traveled some distance x in the ECAL can be related to its original energy as

$$E(x) = E_0 e^{-x/X_0}, \quad (2.7)$$

where X_0 , the radiation length, is a material dependent quantity defined as the mean distance over which the energy of the traveling particle is reduced by a factor of $1/e$. The ECAL is built to be about $22X_0$ in length to fully capture all electromagnetic showers. Hadronic interactions in the HCAL cause the incident particle to lose its energy following a similar exponential law, but parameterised in terms of an interaction length λ ; likewise, the HCAL is $\sim 10\lambda$ in depth and situated further out than the ECAL to catch the longer hadronic showers. The barrel component of the ECAL and all end-cap calorimeters make use of a liquid argon scintillator while the hadronic barrel component uses a tile scintillator. The structure of the calorimeter system is schematically represented in Figure 2.7 and allows a forward coverage up to $|\eta| < 4.9$.

Different relative resolutions are achieved depending on the considered subsystem. They can be parameterised as

$$\frac{\sigma_E}{E} = \frac{a}{\sqrt{E}} \oplus \frac{b}{E} \oplus c, \quad (2.8)$$

where a is a stochastic term from the intrinsic fluctuation of the showers within the calorimeter (number of particles and individual energies), b corresponds to the electric noise and pile-up contributions, and c is a constant systematic (instrumental) offset. The sampling (a) and constant (c) terms for the ECAL are:

$$\frac{\sigma_E}{E} = \frac{10\% \text{ GeV}^{1/2}}{\sqrt{E}} \oplus 0.7\%; \quad (2.9)$$

for the HCAL:

$$\frac{\sigma_E}{E} = \frac{50\% \text{ GeV}^{1/2}}{\sqrt{E}} \oplus 3\%; \quad (2.10)$$

and for the forward components:

$$\frac{\sigma_E}{E} = \frac{100\% \text{ GeV}^{1/2}}{\sqrt{E}} \oplus 10\%. \quad (2.11)$$

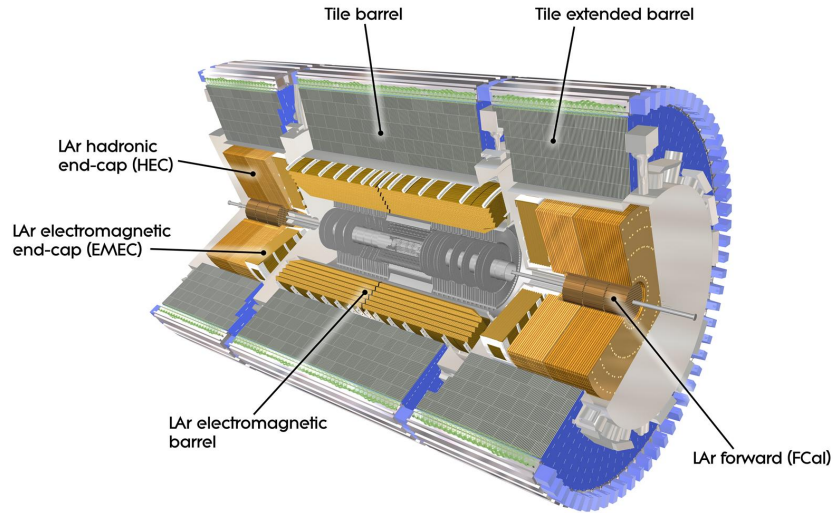


Figure 2.7: Computer generated image of the ATLAS calorimeter, showing its various subsystems. From [145].

Liquid argon electromagnetic and hadronic calorimeter

The liquid argon (LAr) calorimeter [146, 147] consists of the electromagnetic barrel (EMB) [148], covering the range $|\eta| < 1.475$, the electromagnetic end-cap (EMEC, $1.375 < |\eta| < 3.2$) [149], the further hadronic endcap (HEC, $1.5 < |\eta| < 3.2$) [150] and a forward calorimeter (FCAL,

$3.1 < |\eta| < 4.9$) [151]. It is the main tool in measuring the energy of electrons and photons, which both lose energy via *bremsstrahlung* and pair production when interacting with the active material, leading to the generation of electromagnetic showers. A lead absorber separates layers of active LAr material arranged in an accordion or zig-zag fashion, allowing a fully covered and uniform ϕ response and multiple measurements to be made. The ECAL is segmented into $\Delta\eta \times \Delta\phi$ calorimeter cells of 0.025×0.025 , which stack longitudinally to form “towers”.

Tile hadronic calorimeter

The tile calorimeter (**TileCAL**) [152] is the central part of the HCAL and uses a different technology to other components of the ATLAS calorimetry system. The TileCAL is segmented into a central barrel ($|\eta| < 1.0$) and two extended barrels ($0.8 < |\eta| < 1.7$), and uses scintillating plates alternating with steel absorbers. This denser material is required to fully contain the majority of hadronic showers, arising from inelastic interactions proceeding via the strong force. Wavelength shifting fibres transmit the light produced in the scintillator tiles to photomultiplier tubes before producing the final signal. The HCAL has a coarser granularity than the ECAL, with $\Delta\eta \times \Delta\phi$ calorimeter cells of 0.1×0.1 .

2.2.5 Muon spectrometer

The ATLAS **Muon Spectrometer (MS)** [153], depicted in Figure 2.8, is designed to measure the momentum of charged particles exiting the calorimeters within $|\eta| < 2.7$ and trigger on those within $|\eta| < 2.4$. The final and outermost detector system, it relies on the toroid magnets described above to generate a magnetic field orthogonal to the expected trajectories of muons, allowing for high precision tracking. A resolution on the transverse momentum

$$\frac{\sigma_{p_T}}{p_T} = 10\% \cdot \frac{p_T}{\text{GeV}} \quad (2.12)$$

is achieved for 1 TeV tracks.

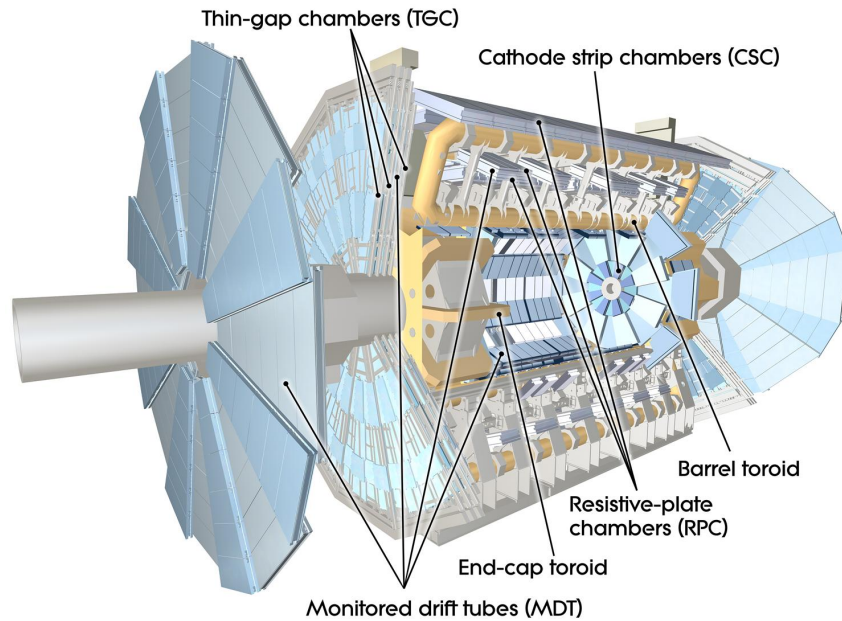


Figure 2.8: Computer generated image of the ATLAS muon spectrometer, showing its various subsystems. From [154].

Monitored drift tubes

Monitored drift tubes (MDT) [155], containing a mixture of argon and carbon dioxide gas, constitute the barrel of the MS and provide precision measurements in η down to $30\ \mu\text{m}$. Muons going through the MDTs ionise the gas and the resulting drifting electrons provide an electrical signal that, when combined over several tubes, allows for tracking. 1088 chambers, each containing three to eight MDTs, are spread across three concentric cylindrical layers, perpendicular to the beamline.

Cathode strip chambers

Near the end-caps, large particle densities prevent the use of long MDTs and cathode strip chambers (CSC) [156] are used there instead. Their finer granularity allows them to provide a spatial resolution of $40\ \mu\text{m}$, while maintaining a coverage of $2.0 < |\eta| < 2.7$. Each CSC is made of four radially-orientated multi-wire proportional chambers with perpendicular cathode planes; a similar argon/CO₂ ionisation process as for the MDTs, albeit with much shorter drift time, leads to tracking of the muons.

Resistive-plate chambers

The electron drift time in both MDTs and CSCs is larger than the spacing between LHC bunches of 25 ns, therefore these subsystems are not adapted for muon triggering. Resistive-plate chambers (RPC) [157] are used in the barrel ($|\eta| < 1.05$) and rely on a predominantly C₂H₂F₄ gas mixture between two parallel resistive plates, with a separation of 2 mm, to provide a position resolution of 10 mm and a time resolution of 1 ns.

Thin-gap chambers

In the same way that MDTs are ill-suited in the dense environment of the end-caps, so are RPCs and they need to be replaced by dedicated thin-gap chambers (TGC) [158], anode wires separated by 2 mm, held between two grounded planes and immersed in a gas mixture (CO₂ and pentane). A time resolution similar to RPCs is achieved, while lowering the space resolution down to 2 – 7 mm.

2.2.6 Trigger system

The dominant process to occur in proton collisions is inelastic scattering (mainly producing jets, as shown in Figure ??), at a significantly higher rate than the processes targeted by ATLAS analyses. Furthermore, with each event representing about 1 MB worth of information, and the collision rate reaching up to 40 MHz, a reduction of the volume of information to store (limited to a maximum writing rate of 100 MB/s) is absolutely required. Hence a multi-level trigger system is used in ATLAS [159], with a Level-1 hardware trigger (L1) [160] accessing the readouts of the calorimeters and MS to provide a basic particle identification and make a decision on the quality of the event at a maximum rate of 100 kHz. The information is then passed on to a high-level software trigger (HLT) [161], which also performs a global track reconstruction with additional information from the ID.

The signatures of interest for both L1 and HLT triggers are listed in the legends of Figure 2.9. An event passing both L1 and HLT is written to disk, thanks to the reduced rate of 1400 Hz, before being reconstructed offline.

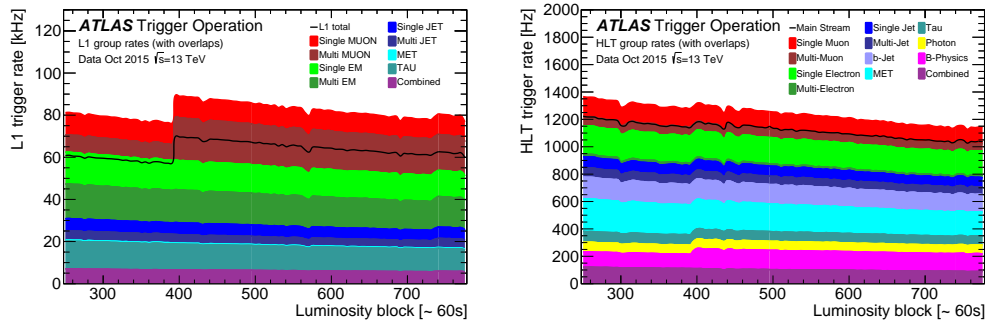


Figure 2.9: L1 (left) and HLT (right) trigger rates grouped by trigger signature during an LHC fill in October 2015 with a peak luminosity of $4.5 \times 10^{33} \text{ cm}^{-2} \text{ s}^{-1}$. Due to overlaps the sum of the individual groups is higher than the L1 (left) total rate and Main physics stream (right) rate, which are shown as black lines. Multi-object triggers are included in the b -jets and tau groups. The B-physics triggers are mainly muon-based triggers. The combined group includes multiple triggers combining different trigger signatures such as electrons with muons, taus, jets or E_T^{miss} . From [162].

2.3 Monte Carlo simulation

The simulation of physical processes using **Monte Carlo (MC)** techniques is essential to virtually all ATLAS analyses, when pure data-driven approaches are not available. It allows the prediction of SM background events under detection conditions, and the study of alternative signal models. The ATLAS simulation infrastructure [163] integrates the various steps necessary to derive physical observables from the calculation of cross sections from Feynman diagrams, and we briefly outline them in what follows.

2.3.1 Generation

The very first step is the event generation (**EVGEN**), whereby the computation of matrix elements (**ME**) is performed by a Monte Carlo generator and the four-vectors of all final state partons in the hard-scatter event are obtained. The precision of these computations is usually either at leading-order (**LO**) or next-to-leading-order (**NLO**) in the strong coupling constant α_s . As described previously in Section 2.1.1, various sets of **PDF** can be used as input to the EVGEN process, resulting in slightly different assignments of the fractional momenta carried by each constituent of the interacting protons. Uncertainties related to the choice of PDF set will therefore be considered in each analysis presented in this document. Since the precision of any MC estimation depends on the size of the randomly generated sample, many more MC events are produced than would be expected in data. A dedicated weight must then be derived to correct the normalisation of each MC event, and possibly include higher-order theoretical corrections.

At this stage of the EVGEN, the so-called “truth” information, the generator-level description of the kinematics of all final state partons, can be extracted and is a useful reference for many analyses, as it is free from any detector-related smearing effects. As defined in Section 2.1.2, additional soft emissions (parton showers, **PS**) and the clustering of quarks into bound states (hadronisation) are then performed using dedicated algorithms, beyond the ME calculation. The **PYTHIA** [164] algorithm is based on the Lund string model [165], while **HERWIG** [166] uses a clustering formalism [167]. This choice in the application of PS results in another modelling systematic in ATLAS analyses. Above a certain momentum threshold, soft emissions can in fact already have been included at the ME-level: in order to prevent double-counting of additional partons, a dedicated merging algorithm must be used to transition from ME to PS. A matrix element matching scale (or merging scale) can for instance be defined in the Catani-Krauss-Kuhn-Webber (**CKKW**) scheme

[168] and represents yet another source of systematic uncertainties on MC modelling, along with the renormalisation scale (μ_R , defining the value of α_s used in the ME), the factorisation scale (μ_F , regulating the PDFs) and the resummation scale (used in PS for computing soft emissions).

The entire generation process is depicted schematically in Figure 2.10. Several MC generators will be used in the ATLAS analyses described in the main body of this document. MADGRAPH [169] was historically developed as a LO ME generator, but now includes loop calculations as well; however, it doesn't provide a hadronisation model and thus needs to be interfaced with a modern PS generator, such HERWIG or PYTHIA. We note that PYTHIA is also able to generate LO ME events, but is rarely used for that purpose in ATLAS. SHERPA [170] is another general-purpose generator with an NLO precision up to two partons, which uses OPENLOOPS [171] to generate additional partons at LO and processes the PS internally using the ME+PS@NLO prescription [172]. Finally, POWHEG [173] is an alternative ME generation framework at NLO precision, with the particularity of only producing events with positive MC weights and providing a PS merging independent of the PS algorithm (which is frequently chosen to be PYTHIA in ATLAS). A comprehensive review of MC generators and the physics behind them can be found in Ref. [174].

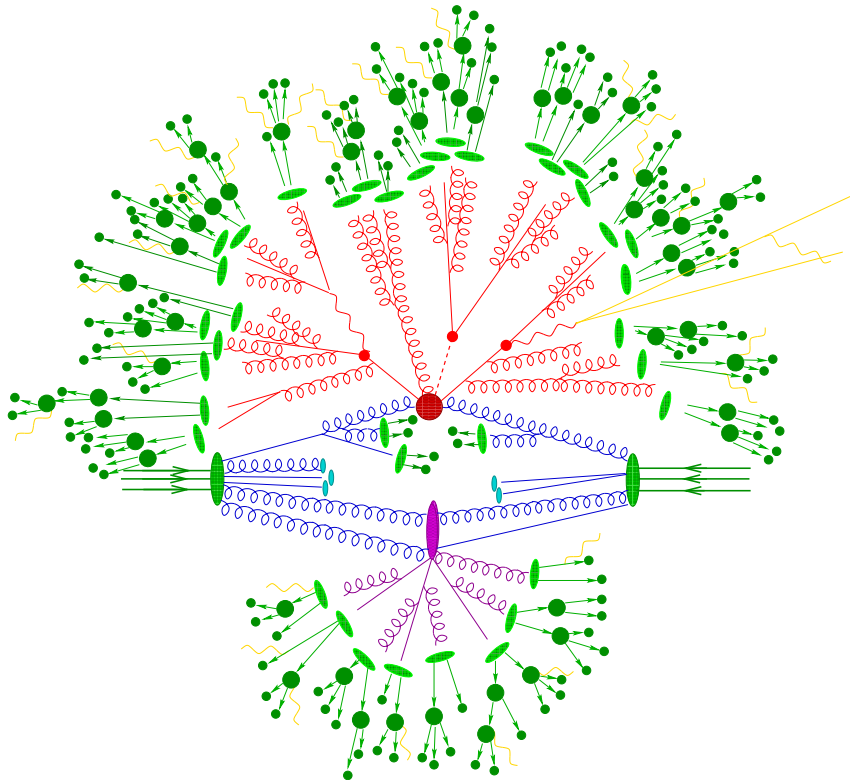


Figure 2.10: Pictorial representation of a $t\bar{t}H$ event as produced by an event generator. The hard interaction (big red blob) is followed by the decay of both top quarks and the Higgs boson (small red blobs). Additional hard QCD radiation is produced (red) and a secondary interaction takes place (purple blob) before the final-state partons hadronise (light green blobs) and hadrons decay (dark green blobs). Photon radiation occurs at any stage (yellow). From [175].

2.3.2 Simulating the ATLAS detector

Having obtained a list of stable ($c\tau > 10\text{mm}$) final state particles from the EVGEN step, including soft emissions and hadronisation, all the necessary kinematic information about these particles is passed on to a dedicated algorithm for the simulation (SIM) step. The GEANT4 software library [176] is used to perform a detailed simulation of the ATLAS detector and its component, and

propagate all particles outwards from the collision point through the **ID** and towards the calorimeter systems. All main hardware components are taken into account and appropriately parameterised, and the trajectory of each particle is time-evolved in discrete steps until all its energy has been deposited or it has gone out of acceptance. The output of the SIM step is therefore a collection of ID hits, **MS** tracks and calorimeter deposits.

These physical effects are then transformed into the corresponding detector signals (voltage, time, etc.) through a digitisation (**DIGI**) step to yield a unique ATLAS data format, common to both simulation and real data. A dedicated reconstruction (**RECO**) step then turns these detector signals into low-level objects such as track and clusters, which are in turn used to define physics objects; this is the subject of the next chapter.

It is worth noting at this point that the detector simulation step is, by far, the most **CPU**-consuming task within the ATLAS Monte Carlo Chain. Figure 2.11 clearly shows the important share of Grid (CERN’s distributed high-performance computing service, a network of over 170 computer farms in 36 countries [177]) CPU attributed to SIM. With the dramatic increase in MC demand predicted for the near future, and culminating with the needs of the **High-Luminosity LHC (HL-LHC)** [178], a simple scaling of computing resources would prove both costly and insufficient. Fast detector simulation techniques have previously been proposed [179–181] as partial or full alternatives to GEANT4, but do not address the problem entirely: with increased luminosity and pile-up, the DIGI and RECO steps become comparable to the SIM one. Figure 2.12 shows that with standard digitisation algorithms, a linear dependence of the CPU time spent in the DIGI step is expected as a function of pile-up.

Developing new techniques for fast and accurate MC production is one of the main challenges of the ATLAS computing community over the next few years.

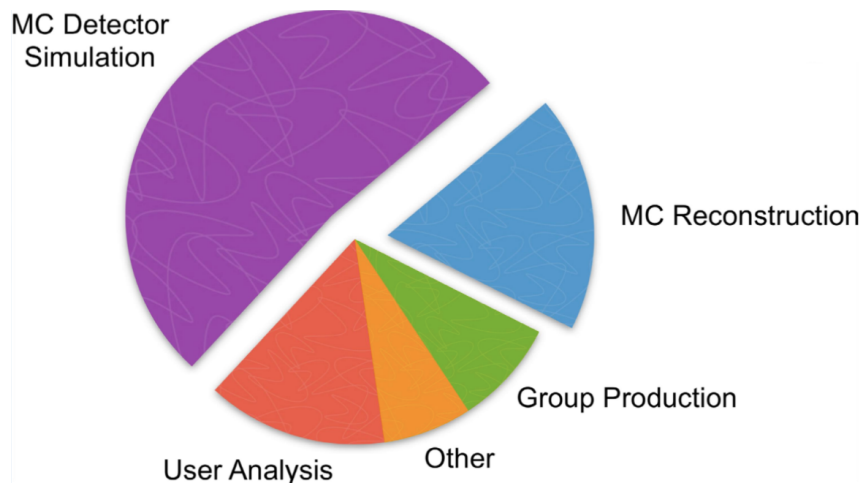


Figure 2.11: Total CPU consumption of the Grid in 2012, broken down by categories of computing tasks. From [182].

2.3.3 Towards a fast MC simulation

The ATLAS Fast Monte Carlo Chain (FastChain) [109] proposes to address these issues. At its core is a long-developed project, the **Integrated Simulation Framework (ISF)** [183]. The ISF ensures complete modularity and flexibility for the user, allowing a choice between fast and “full” settings at each step, thereby offering a trade-off between rapidity of execution and accuracy that can be tuned on a case-by-case basis. A schematical representation of the ISF flow is given in Figure 2.13.

Various approaches can be taken towards accelerating the execution of the MC production steps. Instead of simulating the full path of electrons and photons in the calorimeter, and their

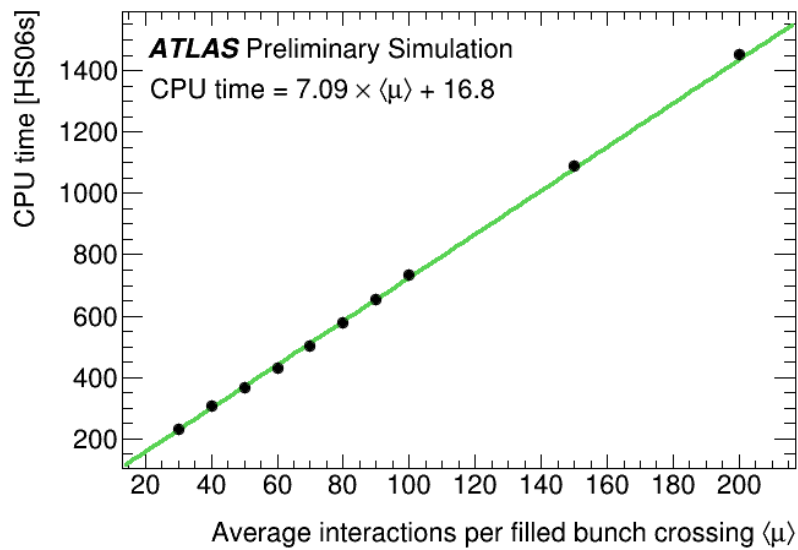


Figure 2.12: Digitisation time per event, in HepSpec06 seconds, as a function of the average number of interactions per bunch crossing, with 25 ns bunch spacing. A linear fit to the times is overlaid. On a modern CPU, one second of wall clock time corresponds to about 10 HepSpec06 seconds. From [182].

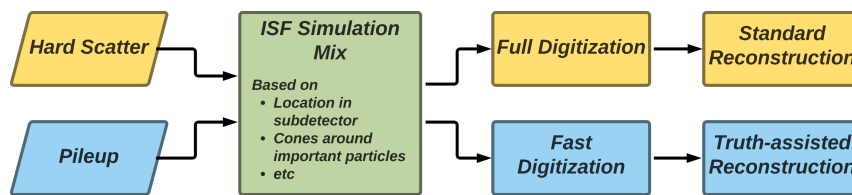


Figure 2.13: Conceptual diagram of the Integrated Simulation Framework. From [183].

ensuing electromagnetic showers, a database of real showers in data can be created and sampled after parameterising the calorimeter response. This semi-data-driven approach is at the core of FastCaloSim [179, 180], which offers a significant speed-up with respect to a full GEANT4 simulation (especially for low energy particles). The combination of GEANT4 for the modelling of the Inner Detector and FastCaloSim for the calorimeter systems is known as ATLFASITII, and is already widely used for the MC production of SUSY signals, amongst others; it is schematically depicted in Figure 2.14. A combination of FATRAS [181] and FastCaloSim (referred to as ATLFASITIF) is currently under development and not yet validated for accuracy; where ATLFASITII offers a 25-fold decrease in CPU consumption with respect to the full GEANT4 simulator, ATLFASITIF could provide a dramatic reduction by a factor of almost 750, as is shown in Figure 2.15. Likewise, a parameterised description of silicon hits enables fast digitisation, while using truth information for tracking (pseudo-tracking [184]) allows for a fast RECO step in MC; both halve the CPU consumption compared to their standard counterparts.

The inclusion of the pile-up (PU) background to the main hard-scatter event is currently done by simulating and digitising both in parallel [186]. Many pile-up processes needing to be generated for a single final MC event, it is clear that this setup doesn't scale well with increased luminosity. The possibility of using a central bank of pre-mixed PU events, randomly sampled and overlaid to the HS event during the DIGI step is being studied, as is that of using a data-driven approach directly. This option is more viable than the parameterisation of out-of-time PU [187], which was found to not reproduce key kinematic distributions accurately. The improvement in CPU consumption

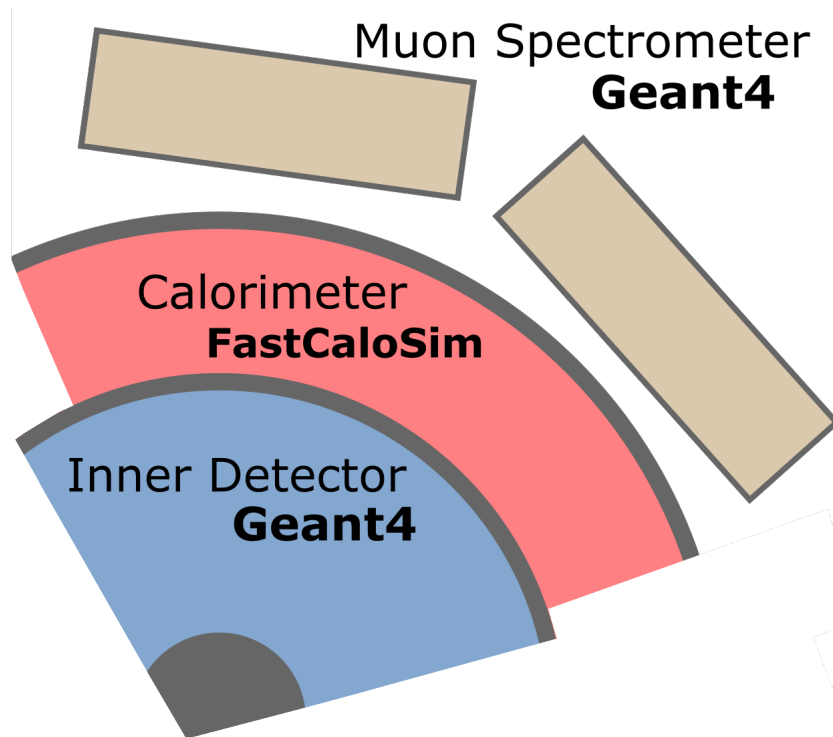


Figure 2.14: Schematic view of the various components of the ATLFastII simulator configuration. From [179].

from using overlay of MC PU events with respect to the standard digitisation process is significant and offers robustness against increased numbers of mean interactions per bunch crossing, as can be observed in Figure 2.16.

The ATLAS MC FastChain [109], with its high level of flexibility between various fast and full options in SIM, DIGI and RECO, as well as PU treatment, is a promising candidate to satisfy the CPU resource needs of the collaboration over the next decade and towards the HL-LHC, as is made explicit in Figure 2.17. Machine learning alternatives are actively being investigated: a recent GAN [189] was able to generate electron showers in the ECAL in $\sim 7s$, when it takes GEANT4 $\sim 17s$; such deep learning algorithms will need extensive physics validation before they are fully integrated in the ATLAS simulation infrastructure.

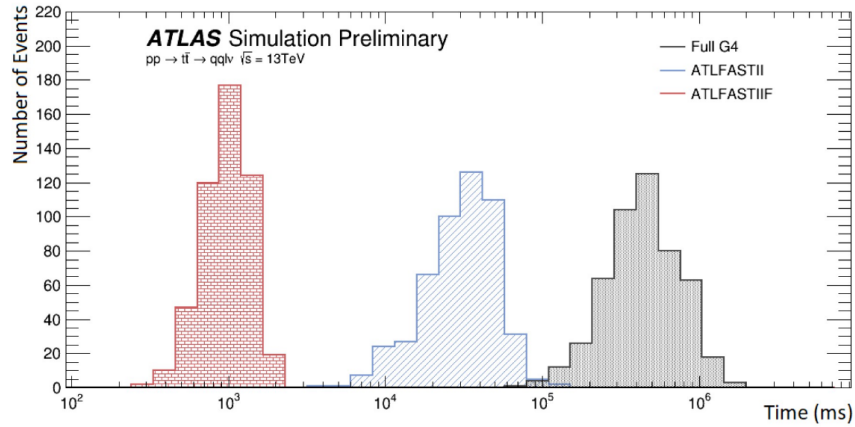


Figure 2.15: Wall clock time spent in the simulation of 500 $t\bar{t}$ events using three different simulators. A factor 25 (750) speed-up is observed between ATLFASII (ATLFASIIIF) and GEANT4. From [185].

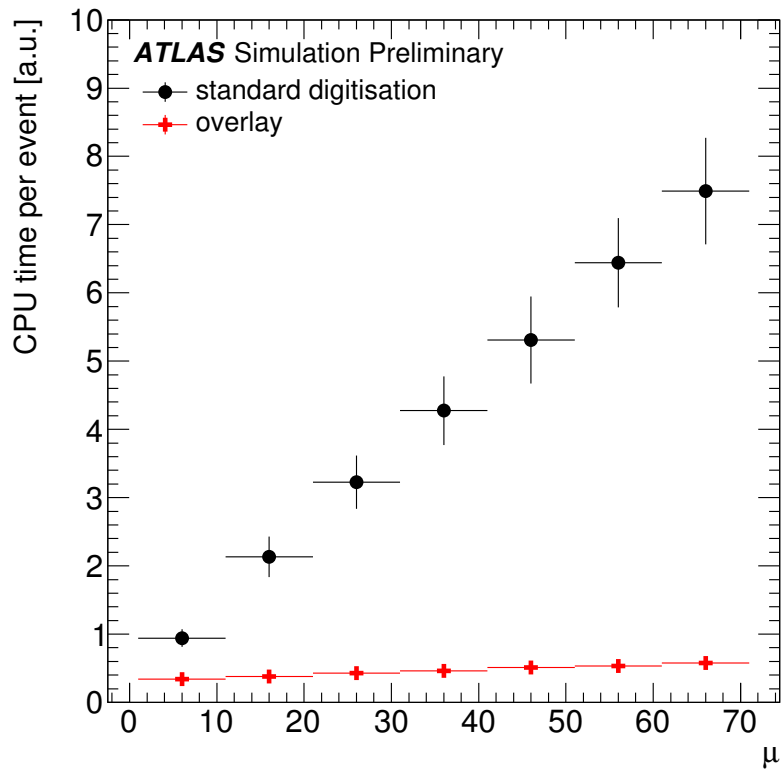


Figure 2.16: Average CPU time per event comparison between the standard digitisation (black circles) and the MC overlay (red crosses) as a function of the number of proton-proton collisions per bunch crossing (μ). Vertical error bars represent standard deviations of multiple measurements of CPU time. From [188].

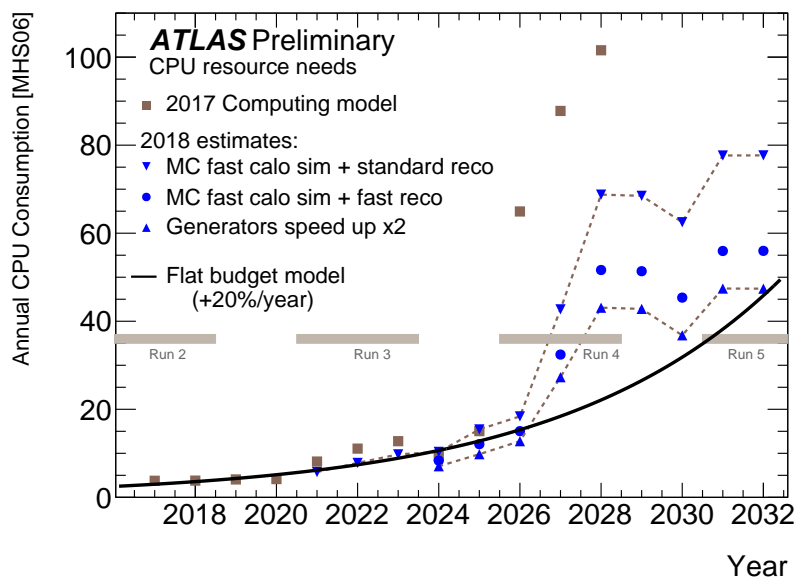


Figure 2.17: Estimated CPU resources needed for the years 2018 to 2032 for MC simulation processing. The blue points show the improvements possible in three different scenarios, which require significant development work: ATLFASII (top curve), ATLFASIIIF (middle curve) and theoretical speed up of the EVGEN (bottom curve). The solid line shows the amount of resources expected to be available if a flat funding scenario (+20%/year) is assumed, based on the current technology trends. From [182].



3. Analysis tools

In this chapter we provide a description of elements common to all experimental analyses studied in the main body of this document. Details are given in Section 3.1 about the datasets used, and in Section 3.2 about the reconstruction of physics objects. In Section 3.3, the notions of fiducial volumes, and particle- and parton-level definitions are introduced. We also review some core concepts of top quark reconstruction techniques in Section 3.4.

3.1 The 2015–2018 ATLAS dataset

The experimental analyses presented in Parts II and III rely on the pp collision data recorded and processed by the ATLAS detector in Run 2 of the LHC, during the 2015–2018 period. As is shown in Figure 3.1, the LHC delivered a total integrated luminosity of 156 fb^{-1} [190], of which 147 fb^{-1} were recorded by the ATLAS detector and 139 fb^{-1} are of sufficiently high quality to be used for physics measurements. A total estimated mean number of interactions per collision, or pile-up, is found to be $\langle \mu \rangle = 33.7$ over the full Run 2; the contributions from each year of data-taking are broken down in Figure 3.2.

The analyses presented in Chapters 5 and 8 are based on the ATLAS data processed in the years 2015 and 2016, corresponding to an integrated luminosity of 36.1 fb^{-1} [191], while Chapter 7 explores the full 139 fb^{-1} dataset.

“View from the ATLAS control room”. Photo credits: ATLAS Experiment. © 2015 CERN.

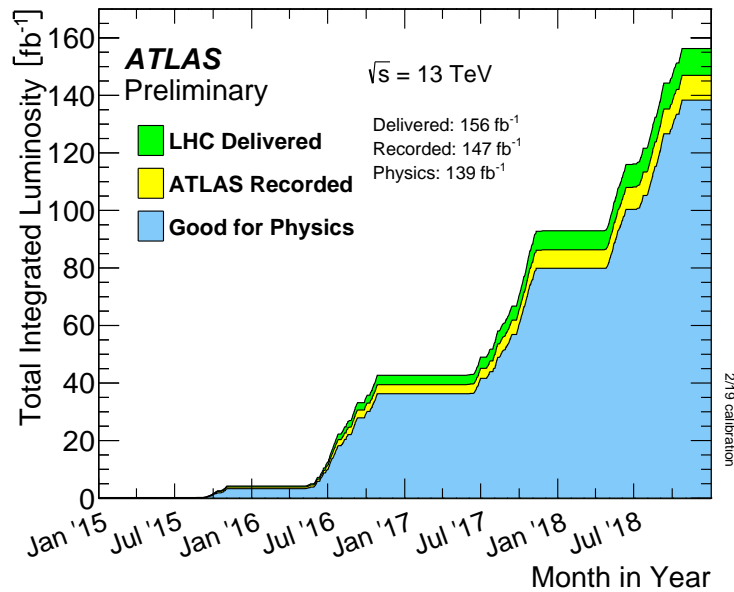


Figure 3.1: Cumulative luminosity versus time delivered to (green) and recorded by (yellow) the ATLAS detector, and certified to be good quality data (blue) during stable beams for pp collisions at $\sqrt{s} = 13 \text{ TeV}$ in 2015–2018. From [192].

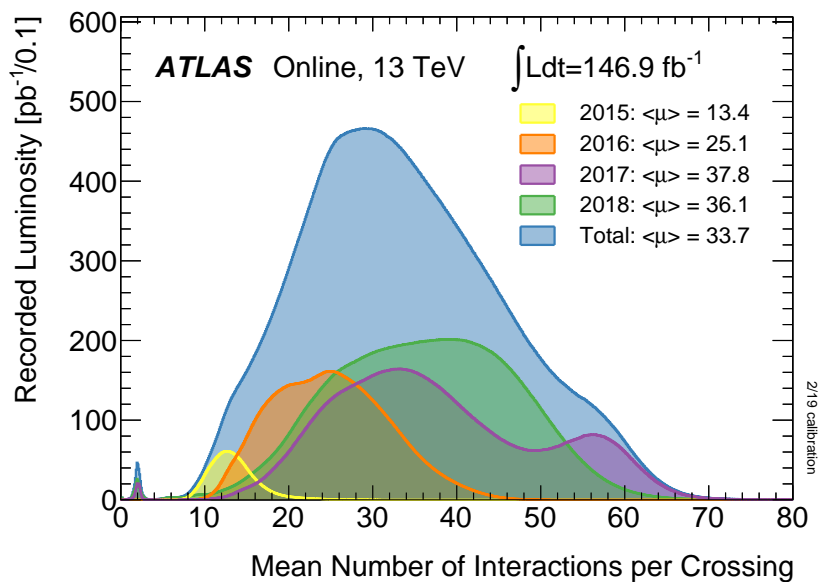


Figure 3.2: Luminosity-weighted distribution of the mean number of interactions per crossing for the pp collision data from 2015 to 2018 at $\sqrt{s} = 13 \text{ TeV}$. From [192].

3.2 Reconstruction of physics objects

Depending on their nature and their interaction with the material of the various detector subsystems, the particles produced in a given collision event will be identified by the ATLAS detector. Figure 3.3 depicts how different particles might interact with each layer of the detector. The corresponding electric signals, time-of-flight and impact parameter information, to name but a few, need to be processed into physics objects to be used in analysis of the data. In what follows, we describe the reconstruction of the main objects of interest, common to all analyses presented in Parts II and III, as well as give details about specific calibrations.

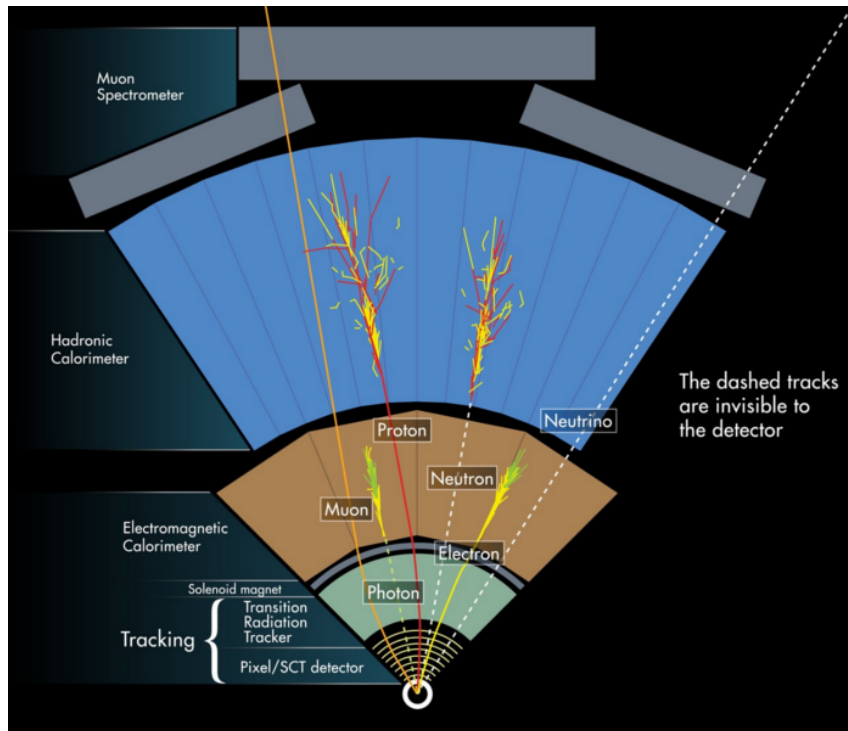


Figure 3.3: Representation of the interaction of various particles and the subsystems of the ATLAS detector. From [193].

3.2.1 Tracks and vertices

Tracks from charged particles are reconstructed in the Inner Detector from Pixel, SCT and TRT information by forming a sequence of three-dimensional points to seed tracks in the innermost layer, before extending them outwards and applying a cleaning and fitting algorithm [194–199]. Tracks originating from pile-up effects and system noise are handled by a dedicated algorithm and can be reduced by e.g. requiring a hit in the IBL. Tracks are finally selected for further use in other physics objects if they have $p_T > 500 \text{ MeV}$ and $|\eta| < 2.5$. Below 5 GeV, a reconstruction efficiency of nearly 90% is achieved.

Tracks are particularly useful in determining the Primary Vertex (PV), defined as that with the largest $\sum p_T^2$ over associated tracks. The PV, understood to originate from the main hard-scatter event of the collision, can then be used to reject pile-up background. Other vertices can also be reconstructed, given at least two associated tracks; the secondary vertex is of particular importance for e.g. b -tagging (described below) and enjoys dedicated finder algorithms.

Two important quantities related to tracks are their transverse (d_0) and longitudinal ($z_0 \sin \theta$) impact parameters. The former is defined as the distance of closest approach in the $R - \phi$ plane of

the track to the PV, and the latter as the distance of the track to the PV in the longitudinal plane at the point of closest approach in $R - \phi$.

3.2.2 Electrons

The charged particle *par excellence*, electrons are associated to tracks in the ID, as well as correlated energy deposits in the ECAL [200–203]. In the analyses presented hereafter using the reconstruction software associated to the 2015–2016 ATLAS dataset, a sliding-window algorithm is employed. Clusters of cells in the ECAL are selected as “seeds” when they satisfy $p_T > 2.5 \text{ GeV}$ and are matched to track seeds with $p_T > 1 \text{ GeV}$, within the tracking acceptance of $|\eta| < 2.47$. Beyond this range in η , electron candidates are referred to as “forward electrons” and are passed to different identification algorithms; only central electrons are used hereafter. The sliding-window algorithm performs a scan of these clusters to find local maxima in energy deposits using 3×5 calorimeter cells, each with $\Delta\eta \times \Delta\phi = 0.025 \times 0.025$. The η and ϕ positions of the clusters associated with central electron candidates are then updated using the track information, and the deposited energy is corrected by reclustering in different calorimeter regions (7×3 cells in the barrel and 5×5 in the endcaps) as well as by considering the efficiency of benchmark processes (such as $Z \rightarrow e^+e^-$). The fixed size of the windows allows for a precise calibration.

A major update to the electron reconstruction software, used in the 2015–2018 ATLAS analyses presented here, uses so-called dynamical topological clusters or “superclusters” [204], an example of which is depicted in Figure 3.4. A topological cluster, or “topocluster”, consists in a seed calorimeter cell, defined as having a signal-to-noise ratio of at least 4, which collects neighbouring cells if these have a signal-to-noise ratio of at least 2. This process is repeated, considering successive neighbours of newly accepted cells after each iteration, until no more cells are found that satisfy this threshold condition. In a very final step, the signal-to-noise ratio threshold is dropped to 0 to collect any remaining soft deposits in a “4-2-0” algorithm. Topoclusters made of a large number of cells offer a very good noise suppression. Once they are formed, the highest energy topocluster is selected as a supercluster seed and a new iterative procedure takes place, checking for all other lower energy topoclusters whether they are in a 3×5 cell window around the seed barycentre. Those that satisfy this condition are considered “satellite” clusters, originating from the *bremsstrahlung* emission of a photon in the ID. The best-fit tracks of the seed and satellite topoclusters are further checked to match. Once the list of satellite candidates has been exhausted for a given seed, all the matched satellites are merged to the seed to form a supercluster. This definition is applied iteratively to all topoclusters, naturally removing the ones used in a previous supercluster definition. This sweeping technique of satellites allows to collect electromagnetic showers down to the 100 MeV scale.

Calibrated electrons are then classified with respect to identification and isolation criteria. Using shower shape, track-cluster matching and ID information, a likelihood-based identification algorithm is used, which offers three “working points” (in order of increasing background rejection): Loose, Medium and Tight. The efficiency of these working is shown as a function of the transverse energy (E_T) of the electron candidate in Figure 3.5.

Standard requirements are applied on the transverse and longitudinal impact parameters, $|d_0/\sigma(d_0)| < 5.0$ and $|z_0 \sin\theta| < 0.5 \text{ mm}$, to mitigate the contribution from charge-misidentified electrons, non-prompt leptons and pile-up.

Isolation criteria, which compare the amount of energy deposited near the electron in the ECAL and the transverse momenta of nearby tracks to those of the electron candidate itself, are used to separate prompt electrons (from hard-scatter events) from photon conversions and hadrons mis-reconstructed as electrons. The energy deposited in a cone of radius Δ around the electron candidate in the ECAL, $E_T^{\text{cone},\Delta}$, and the sum of the transverse momenta of tracks surrounding the candidate electron track, $p_T^{\text{cone},\Delta}$, after appropriate subtraction of contributions from the underlying

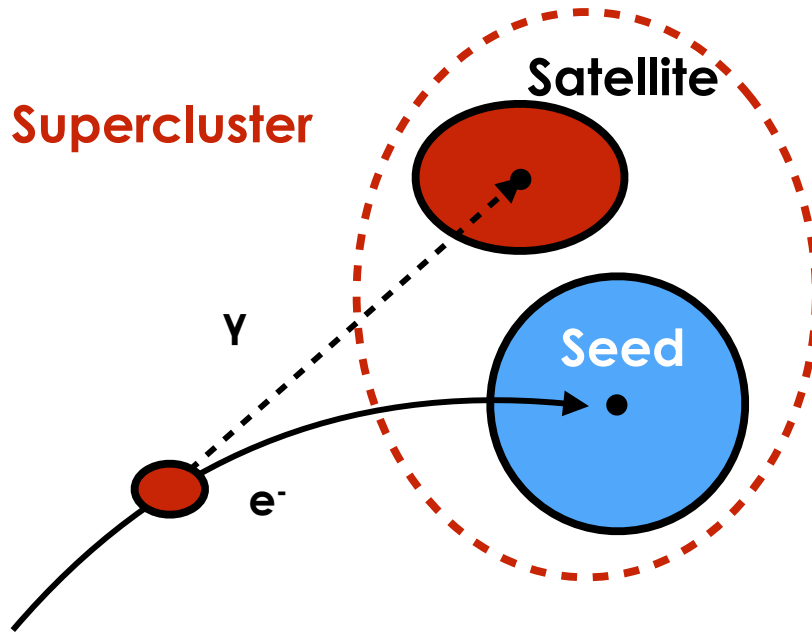


Figure 3.4: Diagram of an example supercluster showing a seed electron cluster and a satellite photon cluster. From [204].

event and pile-up effects, can be used to define various isolation working points. These are reported in Table 3.1.

Figure 3.6 reports the efficiencies of the lowest unrescaled single electron triggers used over Run 2, separately for each year between 2015 and 2016. The turn-on of the efficiency curves happens at around 25 GeV and therefore a requirement of $p_T > 27$ GeV for the leading trigger-matched electron is a common requirement of the analyses presented in the main body of this document.

3.2.3 Muons

Muons are reconstructed by combining information from the ID and MS [207]. Hits in the MS are first fitted into tracks, then matched to charged tracks in the ID. Four types of muon candidates are possible:

- CB: “combined muons” are the simple combination of ID and MS tracks, the most common muon candidates and offer the lowest momentum resolution.
- ST: “segment-tagged” candidates are built by extrapolating only a segment of the MS track to the ID, in cases where the information in the MS is incomplete.
- CT: “calorimeter-tagged” muons have their ID track extrapolated to an energy deposit in the calorimeter, if it is compatible with a minimum ionising particle.
- ME: “extrapolated muons” are based only on the MS track and a loose requirement for compatibility with the interaction point

CB candidates can reach a reconstruction efficiency close to 99% in the central region; CT and ST candidates are used within $|\eta| < 0.1$ to complement the non-hermeticity of the MS, and ME muons to extend reconstruction in the region $2.5 < |\eta| < 2.7$, beyond ID acceptance.

Like electrons, muons are subject to further requirements on their impact parameters, namely $|d_0/\sigma(d_0)| < 3.0$ and $|z_0 \sin \theta| < 0.5$ mm, as well as identification (quality) criteria. The latter correspond to the compatibility of the matching between ID and MS tracks (via a χ^2 test) and that of the momentum measurements, and yield four working points: Loose, Medium, Tight and

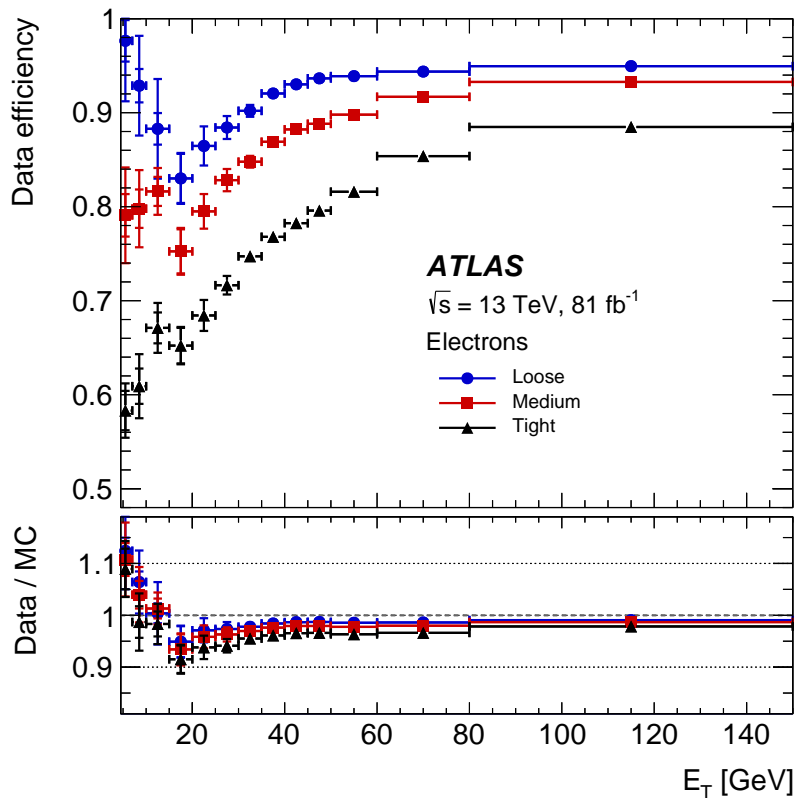


Figure 3.5: The electron identification efficiency in $Z \rightarrow e^+e^-$ events in data as a function of E_T for the Loose, Medium and Tight working points. The efficiencies are obtained by applying data-to-simulation efficiency ratios measured in $J/\psi \rightarrow e^+e^-$ and $Z \rightarrow e^+e^-$ events to $Z \rightarrow e^+e^-$ simulation. The inner uncertainties are statistical and the total uncertainties are the statistical and systematic uncertainties in the data-to-simulation efficiency ratio added in quadrature. The bottom panel shows the data-to-simulation ratios. From [205].

HighPt. The reconstruction efficiency for the Medium quality working point, used throughout this document, is shown in Figure 3.7 as a function of η for a calibration sample of $Z \rightarrow \mu^+\mu^-$ events. Isolation variables are defined in a similar way as for electrons, and used to construct the working points in Table 3.1.

Figure 3.8 reports the efficiencies of the lowest unrescaled single muon triggers used for the data-taking years 2016–2018. The turn-on of the efficiency curves happens at around 25 GeV and therefore a requirement of $p_T > 27$ GeV for the leading trigger-matched muon is a common requirement of the analyses presented in the main body of this document.

3.2.4 Photons

The calorimeter-based reconstruction of photons [209, 210] is very similar to that of electrons (particularly the distinction between sliding-window and supercluster reconstruction in the 2015–2016 vs 2015–2018 datasets); however, prompt photons not being charged, they don't leave any tracks in the ID. Therefore, in the absence of a matching track, a cluster in the ECAL can be attributed to a photon. If a cluster-matched track originates from a secondary vertex (and not the PV), the particle is classified as a converted photon. Loose and Tight identification working points are defined, based on shower shape variables; the former is used for triggering and the latter for physics analysis. Identification efficiencies for central unconverted Tight photons as a function of

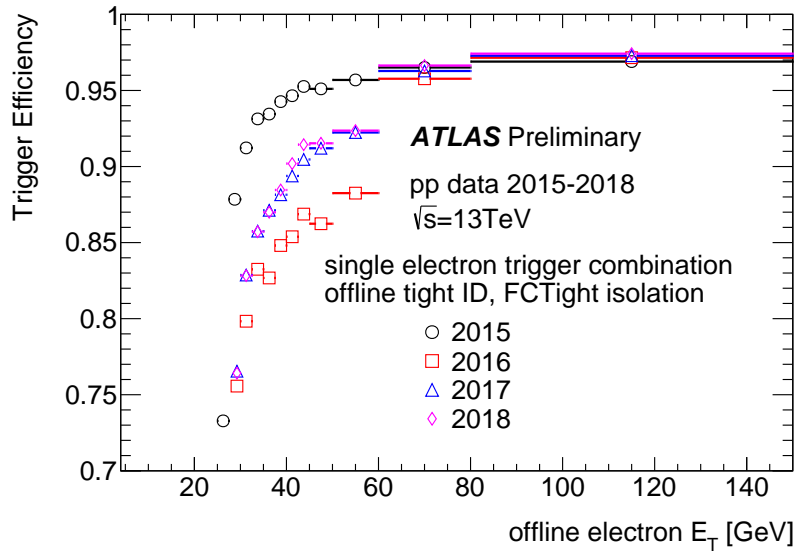


Figure 3.6: Efficiency of the lowest unprescaled single electron trigger combination in 2015–2018 data, compared to $Z \rightarrow e^+e^-$ MC. The efficiency is given as a function of the offline electron transverse energy, E_T , where the offline electron fulfills a `Tight` offline identification requirement as well as a `FCTight` offline isolation requirement. The η -dependency is integrated over $|\eta| < 2.47$ and the μ -dependency over the full range. The trigger efficiency in 2015 is highest because no online isolation requirement and a looser online identification requirement was applied. The inefficiency observed in 2016 is due to too stringent online identification optimisation with respect to the previous offline selection criteria. From [206].

E_T are displayed in Figure 3.9. The definition of the single isolation criterion of interest is reported in Table 3.1, where the photon track isolation variable is defined as the sum of the transverse momenta of tracks with $p_T > 1$ GeV in a cone of radius Δ within $|z_0 \sin \theta| < 3$ mm of the PV and excluding the tracks associated with photon conversions.

Figure 3.10 reports the efficiencies of the lowest unprescaled single photon triggers used in 2016 data. The turn-on of the efficiency curve corresponding to the trigger used in the analysis reported in Chapter 8 is at around 140 GeV and therefore trigger-matched photons (in that analysis) are required to have $p_T > 150$ GeV to be fully efficient.

3.2.5 Jets

Quarks and gluons carry a colour charge, such that, due to the short range of the strong force and the phenomenon of colour confinement in QCD, they can only be observed as colour-neutral bound states (hadrons). This hadronisation process happens on a short timescale of $\mathcal{O}(10^{-24})$ s, and is only evaded by the top quark whose large mass causes it to decay before. By conservation of momentum, the resulting hadrons carry on travelling in the initial direction of the original parton, and thus a spray of collimated particles is observed in the calorimeters (as well as `ID` tracks for charged particles). This flow of particles needs to be considered as a single object, a “jet”, in order to describe the kinematics of the corresponding parton; since quarks and gluons are produced in abundance, the definition of a jet is of crucial importance for physics analysis.

Jets deposit most of their energy in the dedicated hadronical calorimeter, where clusters are constructed from topologically connected energy deposits – “topoclusters”, as defined in Section 3.2.2 – centred around a seed cell and satisfying various conditions to reduce the contribution from dead calorimeter material, leakage and pile-up (the “4-2-0” algorithm). Further calibrations

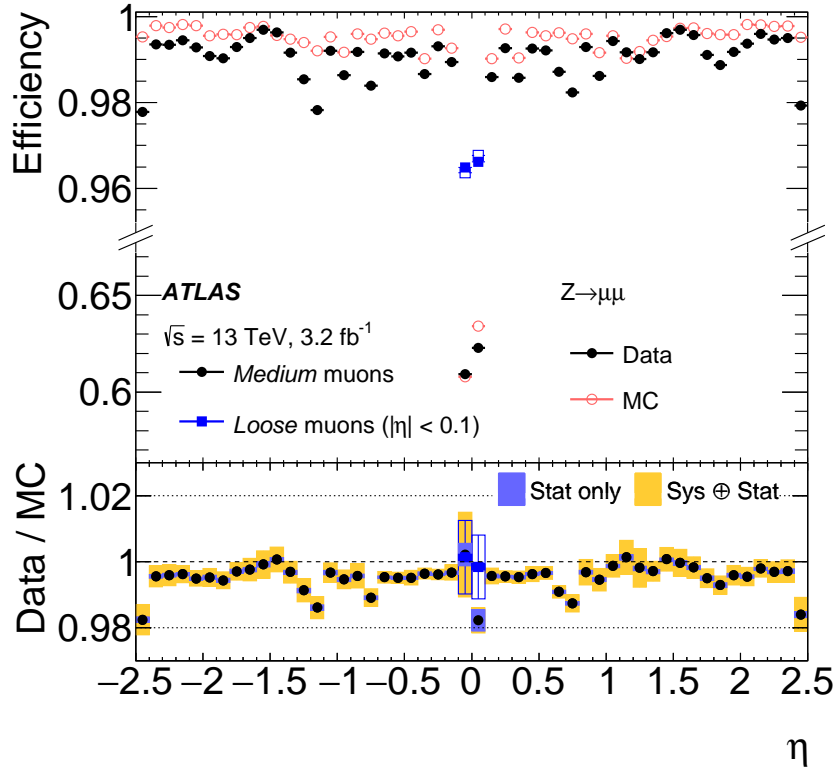


Figure 3.7: Muon reconstruction efficiency as a function of η measured in $Z \rightarrow \mu^+ \mu^-$ events for muons with $p_T > 10 \text{ GeV}$ shown for the Medium muon selection. In addition, the plot also shows the efficiency of the Loose selection (squares) in the region $|\eta| < 0.1$ where the Loose and Medium selections differ significantly. The error bars on the efficiencies indicate the statistical uncertainty. The bottom panel shows the ratio of the measured to predicted efficiencies, with statistical and systematic uncertainties. From [207].

are then applied to the jet candidates, in the form of a **Jet Energy Scale (JES)** [213] that corrects for the mismeasurement of the reconstructed calorimeter energy (compared to MC simulations) as a function of p_T and η . A **Jet Energy Resolution (JER)** [214] is derived as the standard deviation from a Gaussian fit of the jet response function, the ratio of the jet energies at reconstruction- and generator-level, used as a correction. The comparison of the average jet response in data and simulation is presented in Figure 3.11.

When reconstructing a jet, we require the chosen algorithm to be robust against small variations in the hadronisation process. Infrared safety refers to the invariance of jet definitions under the inclusion of soft radiation (e.g. low- p_T gluon), while collinear safety intuitively retains a split parton within the same jet. A simple algorithm, where fixed-size circles are drawn on the calorimeter surface and extrapolated back to the PV as cones, satisfies neither of these robustness criteria. The ATLAS collaboration therefore predominantly uses [215] the anti- k_t algorithm [216], a more sophisticated iterative jet clustering method that relies on the definition of the distance between any two particles i and j for a fixed radius parameter R :

$$d_{ij} = \min(p_{T,i}^{2p}, p_{T,j}^{2p}) \frac{\Delta R_{ij}^2}{R^2}, \quad (3.1)$$

where ΔR_{ij}^2 is the separation between the two particles in the $\eta - \phi$ plane, $\Delta R_{ij}^2 = (\phi_i - \phi_j)^2 +$

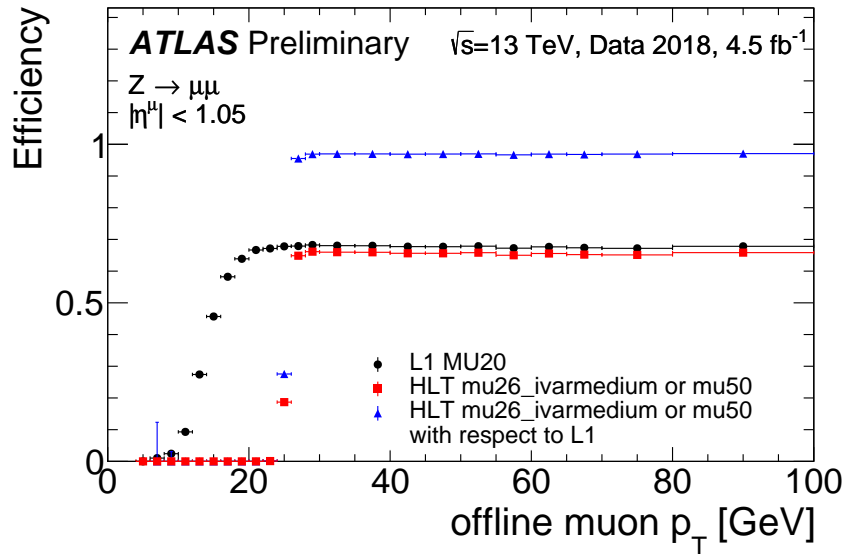


Figure 3.8: Absolute efficiency of the Level 1 (L1) trigger, requiring a candidate passing the 20 GeV threshold of the L1 muon trigger system, and relative efficiencies of the High Level Triggers (HLT). The efficiency is computed with respect to offline isolated muon candidates which are required to pass Medium quality and FixedCutTightTrackOnly isolation requirements, and measured using a tag-and-probe method with $Z \rightarrow \mu^+ \mu^-$ candidates. The η -dependency is integrated over $|\eta| < 1.05$. From [208].

$(\eta_i - \eta_j)^2$, and p_T^{2p} their transverse momenta raised to some power $2p$. The choice of $p = 0$ returns the so-called Cambridge/Aachen algorithm, $p = 1$ the k_t and $p = -1$ the anti- k_t algorithm. An absolute beam distance, $d_{iB} = p_{T,i}^{2p}$, is also defined for particle i : if it smaller than any d_{ij} , particle i is considered a jet; otherwise, it is merged with the particle j that provided the minimum distance. This process is repeated until no clusters are left, such that hard particles “collect” softer contributions in a radius R around them to form conical jets. The radius parameter $R = 0.4$ is adopted throughout the rest of this document.

To reduce the potentially large contributions arising from pile-up events [125, 217], a multivariate algorithm, the **Jet Vertex Tagger (JVT)**, is used. The JVT takes as input of its likelihood function information about the individual tracks identified as constituents of a candidate jet, as well as the **Jet Vertex Fraction (JVF)**, the ratio of tracks associated to the PV to the total number of tracks in the candidate jet. Jet cleaning techniques are further employed to remove contributions from cosmic muons, calorimeter noise and interactions with residual gas in the beampipe and non-detector material.

3.2.6 Jet flavour tagging

The ability to differentiate jets originating from light-flavour quarks (u, d, s) and gluons on the one hand, and heavy-flavour quarks (c, b) on the other is crucial to many ATLAS analyses [219]. For the purpose of this specific document, the reliable identification of jets from the decays of B-hadrons is a first step towards reconstructing top quark candidates. While gluons split and hadronise quickly, and hadrons from light-flavour quarks are either stable or subject to electromagnetic decays, B-hadrons have relatively longer lifetimes (around 1.5×10^{-12} s or $c\tau = 450 \mu\text{m}$, which at energies of $O(100)$ GeV translate into flight distances of 8–9 mm) and hence a separate, secondary vertex can be associated to their decay. Information about the track impact parameters, reconstruction of the secondary vertex and topology of the decay chain is combined within a multivariate algorithm [220,

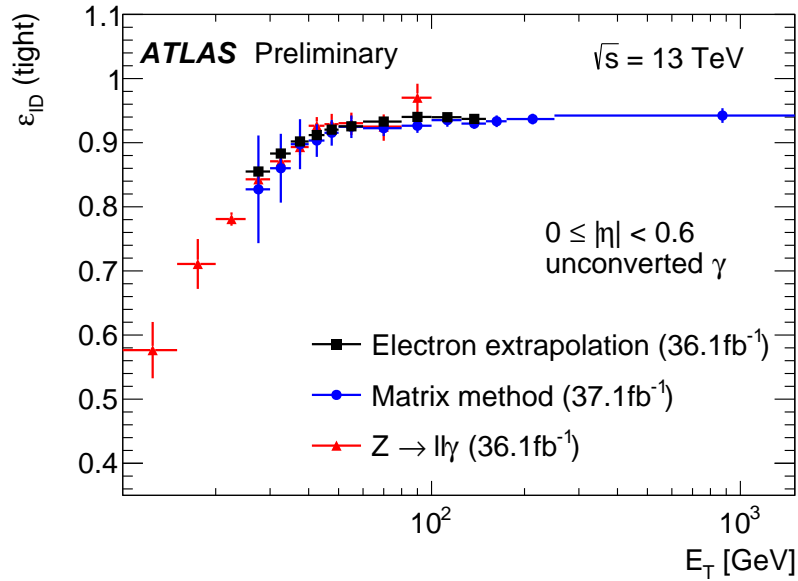


Figure 3.9: Comparison of the data-driven measurements (radiative Z boson decay, electron extrapolation and matrix method [209]) of the identification efficiency for unconverted photons as a function of E_T in the region $10\text{ GeV} < E_T < 1500\text{ GeV}$ for the pseudorapidity interval $|\eta| < 0.6$. For the matrix method, additional data were used when the toroid magnet was turned off that is not used for photon reconstruction. The error bars represent the sum in quadrature of the statistical and systematic uncertainties estimated in each method. From [211].

[221]; during Run 2, this is the MV2c10 algorithm [199], which uses a **Boosted Decision Tree (BDT)** to separate b -tagged jets from light- and c -tagged jets, trained on $t\bar{t}$ events. The BDT is calibrated and systematic uncertainties are assigned for various working points, corresponding to a choice of b -tagging efficiency. The 77% and 85% efficiency working points will be used in the chapters that follow.

Figure 3.12 shows the output of the MV2c10 BDT for various jet flavours in an inclusive sample of $t\bar{t}$ events. Selecting events with a BDT output greater than 0.11 (0.64) yields a b -tagging efficiency of 85% (77%) and a light-jet rejection rate of 28 (113) [222, 223].

3.2.7 Missing transverse energy

The concept of missing transverse momentum is a fundamental one in ATLAS reconstruction. In the **SM**, the neutrino is the only particle that (to a very good approximation) doesn't interact with the detector, while in **BSM** scenarios a Dark Matter candidate would be expected to satisfy this property too. Whether it is produced directly from the hard-scatter event or along the decay chain of some heavy particle, an “invisible” particle will carry away some momentum and hence, after summing up all the visible contributions in the detector, a net deficit will be observed – a non-zero total momentum vector. However, since the hard-scatter event originates from the collision of protons and the exact fraction of momentum carried by each parton is unknown, the assumption of momentum conservation only holds in the transverse plane, with the transverse momentum of the incoming partons safely taken to be negligible.

A missing transverse momentum 2-vector can therefore be defined as [224]

$$\mathbf{p}_T^{\text{miss}} = - \sum_{\text{event}} \mathbf{p}_T, \quad (3.2)$$

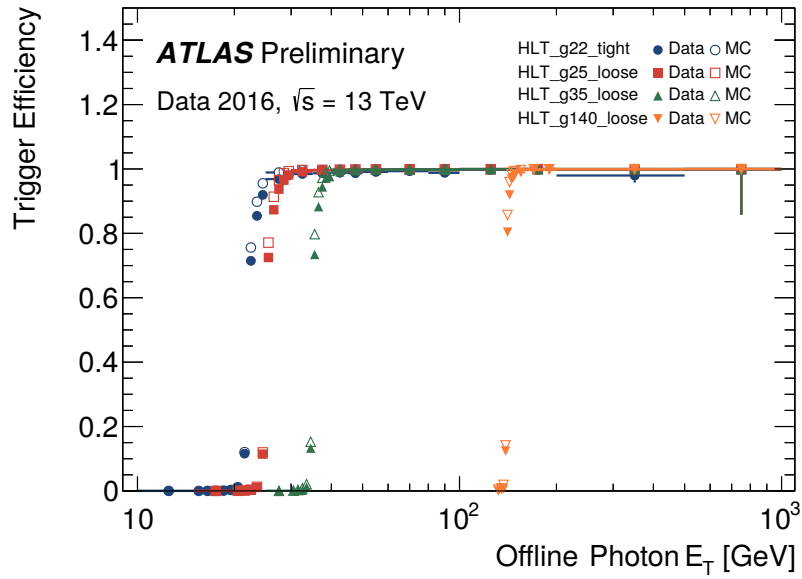


Figure 3.10: Efficiency of photon triggers requiring Loose identification and a transverse energy $E_T > 140 \text{ GeV}$ (inverted triangles) for the analysis of interest presented in [susy analysis], in data (full markers) and MC simulated samples (empty markers), as a function of the transverse energy of the photon candidates reconstructed offline passing the Tight identification with $|\eta| < 2.37$ and excluding the transition region between the barrel and endcap electromagnetic calorimeters at $1.37 < |\eta| < 1.52$. From [212].

with modulus E_T^{miss} , the missing transverse energy. This quantity is computed as the negative vectorial sum of the momenta of all calibrated objects (individual leptons, photons and jets), as well as an additional soft term to account for signals (ID tracks from the PV) not associated to any physics objects in their respective reconstruction process. Although non-zero E_T^{miss} arises from any source of mis-measurement and is generally enhanced with increased pile-up, signal neutrinos or Dark Matter candidates are expected to provide much larger amounts of E_T^{miss} , making this a standard variable in many analyses. The resolution of the E_T^{miss} is obtained from studying $Z \rightarrow \mu^+ \mu^-$ events, where little real E_T^{miss} is expected, and is shown in Figure 3.13 as a function of $\sum E_T$.

Figure 3.14 reports the efficiencies of the E_T^{miss} triggers in the 2016 data-taking year, relevant to the analysis presented in Chapter 8. The turn-on of the efficiency curves happens at around 150 GeV and full efficiency is achieved by requiring a selection of events with $E_T^{\text{miss}} > 250 \text{ GeV}$.

Table 3.1: Isolation criteria for the working points of interest to the analyses presented in this document, applied to electrons, muons and photons according to the variable definitions given previously. Working points starting with the prefix “FC” (instead of “FixedCut”) used an additional track-to-vertex association algorithm in the definition of track-based isolation variables.

Particle	Working point	ECAL- or MS-based	ID-based
Electrons	FCTight	$E_T^{\text{cone},0.2}/p_T < 0.2$	$p_T^{\text{cone},0.2}/p_T < 0.15$
	FixedCutTight	$E_T^{\text{cone},0.2}/p_T < 0.06$	$p_T^{\text{cone},0.2}/p_T < 0.06$
Muons	FCTightTrackOnly	—	$p_T^{\text{cone},0.3}/p_T < 0.06$
	FixedCutTightTrackOnly	—	$p_T^{\text{cone},0.3}/p_T < 0.06$
Electrons+Muons	GradientLoose	$\epsilon = (0.0057 \times p_T [\text{GeV}] + 95.57)\%$	
Photons	FixedCutLoose	$E_T^{\text{cone},0.2}/p_T < 0.065$	$p_T^{\text{cone},0.2}/p_T < 0.05$

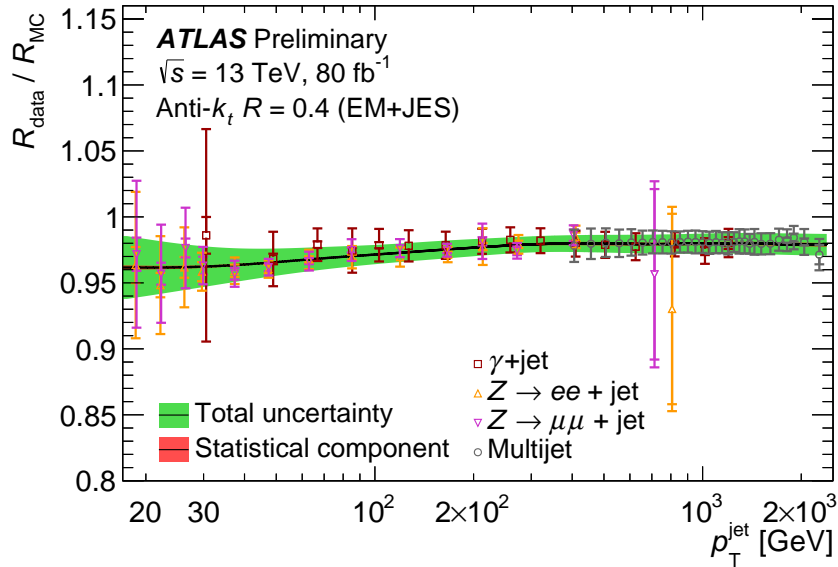


Figure 3.11: Data-to-simulation ratio of the average jet p_T response as a function of jet p_T . The combined result is based on three in situ techniques: the Z+jet balance method (dielectron channel, upward-pointing triangles; and dimuon channel, downward-pointing triangles), γ +jet balance method (open squares) and the multijet balance (open circles). The errors represent the statistical (inner error bars and small inner band) and the total uncertainty (statistical and systematic uncertainties added in quadrature, outer error bars and outer band). These results apply to anti- k_t jets with $R = 0.4$, reconstructed from electromagnetic-scale topo-clusters. The calibration curve and its uncertainty are smoothed using a sliding Gaussian kernel. These in situ measurements were performed following methodology similar to that of [213], and are taken as a residual correction. From [218].

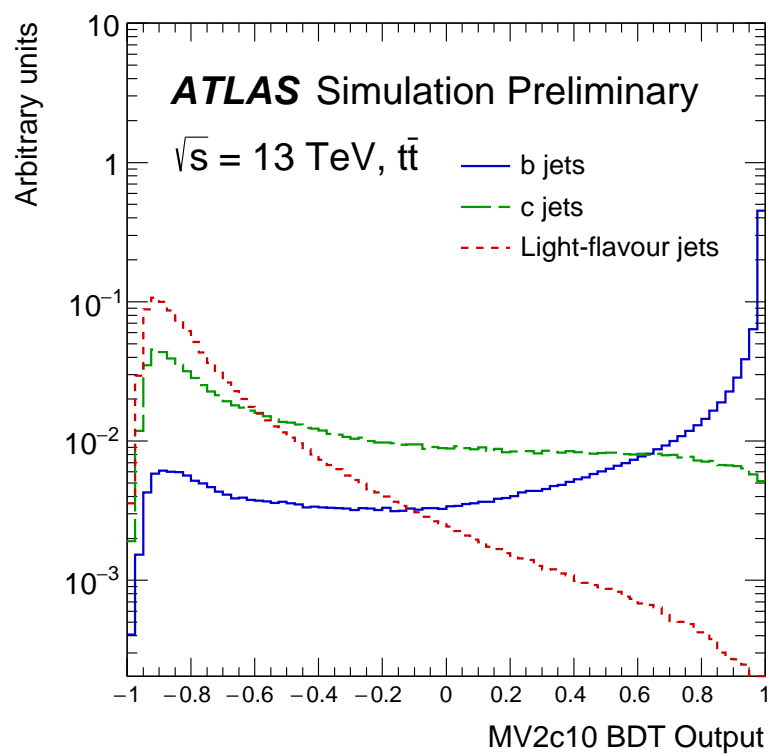


Figure 3.12: MV2c10 BDT output for b - (solid blue), c - (dashed green) and light-flavour (dotted red) jets evaluated with $t\bar{t}$ events. From [199].

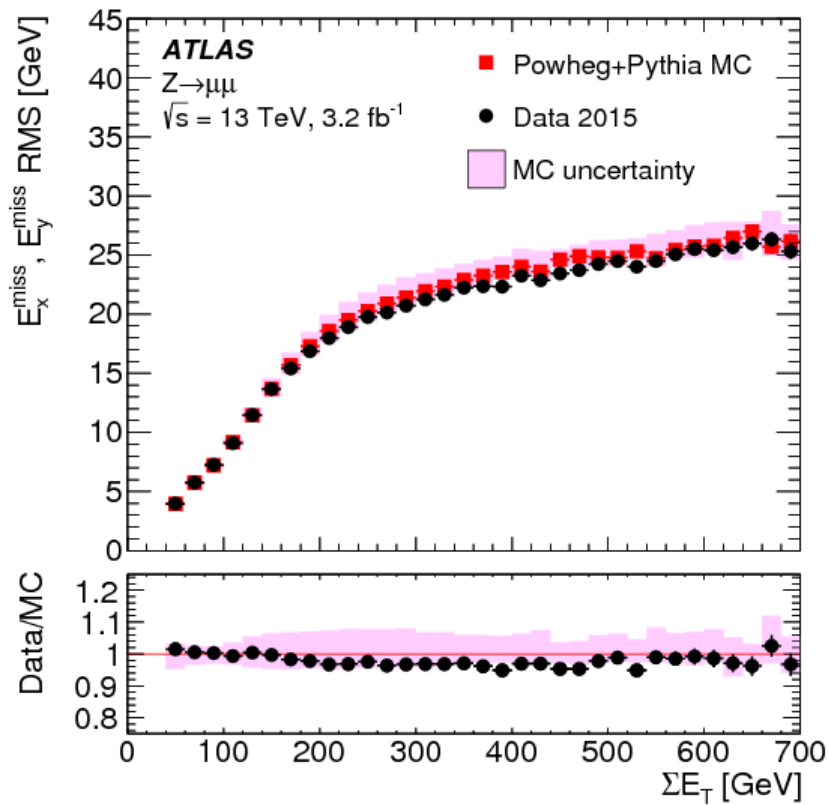


Figure 3.13: The RMS width of the $E_{x(y)}^{\text{miss}}$ in bins of ΣE_T in an inclusive sample of $Z \rightarrow \mu^+ \mu^-$ events. Predictions from MC simulations are overlaid on the data points, and the ratios are shown below the plot. The shaded bands indicate the combined statistical and systematic uncertainties of the resolution measurements. From [224].

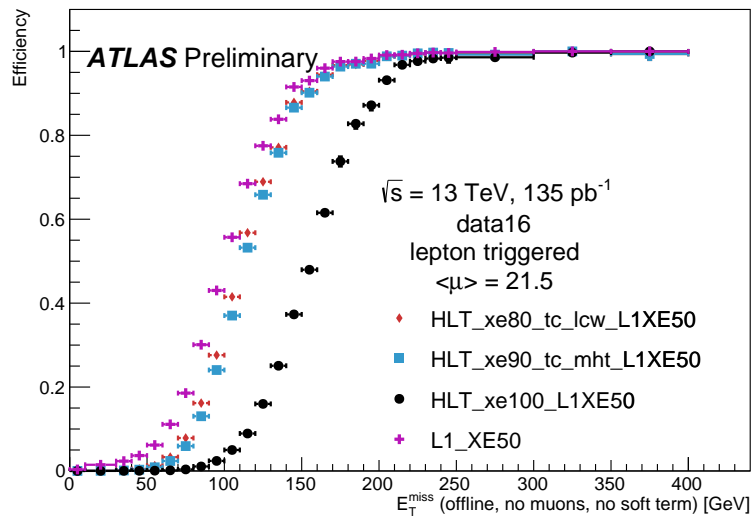


Figure 3.14: Efficiency as a function of modified online E_T^{miss} for three different E_T^{miss} triggers. The events have been selected using single lepton (electron or muon) triggers. Two of the triggers used in [susy analysis] are shown: in blue (black), calculating the E_T^{miss} based on reconstructed jets (calorimeter cells calibrated at the electromagnetic scale) and with a nominal threshold of 90 GeV (110 GeV). All three algorithms are seeded by an L1 trigger with a nominal threshold of 50 GeV which is also shown. From [225].

3.3 Particle- and parton-level definitions

The full simulation and reconstruction of a given process (via Monte Carlo sampling) through the ATLAS detector results in what is referred to as “detector”-level (or “reconstruction”-level) quantities, similar to what is obtained from the direct reconstruction of data. It is however possible to define labelled physics objects before or at earlier stages of the reconstruction step; this gives rise to corresponding “parton-” and “particle”-level quantities, respectively [226].

Information about the final state partons, after final state radiation but before hadronisation, constitutes the parton-level definition. In the case of a $t\bar{t}Z$ simulation for instance, one has direct access to the kinematic of the top quark partons and the Z boson, after all radiative corrections, as well as their decay products (b -quarks, W bosons, etc.) but not e.g. to the corresponding jets. Top quark reconstruction (see next section) at parton-level is therefore unnecessary, but the full information about the $t\bar{t}$ system can be used to drive a reconstruction-level algorithm.

Particle-level information represents the system after the decay of the partons to stable final-state particles, including hadronisation of the quarks. The objects considered in the event record are stable particle (with a mean lifetime $> 0.3 \times 10^{-10}$ s) within the observable pseudorapidity range. Photons from hadron decays, inducing a dependency on the underlying event, are removed. Electrons and muons are only present as prompt leptons from the decay of W and Z bosons (or in BSM scenarios, from a specific new particle), and are dressed with any radiated photon. Neutrinos are selected in the same way as electrons and muons, including tau decays as an additional source, and define the missing transverse energy. Jets are clustered using the previously defined anti- k_t algorithm, looping over all stable particles that haven’t been identified as electrons, muons, neutrinos or photons. b -jets at particle-level are defined as jets containing a ghost-matched B-hadron, following the prescriptions set in Ref. [227].

The topic of unfolding, which we will extensively discuss in Section 4.2, covers a range of algorithms aiming at recovering a “true” underlying distribution at either particle- or parton-level from a detector-level one by inverting the smearing effects induced by the detector reconstruction. Beyond the correction of relevant kinematic distributions, scaling factors are often applied to account for efficiency and acceptance effects. These quantities, to be defined explicitly in Section 4.2, are due to the various selection criteria applied in the analysis; at particle- or parton-level, these criteria form the definition of a so-called “fiducial volume”. It is often the case in ATLAS analyses that particle-level fiducial volumes are kept as kinematically close to detector-level selections as possible in order to reduce the extrapolation over objects such as jets, while considering the full parton-level phase-space as a precision test of Monte Carlo generators.

3.4 Aspects of top quark reconstruction

In what follows we introduce a few notions related to the reconstruction of a $t\bar{t}$ system. In the second part of this document, covering the measurement of the $t\bar{t}Z$ cross section, we will refer to semi-leptonic and di-leptonic $t\bar{t}$ reconstruction. The third part focuses on all-hadronic final states, where both W bosons from the two top quarks decay to light-jets. No explicit top quark reconstruction is performed, so we will simply note for now that the problem there is mainly one of combinatorics, in assigning jets and b -jets to the correct W boson and top quark candidates, and hence a χ^2 method minimising the mass differences between the two top quark and W boson candidates is a first possible approach.

3.4.1 Semi-leptonic $t\bar{t}$ case

In a semi-leptonic $t\bar{t}$ decay, one expects two b -jets, two light-jets, one charged lepton and one neutrino in the final state, at tree-level. To estimate the kinematics of the invisible neutrino, one can make the assumption that it is the leading contribution to the missing transverse energy in the

event. Therefore we can start with estimates of the transverse momentum and azimuthal angle of the neutrino of E_T^{miss} and ϕ^{miss} , respectively. Adding the constraint that the combined system of the neutrino and lepton should have a mass equal to that of a W boson, one can solve for the longitudinal component of the neutrino and retrieve the full kinematics of the top quark.

Given a W boson decaying into a charged lepton ℓ and a neutrino ν , we express conservation of 4-momentum as:

$$p_W^2 = m_W^2 = (p_\nu + p_\ell)^2 = (E_\nu + E_\ell)^2 - (\mathbf{p}_\nu + \mathbf{p}_\ell)^2. \quad (3.3)$$

Assuming a massless neutrino:

$$E_\nu^2 = \mathbf{p}_\nu^2, \quad (3.4)$$

equation 3.3 can be expanded into:

$$\underbrace{m_W^2 - m_\ell^2 + 2(p_x^\nu p_x^\ell + p_y^\nu p_y^\ell)}_{\equiv \alpha} = 2E_\nu E_\ell - 2p_z^\nu p_z^\ell, \quad (3.5)$$

leading to:

$$\frac{\alpha}{2} + p_z^\nu p_z^\ell = E_\nu E_\ell \iff \frac{\alpha^2}{4} + (p_z^\nu)^2 (p_z^\ell)^2 + \alpha p_z^\nu p_z^\ell = E_\nu^2 E_\ell^2. \quad (3.6)$$

Decomposing E_ν as:

$$E_\nu^2 = (p_x^\nu)^2 + (p_y^\nu)^2 + (p_z^\nu)^2, \quad (3.7)$$

and identifying p_z^ν , the longitudinal component of the neutrino's 3-momentum, as the variable of interest, the following quadratic equation is obtained:

$$a (p_z^\nu)^2 + b (p_z^\nu) + c = 0, \quad (3.8)$$

$$\text{with } \begin{cases} a = (p_z^\ell)^2 - E_\ell^2, \\ b = \alpha p_z^\ell, \\ c = \frac{\alpha^2}{4} - E_\ell^2 [(p_x^\nu)^2 + (p_y^\nu)^2]. \end{cases} \quad (3.9)$$

The usual quadratic determinant $\Delta = b^2 - 4ac$ can then be computed, taking p_x^{miss} and p_y^{miss} as first guesses for the neutrino transverse momentum components:

1. Case $\Delta < 0$: the determinant should be computed again, lowering p_x^ν and p_y^ν in small steps, up to computational efficiency. If no real solutions exist after N steps, one should take $p_z^\nu = 0$.
2. Case $\Delta = 0$: this situation is extremely rare, yet possible. Exactly one non-zero solution exists for p_z^ν .
3. Case $\Delta > 0$: two non-zero solutions exist; in the case of semi-leptonic $t\bar{t}$ decays, use the constraint $m_{\text{top}}^{\text{had}} \sim m_{\text{top}}^{\text{lep}}$. To avoid biasing the result towards the top quark mass, one could also pick the solution with smallest $|p_z^\nu|$, expecting the $t\bar{t}$ system from which the W boson originates to be central.

Let us now rewrite the α term, defined in equation 3.5, as:

$$\alpha = m_W^2 - m_\ell^2 + 2(p_x^\nu p_x^\ell + p_y^\nu p_y^\ell) \quad (3.10)$$

$$= m_W^2 - m_\ell^2 + 2\mathbf{p}_T^\nu \cdot \mathbf{p}_T^\ell \quad (3.11)$$

$$= m_W^2 - (m_\ell^2 - 2\mathbf{p}_T^\nu \cdot \mathbf{p}_T^\ell + 2E_T^\nu E_T^\ell) + 2E_T^\nu E_T^\ell \quad (3.12)$$

$$= m_W^2 - m_T^2 + 2E_T^\nu E_T^\ell \quad (3.13)$$

where we defined m_T , the transverse mass of the lepton-neutrino system, as the expression between brackets in equation 3.12. Hereafter we approximate the lepton as massless, that is assume $E_T^\ell \gg m_\ell$, such that we can write $E_T^\ell = p_T^\ell = m_T^\ell$. With those results in mind, we now expand out the real solutions for p_z^ν in the case $\Delta > 0$:

$$p_z^\nu = \frac{-b \pm \sqrt{\Delta}}{2a} = \frac{-\alpha p_z^\ell \pm \sqrt{\alpha^2 (p_z^\ell)^2 - \left((p_z^\ell)^2 - E_\ell^2 \right) \left(\alpha^2 - 4E_\ell^2 (E_T^\nu)^2 \right)}}{2 \left((p_z^\ell)^2 - E_\ell^2 \right)} \quad (3.14)$$

$$= \frac{-\alpha p_z^\ell \pm \sqrt{E_\ell^2 \left(4 (p_z^\ell)^2 (E_T^\nu)^2 + \alpha^2 - 4E_\ell^2 (E_T^\nu)^2 \right)}}{-2 (p_T^\ell)^2} \quad (3.15)$$

$$= \frac{\alpha p_z^\ell \mp E_\ell \sqrt{-4 (E_T^\nu)^2 (p_T^\ell)^2 + \alpha^2}}{2 (p_T^\ell)^2} = \frac{\alpha p_z^\ell \mp E_\ell \sqrt{(\alpha - 2E_T^\nu E_T^\ell) (\alpha + 2E_T^\nu E_T^\ell)}}{2 (p_T^\ell)^2} \quad (3.16)$$

$$= \frac{\alpha p_z^\ell \mp E_\ell \sqrt{(m_W^2 - m_T^2) (m_W^2 - m_T^2 + 4E_T^\nu E_T^\ell)}}{2 (p_T^\ell)^2} \quad (3.17)$$

$$= \frac{\beta p_z^\ell \mp E_\ell \sqrt{\gamma (m_W^2 - m_T^2)}}{(p_T^\ell)^2}, \quad (3.18)$$

where in the last line we have introduced the new parameters β and γ , defined as:

$$\beta = \frac{1}{2} (m_W^2 - m_T^2) + p_T^\ell E_T^\nu = \frac{\alpha}{2}, \quad (3.19)$$

$$\gamma = \beta - \frac{1}{4} (m_W^2 - m_T^2) = \frac{1}{4} (m_W^2 - m_T^2) + p_T^\ell E_T^\nu. \quad (3.20)$$

Equation 3.18 makes explicit the dependence of the existence of a real solution of p_z^ν on $\text{sgn}(m_W^2 - m_T^2)$. Phrased another way, the reconstruction of the longitudinal component of the neutrino's momentum is only possible before m_T reaches its kinematic endpoint (which is exactly m_W); in situations where additional large sources of missing transverse energy are present (e.g. production of Dark Matter particles), the computed m_T (based on E_T^{miss}) is propelled beyond m_W and no real solution exists.

This derivation of the longitudinal component of the momentum of the neutrino provides the basis of the full top quark reconstruction performed in the semi-leptonic $t\bar{t}$ channel used for the analysis presented in Chapter 7.

3.4.2 Di-leptonic $t\bar{t}$ case

In a di-leptonic $t\bar{t}$ decay, two neutrinos are expected yet the only available corresponding reconstruction-level observable remains the transverse missing momentum. One therefore has to solve a set of under-constrained equations to retrieve the longitudinal component of the momentum of each individual neutrino. A straightforward numerical approach consists in scanning every possible bi-partition of the transverse momentum (in steps of fixed size), attributing various amounts of transverse energy to each neutrino until solutions are found that are consistent with the W mass constraints.

In order to by-pass the complications associated with such an under-constrained system (determination of bias and systematic uncertainties), in Chapter 7 only a partial reconstruction of the $t\bar{t}$

system is performed, purely in the transverse plane. Still making the assumption that the pair of neutrinos represent the largest contribution to the event E_T^{miss} , the missing transverse momentum vector can be taken as a reasonable proxy for the vector sum of the neutrino momenta in the transverse plane. Further adding the two charged leptons and selected b -jets yields an estimate of the transverse momentum vector of the whole $t\bar{t}$ system, allowing to derive two quantities of interest, its magnitude and direction.



4. Statistical techniques

In this chapter we review various elements of statistical analysis relevant to the measurements presented in the main body of this document. We first consider the formalism of a likelihood fit in Section 4.1, introducing the role of nuisance parameters and profiling. We then build on these concepts to describe hypothesis testing, defining p -values for discovery and the setting of exclusion limits. In Section 4.2, we focus on the fundamental theory of unfolding, relevant to Chapter 7, and more specifically a regularised iterative method. The discussion is condensed and adapted from [228–230].

4.1 Around profile likelihoods

While actual examples of statistical analysis in ATLAS can become quickly untractable due to the complex models used and the multiple correlations between systematics, it is quite illuminating to reduce the problem to its conceptual foundations in an effort to describe the role of likelihood fitting in high energy data analysis.

4.1.1 Extended likelihood and maximal likelihood estimators

Suppose an abstract set of measurements \mathbf{x} , dependent on a set of parameters θ , such that the conditional probability $P(\mathbf{x}|\theta)$ is the likelihood of θ , $L(\theta)$. Maximum likelihood estimators (MLE) for θ are found by solving the set of equations

$$\frac{\partial \ln L}{\partial \theta_i} = 0, \quad (4.1)$$

where i indexes elements of θ and the logarithm of the likelihood function is taken without loss of generality (as we will see, its properties tend to simplify a number of analytical problems). MLE for θ will generally have to be solved numerically, but offer the guarantee of being unbiased and

“Announcement of the discovery of the Higgs boson”. Photo credits: Denis Balibouse. © 2012 NY Times.

efficient (i.e. with minimum variance) in the large sample limit. As is often the case in particle physics, the data can be independent and identically distributed (i.i.d.), which leads to further simplifications. Under this assumption, the n independent quantities $\mathbf{x} = (x_1, \dots, x_n)$ follow the same probability distribution function $f(x; \theta)$ and the likelihood function factorises to

$$L(\theta) = \prod_{i=1}^n f(x_i; \theta). \quad (4.2)$$

Here the number of data observations n is fixed. In keeping with the particle physics context relevant to us, we will instead make n dependent on the parameters θ and follow a Poisson distribution with mean μ (an implicit function of θ), such that the corresponding likelihood is now

$$L(\theta) = \frac{\mu^n}{n!} e^{-\mu} \prod_{i=1}^n f(x_i; \theta). \quad (4.3)$$

This extended likelihood has the merit of bringing additional information about θ and should improve the statistical uncertainties of the fit results.

4.1.2 Extended likelihood with background components

In a brief parenthesis, we give the formalism for the differentiation of background and signal components in a given measurement, leading to the definition of the signal strength μ_s (not to be confused with the statistical mean!) that is the object of many ATLAS analyses. If the expectation of the data can now be replaced by the sum of the expectations of the signal (s) and background (b) components, distributed according to $f_s(x; \theta)$ and $f_b(x; \theta)$ respectively, the extended likelihood function becomes

$$L(\theta) = \frac{(s+b)^n e^{-(s+b)}}{n!} \prod_{i=1}^n \frac{s}{s+b} f_s(x_i; \theta) + \frac{b}{s+b} f_b(x_i; \theta) \quad (4.4)$$

$$= \frac{e^{-(s+b)}}{n!} \prod_{i=1}^n s f_s(x_i; \theta) + b f_b(x_i; \theta). \quad (4.5)$$

In many cases, instead of using s as a parameter of interest, the signal strength μ_s is introduced, for some prior (e.g. theoretical prediction) s_0 , as

$$s = \mu_s \cdot s_0. \quad (4.6)$$

4.1.3 Maximisation of a binned likelihood

In the large sample limit, the data can be grouped into N bins, such they are now represented by a vector $\mathbf{n} = (n_1, \dots, n_N)$ with mean $\boldsymbol{\mu} = \mathbb{E}[\mathbf{n}]$ and following some $f(\mathbf{n}; \boldsymbol{\mu})$, where $\boldsymbol{\mu}$ is implicitly a function of θ . Still considering i.i.d. data, they can be described by

$$f(\mathbf{n}; \theta) = \prod_{i=1}^N \frac{\mu_i^{n_i}}{n_i!} e^{-\mu_i}, \quad (4.7)$$

and the total number of events $n_{\text{tot}} = \sum_i n_i$ is Poisson-distributed, with mean $\mu_{\text{tot}} = \sum_i \mu_i$. The problem of maximising the binned likelihood $L(\boldsymbol{\theta}) = f(\mathbf{n}; \boldsymbol{\theta})$ can be equivalently formulated as that of maximising the ratio

$$\lambda(\boldsymbol{\theta}) = \frac{f(\mathbf{n}; \boldsymbol{\theta})}{f(\mathbf{n}; \hat{\boldsymbol{\mu}})}, \quad (4.8)$$

where $f(\mathbf{n}; \boldsymbol{\mu})$ is a particular model with an adjustable parameter for each bin, $\boldsymbol{\mu} = (\mu_1, \dots, \mu_N)$, and corresponding MLE $\hat{\boldsymbol{\mu}} = (n_1, \dots, n_N)$. As mentioned above, the natural logarithm (with a possible prefactor of 2) of the likelihood (or equivalently of $\lambda(\boldsymbol{\theta})$) is often preferred, providing a simpler minimisation problem of linearly combined terms:

$$-\ln \lambda(\boldsymbol{\theta}) = -\ln \prod_{i=1}^N \frac{\mu_i^{n_i}}{n_i!} e^{-\mu_i} \cdot \frac{n_i!}{n_i^{n_i}} e^{+n_i} \quad (4.9)$$

$$= -\sum_{i=1}^N \ln \left[\frac{\mu_i^{n_i}}{n_i!} e^{-\mu_i} \cdot \frac{n_i!}{n_i^{n_i}} e^{+n_i} \right] \quad (4.10)$$

$$= -\sum_{i=1}^N n_i \ln \mu_i - \mu_i - n_i \ln n_i + n_i \quad (4.11)$$

$$= +\sum_{i=1}^N \mu_i - n_i + n_i \ln \frac{n_i}{\mu_i} \quad (4.12)$$

In a typical ATLAS analysis, histograms of the distributions of physical quantities of interest (e.g. the kinematic properties of some particle) are first defined, with an arbitrary choice for the number of bins and their respective widths (based on e.g. the detector resolution for that particle). Monte Carlo simulations are used to generate estimates of those quantities of interest according to a given model (e.g. the SM): they provide the expectations $\boldsymbol{\mu}$ in the equations above, for a particular choice of $\boldsymbol{\theta}$. On the other hand, the actual particle collision data recorded by the ATLAS detector provide another set of histograms with bin content n_i for each bin i . One can therefore interpret the equations above as measuring the difference between the observed data and the predictions of some theoretical model with a given choice of parameters $\boldsymbol{\theta}$. If one fixes $\boldsymbol{\theta}$ to some value, a large enough discrepancy between the observed n_i and the predicted μ_i might provide a statistically significant exclusion of that model; to the contrary, by allowing $\boldsymbol{\theta}$ to vary and solving the minimisation problem above, one finds the optimal choice of parameters for that model to describe the data. These concepts will be formalised in a following section, in the context of hypothesis testing.

4.1.4 Nuisance parameters

In practice, our original assumption of an exact model $P(\mathbf{x}|\boldsymbol{\theta})$ doesn't hold: Nature isn't perfectly described by our theories (e.g. the SM), and in the best cases is merely asymptotically approximated by them. Therefore our estimation of $\boldsymbol{\theta}$ will be biased. It is however possible to extend our model to contain additional nuisance parameters $\boldsymbol{\nu}$, which are not relevant to our theory but to our ignorance of its realisation in Nature. These nuisance parameters offer a trade-off between a reduction in systematic bias and an increase in statistical uncertainty on the parameters of interest (due to correlations). The $\boldsymbol{\nu}$ parameters themselves then need to be constrained.

In ATLAS analyses, these constraints arise from two types of auxiliary measurements: those in control regions for some parameter space of interest, and independent measurements of systematic

effects and calibrations of reconstructed physics objects. Having found some additional, independent dataset \mathbf{y} that is not (or only partially) dependent on $\boldsymbol{\theta}$, the joint model is then described by the likelihood

$$L(\boldsymbol{\theta}, \boldsymbol{\nu}) = P_x(\mathbf{x}|\boldsymbol{\theta}, \boldsymbol{\nu}) P_y(\mathbf{y}|\boldsymbol{\nu}). \quad (4.13)$$

We have made the problem of maximising the likelihood more difficult by introducing a whole new set of parameters $\boldsymbol{\nu}$, but in fact it can be shown that an equivalent result can be obtained from the maximisation of the profile likelihood, which effectively only depends on $\boldsymbol{\theta}$:

$$L_p(\boldsymbol{\theta}) = L(\boldsymbol{\theta}, \hat{\boldsymbol{\nu}}(\boldsymbol{\theta})), \quad (4.14)$$

where $\hat{\boldsymbol{\nu}}(\boldsymbol{\theta})$, the profiled values of $\boldsymbol{\nu}$, are those that maximise L for a given $\boldsymbol{\theta}$.

4.1.5 Hypothesis testing

We now turn to the application of the statistical constructs described above, in the context of the analysis of experimental to perform hypothesis testing. At the core of this approach is the expression of the likelihood function L :

$$L(\mathbf{N}_{\text{obs}}|\boldsymbol{\mu}_s, \boldsymbol{\mu}_b, \boldsymbol{\theta}) = \prod_{\omega \in \{\text{SR}, \text{CR}\}} P(N_{\text{obs}}^\omega | N_{\text{pred}}^\omega(\boldsymbol{\mu}_s, \boldsymbol{\mu}_b, \boldsymbol{\theta})) \times G_{\text{sys}}, \quad (4.15)$$

expressed as a product of Poisson distributions in all signal and control regions, in terms of the observed and predicted event counts \mathbf{N} , the signal and background normalisation factors $\boldsymbol{\mu}$ and the set of nuisance parameters $\boldsymbol{\theta}$. The additional term G_{sys} is a unit Gaussian function taken as a regularisation on the fitted values of $\boldsymbol{\theta}$, such that they are constrained around zero. The procedure of maximising L yields the quantities of interest $\boldsymbol{\mu}_s$ and $\boldsymbol{\mu}_b$.

We can therefore distinguish between three different scenarios. In the first, we conduct a background-only fit by ignoring the signal component altogether. This corresponds to the null hypothesis H_0 according to which there is e.g. no further physics beyond the Standard Model. In other words, it serves as probe of the SM in a potentially difficult region of kinematic phase-space, where deviations of the data from the predictions are indicative of mis-modelling. The second scenario, where one includes $\boldsymbol{\mu}_s$ in the description of the likelihood L , aims at measuring the contribution of a hypothetical (under some model H_1) signal in the observed data. Should the outcome of this measurement not be statistically significant, a third approach consists in using H_0 and H_1 to interpret the fit results as an exclusion of H_1 .

Following the discussion found in Refs. [228–230], a test statistic q_μ is constructed according to a probability distribution function $f(q_\mu|\mu)$, such that large values of q_μ represent increasing incompatibility with the data under H_0 . As usual, the PDF f is estimated from toy MC pseudo-experiments where the physical parameters in question are varied randomly. The p -value, i.e. the probability of obtaining the expected results under the assumption of H_0 , is then computed as:

$$p_\mu = \int_{q_{\mu, \text{obs}}}^{\infty} f(q_\mu|\mu) dq_\mu, \quad (4.16)$$

that is, the integral of the PDF over q_μ from its observed value $q_{\mu, \text{obs}}$ onwards. In the case of the discovery fit described above, we fix $\mu_s = 0$ under H_0 and so the p -value for discovery becomes:

$$p_0 = \int_{q_{0, \text{obs}}}^{\infty} f(q_0|0) dq_0. \quad (4.17)$$

This number is often quoted as the equivalent signal significance Z , expressed as the number of standard deviations required for the integral of a normal Gaussian distribution tail to evaluate to p_0 :

$$Z = \Phi^{-1}(1 - p_0), \quad (4.18)$$

where Φ is the cumulative Gaussian distribution function. The arbitrary threshold $p = 0.05$ (equivalently $Z = 1.64$), often quoted in the wider scientific community, is in experimental particle physics used for signal exclusion (see below). Instead, the more robust $Z = 3$ ($p = 1.3 \times 10^{-3}$) and $Z = 5$ ($p = 2.9 \cdot 10^{-7}$) are chosen to express evidence and discovery, respectively, of the hypothesis H_1 .

4.1.6 Discovery and exclusion

The generalised likelihood L we've defined above can be used to construct a profile likelihood ratio

$$\lambda(\mu) = \frac{L(\mu, \hat{\theta})}{L(\hat{\mu}, \hat{\theta})}, \quad (4.19)$$

where the estimators $\hat{\mu}$ and $\hat{\theta}$ maximise the likelihood in the denominator, while $\hat{\theta}$ represents the MLE for L at a specific value of μ . It should be clear that $0 < \lambda \leq 1$, with the upper bound saturated for the exact choice of $\mu = \hat{\mu}$ (that is, the larger λ the better the agreement between data and the hypothesis being considered). We can then try to reject the background-only hypothesis H_0 by means of a test statistic

$$q_0 = \begin{cases} -2 \ln \lambda(0) & \hat{\mu} \geq 0 \\ 0 & \hat{\mu} < 0 \end{cases}, \quad (4.20)$$

where the case $\hat{\mu} < 0$ prevents us from excluding H_0 in the case of a deficit of observed events in the signal region. This expression of q_0 as a function of the profile likelihood ratio lends itself well to sensitivity studies (using an Asimov dataset), and it can be shown analytically (using Wald's approximation) that in the large sample limit, the discovery significance is simply

$$Z = \sqrt{q_0}. \quad (4.21)$$

For exclusion or upper-limit setting purposes, a similar test statistic is employed:

$$q_\mu = \begin{cases} -2 \ln \lambda(\mu) & \hat{\mu} \leq \mu \\ 0 & \hat{\mu} > \mu \end{cases}, \quad (4.22)$$

where again, in the second case $\hat{\mu} > \mu$ upwards fluctuations of the data are not used to exclude H_1 . Similarly, under the large sample approximation

$$p_\mu = 1 - \Phi(\sqrt{q_\mu}), \quad (4.23)$$

and a 95% CL upper limit on μ can be set as the highest value of μ for which p_μ is not less than 0.05. However in the context of exclusions, an issue arises in cases of low sensitivity to μ . If the

PDF distributions $f(q_\mu|\mu)$ and $f(q_\mu|0)$ are very similar, the rejection and discovery powers will be comparable. This leads to spurious exclusions, where one excludes hypotheses to which one has almost no sensitivity (thereby enforcing $f(q_\mu|\mu) \sim f(q_\mu|0)$).

An alternative set of numbers should then be quoted along the exclusion p -values, following recommendations set by early LEP searches for the Higgs boson [231]. The so-called “ CL_s method” prevents exclusion if sensitivity is too low, by basing the test not on the usual p -value (CL of the signal and background hypothesis H_1) but on

$$CL_s = \frac{P_\mu}{1 - p_b}, \quad (4.24)$$

where the denominator corresponds to the CL of H_0 . The signal hypothesis is rejected if CL_s is smaller than 0.05, the $\sim 2\sigma$ cut-off. By construction, whenever $f(q_\mu|\mu) \sim f(q_\mu|0)$, this fraction will evaluate close to one, guaranteeing that no spurious exclusion is made.

4.2 An unfolding primer

We now turn to a different problem altogether, when we are not concerned about the presence or not of hypothetical new signals but purely about the modelling of a given process: we want to determine the underlying probability distribution function $f(y)$ of some random variable y , given a set of data $\{y_1, \dots, y_n\}$. In the case where it can be modelled using some known parameters θ , we write $f(y; \theta)$ and this problem reverts to the likelihood maximisation described in the previous section. Otherwise, if no parameterisation of $f(y)$ is known, we resort to constructing a histogram of y with M bins. The expectation value of the number of events in each bin i is denoted μ_i , with a finite sum $\mu_{\text{tot}} = \sum_i \mu_i$, such that the probability of finding y in bin i is $p_i = \mu_i / \mu_{\text{tot}}$. By unfolding the outcome of an experiment, we want to obtain an estimator for the M -vector μ , or equivalently \mathbf{p} .

4.2.1 The response matrix

Having performed said experiment in real data, subject to statistical fluctuations and systematic errors, we relate the measured quantity x to its unknown underlying true value y by a convolution:

$$f_{\text{meas}}(x) = \int R(x|y) f_{\text{true}}(y) dy, \quad (4.25)$$

where the response function $R(x|y)$ encodes the smearing effects of the experimental apparatus used. We simply assume that $R(x|y)$ is either known analytically or can be determined from pseudo-experiments or Monte Carlo simulations (this is indeed the case in ATLAS). The above expression can be discretised as

$$v_i = \sum_{j=1}^M R_{ij} \mu_j, \quad (4.26)$$

where μ are the expectation values of the y -histogram, $R(x|y)$ has been interpreted as a response matrix, and \mathbf{v} are the expected numbers of events in bins of the measured x observable. It is understood that \mathbf{v} can take non-integer values, while the actual data $\mathbf{n} = (n_1, \dots, n_N)$ are integer counts.

The response matrix is further interpreted as a conditional probability:

$$R_{ij} = P(\text{observed in } i | \text{true value in } j), \quad (4.27)$$

and an auxiliary quantity, the efficiency, can be defined as:

$$\epsilon_j \equiv \sum_{i=1}^N R_{ij} = P(\text{observed anywhere} | \text{true value in } j). \quad (4.28)$$

Including the expected background contribution in bin i , β_i , the measured data take an expectation value

$$\mathbb{E}[\mathbf{n}] = \boldsymbol{\nu} = R\boldsymbol{\mu} + \boldsymbol{\beta}. \quad (4.29)$$

4.2.2 Inverting the response matrix

Assuming the response matrix R to be positive-definite, and hence invertible, we can write:

$$\boldsymbol{\mu} = R^{-1}(\boldsymbol{\nu} - \boldsymbol{\beta}). \quad (4.30)$$

Further making the reasonable assumption of Poisson *i.i.d.* data:

$$P(n_i; \nu_i) = \frac{\nu_i^{n_i}}{n_i!} e^{-\nu_i}, \quad (4.31)$$

the corresponding likelihood and log-likelihoods are:

$$L(\boldsymbol{\mu}) = \prod_{i=1}^N P(n_i; \nu_i) \quad (4.32)$$

$$\ln L(\boldsymbol{\mu}) = \sum_{i=1}^N (n_i \ln \nu_i - \nu_i - \ln(n_i!)), \quad (4.33)$$

which gives rise to the usual **MLE** $\hat{\boldsymbol{\nu}} = \mathbf{n}$ such that

$$\hat{\boldsymbol{\mu}} = R^{-1}(\mathbf{n} - \boldsymbol{\beta}). \quad (4.34)$$

Although this simple matrix inversion seems to work, and it does, it usually yields an unacceptably large variance, as well as strong negative correlations from bin to bin: this is sometimes referred to as the ‘‘oscillating maximum likelihood solution’’. The cause can be large off-diagonal elements of the response matrix or too small a bin size compared to the resolution of the experimental apparatus. In fact, if the true distribution $\boldsymbol{\mu}$ really had such an oscillating distribution, with many peaks indicative of some fine structure, $R\boldsymbol{\mu}$ would smear it out almost completely while $R^{-1}\boldsymbol{\nu}$ would bring back the original spectrum identically. However, we crucially do not have access to $\boldsymbol{\nu}$ itself, but only to \mathbf{n} (which takes $\boldsymbol{\nu}$ as expectation value). Furthermore, \mathbf{n} is subject to statistical fluctuations, which R , in a very qualitative understanding, is ‘‘unable’’ to distinguish from a truly finely-structured smeared spectrum. Statistical fluctuations in data are responsible for the oscillating behaviour of our estimator.

This is not to say however that the **MLE** solution is wrong – it isn’t. It simply comes with a variance that is in practice not useful. By construction, the **MLE** $\hat{\boldsymbol{\mu}}$ is unbiased:

$$\mathbb{E}[\hat{\boldsymbol{\mu}}] = R^{-1}(\mathbb{E}[\mathbf{n}] - \boldsymbol{\beta}) = \boldsymbol{\mu}, \quad (4.35)$$

and it can be shown to have covariance:

$$U_{ij} = \text{cov} [\hat{\mu}_i, \hat{\mu}_j] = \sum_{k=1}^N R_{ik}^{-1} R_{jk}^{-1} v_k, \quad (4.36)$$

which is exactly the Cramér-Rao lower bound. Matrix inversion therefore provides an unbiased solution with minimal variance. This opens up the possibility of alternative approaches, where one trades some amount of bias for a possibly large reduction in variance.

4.2.3 Bin-by-bin unfolding

Let us now consider the case where equal binning is used in the histograms for μ and ν , and the response matrix is highly diagonal, i.e. has low bin-to-bin migration. A very simple approach to the unfolding problem is precisely to ignore such migrations, and construct the bin-wise correction factors C_i :

$$C_i = \frac{\mu_i^{\text{MC}}}{\nu_i^{\text{MC}}}, \quad (4.37)$$

where the superscripts “MC” emphasise that these quantities can be determined purely from simulation of the signal process and should only be dependent on the experimental apparatus itself. The corresponding estimator in bin i then reads

$$\hat{\mu}_i = C_i (n_i - \beta_i), \quad (4.38)$$

with covariance

$$U_{ij} = \text{cov} [\hat{\mu}_i, \hat{\mu}_j] = C_i^2 \text{cov} [n_i, n_j] = C_i^2 \text{Var} [n_i] \delta_{ij}. \quad (4.39)$$

We have therefore obtained a variance that is very similar to that expected from the statistical uncertainty of the Poisson-distributed data, if the correction factors are of order 1. We have however introduced a bias:

$$b_i = \mathbb{E} [\hat{\mu}_i] - \mu_i = \left(\frac{\mu_i^{\text{MC}}}{\nu_i^{\text{MC}}} - \frac{\mu_i}{\nu_i^{\text{sig}}} \right) \nu_i^{\text{sig}}, \quad (4.40)$$

with $\nu_i^{\text{sig}} = \nu_i - \beta_i$. It is quite clear that this bias is zero if and only if our model is exactly realised in Nature.

The assumption of (very) small bin-to-bin migration when using such correction factors is an important one to keep in mind, and often makes this method impractical. A simple numerical example, due to Robert Cousins [232], highlights its limitations. Imagine a scenario where in some bin i we have $C_i = 0.1$, $\beta_i = 0$ and $n_i = 100$. We would be quite happy to quote our estimator as $\hat{\mu}_i = C_i n_i = 10$, with $\sigma_{\hat{\mu}_i} = C_i \sqrt{n_i} = 1.0$, i.e. a statistical uncertainty of only 10%. The issue is the following: only 10 out of 100 measured events actually belong in this bin i – how can we reconcile that fact with the statement of a 10% uncertainty?

A common recommendation is to only employ bin-by-bin correction factors when the migration between bins is around or below 5%.

4.2.4 An iterative approach to regularised unfolding

It is possible to approach the maximum of the likelihood carefully, by adding a so-called “regularisation function”, which controls the smoothness of the solution. An associated regularisation parameter needs to be defined, which if taken very large returns the oscillating maximal likelihood spectrum, and in the limit where it vanishes, completely removes the dependence of the data, achieving a meaningless null variance (and a clear bias).

Here we focus on an iterative method, first described by d’Agostini [233], which circumvents the problem of inverting the response matrix by successive applications of Bayes’ theorem. Although this approach does not strictly adhere to the framework of regularised unfolding, we note a similarity in the impact of the number of iterations on the behaviour of the unfolding, which we can refer to informally as a “regularisation parameter”.

The principal idea is to start with some “prior” (used in a loose sense of the term, as will be discussed later) for the probabilities $\mathbf{p} = (p_1, \dots, p_M)$ for an event to be generated in each bin. It can simply be taken to be the flat distribution $p_i^{(0)} = 1/M$, if the M bins of the true histogram have the same width. An initial set of estimators, $\hat{\boldsymbol{\mu}}^{(0)}$, is then

$$\hat{\boldsymbol{\mu}}^{(0)} = n_{\text{tot}} \mathbf{p}^{(0)}, \quad (4.41)$$

with $n_{\text{tot}} = \sum_i n_i$ the total number of observed events. These estimators are then updated iteratively as

$$\hat{\mu}_i^{(t+1)} = \frac{1}{\epsilon_i} \sum_{j=1}^N P(\text{true value in } i | \text{observed in } j) n_j = \frac{1}{\epsilon_i} \sum_{j=1}^N \left(\frac{R_{ji} p_i^{(t)}}{\sum_k R_{jk} p_k^{(t)}} \right) n_j, \quad (4.42)$$

where Bayes’ theorem was implicitly applied as:

$$P(\text{true value in } i | \text{observed in } j) = \frac{P(\text{true value in } i | \text{observed in } j) \cdot P(\text{true in } i)}{P(\text{observed in } j)} \quad (4.43)$$

$$= \frac{P(\text{true value in } i | \text{observed in } j) \cdot P(\text{true in } i)}{\sum_k P(\text{observed in } j | \text{true value in } k)} \quad (4.44)$$

$$= \frac{R_{ji} \cdot p_i}{\sum_k R_{jk} p_k} \quad (4.45)$$

It is then possible to compare pairs of successive estimators within the set $\{\hat{\boldsymbol{\mu}}^{(t)}\}$ and compute a corresponding χ^2 test. After several iterations, one should observe convergence of the χ^2 values. Going beyond this point of convergence, which should be taken as the optimal value of the “regularisation parameter” in this iterative method, the graph of χ^2 versus successive iterations should trace out a parabolic curve: the gradual divergence in χ^2 for large numbers of iterations indicates increasing statistical fluctuations, and eventually approaches the oscillating ML solution.

A remark on Bayesianism

The method described above is often referred to as “iterative Bayesian unfolding” (IBU), after the original work by d’Agostini [233]. As we’ve seen, the “Bayesian” component stems from the use of Bayes’ theorem in the iterative step. However, the fact that the number of iterations effectively acts as a regularisation parameter should instead remind one of frequentism. Furthermore, the estimators we derive do not describe a joint posterior PDF for $\boldsymbol{\mu}$, nor do we use any joint prior either. Thus the central tenet of Bayesian statistics,

$$\text{posterior} \propto \text{likelihood} \times \text{prior} \quad (4.46)$$

doesn't hold here. By taking the mode of the joint posterior PDF for μ , one could define a Bayesian estimator: this is indeed done in the Fully Bayesian Unfolding (FBU) approach [234], but not here. The term $\mathbf{p}^{(0)}$ used in the initial stage of d'Agostini's algorithm corresponds to a set of probabilities (perhaps uniform) used as a first guess for μ ; they are not a probability density in μ -space.

Since the method can be represented as an expectation-maximisation iteration [235] for finding the MLE of μ , and that it reproduces the exact MLE solution in the large iteration limit, it is in fact a fully frequentist technique for finding the regularised MLE and should hence not be referred to as ‘‘Bayesian’’ unfolding.

4.2.5 Implementation in an ATLAS analysis

The motivation for unfolding results in particle physics is quite straightforward: one wishes to remove the effects of the detector to access an underlying quantity that is directly comparable to alternative generators and simulations, various theory predictions or even to results obtained by another detector (e.g. CMS). To try and ground these abstract notions of unfolding in the context of an actual ATLAS analysis, we focus on the master formula for the differential cross section of a given process $d\sigma$ in bin i of some observable X ,

$$\frac{d\sigma}{dX^i} = \frac{1}{\mathcal{L} \cdot \mathcal{B} \cdot \Delta X^i \cdot f_{\text{acc}}^i} \cdot \sum_j R_{ij}^{-1} \cdot \epsilon_{\text{eff}}^j \cdot (N_{\text{obs}}^j - N_{\text{bkg}}^j). \quad (4.47)$$

The terms \mathcal{L} , \mathcal{B} and ΔX^i are scaling factors corresponding, respectively, to the integrated luminosity, the branching ratio of the process and the particular bin width; these ensure the proper normalisation of the final differential cross section in the correct units. The bracketed term on the right-hand side of the equation above corresponds to the background-subtracted data in the given bin, i.e. the estimation of the signal contribution in data after proper treatment of all other SM backgrounds (either modelled from MC, obtained from data-driven techniques, or normalised in a dedicated control region). Finally, the efficiency and acceptance correction terms are taken from a signal MC sample and defined as:

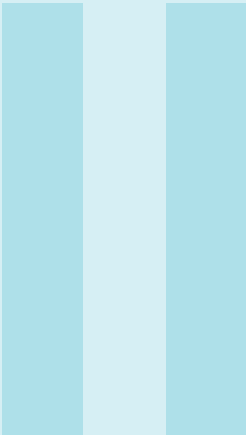
$$\epsilon_{\text{eff}} = \frac{N^{\text{reco} \wedge \text{truth}}}{N^{\text{reco}}}, \quad (4.48)$$

$$f_{\text{acc}} = \frac{N^{\text{reco} \wedge \text{truth}}}{N^{\text{truth}}}, \quad (4.49)$$

where N^{reco} is the bin content at reconstruction-level, N^{truth} that at generator-level and $N^{\text{reco} \wedge \text{truth}}$ the number of events within that bin that are exactly matched at reconstruction- and generator-level. Therefore ϵ_{eff} can be understood qualitatively as ‘‘contracting’’ the reconstructed data distribution to only the number of events that were observed in the MC simulation of the signal process to be within the fiducial volume of interest, before performing the unfolding via R_{ij}^{-1} , the inverse of the response matrix. The unfolded quantity, in this restricted matched phase-space, is then ‘‘expanded’’ back again to the full fiducial volume. In the limit where the fiducial volume is maximal, i.e. contains all possible generated events, $N^{\text{reco} \wedge \text{truth}} = N^{\text{reco}}$ and the efficiency correction is identically one.

Finally, it is worth noting that in our practical discussion of unfolding in Chapter 7, we will present so-called migration matrices, instead of the response matrices usually found in literature. The former are simply row-normalised version of the latter, making their visual inspection easier by simply reporting the percentage of migration from a given generator-level bin to any of the reconstruction-level ones.

The iterative algorithm described in the previous section is implemented in the RooUnfold software package [236].



Top quark pair production in association with a Z boson

5 Inclusive cross section with the 2015–2016 dataset

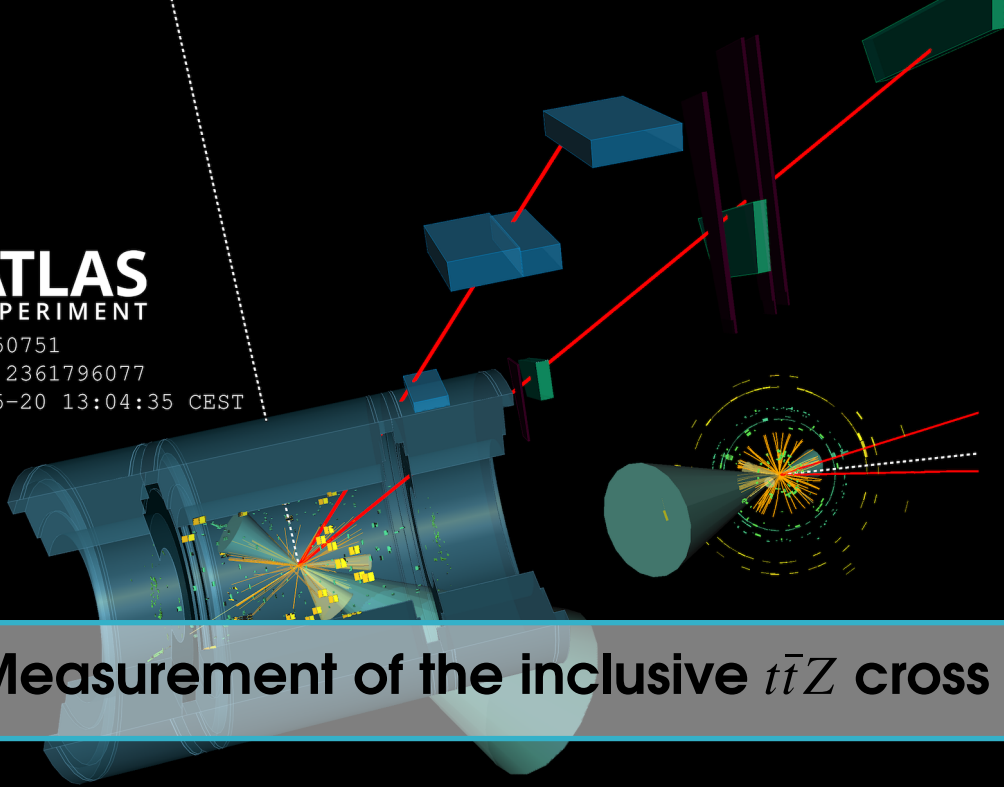
- 5.1 Analysis strategy
- 5.2 Object definitions
- 5.3 Event selection
- 5.4 Signal regions
- 5.5 Prediction of the Standard Model backgrounds
- 5.6 Systematic uncertainties
- 5.7 Results
- 5.8 EFT interpretation

6 Inclusive cross section with the full Run 2 dataset

- 6.1 Analysis strategy
- 6.2 Object definitions
- 6.3 Event selection
- 6.4 Signal regions
- 6.5 Prediction of the Standard Model backgrounds
- 6.6 Systematic uncertainties
- 6.7 Results

7 Differential cross section with the full Run 2 dataset

- 7.1 Event reconstruction and differential variables
- 7.2 Unfolding tests
- 7.3 Results



5. Measurement of the inclusive $t\bar{t}Z$ cross section

In this chapter we review the measurement of the inclusive $t\bar{t}V$ ($V = W, Z$) cross sections in the multi-lepton final state using the intermediate (2015–2016) Run 2 dataset with 36.1 fb^{-1} of pp collisions at $\sqrt{s} = 13 \text{ TeV}$. We focus on the $t\bar{t}Z$ process in the three- and four-lepton channels, the author’s main contribution to this analysis. We start by describing the general strategy in Section 5.1, giving definitions of reconstructed physics objects (Section 5.2) and event selection (Section 5.3). The event topology of the signal $t\bar{t}Z$ process is identified in Section 5.4, while the main background processes and their estimates are outlined in Section 5.5. Systematic uncertainties are introduced in Section 5.6 and their impact on the final results is discussed in Section 5.7. A further interpretation of the results in the context of effective field theory models is also presented in Section 5.8. This analysis was published by the ATLAS Collaboration in Ref. [1].

5.1 Analysis strategy

As discussed in the [Motivation and outline](#), the $t\bar{t}V$ ($V = W, Z$) process is an irreducible background for a number of [BSM](#) searches and a precise measurement of its cross section is necessary to reduce the associated modelling uncertainties in these searches. The multi-lepton final state is chosen for this analysis, as electrons and muons are the most accurately reconstructed physics objects in the ATLAS detector. Three channels are investigated for the measurement of the $t\bar{t}Z$ cross section: two leptons of opposite sign charge (2LOS), three leptons (3L) and four leptons (4L). The $t\bar{t}W$ process, not discussed further in this thesis, is measured in the same-sign two-lepton channel (2LSS) as well as three-lepton regions orthogonal to those used to measure $t\bar{t}Z$.

Due to the high $t\bar{t}$ background in the 2LOS channel, multivariate techniques ([BDT](#)) are used to separate it from the signal $t\bar{t}Z$. This particular analysis is also not reproduced here and we focus instead on the 3L and 4L channels, which bring the highest sensitivity to $t\bar{t}Z$ and are the author’s main contribution to the analysis.

“Event display of a three lepton $t\bar{t}Z$ candidate”. Image credits: Meirin Oan Evans. © 2020 CERN.

5.1.1 Signal processes

The associated production of a top quark pair with a Z boson is generated at NLO with MG5_AMC@NLO interfaced to PYTHIA 8. For the matrix elements, a dynamic scale is used ($H_T/2$, where H_T is the sum of the transverse momenta of all final state partons) and the PDF set is NNPDF3.0NLO [237]. The A14 [238] underlying event tune is applied. The contributions from off-shell Z bosons as well as the Z/γ^* interference are included, down to a minimum invariant mass $m_{ll} > 5$ GeV to remove low-mass resonances. The cross section is normalised to fixed-scaled ($m_t + \frac{m_Z}{2}$) NLO QCD+EWK calculations [239].

5.2 Object definitions

Physics objects, as introduced in Section 3.2, are first defined as baseline objects, following a preliminary (so-called “loose”) set of selection criteria. Ambiguities, such as mis-identification of leptons as jets, are removed at this stage through an **Overlap Removal (OR)** procedure. The selection on remaining objects is then enhanced, leading to “tight” definitions.

Electrons baseline electrons are required to have $|\eta| < 2.47$ and $p_T > 7$ GeV, as well as pass the LooseAndBLayerLH likelihood-based identification [240] without any isolation requirement. Signal electrons pass the MediumLH identification and FixedCutTight isolation requirements. To reduce the number of electrons with incorrect charge assignment, the ATLAS **Electron Charge Identification Selection (ECIDS)** tool is used, at a working point corresponding to a signal efficiency of 97%.

Muons baseline muons are required to have $|\eta| < 2.5$ and $p_T > 7$ GeV, as well as pass the Loose quality selection with no isolation requirement [207]. Signal muons pass the Medium quality and FixedCutTightTrackOnly isolation requirements.

Jets they are reconstructed using the anti- k_r algorithm [216] with a distance parameter $R = 0.4$. Baseline jets are required to have $|\eta| < 4.8$ and $p_T > 25$ GeV. Signal jets have $|\eta| < 2.5$ and pass the **JVT** requirement. Out of these signal jets, those that are positively identified by the MV2c10 algorithm (using a 77% b -tagging efficiency) are considered b -jets.

Missing Transverse Energy overlap-removed baseline electrons, muons and jets are used in the recalculation of the object-based E_T^{miss} [241]. An extra term takes into account soft energy not originating from any of the selected objects, as described in Section 3.2.7.

Overlap Removal in the case of candidate objects overlapping with each other, all but one object must be removed from the event. The distance metric used to define overlapping objects is $\Delta R = \sqrt{(\Delta\eta)^2 + (\Delta\phi)^2}$:

1. If an electron shares a track with a muon, consider the object a muon and remove the electron.
2. If an electron and jet are located within $\Delta R < 0.2$, consider the object an electron and remove the jet.
3. If a muon and jet are located within $\Delta R < 0.4$, consider the object a jet and remove the muon, unless the object has fewer than three tracks in which case the jet is removed and the muon is kept.
4. If an electron and jet are located within $0.2 \leq \Delta R < 0.4$, consider the object a jet and remove the electron.

5.3 Event selection

5.3.1 Triggers

In order to collect events with leptons, dedicated triggers (**HLT**) are used whose requirements are summarised in Table 5.1 below.

Table 5.1: Summary of trigger p_T -thresholds used in the analysis. Commas in the individual p_T selections denote a logical OR of multiple cuts. Different identification and isolation requirements are used in each trigger, such that their combination is not trivially equivalent to only the first one listed.

Trigger	Data 2015	Data 2016
Electron	$p_T > 24, 60, 120$ GeV	$p_T > 26, 60, 140$ GeV
Muon	$p_T > 20, 50$ GeV	$p_T > 26, 50$ GeV

Once events selected by the various triggers have been selected, further offline cuts are applied to ensure the relevant objects are in the plateau region, where the trigger is fully efficient (see Figures 3.6 and 3.8). This is done by requiring slightly higher-than-threshold transverse momenta: for data collected in 2015 (2016), this is $p_T > 25(27)$ GeV.

5.3.2 Event cleaning

A number of offline cuts are applied to trigger-selected events. These aim at removing events recorded during a detector fault (by checking the status of the **ECAL** and **HCAL**), non-**HS** events (by reconstructing a primary vertex with at least two tracks above the $p_T > 400$ MeV threshold), events with potential cosmic muons or poorly reconstructed jets (sensitive to large fake-jet contamination).

5.4 Signal regions

Multiple signal regions (**SR**) are considered in this analysis to maximise the sensitivity to the $t\bar{t}Z$ signal, targeting the leptonic decay of the Z boson and either the semi- or di-leptonic decay of the $t\bar{t}$ system. Figure 5.1 highlights the lepton multiplicity as a straightforward selection criterion.

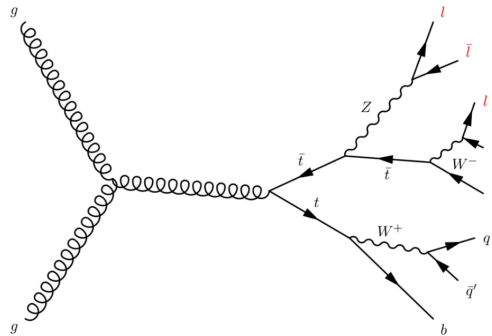


Figure 5.1: Example of a leading-order Feynman diagram for $t\bar{t}Z$ production via gluon fusion and splitting into a $t\bar{t}$ pair with **FSR** of a Z boson. The semi-leptonic decay of the $t\bar{t}$ system together with the leptonic decay of the Z boson lead to the presence of three prompt leptons in the final state, indicated in red.

In the 3L and 4L channels, cuts on simple kinematic variables are applied to ensure an on-shell Z -like pair of signal leptons (required to be of opposite charge and same flavour, **OSSF**, and within

10 GeV of the reference value for the Z mass) in all but one region (targeting off-shell Z production and γ^* interference). Jet and b -jet multiplicities are then used to divide the channels further.

In the 4L channel, special consideration is given to the two leptons not associated to the signal Z candidate. For a signal event, these originate from the leptonic decay of the two top quarks and there is no preference as to their flavour, whereas for a ZZ +jets background event the two leptons are again expected to be **OSSF**. This second lepton pair, referred to as Z_2 , is classified into same-flavour (SF) or different-flavour (DF) categories. To reduce the contamination from events with non-prompt leptons, additional requirements on the transverse momenta of the trailing lepton (p_{T4}) and the scalar sum of the transverse momenta of the third and fourth leptons (p_{T34}) are imposed.

All signal region requirements for the 3L channel are outlined in Table 5.2 and for the 4L channel in Table 5.3. Distributions of key kinematic variables are shown in Figures 5.2 and 5.3.

Table 5.2: Selection criteria for the trilepton signal regions sensitive to $t\bar{t}Z$.

Object	3L-Z-1b4j	3L-Z-2b3j	3L-Z-2b4j	3L-noZ-2b4j
Event cleaning	Common to all SRs			
N_{lep}	3			
p_T of leptons	$> (27, 20, 20)$ GeV			
Sum of lepton charges	± 1			
OSSF lepton pair	yes			
On-shell Z candidate	yes			no
N_{jets}	≥ 4	3	≥ 4	≥ 4
N_{b-jets}	1	≥ 2		

Table 5.3: Selection criteria for the tetralepton signal regions sensitive to $t\bar{t}Z$.

Object	4L-DF-1b	4L-DF-2b	4L-SF-1b	4L-SF-2b
Event cleaning	Common to all SRs			
N_{lep}	4			
N_{jets}	≥ 1			
OSSF lepton pair	yes			
On-shell Z candidate	yes			
Z_2 leptons	$e^\pm \mu^\mp$		$e^\pm e^\mp, \mu^\pm \mu^\mp$	
p_{T4}	> 7 GeV	> 10 GeV	> 7 GeV	> 10 GeV
p_{T34}	> 35 GeV	—	> 25 GeV	—
$ m_{Z_2} - m_Z^{ref} $	—	—	> 10 GeV < 10 GeV	> 10 GeV < 10 GeV
E_T^{miss}	—	—	> 40 GeV > 80 GeV	— > 40 GeV
N_{b-jets}	1	≥ 2	1	≥ 2

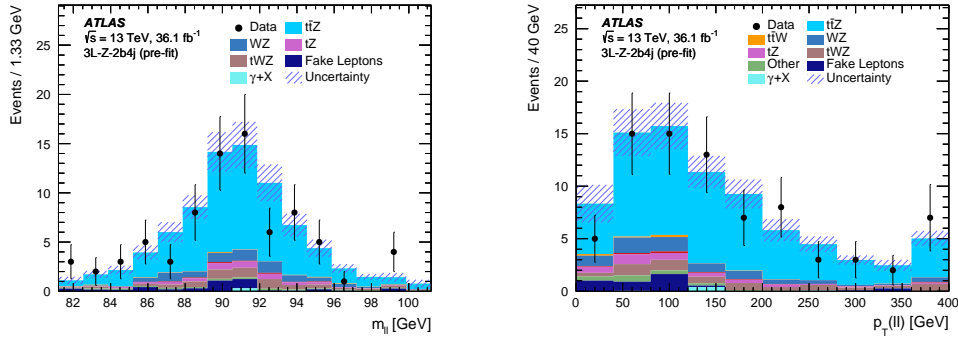


Figure 5.2: Distributions of the invariant mass (left) and transverse momentum (right) of the reconstructed Z candidate for events in 3L-Z-2b4j, before normalisation of the backgrounds (pre-fit). The “Other” process contains SM processes with small cross sections producing three prompt leptons (e.g. $t\bar{t}H$, triboson processes). The shaded band represents the total uncertainty. The last bin each of the distributions includes the overflow.

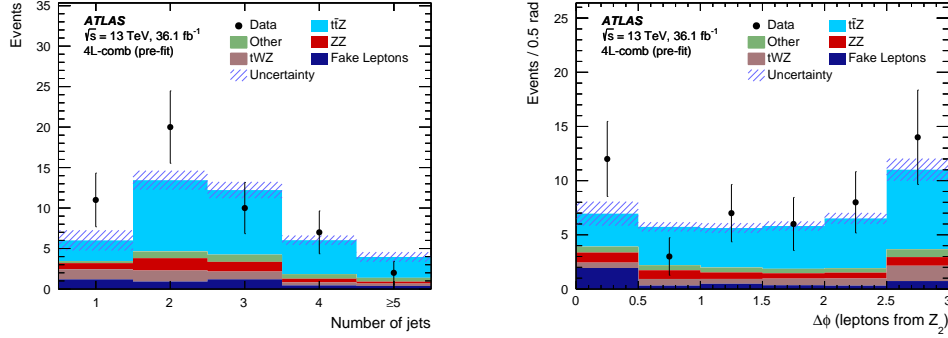


Figure 5.3: Distributions of the number of jets (left) and azimuthal angle $\Delta\phi$ between the two leptons from the Z_2 candidate (right) for events in all the tetralepton signal regions combined, before normalisation of the backgrounds (pre-fit). The “Other” process contains SM processes with small cross sections producing four prompt leptons (e.g. $t\bar{t}H$, triboson processes). The shaded band represents the total uncertainty. The last bin each of the distributions includes the overflow.

5.5 Prediction of the Standard Model backgrounds

The following processes yield final states that mimic, completely or in part, the sought-after signal signature of multiple leptons and (b -)jets. In order to estimate their contribution to the various SRs, a number of techniques can be employed: a pure MC-based estimation, a semi-data-driven approach employing control regions (CR) or fully-data-driven methods (fake lepton estimation).

Diboson The WZ +jets process, where both bosons decays leptonically and the Z is on-shell, is a major background in the 3L channel. Its modelling is taken from MC simulations (SHERPA 2.1 at LO precision with up to two additional partons, normalised to the NLO cross section, and using the CT10 [242] PDF set) and its cross section is normalised in data in a dedicated three-lepton control region. The ZZ +jets process, yielding four leptons, is a similarly leading background in the 4L channel, specifically in 4L-SF-1b and 4L-SF-2b. It is estimated from the same SHERPA 2.1 setup and normalised in a four lepton control region.

Single top with vector bosons tWZ all-leptonic production is an important background in both channels, while leptonic tZq with one additional heavy-flavour jet is relevant only in the 3L channel. These rare processes both have a final state too close to the signal $t\bar{t}Z$ to be able to construct dedicated control regions without resorting to accurate $t\bar{t}$ reconstruction techniques, which are beyond the scope of this analysis. Their modelling is therefore purely taken from MC simulations, using MADGRAPH +PYTHIA 6 at LO precision with the CTEQ6L1 PDF set for tZq , and aMC@NLO +PYTHIA 8 at NLO with NNPDF3.0NLO for tWZ .

Fake or non-prompt leptons The background consisting of events with fake leptons (i.e. any reconstructed lepton not coming from a W , Z or τ decay) is important in the 3L channel. A data-driven method (matrix method, described hereafter) is used to estimate it from a control sample of events for which lepton isolation and electron identification criteria are relaxed. In the 4L channel, due to the reduced number of data events available, a semi-data-driven fake factor method is used.

5.5.1 Three-lepton control region

As described above, the normalisation of the WZ +jets background is estimated in a 3L CR. To minimise the $t\bar{t}Z$ signal contamination, exactly three reconstructed jets are required, including a veto on b -jets. The missing transverse momentum in each selected event is required to be larger than 40 GeV. With the requirements detailed in Table 5.4, the expected sum of $t\bar{t}Z$ and $t\bar{t}W$ contributions in the CR-WZ is roughly 2.5% of the total number of events. Figure 5.4 shows the distributions of the transverse momenta of the leading lepton and leading jet in CR-WZ, indicating no significant mis-modelling and a scale factor slightly lower than one.

Table 5.4: Summary of the selection criteria for the three-lepton control region for $WZ(\rightarrow \ell\ell\ell\nu)$ +jets.

Object	CR-WZ
N_{lep}	3
N_{jets}	3
$N_{b\text{-jets}}$	0
p_{T} of leptons	$> (27, 20, 20)$ GeV
OSSF lepton pair	yes
On-shell Z candidate	yes
Sum of lepton charges	± 1
$E_{\text{T}}^{\text{miss}}$	> 40 GeV

5.5.2 Four-lepton control region

The ZZ +jets background is particularly important in the tetralepton channel, and therefore a control region is constructed to constrain this background, following the requirements outlined in Table 5.5. A low cut on the transverse missing energy $E_{\text{T}}^{\text{miss}}$ is necessary to minimise signal contamination in this CR-ZZ. Distributions of lepton and jet kinematics are shown in Figure 5.5, and a good agreement between data and the SM estimation is observed.

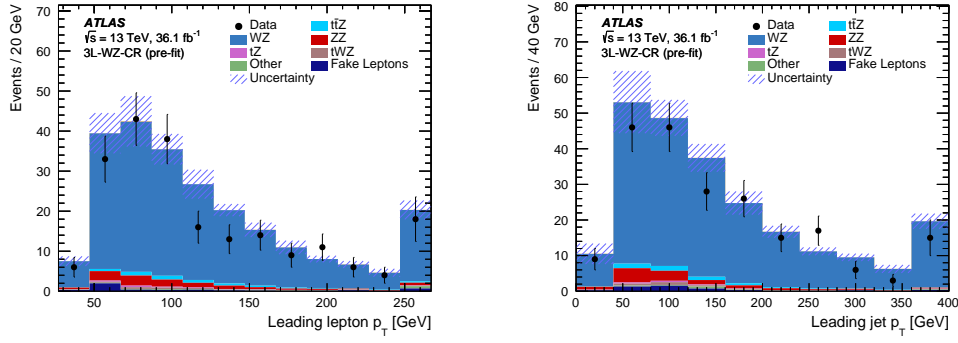


Figure 5.4: Distributions of the leading lepton transverse momentum p_T (left) and the leading jet p_T (right) in the three-lepton CR-WZ region before the fit. The “Other” background contains SM processes with small cross sections producing three prompt leptons (e.g. $t\bar{t}H$, $t\bar{t}W$). The shaded band represents the total uncertainty. The last bin in each of the distributions includes the overflow.

Table 5.5: Summary of the selection criteria for the four-lepton control region for $ZZ(\rightarrow \ell\ell\ell\ell)+\text{jets}$.

Object	CR-ZZ
N_{lep}	4
OSSF lepton pair	yes
On-shell Z candidate	yes
Z_2 leptons	$e^\pm e^\mp, \mu^\pm \mu^\mp$
$ m_{Z_2} - m_Z^{\text{ref}} $	$< 10 \text{ GeV}$
E_T^{miss}	$\in [20, 40] \text{ GeV}$

5.5.3 Fake lepton estimation

In the 3L channel, the contribution from events with a fake lepton, e.g. a dileptonic $t\bar{t}$ or $Z+\text{jets}$ event where the decay of a b -jet produces an additional tight lepton, is estimated using the matrix method, described below. In the 4L channel, a semi-data-driven method (fake factors) is used instead.

Matrix method

In its simplest form, the method consists in separating the observed data count into tight and loose events, based on lepton definitions. These are denoted N_T and N_L respectively. By measuring the associated real and fake efficiencies (ϵ_{real} and ϵ_{fake}) in a control sample, the measured N_L and N_T can then be related to the estimators of the real and fake lepton components, $N_{\text{tight}}^{\text{real}}$ and $N_{\text{tight}}^{\text{fake}}$. From the definition of the efficiencies:

$$\epsilon_{\text{real}} = \frac{N_{\text{tight}}^{\text{real}}}{N_{\text{loose}}^{\text{real}}}, \quad (5.1)$$

$$\epsilon_{\text{fake}} = \frac{N_{\text{tight}}^{\text{fake}}}{N_{\text{loose}}^{\text{fake}}} \quad (5.2)$$

it follows that

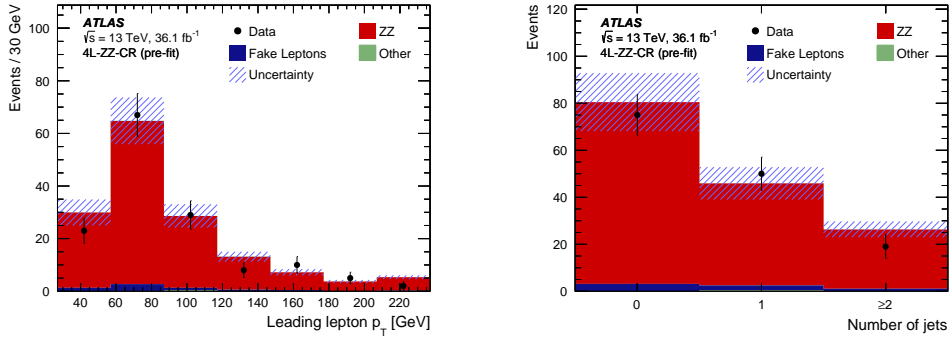


Figure 5.5: Distributions of the leading lepton transverse momentum p_T (left) and jet multiplicity (right) in the four-lepton CR-ZZ region before the fit. The “Other” background contains SM processes with small cross sections producing four prompt leptons (e.g. $t\bar{t}H$, triboson processes). The shaded band represents the total uncertainty. The last bin in each of the distributions includes the overflow.

$$N_L = (1 - \epsilon_{\text{real}}) \cdot N_{\text{loose}}^{\text{real}} + (1 - \epsilon_{\text{fake}}) \cdot N_{\text{loose}}^{\text{fake}} \quad (5.3)$$

$$N_T = \epsilon_{\text{real}} \cdot N_{\text{loose}}^{\text{real}} + \epsilon_{\text{fake}} \cdot N_{\text{loose}}^{\text{fake}}. \quad (5.4)$$

As a sanity check, note that the mutually exclusive categories N_L and N_T do sum up to the total number of loose leptons identified. The equation above can be written in matrix form as

$$\begin{pmatrix} N_L \\ N_T \end{pmatrix} = \begin{pmatrix} 1 - \epsilon_{\text{real}} & 1 - \epsilon_{\text{fake}} \\ \epsilon_{\text{real}} & \epsilon_{\text{fake}} \end{pmatrix} \begin{pmatrix} N_{\text{loose}}^{\text{real}} \\ N_{\text{loose}}^{\text{fake}} \end{pmatrix}. \quad (5.5)$$

By inverting the matrix, we recover the sought-after quantities:

$$\begin{pmatrix} N_{\text{loose}}^{\text{real}} \\ N_{\text{loose}}^{\text{fake}} \end{pmatrix} = \frac{1}{\epsilon_{\text{fake}} - \epsilon_{\text{real}}} \begin{pmatrix} \epsilon_{\text{fake}} & \epsilon_{\text{fake}} - 1 \\ -\epsilon_{\text{real}} & 1 - \epsilon_{\text{real}} \end{pmatrix} \begin{pmatrix} N_L \\ N_T \end{pmatrix} \quad (5.6)$$

such that we finally obtain an expression for the number of fake leptons passing our tight selection:

$$N_{\text{tight}}^{\text{fake}} = \frac{\epsilon_{\text{fake}}}{\epsilon_{\text{real}} - \epsilon_{\text{fake}}} (\epsilon_{\text{real}} N_L - (1 - \epsilon_{\text{real}}) N_T). \quad (5.7)$$

For two or more leptons, the matrix should be extended to $2^{N_{\text{lep}}}$ dimensions to accept all possible efficiency combinations. When more than a single control sample is used, a more general likelihood-minimisation method is employed [243].

This is indeed the case for this analysis, where the data-driven real and fake lepton efficiencies are obtained from a simultaneous fit in dilepton events (separated into ee , $e\mu$ and $\mu\mu$ channels). Events are further categorised according to their b -tag multiplicity, with one or at least two b -jets. The parameter ϵ_{real} is determined from $Z \rightarrow \ell^+ \ell^-$ events in an opposite-sign same-flavour two-lepton control region, whereas the fake efficiencies are extracted from a similar dilepton same-sign

sample (after subtraction of the prompt and charge-misidentified backgrounds from Monte Carlo). For improved modelling purposes, both efficiencies are further binned in p_T and $|\eta|$.

Figure 5.6 shows the distribution of E_T^{miss} and the sub-leading lepton p_T , in two-lepton same-sign validation regions. The data and the expectation agree well, demonstrating the validity of the description of the fake-lepton background determined by the matrix method.

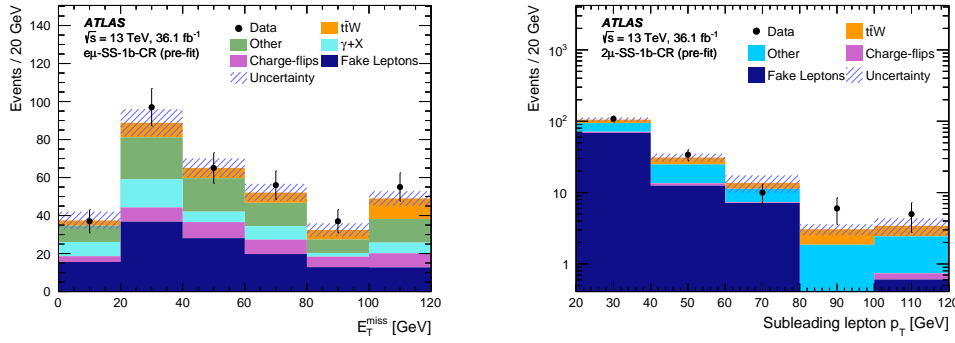


Figure 5.6: Distributions of the missing transverse energy E_T^{miss} in the $e^\pm\mu^\pm$ channel (left) and sub-leading lepton transverse momentum p_T in the $\mu^\pm\mu^\pm$ channel (right) before the fit. The “Other” background contains SM processes with small cross sections producing two same-sign prompt leptons (e.g. $t\bar{t}H$, diboson processes). The shaded band represents the total uncertainty. The last bin in each of the distributions includes the overflow.

Fake factor method

The fake factor method is used in the 4L channel for the estimation of the non-prompt background, the limited statistics available in the signal regions preventing the use of the matrix method. A semi-data-driven method, it relies on the correct modelling of lepton kinematics from Monte Carlo and corrects only the overall normalisation of various sources of fake leptons. These corrections, the so-called fake factors (denoted $\mu_{\text{source}}^{\text{flavour}}$), are derived by comparing MC to data in dedicated control regions (enriched with processes that contain at least one fake electron or muon) and split according to the flavour and origin of the fake lepton: electron or muon, from heavy-flavour decays or other sources.

Heavy-flavour fakes are non-prompt leptons coming from the decay of c - or b -mesons and baryons. Additional electron fakes can be obtained mainly from photon conversion, and to a lesser extent from pion and kaon decays. Since there are no muon fakes from photon conversion, the contribution of muon fakes from other sources is very small. Therefore the final fake factor μ_{other}^μ is set to 1 with an uncertainty of 50%.

To perform a simultaneous fit of these four parameters in data, two control samples are built, one enriched in $t\bar{t}$ (PYTHIA 8) events and one in Z +jets events (SHERPA). The exact event selections are given in Table 5.6 below. Each of these regions nominally requires two leptons; a third lepton is identified as non-prompt if it is not a constituent of the Z candidate or if it is the lowest p_T member of the same-sign pair in the $t\bar{t}$ case. The events are further classified according to the flavour of this identified fake lepton.

The following fake factors are finally obtained (where the uncertainty includes both statistical

and systematic components):

$$\mu_{\text{heavy}}^e = 0.90 \pm 0.14 \quad (5.8)$$

$$\mu_{\text{other}}^e = 1.84 \pm 0.27 \quad (5.9)$$

$$\mu_{\text{heavy}}^\mu = 1.07 \pm 0.09 \quad (5.10)$$

$$\mu_{\text{other}}^\mu = 1.00 \pm 0.50 \quad (5.11)$$

Table 5.6: Summary of the selection criteria for the fake-factor control regions.

Object	Z+jets	$t\bar{t} \rightarrow \ell\ell$
N_{jets}	≥ 2	
N_{lep}	4	
OSSF lepton pair	yes	no
On-shell Z candidate	yes	no
Sum of lepton charges	± 1	
m_T	$< 50 \text{ GeV}$	—
E_T^{miss}	$< 50 \text{ GeV}$	—
p_T of leading jet	—	$> 30 \text{ GeV}$

5.6 Systematic uncertainties

In what follows, we distinguish between two types of systematic uncertainties: those related to detector effects and the reconstruction and calibration of physics objects on one hand, and to the modelling of the various background processes from theoretical calculations on the other.

5.6.1 Experimental uncertainties

Luminosity The luminosity estimate for the data-taking years 2015 and 2016 has an uncertainty of 2.1% in $\sqrt{s} = 13 \text{ TeV}$ analyses, using a method similar to that in Ref. [244]. The luminosity measurement and its uncertainty are based on calibrations performed in low-luminosity runs of the LHC by the LUCID-2 detector [245] (van der Meer scans) and transferred to the high-luminosity range. This uncertainty is applied to all processes determined from Monte Carlo simulations.

Pile-up An uncertainty related to the scaling factors applied in MC to account for differences in pile-up distributions between MC and data is considered.

Lepton efficiencies The reconstruction, identification and isolation efficiencies of electrons and muons, as well as the efficiency of the triggers used to record the events, differ between data and simulation. Scale factors and their uncertainties are derived using a tag-and-probe method applied to electrons and muons from W and Z bosons and J/ψ mesons [207, 240, 246, 247].

Lepton momentum scale and resolution The accuracy of lepton momentum scale and resolution in simulation is checked using reconstructed distributions of the $Z \rightarrow \ell^+\ell^-$ and $J/\psi \rightarrow \ell^+\ell^-$ masses [207, 240, 246, 247]. In the case of electrons, E/p studies using $W \rightarrow e\nu$ events are also

used. Small discrepancies are observed between data and simulation, and corrections for the lepton energy scale and resolution in the latter are implemented using dedicated ATLAS tools. In the case of muons, momentum scale and resolution corrections are only applied to the simulation. Uncertainties on both the momentum scale and resolution in the muon spectrometer and the tracking systems are considered, and varied separately.

Jet Energy Scale (JES) and Jet Energy Resolution (JER) The **JES** and its uncertainty are derived combining information from test-beam data, LHC collision data and simulation [213]. A strongly reduced set of 4 nuisance parameters is used: three effective parameters plus one η inter-calibration non-closure parameter (for $|\eta| \sim 2.5$). The **JER** uncertainty is derived as a one-sided variation by comparing data to MC simulation in-situ. Both JES and JER variations are propagated to the calculation of the E_T^{miss} .

Jet vertex tagger efficiency The uncertainty related to the **JVT** scaling factors applied to the MC simulation includes the statistical uncertainty, a 20% uncertainty on the estimation of the residual contamination from pile-up jets after pile-up suppression and a systematic uncertainty assessed by using different generators for the MC simulation of the Z +jets events. It is included in the fit as a single nuisance parameter.

b-tagging Flavour-dependent efficiencies are measured in data [222, 248–250]. The scale factors and their uncertainties are applied to each jet in the simulation depending on flavour, p_T and η .

Fake estimation In the 4L channel, fake lepton systematic uncertainties are covered by the scale-factor uncertainties used to calibrate the simulated fake lepton yields in the control regions. In the case of the 3L channel, the matrix method yield uncertainty on the fake lepton background is estimated by shifting the MC real lepton event subtraction up and down by 30% during the efficiency measurements. The uncertainty from the efficiency fit is then added to the overall systematic uncertainty by taking the maximum and minimum envelope among all shifts, separately for each lepton flavour. All systematic uncertainties associated with fake leptons are considered to be correlated among analysis channels and regions.

5.6.2 Theoretical uncertainties

Theoretical uncertainties affect both the background normalisation and the shape of kinematic distributions, impacting the background prediction in the signal regions. Statistical uncertainties in the evaluation of systematics are neglected in general, thanks to the large number of available MC events. The theoretical uncertainties listed below are evaluated from the signal regions by considering variations with respect to the default settings and choices for the event generation. For each variation of a background normalised in a control region, the associated systematic is taken on the corresponding transfer factor.

Diboson Prescriptions for the estimation of the modelling uncertainties on the WZ +jets and ZZ +jets background include the variations of the renormalisation, factorisation and resummation scales by factors of 2 and $\frac{1}{2}$. The **CKKW** matching scale, nominally set at 20 GeV, is also varied to 15 GeV and 30 GeV. For WZ +jets, the total uncertainty on the transfer factor to each 3L SR ranges from 30% (in 3L-Z-1b4j) to 50% (in 3L-Z-2b4j). In 4L SRs with one b -jet, the total ZZ +jets modelling uncertainty is found to be 21%; due to insufficient statistics, it is conservatively doubled to 42% in SRs with two b -tagged jets.

Single top with vector bosons A large uncertainty on the tWZ normalisation originates from the interference between this process at NLO and the signal $t\bar{t}Z$ at LO. This interference is set to zero when removing the overlap between the processes using a Diagram Removal method (DR1) [251], which introduces a systematic uncertainty on the predicted number of events. The interference of tWZ with $t\bar{t}Z$ and $t\bar{t}$ is estimated in a similar fashion (DR2). The difference between the tWZ cross section computed with DR1 and DR2 gives an estimate of the interference between the tWZ and $t\bar{t}Z$ processes. This effect is found to be negative and 10% of the DR1 estimate; therefore a normalisation uncertainty of $\pm 10\%$ is applied. In addition, a systematic uncertainty is attributed to the modelling of parton showers, by comparing the nominal PYTHIA 8 generator to a Herwig++ alternative. In the case of tZq , a conservative uncertainty of 30% is applied on the normalisation [252, 253], along with scale and shower radiation variations.

Rare SM processes A 50% uncertainty is considered for all rare SM backgrounds, including three- and four-top quark production as well as triboson processes. In the special case of $t\bar{t}H$, most relevant in the 2L channel and the $t\bar{t}W$ measurement, a $+5.8\% - 9.2\%$ normalisation uncertainty is used, corresponding to the scale and α_s uncertainties in the NLO cross section computation [239].

Signal component To estimate the uncertainties on the $t\bar{t}Z$ signal (and similarly for $t\bar{t}W$), the renormalisation and factorisation scales are varied by factors of 2 and $\frac{1}{2}$, both individually and together (yielding a seven-point variation). The Var3c parameter of the nominal A14 tune is also varied, regulating the emission of ISR gluons [254]. PDF uncertainties are obtained from internal variations of the nominal NNPDF3.0NLO set. A generator uncertainty of a few percents in all SRs is estimated by comparing the nominal aMC@NLO sample with one generated with SHERPA 2.2.1 using NNPDF3.0NNLO.

5.7 Results

5.7.1 Fit strategy

As discussed in the previous sections, the background estimation strategy relies on the normalisation of the WZ +jets and ZZ +jets processes in dedicated control regions designed to enrich the selected sample in each of them, while limiting the contamination from signal $t\bar{t}V$. The extrapolation of the renormalised yields from the CRs to the SRs is performed by a profile likelihood fit, as introduced in Section 4.1.

The systematic uncertainties on the expected values are included in a likelihood function as nuisance parameters (NP) with a Gaussian probability density function, and their correlations are taken into account. NP corresponding to the MC statistical uncertainties (referred to as “gammas” or γ_i) are also introduced in the fit for each region, acting on all MC samples in a correlated manner.

Three different kinds of fit are performed, and for each the significance for the $t\bar{t}Z$ signal process is reported, assuming the null hypothesis.

Individual fits to $t\bar{t}Z$ In the 3L (4L) channel, the normalisation factor associated with the WZ +jets (ZZ +jets) background is determined in its corresponding control region, CR- WZ (CR- ZZ). The $t\bar{t}Z$ signal strength is a free parameter in all four signal regions. Details of the 2LOS analysis strategy or fit are not reported here, but relevant results will be included later for comparison with other channels. A similar set of individual fits target the $t\bar{t}W$ signal process alone. For the individual fits to $t\bar{t}Z$ ($t\bar{t}W$), the $t\bar{t}W$ ($t\bar{t}Z$) cross section is fixed to its nominal value, and a theoretical uncertainty of 13% (12%) is applied.

Combined $t\bar{t}Z$ fit Here, all backgrounds are simultaneously normalised in their respective control regions and the $t\bar{t}Z$ signal strength is treated as a free parameter in all signal regions. A similar fit is performed with $t\bar{t}W$ as parameter of interest.

Combined $t\bar{t}V$ fit Likewise, all backgrounds are normalised and both the $t\bar{t}Z$ and $t\bar{t}W$ signal strengths are extracted from a two-dimensional fit to all signal regions.

5.7.2 Results in the 3L channel

In the trilepton channel sensitive to $t\bar{t}Z$ (regions 3L-Z-1b4j, 3L-Z-2b4j, 3L-Z-2b3j and 3L-noZ-2b4j), including the control region CR-WZ, the observed results are:

$$\mu_{t\bar{t}Z} = 1.08 \pm 0.12(\text{stat.})_{-0.12}^{+0.13}(\text{syst.}) = 1.08_{-0.17}^{+0.18} \quad (5.12)$$

$$\mu_{WZ} = 0.93 \pm 0.07(\text{stat.}) \pm 0.10(\text{syst.}) = 0.93 \pm 0.12 \quad (5.13)$$

with an observed (median) significance of 6.8σ (6.2σ) over the null hypothesis. The post-fit yields are given in Table 5.7. The systematic uncertainty ranking plot in Figure 5.7 shows that the uncertainties on b -tagging, WZ +jets modelling (in particular in the 3L-Z-1b4j region) and $t\bar{t}Z$ generator choice have the largest impact in the 3L channel.

Table 5.7: The post-fit event yields in the 3L channel signal regions and the WZ +jets control region for an integrated luminosity of 36.1 fb^{-1} after the fit to the trilepton channel only. The expected (“exp.”) and fitted (“fit.”) total SM contributions are indicated separately. Statistical and systematic uncertainties are included as described in Section 5.6.

Yields	3L-Z-1b4j	3L-Z-2b4j	3L-Z-2b3j	3L-noZ-2b4j	CR-WZ
Observed	86	78	45	37	211
Total SM (fit.)	92 ± 8.6	82 ± 8.4	37 ± 4.8	34 ± 4.5	210 ± 17
$t\bar{t}Z$	45 ± 9.1	60 ± 10	22 ± 4.4	13 ± 2.9	5.5 ± 1.6
$t\bar{t}W$	0.48 ± 0.28	0.49 ± 0.32	0.83 ± 0.42	3.6 ± 1.9	0.17 ± 0.095
WZ +jets	26 ± 6.9	5.7 ± 3.0	3.6 ± 1.8	1.0 ± 0.56	180 ± 17
ZZ +jets	2.7 ± 0.55	0.54 ± 0.10	0.67 ± 0.26	0.32 ± 0.19	10 ± 1.6
tZ	2.8 ± 0.91	3.4 ± 1.1	4.0 ± 1.3	0.33 ± 0.14	1.4 ± 0.49
tWZ	6.2 ± 1.7	6.0 ± 2.1	2.1 ± 0.45	0.67 ± 0.30	2.2 ± 0.67
$t\bar{t}H$	1.2 ± 0.19	1.4 ± 0.21	0.55 ± 0.088	4.8 ± 0.63	0.11 ± 0.034
Other	0.32 ± 0.17	0.23 ± 0.21	1.2 ± 1.2	2.3 ± 1.2	1.6 ± 1.2
Fakes (MM)	6.4 ± 2.8	3.9 ± 2.2	1.2 ± 1.2	3.2 ± 2.0	5.7 ± 3.1
$\gamma + X$	1.3 ± 1.2	0.51 ± 0.59	0.77 ± 1.1	5.1 ± 2.6	—
Total SM (exp.)	104 ± 14.2	80.6 ± 10.2	30.4 ± 4.47	33.8 ± 4.70	238 ± 23.0

5.7.3 Results in the 4L channel

In the tetra-lepton channel sensitive to $t\bar{t}Z$ (regions 4L-SF-1b, 4L-SF-2b, 4L-DF-1b and 4L-DF-2b), including the control region CR-ZZ, the observed results are:

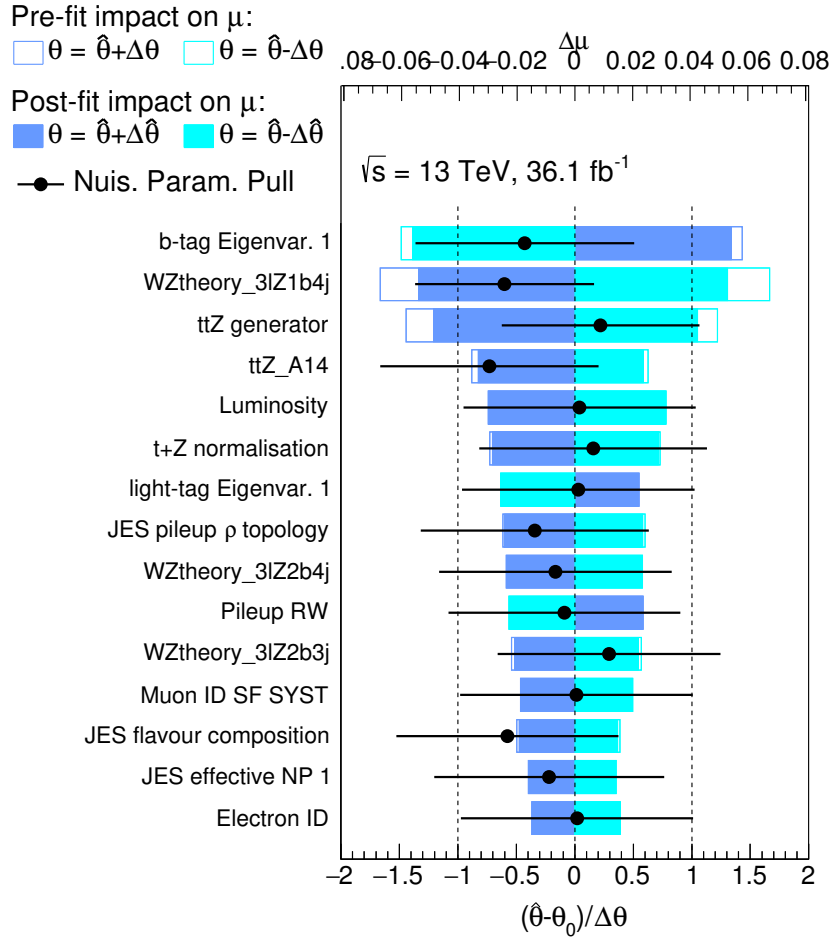


Figure 5.7: The ranking plot for the $t\bar{t}Z$ trilepton channel fit together with the WZ +jets control region. The empty and filled blue rectangles indicate the pre-fit and post-fit impact, respectively, of a $\pm 1\sigma$ shift in each systematic on the measured signal strength parameter, while the corresponding pulls are indicated by the black dots and their error bars. Large pulls (black dots beyond the $\pm 1\sigma$ vertical dotted lines) indicate that some feature of the data has been absorbed in the nuisance parameters and need to be investigated. Small pull widths (black horizontal error bars) indicate a constraint of the nuisance parameters by the data, which can sometimes indicate a modelling issue.

$$\mu_{t\bar{t}Z} = 1.21_{-0.25}^{+0.28}(\text{stat.})_{-0.12}^{+0.11}(\text{syst.}) = 1.21_{-0.28}^{+0.30} \quad (5.14)$$

$$\mu_{ZZ} = 0.94 \pm 0.09(\text{stat.}) \pm 0.16(\text{syst.}) = 0.94 \pm 0.18 \quad (5.15)$$

with an observed (median) significance of 5.7σ (5.1σ) over the null hypothesis. The post-fit yields are given in Table 5.8. The ranking plot in Figure 5.8 shows that the uncertainties on b -tagging and $t\bar{t}Z$ generator choice have the largest impact in the 4L channel.

5.7.4 Results of the combined $t\bar{t}Z$ fit

The combined $t\bar{t}Z$ fit includes all regions from the 3L and 4L individual fits, as well as the 2LOS channel. The observed signal strength parameter is:

$$\mu_{t\bar{t}Z} = 1.05_{-0.09}^{+0.10}(\text{stat.}) \pm 0.11(\text{syst.}) = 1.05_{-0.14}^{+0.15} \quad (5.16)$$

Table 5.8: The post-fit event yields in the 4L channel signal regions and the ZZ+jets control region for an integrated luminosity of 36.1 fb^{-1} after the fit to the tetralepton channel only. The expected (“exp.”) and fitted (“fit.”) total SM contributions are indicated separately. Statistical and systematic uncertainties are included as described in Section 5.6.

Yields	4L-SF-1b	4L-SF-2b	4L-DF-1b	4L-DF-2b	CR-ZZ
Observed	18	14	11	5	144
Total SM (fit.)	14 ± 2.2	11 ± 1.9	12 ± 2.1	8.6 ± 1.7	140 ± 13
$t\bar{t}Z$	8.0 ± 2.0	7.3 ± 1.7	8.9 ± 2.2	7.0 ± 1.7	0.15 ± 0.066
ZZ+jets	2.2 ± 0.62	1.0 ± 0.53	0.18 ± 0.068	0 ± 0	140 ± 15
tWZ	1.6 ± 0.49	0.57 ± 0.29	1.6 ± 0.37	0.52 ± 0.28	0 ± 0
$t\bar{t}H$	0.58 ± 0.078	0.61 ± 0.10	0.67 ± 0.085	0.57 ± 0.094	0 ± 0
Other	0.12 ± 0.037	0.088 ± 0.038	0.20 ± 0.067	0.10 ± 0.029	0.51 ± 0.50
Fakes (FF)	1.9 ± 1.1	1.3 ± 0.83	0.93 ± 0.20	0.39 ± 0.14	6.8 ± 8.6
Total SM (exp.)	12.97 ± 1.33	9.69 ± 1.17	10.95 ± 0.65	7.57 ± 0.88	153.92 ± 24.71

with an observed (median) significance of 8.9σ (8.4σ). The breakdown of the signal sensitivity per channel is further reported in Table 5.9. The ranking plot in Figure 5.9 shows that the uncertainties on b -tagging, WZ +jets modelling (in particular in the 3L-Z-1b4j region) and $t\bar{t}Z$ generator choice have the largest impact in the combined channels. This is expected, as the high-statistics 3L channel has a large impact on the fit.

Table 5.9: Expected and observed signal significances for the $t\bar{t}Z$ processes determined from the fit to the separate channels and from the combined fit to all $t\bar{t}Z$ channels.

Channel	$t\bar{t}Z$ significance	
	Expected	Observed
2LOS	3.8σ	3.0σ
3L	6.2σ	6.8σ
4L	5.1σ	5.7σ
Combination	8.4σ	8.9σ

5.7.5 Results of the two-dimensional fit

In the two-dimensional fit, both $\mu_{t\bar{t}Z}$ and $\mu_{t\bar{t}W}$ are treated as free parameters in all signal regions. The observed signal strengths are:

$$\mu_{t\bar{t}Z} = 1.08 \pm 0.14 \quad (5.17)$$

$$\mu_{t\bar{t}W} = 1.44 \pm 0.32 \quad (5.18)$$

with an observed (median) significance of 4.3σ (3.4σ) over the null hypothesis for $t\bar{t}W$. For

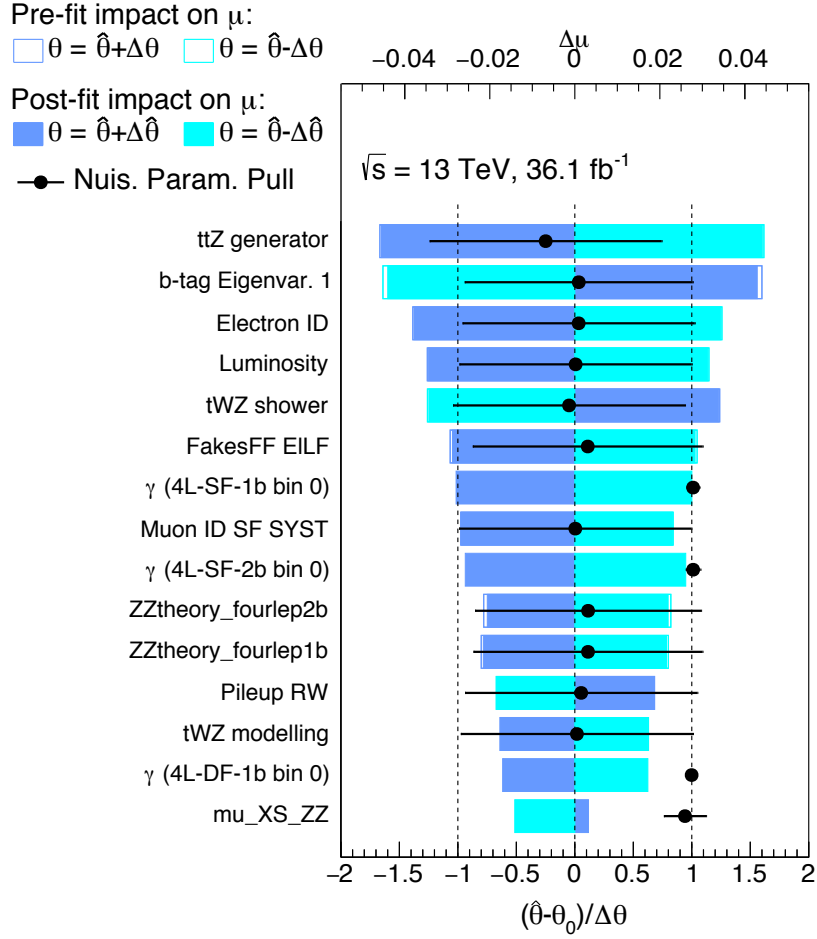


Figure 5.8: The ranking plot for the $t\bar{t}Z$ tetralepton channel fit together with the ZZ +jets control region.

the $t\bar{t}Z$ process, both the observed and the expected significances are found to be much larger than five standard deviations. The corresponding observed cross sections are:

$$\sigma_{t\bar{t}Z} = 0.95 \pm 0.08(\text{stat.}) \pm 0.10(\text{syst.}) \text{ pb} = 0.95 \pm 0.13 \text{ pb} \quad (5.19)$$

$$\sigma_{t\bar{t}W} = 0.87 \pm 0.13(\text{stat.}) \pm 0.14(\text{syst.}) \text{ pb} = 0.87 \pm 0.19 \text{ pb} \quad (5.20)$$

demonstrating good agreement with theoretical predictions [255]:

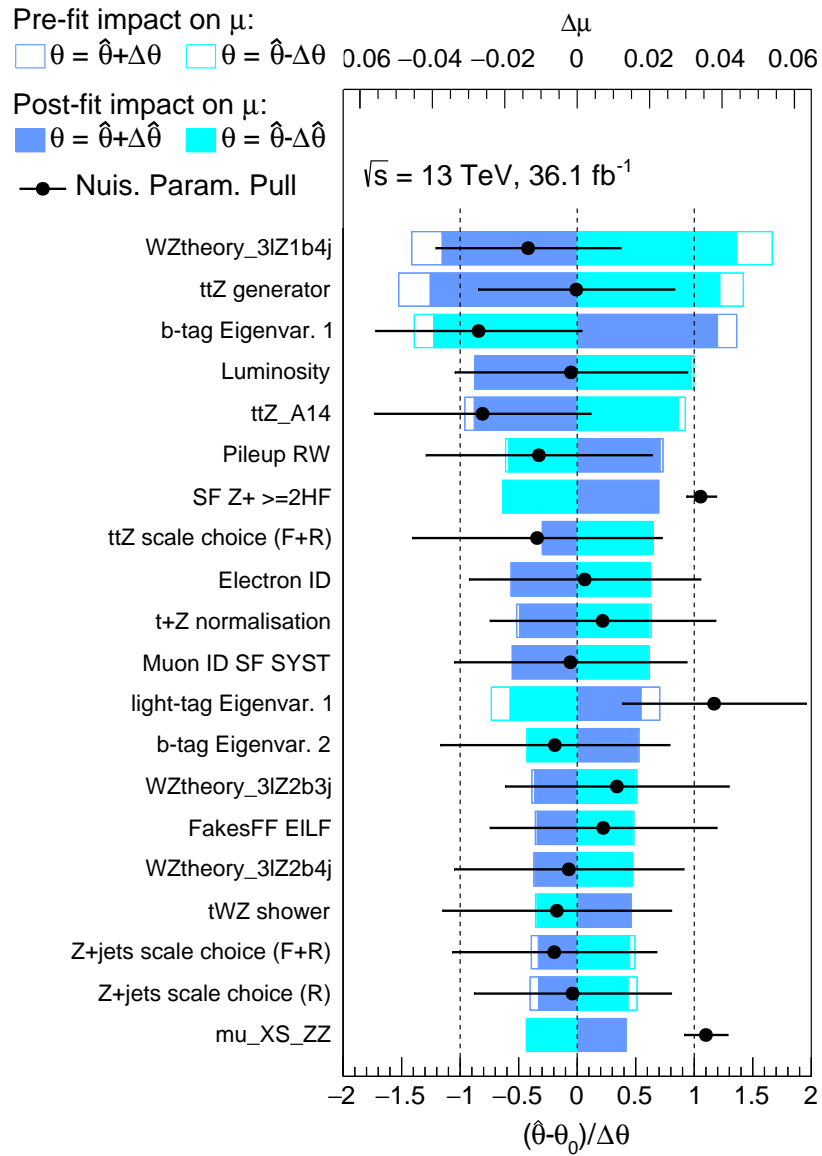
$$\sigma_{t\bar{t}Z}^{\text{theory}} = 0.88^{+0.09}_{-0.11} \text{ pb} \quad (5.21)$$

$$\sigma_{t\bar{t}W}^{\text{theory}} = 0.60^{+0.08}_{-0.07} \text{ pb} \quad (5.22)$$

The observed and predicted cross section are further summarised in Figure 5.10, where it is apparent that the $t\bar{t}W$ measurement is driving a 1σ tension with the SM prediction. The event yields after the fit are shown in Figure 5.11 for all the 3L and 4L signal regions, as well as the two control regions, CR-WZ and CR-ZZ. A breakdown of the impact of relative systematic uncertainties on the various $t\bar{t}Z$ fits, both in individual channels and combined, is given in Table 5.10.

Table 5.10: Impact of the relative statistical and systematic uncertainties in the fits to the individual channels, the combined $t\bar{t}Z$ fit (“combined”), and the simultaneous fit to both $t\bar{t}Z$ and $t\bar{t}W$ (“2D”). The parameter strengths $\mu_{t\bar{t}Z}$ are dimensionless quantities; all other numbers are expressed in percent.

Category	2LOS	3L	4L	Combined	2D
$\mu_{t\bar{t}Z}$	0.73	1.08	1.21	1.05	1.08
Luminosity	2.6	2.9	2.9	2.9	2.9
CR and simulated sample statistics	14.1	2.0	3.6	2.3	1.8
JES/JER	4.3	4.0	1.1	1.8	1.9
Flavour tagging	6.0	5.8	3.9	4.6	4.2
Other object-related	2.8	3.4	4.8	3.7	3.7
Data-driven background normalisation	14.1	11.2	11.6	2.7	2.4
Modelling of backgrounds from simulation	17.4	6.1	3.6	5.7	5.3
Background cross section	12.1	3.1	1.8	2.5	2.3
Fake leptons	—	1.9	2.4	1.7	1.8
$t\bar{t}Z$ modelling	7.7	5.1	3.9	5.2	4.9
$t\bar{t}W$ modelling	—	—	—	0.3	0.3
Total systematic uncertainty	26.2	10.5	9.5	10.5	10.2
Statistical uncertainty	26.3	11.1	22.3	9.5	8.4
Total uncertainty	38.4	16.4	24.0	14.3	13.0

Figure 5.9: The ranking plot for the combined fit to all $t\bar{t}Z$ channels.

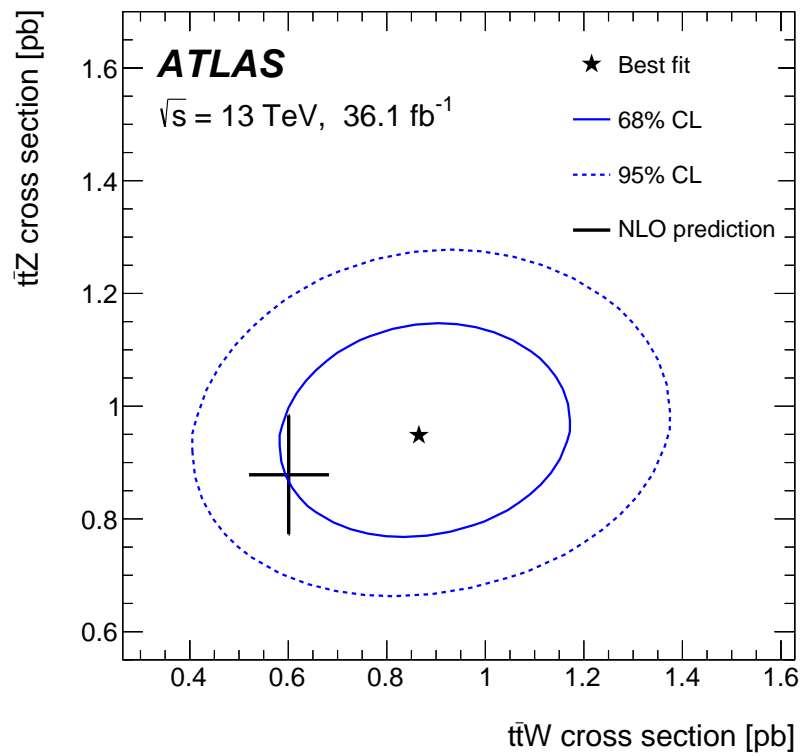


Figure 5.10: The result of the simultaneous fit to the $t\bar{t}Z$ and $t\bar{t}W$ cross sections along with the 68% (solid line) and 95% (dashed line) confidence level (CL) contours. The cross shows the SM calculations [255] and their uncertainties, including renormalisation and factorisation scale uncertainties as well as α_s variations.

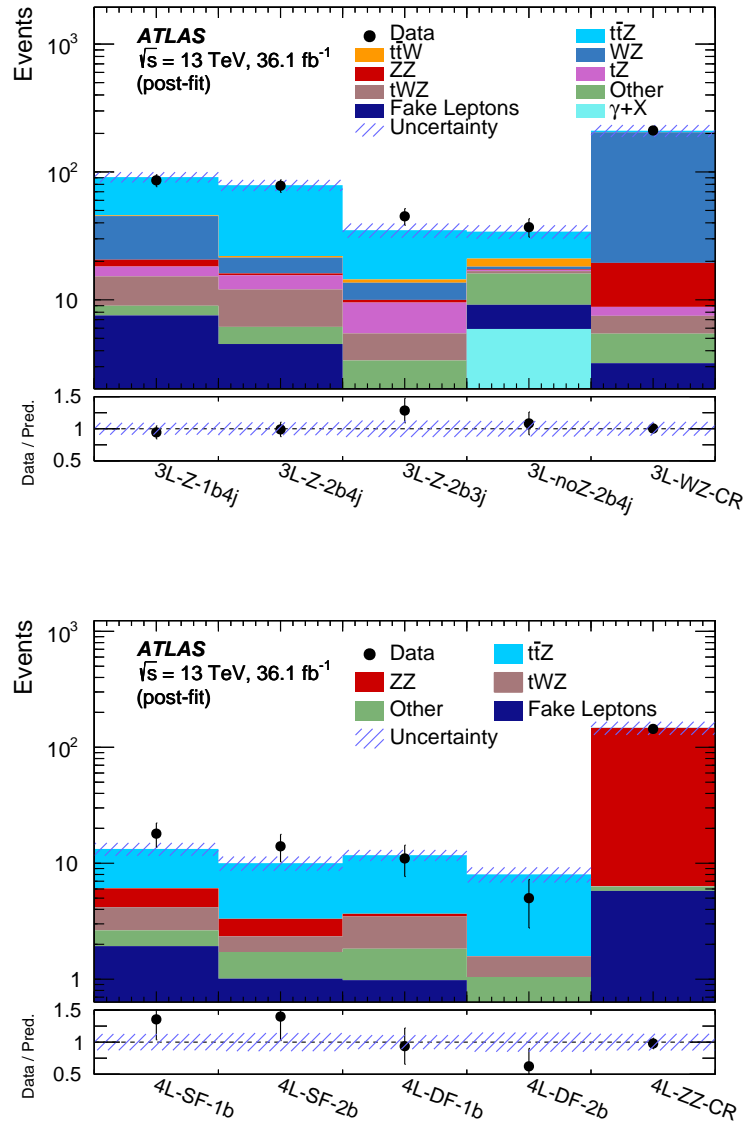


Figure 5.11: Event yields in data compared with the results of the fit that extracts $\sigma_{t\bar{t}Z}$ and $\sigma_{t\bar{t}W}$ simultaneously in the trilepton (top) and tetralepton (bottom) signal regions targeting the $t\bar{t}Z$ process. Yields for the control regions used to extract the normalisation of the WZ +jets and ZZ +jets backgrounds are also shown. The “Other” process contains SM processes with small cross sections producing three or four prompt leptons (e.g. $t\bar{t}H$, triboson processes). The shaded band represents the total uncertainty.

5.8 EFT interpretation

As previously introduced in Section 1.1.3, the EFT framework provides a model-independent approach to the parameterisation of possible deviations from the SM predictions. In particular, BSM effects related to the coupling of the top quark to the Z boson can be represented as a set of five dimension six operators O_i , associated with a Wilson coefficient C_i , entering the modified Lagrangian density in the form $(C_i/\Lambda^2)O_i$, where Λ is the characteristic energy scale of the new physics [256–258].

These five operators are listed in Table 5.11. The first two of them enter the $t\bar{t}Z$ vertex as a linear combination, such that this analysis is only sensitive to their difference. For that reason, the effect of this combination is evaluated by varying $C_{\phi Q}^{(3)}$ with $C_{\phi Q}^{(1)}$ set to zero. Any observable, including the event rate itself, is expected to receive corrections of the form

$$\sigma_{\text{total},i} = \sigma_{\text{SM}} + \frac{C_i}{(\Lambda/1\text{TeV})^2} \sigma_i^{(1)} + \frac{C_i^2}{(\Lambda/1\text{TeV})^4} \sigma_{ii}^{(2)}, \quad (5.23)$$

where the linear term results from the interference of the BSM operators with the SM. For C_i/Λ^2 of order 1TeV^{-2} , this interference term dominates for $O_{\phi Q}^{(3)}$ and $O_{\phi t}$, while the quadratic term dominates for O_{tW} and O_{tB} . Dedicated samples are generated, implementing computations at NLO of $\sigma_i^{(1)}$ and $\sigma_{ii}^{(2)}$ for each operator. A fit similar to the $t\bar{t}Z$ -only combination described previously is performed, with the Wilson coefficients as parameters of interest. The 2LOS channel is not included in the fit due to its low sensitivity, and a flat 12% uncertainty is applied to the normalisation of the SM $t\bar{t}Z$ prediction, corresponding to the uncertainty in the NLO cross section computation [255].

The 68% and 95% confidence intervals are shown in Table 5.12, together with previous constraints on the EFT coefficients. The lower boundary of the 95% confidence interval for $C_{\phi t}$ is at large negative values, which are excluded by indirect constraints. The $t\bar{t}Z$ measurement provides competitive constraints for positive $C_{\phi t}$ values, and a full likelihood scan of this operator is shown in Figure 5.12.

Table 5.11: Effective field theory operators considered and their form in terms of SM fields.

Operator	Expression
$O_{\phi Q}^{(3)}$	$(\phi^\dagger i \overleftrightarrow{D}_\mu^I \phi)(\bar{Q}\gamma^\mu \tau^I Q)$
$O_{\phi Q}^{(1)}$	$(\phi^\dagger i \overleftrightarrow{D}_\mu \phi)(\bar{Q}\gamma^\mu Q)$
$O_{\phi t}$	$(\phi^\dagger i \overleftrightarrow{D}_\mu \phi)(\bar{t}\gamma^\mu t)$
O_{tW}	$(\bar{Q}\sigma^{\mu\nu} \tau^I t)\tilde{\phi}W_{\mu\nu}^I$
O_{tB}	$(\bar{Q}\sigma^{\mu\nu} t)\tilde{\phi}B_{\mu\nu}$

Table 5.12: The expected and observed 68% and 95% confidence intervals, which include the value 0, for C_i/Λ^2 for the EFT coefficients $C_{\phi Q}^{(3)}$, $C_{\phi t}$, C_{tB} and C_{tW} . The intervals for $C_{\phi Q}^{(3)}$ are derived setting $C_{\phi Q}^{(1)}$ to zero; the measurement is sensitive to the difference $C_{\phi Q}^{(3)} - C_{\phi Q}^{(1)}$. All results are obtained by varying one coefficient at the time and are given in units of $1/\text{TeV}^2$. Previous indirect 68% CL constraints are also quoted [259–262].

Coefficients	$C_{\phi Q}^{(3)}/\Lambda^2$	$C_{\phi t}/\Lambda^2$	C_{tB}/Λ^2	C_{tW}/Λ^2
Previous indirect constraints at 68% CL	[-4.7, 0.7]	[-0.1, 3.7]	[-0.5, 10]	[-1.6, 0.8]
Previous direct constraints at 95% CL	[-1.3, 1.3]	[-9.7, 8.3]	[-6.9, 4.6]	[-0.2, 0.7]
Expected limit at 68% CL	[-2.1, 1.9]	[-3.8, 2.7]	[-2.9, 3.0]	[-1.8, 1.9]
Expected limit at 95% CL	[-4.5, 3.6]	[-23, 4.9]	[-4.2, 4.3]	[-2.6, 2.6]
Observed limit at 68% CL	[-1.0, 2.7]	[-2.0, 3.5]	[-3.7, 3.5]	[-2.2, 2.1]
Observed limit at 95% CL	[-3.3, 4.2]	[-25, 5.5]	[-5.0, 5.0]	[-2.9, 2.9]

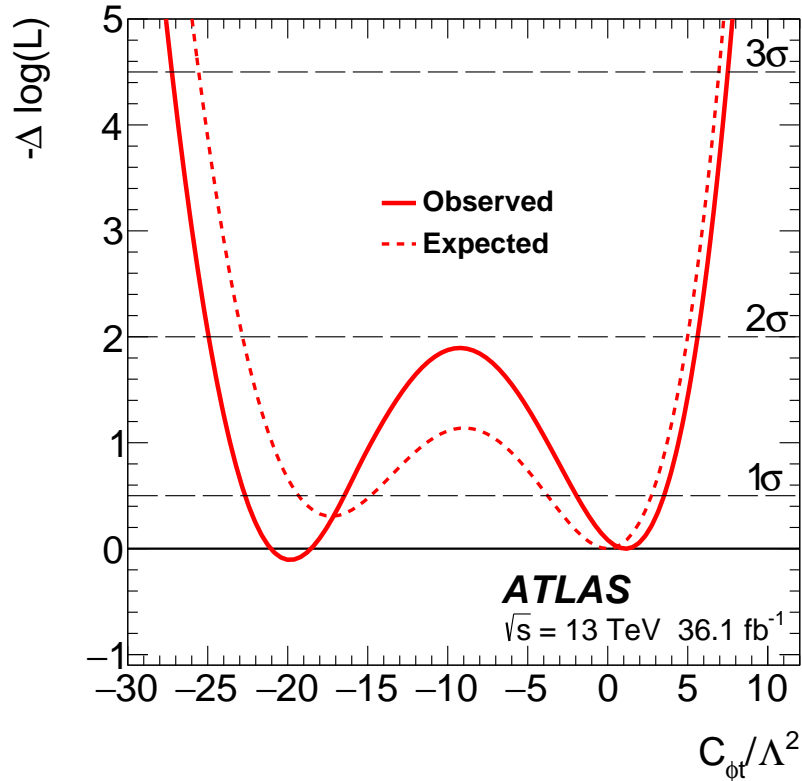


Figure 5.12: The value of the profile-likelihood test statistic as a function of $C_{\phi t}/\Lambda^2$. Another, deeper minimum exists for large negative values of $C_{\phi t}$, which is excluded by indirect measurements. The vertical axis is chosen such that the value of the likelihood function at the minimum near $C_{\phi t} = 0$ is zero.

6. Update on the inclusive measurement

In this chapter we review the measurement of the inclusive $t\bar{t}Z$ cross section in multi-lepton final states using the full Run 2 dataset with 139fb^{-1} of pp collisions at $\sqrt{s} = 13\text{TeV}$. An updated analysis strategy is presented in Section 6.1, as well as reconstructed physics objects (Section 6.2) and event selection (Section 6.3). Signal regions are defined in Section 6.4 and the estimation of background processes in Section 6.5. Since this measurement is a direct continuation of the one extensively discussed in the previous chapter, we focus here only on the differences between the two, before comparing the impact of systematic uncertainties (re-evaluated in Section 6.6) on the final results in Section 6.7. The author’s contributions concern all these topics in the trilepton channel. The analysis has been made public by the ATLAS Collaboration in [2].

6.1 Analysis strategy

Motivations for precise measurements of the $t\bar{t}Z$ cross section were outlined in Chapter 5 and the [Motivation and outline](#). In this follow-up analysis to the inclusive $t\bar{t}V$ measurement [1], the focus is placed on $t\bar{t}Z$ and its cross section measured differentially for the first time at ATLAS (see Chapter 7). The $t\bar{t}W$ component is therefore removed altogether, along with the 2LOS channel which was shown to be only difficultly sensitive to $t\bar{t}Z$. For the purposes of conducting a differential cross section measurement, good modelling of the main backgrounds must be ensured, including normalisations in control regions and data-driven fake lepton estimates, motivating this updated inclusive measurement.

The same $t\bar{t}Z$ Monte Carlo samples as described in Section 5.1.1 are used for the nominal estimate of the $t\bar{t}Z$ process, but Section 6.6 introduces additional samples with alternative generators or parton showers to derive modelling systematic uncertainties.

“Event display of a four lepton $t\bar{t}Z$ candidate”. Image credits: Meirin Oan Evans. © 2020 CERN.

6.2 Object definitions

We outline here only the differences in object definitions with respect to Section 5.2. As detailed in Section 3.2, an important change concerns the reconstruction of electrons, previously using a sliding-window algorithm and, in what follows, superclusters.

Electrons the signal isolation requirement is updated from FixedCutTight to FCTight. The ECIDS tool is dropped, as no charge-dependency is required in this version of the analysis.

Muons the signal isolation requirement is updated from FixedCutTightTrackOnly to FCTightTrackOnly.

Jets the definition of light-flavour jets remains identical. The MV2c10 algorithm is used to identify b -jets, but the b -tagging efficiency is relaxed from 77% to 85% in the differential measurement and in the 4L channel of the inclusive measurement. In the 3L channel of the inclusive measurement, a different approach is used, which employs a so-called pseudo-continuous b -tagging (PCBT) algorithm [263]. This allows for a flexible choice of efficiency working point for the leading and sub-leading b -tag-valued jets.

The definition of E_T^{miss} and the overlap removal algorithm remain identical to those described in Section 5.2.

6.3 Event selection

6.3.1 Triggers

In order to collect events with leptons, dedicated triggers are used whose requirements are summarised in Table 6.1 below. Note the similarity with respect to Table 5.1 for the analysis at 36.1 fb^{-1} . Di- and multi-lepton triggers were tested and found to provide no significant improvement with respect to the application of single lepton triggers.

Table 6.1: Summary of trigger p_T -thresholds used in the analysis. Commas in the individual p_T selections denote a logical OR of multiple cuts. Different identification and isolation requirements are used in each trigger, such that their combination is not trivially equivalent to only the first one listed.

Trigger	Data 2015	Data 2016–2018
Electron	$p_T > 24, 60, 120 \text{ GeV}$	$p_T > 26, 60, 140 \text{ GeV}$
Muon	$p_T > 20, 50 \text{ GeV}$	$p_T > 26, 50 \text{ GeV}$

Once events selected by the various triggers have been selected, further offline cuts are applied to ensure the relevant objects are in the plateau region, where the trigger is fully efficient (see Figures 3.6 and 3.8). This is done by requiring slightly higher-than-threshold transverse momenta: for data collected in 2015 (2016–2018), this is $p_T > 25(27) \text{ GeV}$.

6.3.2 Event cleaning

A number of offline cuts are applied to trigger-selected events. These aim at removing events recorded during a detector fault (by checking the status of the ECAL and HCAL), non-HS events (by reconstructing a primary vertex with at least two tracks above the $p_T > 400 \text{ MeV}$ threshold), events with potential cosmic muons or poorly reconstructed jets (sensitive to large fake-jet contamination).

6.4 Signal regions

Very similar signal regions to the previous analysis are considered here. In the 3L channel, the SR previously known as 3L-Z-2b3j and 3L-Z-2b4j are combined into a single, 2- b -jet inclusive region (3L-Z-2b3j) using a fixed 85% b -tagging efficiency. This combined region is used for the differential measurement. Switching to a pseudo-continuous b -tagging (PCBT) algorithm (70% b -tagging efficiency), the new SR 3L-Z-2b3j-PCBT is used for the inclusive measurement. Similarly, the previous 3L-Z-1b4j becomes 3L-Z-1b4j-PCBT, with a requirement of exactly one b -tagged jet at 60% efficiency and a veto applied on any additional b -jets at 70% efficiency, ensuring orthogonality with 3L-Z-2b3j-PCBT. The previous region sensitive to off-shell Z contributions and Z/γ^* interference, 3L-noZ-2b4j, is not considered for this measurement. These selections are summarised in Table 6.2.

The 4L channel SRs do not use PCBT and rely instead on a fixed 85% b -tagging efficiency. The exact selection criteria are presented in Table 6.3 but the strategy remains mostly identical to that of the previous analysis, categorising events in terms of b -jet multiplicity and flavour of the second lepton pair (nominally assigned to the $t\bar{t}$ system). The cuts on E_T^{miss} and p_T of the leptons are adapted as a response to the presence of more background events with increased luminosity.

Table 6.2: Selection criteria for the trilepton signal regions sensitive to $t\bar{t}Z$.

Object	3L-Z-1b4j-PCBT	3L-Z-2b3j-PCBT	3L-Z-2b3j
Event cleaning	Common to all SRs		
N_{lep}	3		
p_T of leptons	$> (27, 20, 20)$ GeV		
Sum of lepton charges	± 1		
OSSF lepton pair	yes		
On-shell Z candidate	yes		
N_{jets}	≥ 4	≥ 3	≥ 3
$N_{b\text{-jets}}$	1 @ 60% veto add. b -jets @ 70%	≥ 2 @ 70%	≥ 2 @ 85%

Table 6.3: Selection criteria for the tetralepton signal regions sensitive to $t\bar{t}Z$.

Object	4L-DF-1b	4L-DF-2b	4L-SF-1b		4L-SF-2b	
Event cleaning	Common to all SRs					
N_{lep}	4					
N_{jets}	≥ 2					
OSSF lepton pair	yes					
On-shell Z candidate	yes					
p_{T} of leptons	$> (27, 20, 20, 7)$ GeV					
Z_2 leptons	$e^\pm \mu^\mp$		$e^\pm e^\mp, \mu^\pm \mu^\mp$			
$ m_{Z_2} - m_Z^{\text{ref}} $	—		> 10 GeV	< 10 GeV	> 10 GeV	< 10 GeV
$E_{\text{T}}^{\text{miss}}$	—		> 50 GeV	> 1000 GeV	—	> 50 GeV
$N_{b\text{-jets}}$	1	≥ 2	1		≥ 2	

6.5 Prediction of the Standard Model backgrounds

The same processes as described in Section 5.5 are still relevant to this analysis. We note here that the accuracy of Monte Carlo simulations used to estimate most of these backgrounds have benefitted from updates of their respective generators.

Diboson For WZ +jets, the leading background with three prompt leptons, the generator is updated from SHERPA 2.1 to SHERPA 2.2.2 and the PDF set from CT10 to NNPDF3.0NL0. A similar set up is employed for the simulation of ZZ +jets events. Dedicated control regions for the normalisation of both processes in the 3L and 4L channels are maintained and further described below.

Single top with vector bosons The samples used to model the tWZ background remain the same. However, the parton showering for the tZq process is here performed with PYTHIA 8 (PYTHIA 6 in the previous iteration) and the NNPDF3.0NL0 PDF set is used (CTEQ6L1 previously).

Fake leptons A data-driven estimation of the non-prompt lepton background in 3L is still performed using the matrix method described in Section 5.5.3. Thanks to the higher statistics in the 4L channel at 139fb^{-1} , this method is also used in all 4L signal regions, instead of the previous fake factor method.

6.5.1 Three-lepton control region

The selection criteria for the new CR-WZ control region for the $WZ(\rightarrow \ell\ell\nu)$ +jets background is very similar to that previously shown in Table 5.4 and are given in Table 6.4 below. The cut on the missing transverse momentum $E_{\text{T}}^{\text{miss}}$ is dropped, and the veto on b -jets is here understood to be at an 85% efficiency rather than the 77% used in the previous measurement. The $t\bar{t}Z$ signal contamination in CR-WZ is still around the level of 2.5%.

The distribution of the p_{T} of the leading lepton is shown in Figure 6.1. A small overestimation of the WZ +jets background ($\approx 12\%$) is observed in the total event yields, but also visible in the kinematic distribution. This effect is mostly absorbed by the normalisation parameter derived in data and expected to be slightly lower than one.

Table 6.4: Summary of the selection criteria for the three-lepton control region for WZ +jets.

Object	CR-WZ
N_{lep}	3
N_{jets}	≥ 3
$N_{b\text{-jets}}$	0
p_{T} of leptons	$> (27, 20, 20)$ GeV
OSSF lepton pair	yes
On-shell Z candidate	yes

6.5.2 Four-lepton control region

The definition of the tetralepton control region for the ZZ +jets background, presented in Table 6.5, remains largely unchanged with respect to Table 5.5. A requirement on the transverse momenta of the leptons is simply added, to bring the kinematic selection of the CR- ZZ closer to that of the 4L SRs. As can be seen in Figure 6.2, imposing additional cuts on the number of jets (or b -jets) would significantly reduce the number of events in the CR and any further modelling checks would suffer from large statistical uncertainties. The $t\bar{t}Z$ signal contamination in CR- ZZ is $< 0.1\%$.

Table 6.5: Summary of the selection criteria for the four-lepton control region for ZZ +jets.

Object	CR-ZZ
N_{lep}	4
p_{T} of leptons	$> (27, 20, 20, 7)$ GeV
OSSF lepton pair	yes
On-shell Z candidate	yes
Z_2 leptons	$e^{\pm}e^{\mp}, \mu^{\pm}\mu^{\mp}$
$ m_{Z_2} - m_Z^{\text{ref}} $	< 10 GeV
$E_{\text{T}}^{\text{miss}}$	$\in [20, 40]$ GeV

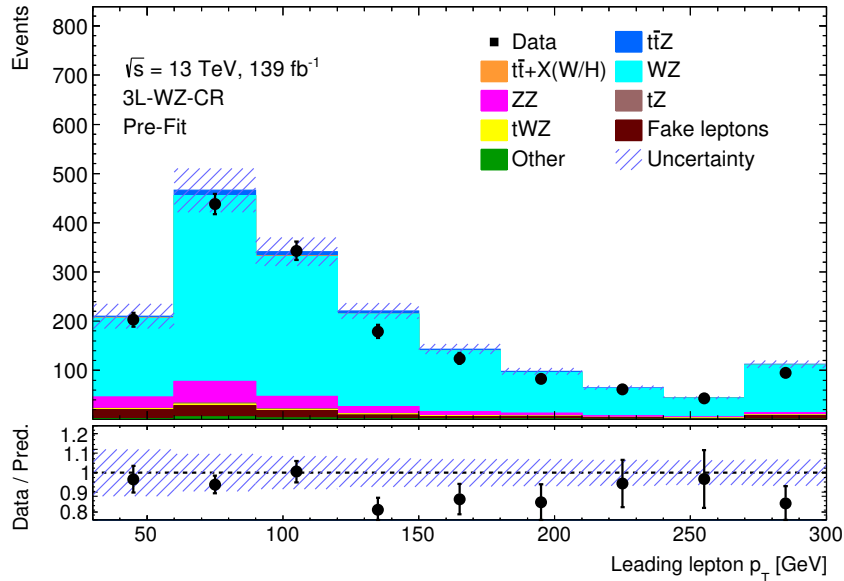


Figure 6.1: Distributions of the leading lepton transverse momentum p_T in the three-lepton CR-WZ region before the fit. The “Other” background contains SM processes with small cross sections producing three prompt leptons (e.g. $t\bar{t}H$, triboson processes). The shaded band represents the total uncertainty. The last bin in each of the distributions includes the overflow.

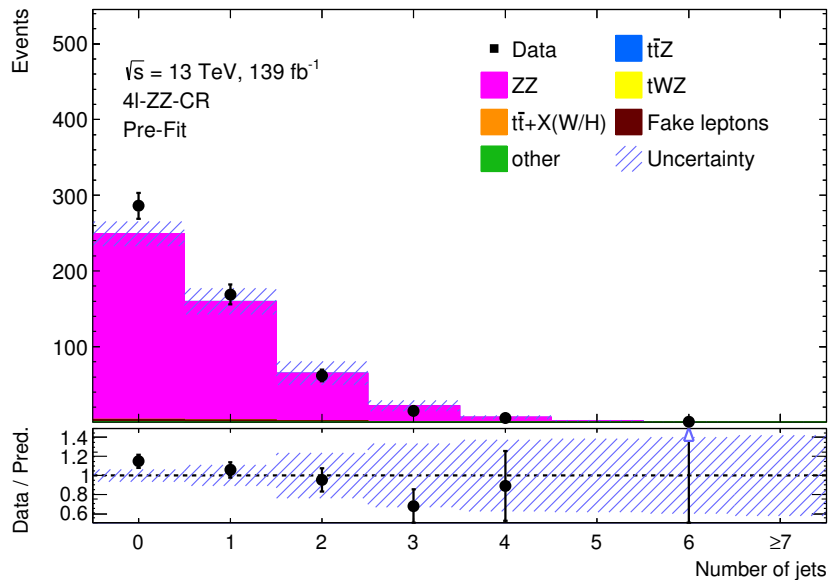


Figure 6.2: Distribution of the jet multiplicity of jets with $p_T > 25$ GeV in the four-lepton CR-ZZ region before the fit. The “Other” background contains SM processes with small cross sections producing four prompt leptons (e.g. $t\bar{t}H$, triboson processes). The shaded band represents the total uncertainty. The last bin in each of the distributions includes the overflow.

6.6 Systematic uncertainties

6.6.1 Experimental uncertainties

The definition of experimental uncertainties, covering the reconstruction and identification of the various physics objects used in this analysis remain the same as those detailed in Section 5.6. The impact of these uncertainties on the final measurement, to be discussed in the next section, is lowered thanks to the improved statistics available to derive systematic uncertainties on the reconstruction of all physics objects. For example, we note that the relative uncertainty on the luminosity estimate at $\sqrt{s} = 13$ TeV, which was 2.1% for the 2015–2016 dataset, is now 1.7% for the 2015–2018 full Run 2 dataset [190].

Improvements in the treatment of theoretical uncertainties, related to the modelling of various backgrounds, have been made in this analysis and are reported below.

6.6.2 Theoretical uncertainties

In what follows, we consider only changes in the assignment of theoretical uncertainties to the main backgrounds with respect to Section 5.6.

Diboson Thanks to the new availability of dedicated samples, an additional uncertainty on the parton shower is considered for both the WZ +jets and ZZ processes, whereby an alternative recoil scheme is compared to the nominal one. PDF uncertainties are also taken into account [264], with internal and α_s variations of the nominal NNPDF3.0NLO set as well as comparisons to the CT14 [265] and MMHT14 [266] PDF sets. The total uncertainty on the WZ +jets transfer factor from control region to the combination of 3L signal regions is found to be 12.5%. This represents a significant improvement with respect to the previous measurement. The treatment of modelling uncertainties on ZZ +jets remains largely the same. An additional 20% normalisation uncertainty is applied on both the $WZ + c$ and $ZZ + c$ heavy-flavour components, as well as a 30% uncertainty on the $WZ + b$ and $ZZ + b$ components. Separating these diboson components helps reflect the different flavour composition of the CRs and SRs.

Single top with vector bosons The modelling uncertainty on tWZ is made more precise by including a variation of the renormalisation and factorisation scales by factors of 2 and $\frac{1}{2}$, as well as internal NNPDF2.3LO PDF variations. While the parton shower scheme and PDF set for the tZq MC sample have been updated, the previous conservative uncertainty of 30% on its normalisation [252, 253] is maintained since no new direct measurement of the tZq cross section has been performed at ATLAS or CMS in the timeframe of this analysis. We note however that a later publication [267] quotes a 15% uncertainty on the tZq cross section.

Rare SM processes The $t\bar{t}H$ background in particular benefits from an additional flat $\pm 3.6\%$ PDF uncertainty. The $t\bar{t}W$ process, an additional signal of the previous analysis, is now treated as a rare SM process (with a contribution below 2% in all regions) and covered by the generic 50% normalisation uncertainty applied to all such backgrounds.

Signal component An alternative signal sample is generated, also using aMC@NLO for the matrix elements but interfaced to HERWIG 7 instead of the nominal PYTHIA 8, to derive a parton shower uncertainty. Since HERWIG uses a different underlying event (UE) tune, this sample provides additional systematic coverage. Variations of the Var3c parameter of the nominal A14 UE tune are no longer considered as a theoretical uncertainty, but rather used to cross-check the above parton shower uncertainty. Additionally, it is worth noting that the A14 tune wasn't derived in the context of $t\bar{t}Z$ production but $t\bar{t}$ instead, and that such biases should be avoided for a very

first differential measurement of the $t\bar{t}Z$ cross section, granted the A14 uncertainty is covered by the PS one. This is indeed the case, as can be seen in Table 6.6 below. Similarly, an alternative signal sample is simulated with the SHERPA 2.2.1 generator at NLO accuracy and using the NNPDF3.0NLO PDF set [170]. An additional SHERPA 2.2.1 sample, produced in the later stages of this analysis, includes the production of two additional partons at LO (multi-leg) and surpasses the precision of the nominal signal sample; therefore, the uncertainty related to the choice of generator is taken from the former NLO sample, while the latter NLO+LO is reserved for comparison purposes in the differential part of the analysis (see Chapter 7). This generator uncertainty is found to be well covered already by scale, PDF and parton shower variations. To avoid double-counting of uncertainty sources, it is not included in the final theoretical uncertainties for $t\bar{t}Z$.

Table 6.6: Summary of the relative differences on the nominal $t\bar{t}Z$ yields in each region as a function of the signal modelling systematics. These are: HERWIG 7 for the parton shower (PS), the μ_F and μ_R scales varied by factors of 2 (S \uparrow) and $\frac{1}{2}$ (S \downarrow), internal up and down PDF scale variations (PDF \uparrow and \downarrow) as well as PDF choice (PDF C). Also shown are additional variations that would induce double-counting of systematic sources if included in the fit: SHERPA 2.2.1 at NLO for the generator (GEN), and up and down variations of Var3c parameter of the A14 tune (A14 \uparrow and \downarrow). All numbers are given in percent.

Region	PS	S \uparrow	S \downarrow	PDF \uparrow	PDF \downarrow	PDF C	GEN	A14 \uparrow	A14 \downarrow
3L-Z-2b3j	-5.7	-0.8	+0.3	+2.7	-2.7	-0.1	+2.9	+1.1	-1.6
3L-Z-1b4j-PCBT	-6.0	-1.8	+0.8	+2.1	-2.1	-0.4	-4.3	+3.4	-4.2
3L-Z-2b3j-PCBT	-1.7	-0.8	+0.4	+2.7	-2.7	-0.2	+6.4	+1.6	-1.2
4L-SF-1b	-11.0	-0.4	+0.1	+2.6	-2.6	-0.1	-6.6	+3.5	-3.2
4L-SF-2b	-5.8	-0.4	+0.1	+2.6	-2.6	-0.1	+4.8	+0.6	-1.2
4L-DF-1b	-6.8	-0.2	+0.1	+2.8	-2.8	-0.3	-3.9	+1.5	-2.6
4L-DF-2b	-6.3	-0.4	+0.2	+2.7	-2.8	-0.2	+4.2	+3.1	-1.8
3L/4L combined	-5.6	-0.7	+0.3	+2.7	-2.7	-0.2	+2.7	+0.9	-1.5

6.7 Results

6.7.1 Fit strategy

Several fits are performed, following a similar prescription as to what was described in Section 5.7: first individually to each channel, and then to the combination of both channels. The 3L signal regions, 3L-Z-1b4j-PCBT and 3L-Z-2b3j-PCBT, are combined in both cases. In the 3L fit only, the ZZ+jets background is fixed to its nominal value and is allowed to vary within an uncertainty of 50%.

Given the additional uncertainties associated with the heavy-flavour composition of the WZ+jets and ZZ+jets backgrounds, corresponding nuisance parameters θ_b and θ_c are used as well as a nuisance parameter to cover the extrapolation from CR to SR, θ_e . For instance, the number of WZ+jets events in the 3L combined SR, $N(WZ)$, can be written as:

$$N(WZ) = \mu_{WZ} \cdot (1 + 0.125)^{\theta_e} \cdot \left(N(WZ + l) + (1 + 0.2)^{\theta_c} \cdot N(WZ + c) + (1 + 0.3)^{\theta_b} \cdot N(WZ + b) \right), \quad (6.1)$$

and similarly for ZZ +jets.

6.7.2 Results in the 3L channel

In the trilepton channel (combination of signal regions 3L-Z-1b4j-PCBT and 3L-Z-2b3j-PCBT), including the control region CR-WZ, the observed results are:

$$\mu_{t\bar{t}Z} = 1.21 \pm 0.07(\text{stat.})_{-0.10}^{+0.11}(\text{syst.}) = 1.21_{-0.12}^{+0.13} \quad (6.2)$$

$$\mu_{WZ} = 0.95 \pm 0.03(\text{stat.})_{-0.09}^{+0.10}(\text{syst.}) = 0.95_{-0.10}^{+0.11} \quad (6.3)$$

The post-fit event yields are given in Table 6.7. The systematic uncertainty ranking plot in Figure 6.3 shows that the uncertainty associated with the modelling of tWZ is leading in impact, followed by the parton shower and PDF scale components of the $t\bar{t}Z$ theoretical uncertainty.

Table 6.7: The post-fit event yields in the 3L channel signal regions and the WZ +jets control region for an integrated luminosity of 139 fb^{-1} after the fit to the trilepton channel only. The expected (“exp.”) and fitted (“fit.”) total SM contributions are indicated separately. Statistical and systematic uncertainties are included as described in Section 6.6.

Yields	3L-Z-2b3j-PCBT	3L-Z-1b4j-PCBT	CR-WZ
Observed	343	272	1569
Total SM (fit.)	330 ± 14	290 ± 13	1600 ± 41
$t\bar{t}Z$	250 ± 18	190 ± 15	44 ± 11
$WZ + b$	14 ± 4.9	24 ± 8.1	14 ± 4.6
$WZ + c$	1.9 ± 0.60	11 ± 2.7	210 ± 39
$WZ + l$	0.20 ± 0.20	2.2 ± 1.7	1100 ± 84
ZZ +jets	2.6 ± 1.3	4.7 ± 2.4	140 ± 71
tWZ	19 ± 7.3	22 ± 4.7	12 ± 1.9
tZ	21 ± 3.8	8.1 ± 1.7	6.3 ± 1.3
$t\bar{t}W$	4.4 ± 2.1	1.5 ± 0.70	0.70 ± 0.30
$t\bar{t}H$	2.8 ± 0.30	1.6 ± 0.20	0.50 ± 0.10
Fakes (MM)	11 ± 5.4	23 ± 11	67 ± 32
Other	1.5 ± 0.70	0.70 ± 0.40	13 ± 7.8
Total SM (exp.)	290 ± 18	280 ± 27	1700 ± 160

6.7.3 Results in the 4L channel

In the tetralepton channel (signal regions 4L-SF-1b, 4L-SF-2b, 4L-DF-1b and 4L-DF-2b), including the control region CR-ZZ, the observed results are:

$$\mu_{t\bar{t}Z} = 1.22_{-0.14}^{+0.15}(\text{stat.})_{-0.10}^{+0.11}(\text{syst.}) = 1.22_{-0.17}^{+0.19} \quad (6.4)$$

$$\mu_{ZZ} = 1.09 \pm 0.05(\text{stat.})_{-0.09}^{+0.10}(\text{syst.}) = 1.09_{-0.10}^{+0.11} \quad (6.5)$$

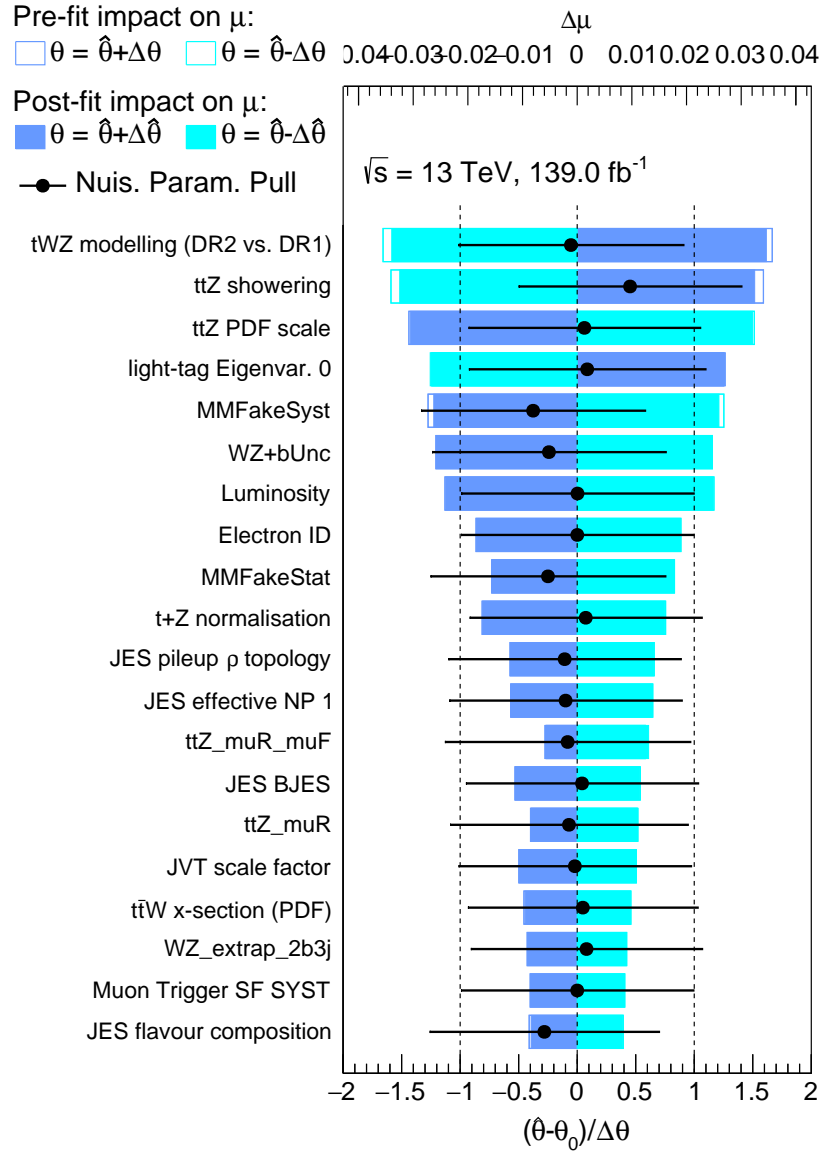


Figure 6.3: The ranking plot for the $t\bar{t}Z$ trilepton channel fit together with the WZ +jets control region.

The post-fit yields are given in Table 6.8. The systematic uncertainty ranking plot in Figure 6.4 shows that the parton shower and PDF scale components of the $t\bar{t}Z$ theoretical uncertainty have the largest impact on the measurement in the 4L channel, followed by the uncertainties on the electron identification efficiency and the normalisation of the ZZ +jets background.

6.7.4 Results of the combined $t\bar{t}Z$ fit

The combined $t\bar{t}Z$ fit includes all regions from the 3L and 4L individual fits (including CR-WZ and CR-ZZ). The observed signal strength parameter is:

$$\mu_{t\bar{t}Z} = 1.22 \pm 0.06(\text{stat.})_{-0.09}^{+0.10}(\text{syst.}) = 1.22_{-0.10}^{+0.11} \quad (6.6)$$

Table 6.8: The post-fit event yields in the 4L channel signal regions and the ZZ+jets control region for an integrated luminosity of 139 fb^{-1} after the fit to the tetralepton channel only. The expected (“exp.”) and fitted (“fit.”) total SM contributions are indicated separately. Statistical and systematic uncertainties are included as described in Section 6.6.

Yields	4L-SF-1b	4L-SF-2b	4L-DF-1b	4L-DF-2b	CR-ZZ
Observed	19	33	33	32	539
Total SM (fit.)	23 ± 1.8	36 ± 2.4	26 ± 1.8	30 ± 2.1	540 ± 23
$t\bar{t}Z$	14 ± 1.6	27 ± 2.2	19 ± 1.7	27 ± 2.2	0.77 ± 0.11
$ZZ+l$	1.7 ± 0.56	0.90 ± 0.41	0.44 ± 0.13	0.020 ± 0.010	490 ± 23
$ZZ+c$	0.95 ± 0.33	1.2 ± 0.43	0.19 ± 0.060	0.020 ± 0.010	21 ± 4.9
$ZZ+b$	1.1 ± 0.41	2.8 ± 1.1	0.23 ± 0.10	0.080 ± 0.030	15 ± 4.7
tWZ	2.6 ± 0.25	2.1 ± 0.64	3.7 ± 0.71	2.2 ± 0.68	0.10 ± 0.17
$t\bar{t}H$	0.46 ± 0.040	0.76 ± 0.070	0.56 ± 0.050	0.78 ± 0.070	$0.010 \pm 0.$
Fakes (MM)	0.70 ± 0.31	0.91 ± 0.36	0.88 ± 0.46	0.27 ± 0.13	7.9 ± 3.1
Other	0.66 ± 0.33	0.25 ± 0.12	0.71 ± 0.36	0.22 ± 0.11	0.96 ± 0.47
Total SM (exp.)	21 ± 2.4	32 ± 3.1	23 ± 2.0	26 ± 1.5	510 ± 45

The corresponding observed cross section is:

$$\sigma_{t\bar{t}Z} = 1.09 \pm 0.05(\text{stat.})_{-0.08}^{+0.09}(\text{syst.})\text{pb} = 1.09 \pm 0.10\text{pb} \quad (6.7)$$

demonstrating agreement with the most recent (NLO+NNLL) theoretical prediction [35]:

$$\sigma_{t\bar{t}Z}^{\text{theory}} = 0.863_{-0.10}^{+0.09}(\text{scale}) \pm 0.03(\text{PDF}+\alpha_s)\text{pb} \quad (6.8)$$

The ranking plot in Figure 6.5 shows that the uncertainty associated with the modelling of tWZ is leading in impact, followed by the parton shower and PDF scale components of the $t\bar{t}Z$ theoretical uncertainty. The predominance of the tWZ modelling uncertainty is expected, as the high-statistics 3L channel has a large impact on the fit due to its statistical power.

The event yields after the fit are shown in Figure 6.6 for all the 3L and 4L signal regions, as well as the two control regions, CR-WZ and CR-ZZ. A breakdown of the impact of systematic uncertainties on the combined $t\bar{t}Z$ fit is given in Table 6.9. Figure 6.7 shows the distributions of the jet multiplicity of jets with $p_T > 25 \text{ GeV}$ and the transverse momentum of the leading lepton in the 3L channel after the combined fit, and Figure 6.8 the same variables in the 4L channel.

Table 6.9: List of relative uncertainties in the measured cross sections of the $t\bar{t}Z$ process from the combined fit to all channels. The uncertainties are symmeterised and grouped into categories. The quadratic sum of the individual uncertainties may not be equal to the total uncertainty due to correlations introduced by the fit.

Uncertainty	$\Delta\sigma_{t\bar{t}Z}/\sigma_{t\bar{t}Z}$ [%]
Flavour tagging	2.8
tWZ modelling	2.7
$t\bar{t}Z$ parton shower	2.6
$t\bar{t}Z$ PDF	2.6
Fake leptons	2.5
Data-driven background normalisation	2.4
Lepton	2.2
Jets+ E_T^{miss}	2.0
Luminosity	2.0
Other backgrounds	1.2
$t\bar{t}Z$ scale	1.0
Pile-up	0.6
Total systematic uncertainty	7.6
Statistical uncertainty	5.1
Total uncertainty	9.1

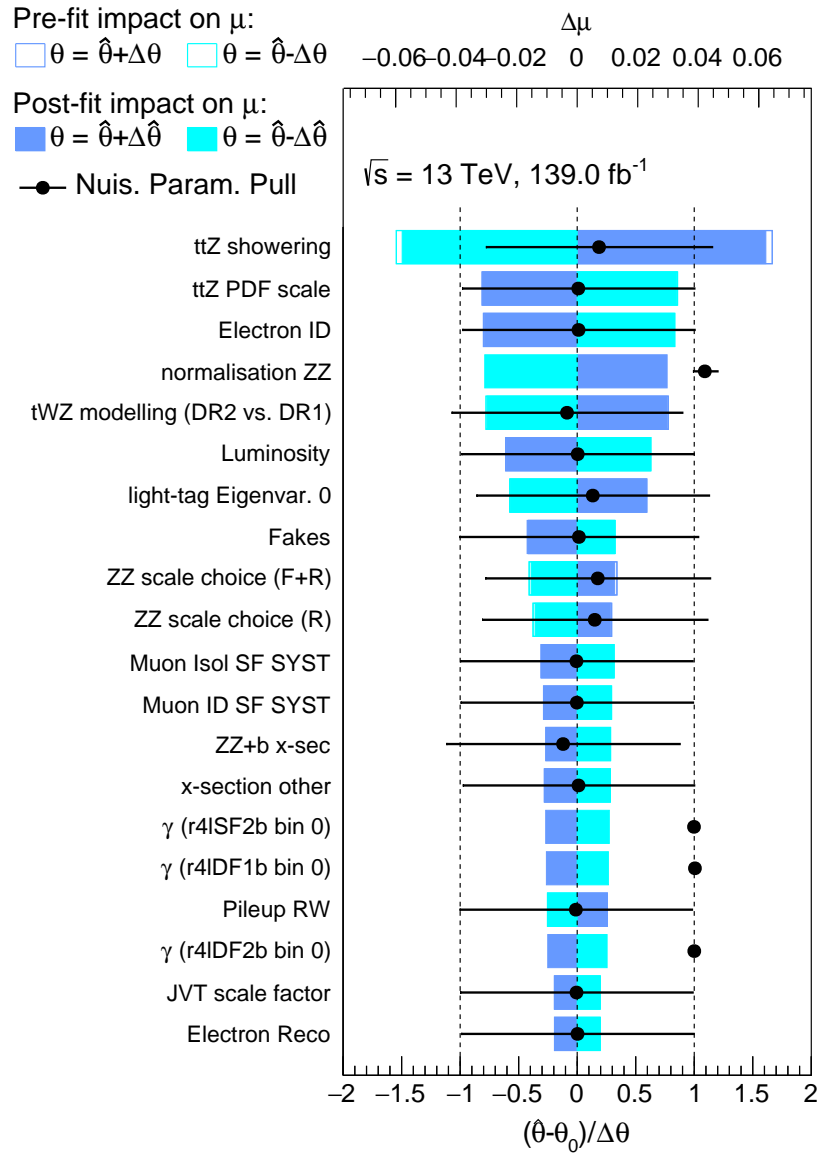
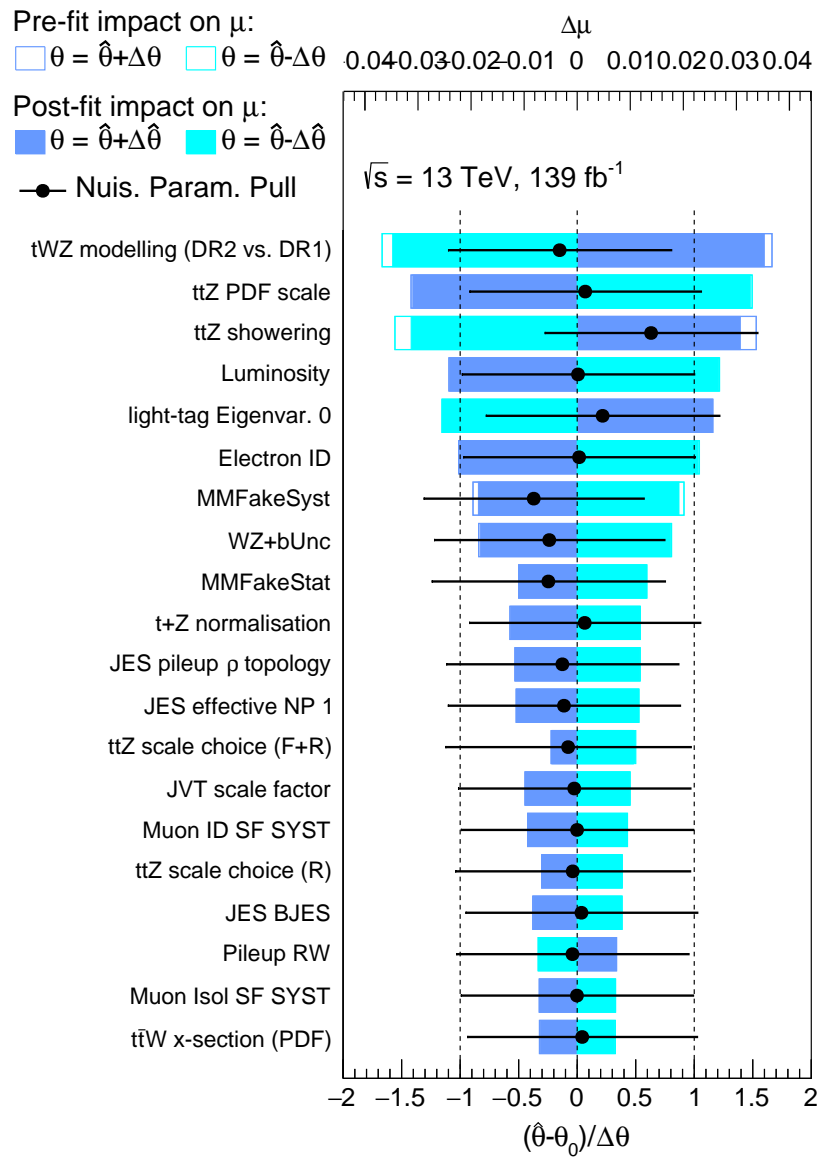


Figure 6.4: The ranking plot for the $t\bar{t}Z$ tetraelectron channel fit together with the ZZ +jets control region.

Figure 6.5: The ranking plot for the combined fit to all $t\bar{t}Z$ channels.

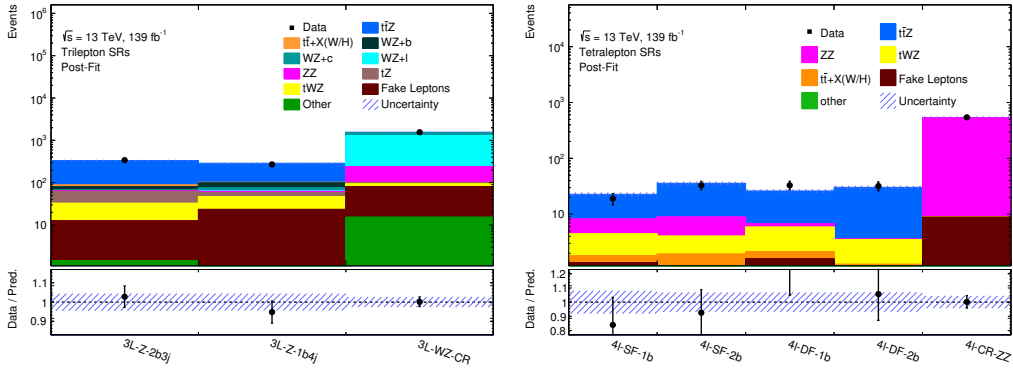


Figure 6.6: Event yields in data compared with the results of the fit that extracts $\sigma_{t\bar{t}Z}$ simultaneously in the triplepton (left) and tetralepton (right) signal regions. Yields for the control regions used to extract the normalisation of the WZ +jets and ZZ +jets backgrounds are also shown. The “Other” process contains SM processes with small cross sections producing three or four prompt leptons (e.g. $t\bar{t}H$, triboson processes). The shaded band represents the total uncertainty.

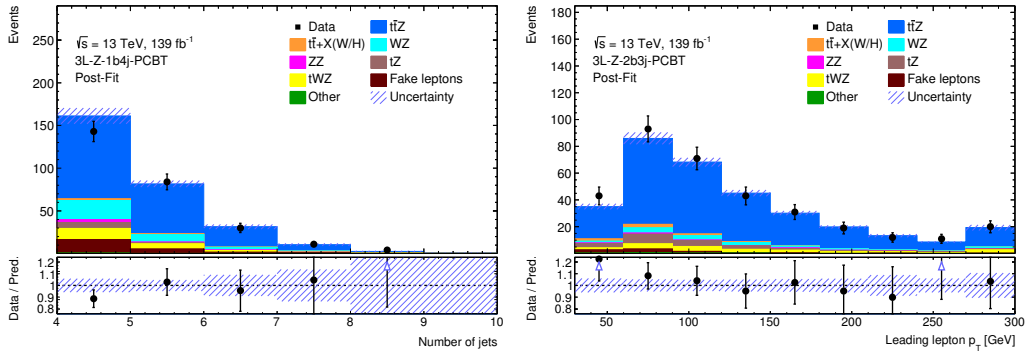


Figure 6.7: Distributions of the jet multiplicity of jets with $p_T > 25$ GeV in 3L-Z-1b4j-PCBT (left) and transverse momentum p_T of the leading lepton in 3L-Z-2b3j-PCBT (right) in the 3L channel after the combined fit to all 3L and 4L channels. The “Other” background summarises all small SM backgrounds. The shaded band represents the total uncertainty.

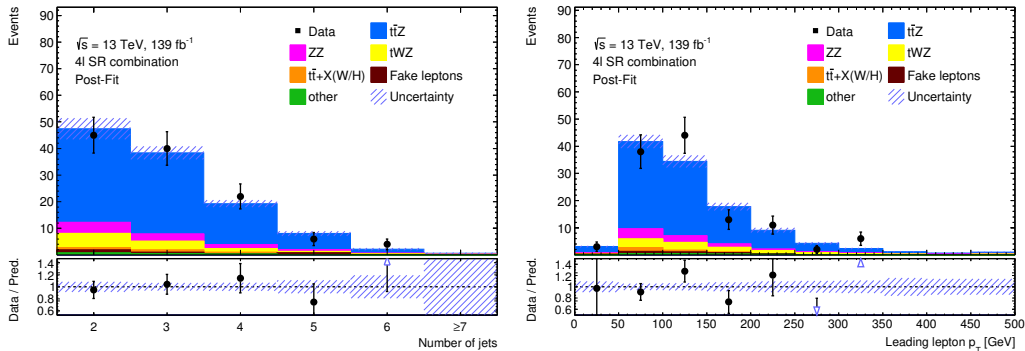


Figure 6.8: Distributions of the jet multiplicity (left) and transverse momentum p_T of the leading lepton (right) in the combination of all 4L signal regions after the combined fit to all channels. The “Other” background summarises all small SM backgrounds. The shaded band represents the total uncertainty.



7. Differential cross section measurement

In this chapter we review the differential measurement of the $t\bar{t}Z$ cross section in the multi-lepton final state using the full Run 2 dataset with 139fb^{-1} of pp collisions at $\sqrt{s} = 13\text{TeV}$. We start by motivating the choice of phase-space to unfold to and the selection of variables in Section 7.1, before describing the various tests performed (Section 7.2) before obtaining the final differential results in Section 7.3. Further results are available in Appendix A. The terminology used here was introduced in Section 4.2. The work described in what follows is the author’s main and largest contribution to the ATLAS Collaboration paper [2] covered in this and the previous chapter.

7.1 Event reconstruction and differential variables

Both the 3L and 4L channels described in Section 6.4 are used at reconstruction-level, as well as the combination of both channels. The background modelling strategy is the same as that of the inclusive measurement, and the fitted scale factors for the diboson backgrounds, μ_{WZ} and μ_{ZZ} , are used. There is only one signal region in the 3L channel, 3L-Z-2b3j; in the 4L channel, all four orthogonal signal regions are combined into one selection (through a logical OR).

7.1.1 Fiducial volumes in the 3L channel

The parton-level fiducial volume in the 3L channel is defined as the top quark pair decaying semi-leptonically ($e, \mu + \text{jets}$ only) and the Z boson decay dileptonically via $Z \rightarrow ee, \mu\mu$. Events featuring tau leptons which originate directly from either the Z (via $Z \rightarrow \tau\tau$) or the W bosons from the $t\bar{t}$ system (via $W \rightarrow \tau\nu_\tau$) are removed from the fiducial volume and are not considered for the unfolding, regardless of their subsequent decay. The differential variables are reconstructed from the top quarks after final state radiation, immediately prior to their decays. The invariant mass of the two leptons from the Z decay is required to be within 15 GeV of the m_Z value from [20].

The particle-level fiducial volume is constructed to emulate the reconstruction-level 3L-Z-2b3j inclusive region: exactly three leptons with the same p_T requirements as in Table 6.2, an *OSSF* pair

“Makalu”. Photo credits: Michał Kosmulski. © Creative Commons.

of leptons within an invariant mass at most 10 GeV away from m_Z , and at least three jets, two of which must be b -tagged (ghost-matched to a B-hadron [227]).

7.1.2 Top reconstruction in the 3L channel

The $t\bar{t}$ reconstruction of 3L events is limited to the leptonic-side top quark; no full reconstruction of the $t\bar{t}$ system is performed. This partial reconstruction allows for two variables to be used for the differential measurement: the absolute difference in rapidity between the Z boson and the leptonic-side top quark, and the absolute angular separation between the Z boson and the leptonic-side top quark in the transverse plane. Although the analogous two variables constructed from leptons alone are more straightforward, those incorporating the reconstructed leptonic-side top quark offer greater sensitivity to the underlying top quark kinematics, recognisably at the cost of degraded resolution.

For the reconstruction- and particle-level definitions of the above variables, the assumption is that the neutrino from the leptonically decaying W boson represents the dominant source of missing energy in the event. Both the magnitude and the azimuthal angle in the transverse plane of the E_T^{miss} are assigned to the neutrino directly. The invariant mass of the neutrino and the lepton not associated to the Z (referred to as the non- Z lepton), added together by means of a 4-vector sum, is set to be 80.385 GeV. The application of such a W mass constraint allows for the determination of the neutrino momentum in the z -direction ($p_{\nu z}$) via a quadratic equation of the form:

$$Ap_{\nu z}^2 + Bp_{\nu z} + C = 0, \quad (7.1)$$

which we previously solved in Section 3.4. In the above expression, the terms A , B and C depend solely on the neutrino p_T and ϕ , the fixed value of the W mass and the kinematics of the non- Z lepton. In the case that the discriminant of the equation is positive ($B^2 > 4AC$), two possible values of $p_{\nu z}$ are obtained. These two values, which give rise to two unique candidate neutrino 4-vectors, are both considered for the subsequent step.

For a certain fraction of events, the values of A , B and C will be such that the discriminant of the quadratic equation is negative, yielding no real solutions. This was found to be roughly 35% in the case of simulated signal $t\bar{t}Z$ events. In such cases the E_T^{miss} (or, equivalently, the assigned neutrino p_T) can be decreased in incremental steps of 100 MeV until such time as a single solution for $p_{\nu z}$ can be found; this is equivalent to solving analytically for the value of p_T which yields a non-negative discriminant ($B^2 = 4AC$).

The single neutrino candidate (or pair of neutrino candidates where applicable) is then combined with a jet in order to form the reconstructed top quark candidate. For the reconstruction-level definition of the variables, only the two jets with the highest b -tagging output weight are considered; the jet which gives the smallest ΔR separation from the given $\ell\nu$ system is selected. Since the $\Delta R(W, \text{jet})$ criterion is applied separately for the two neutrino solutions (where applicable), it is possible that the selected jets for the two candidate neutrinos differ. In the case of the particle-level definition the same procedure is applied, but for the jet selection, only those jets in the event which have been ghost-matched to B-hadrons from the truth record are considered. Since the particle-level fiducial volume for 3L requires at least two such jets, there could in principle be events with additional ghost-matched b -jets; in such rare cases only the leading two jets, ordered in p_T , are considered.

An output weight from the leptonic-side top quark reconstruction is defined based on the invariant mass distribution from correctly reconstructed top quarks in simulated $t\bar{t}Z$ events ($m_{b\ell\nu}$); the reconstructed top quarks used to fill the distribution are formed from the parton-level neutrino and the reconstruction-level lepton and jet matched to the corresponding parton-level objects. In this sense, the weighting function represents the idealised distribution one could hope to achieve

with a perfect assignment of reconstruction- to parton-level objects, barring any residual corrections to the object kinematics. Such an approach was adopted over the use of a χ^2 variable in order to account for the asymmetric and non-Gaussian nature of the distribution.

For events with two possible top quark candidates, the two invariant masses are assigned an output weight based on the interpolation of the $m_{b\ell\nu}$ distribution described above. The top quark with an invariant mass most consistent with a leptonically decaying top quark is selected; the other solution, where applicable, is not considered at any later point.

7.1.3 Fiducial volumes in the 4L channel

The parton-level fiducial volume in the 4L channel is defined as a top quark pair decaying dileptonically ($ee, e\mu, \mu\mu$ only) and the Z boson decaying via $Z \rightarrow ee, \mu\mu$. As in the case of the tripleton fiducial volume, events featuring tau leptons from the decays of either the Z or W bosons, are removed. The invariant mass of the two leptons from the Z decay is also required to be within 15 GeV of the m_Z value from [20].

Similarly, the particle-level fiducial definitions mimic those of the combination of 4L signal regions at reconstruction-level in Table 6.3: exactly 4 leptons (with the same p_T requirements as in Table 6.3), making up one **OSSF** pair (Z candidate) and one **OS** pair (leptons from the $t\bar{t}$ system), and at least two jets, including one b -jet (through ghost-matching).

7.1.4 $t\bar{t}$ reconstruction in the 4L channel

In the tetralepton channel a reconstruction of the $t\bar{t}$ system is performed, but in the transverse plane only. The underlying assumption is that the two neutrinos from the $t\bar{t}$ decay represent the only source of missing transverse momentum in the event; the E_T^{miss} can therefore be taken to be a reasonable proxy for the vector sum of the neutrino momenta in the ϕ -plane.

Such a partial reconstruction avoids having to determine the full kinematics of the two neutrinos separately, while still allowing for two of the variables used for the differential measurement: the transverse momentum of the $t\bar{t}$ system, and the absolute azimuthal separation between the $t\bar{t}$ system and the Z boson.

In order to perform the reconstruction, it is necessary to identify the lepton pair associated with the Z boson, and the lepton pair associated with the top quark pair and both b -jets.

The selection of the two b -jets is different at particle- and reconstruction-level. At reconstruction-level, the two jets with the highest b -tagging weight are considered to be the b -jets from the top quark pair. In case of exactly one b -jet at particle-level, the jet with the highest p_T (from the collection of remaining jets) is considered to be the other b -jet from the top quark pair. Where at least two b -jets are available, the leading two in p_T are selected.

For both the reconstruction- and particle-level definitions, the transverse missing energy is added in a vector sum in the ϕ -plane to the two charged leptons not associated to the Z boson and the two selected jets, to yield a candidate vector for the transverse momentum of the $t\bar{t}$ system.

7.1.5 Definition of differential variables

Table 7.1 summarises the definitions of the variables used for the unfolding in order to perform a differential cross section measurement. Two of the variables, namely the transverse momentum and the absolute rapidity of the Z boson, are defined for the orthogonal combination of 3L and 4L events, whereas other variables are considered only in the individual channels. In the remainder of this chapter, we will focus only on these two Z kinematic variables. The results for all other variables can be found in Appendix A.

The number of reconstructed jets is defined only at reconstruction- and particle-level. Furthermore, since the nominal number of jets expected from the leading-order $t\bar{t}Z$ process differs

between the 3L and 4L channels, the N_{jets} variable is treated separately in each, rather than taking the combination of both channels.

The motivation for the set of variables outlined in Table 7.1 is outlined briefly in what follows. The transverse momentum of the non- Z lepton in the 3L channel provides a good test of the p_{T} modelling of the top quarks and the hard-scatter decay products in the MC generator. It is also sensitive to the modelling of initial- and final-state radiation. The p_{T} of the leptonic-side top quark itself probes the same underlying physics – there one gains additional sensitivity to the modelling of top quark kinematics, but at the cost of degraded resolution due to jet energy response- and resolution-related effects, as well as the combinatorial and reconstruction effects introduced from the choice of N_{jets} assignment and the unknown neutrino 4-vector. Since other variables also involve the reconstructed top quark, the non- Z lepton p_{T} is here preferred over the full top quark p_{T} . The absolute azimuthal and rapidity separations between the Z boson and the leptonic-side top quark in the 3L channel, the absolute azimuthal separation between the $t\bar{t}$ system and the Z boson in the 4L channel, and the combined-channel variables involving the Z kinematics, all directly probe the SM $t\bar{t}Z$ vertex and their distributions therefore offer sensitivity to a number of non-SM effects which could modify the top- Z coupling (as made explicit in Section 1.1.3).

The jet multiplicity is a natural variable in order to provide comparisons between different generator models as well as models of the parton-shower and hadronisation.

In the 4L channel, the transverse momentum of the $t\bar{t}$ system, similarly to the p_{T} of the non- Z lepton above, offers sensitivity to the generator modelling for the hard-scatter process as well as ISR and FSR, and the effect of various MC shower tunes. The same is the case for the absolute angular separation between the two leptons from the $t\bar{t}$ system, which in addition offers sensitivity to possible non-SM effects which could modify the spin-correlation between the two top quarks.

Table 7.1: Observables defined for the differential measurements. The direct Z kinematics, measured in the combination of the 3L and 4L channels, are the focus of this chapter.

Variable	Definition	Region
N_{jets}	Number of selected jets with $p_{\text{T}} > 25\text{GeV}$ and $ \eta < 2.5$	3L
$p_{\text{T}}^{\ell_{\text{non-Z}}}$	Transverse momentum of the lepton not associated with the Z boson	3L
$ \Delta\phi(Z, t_{\text{lep}}) $	Absolute angular separation between the Z boson and the leptonic-side top quark	3L
$ \Delta y(Z, t_{\text{lep}}) $	Absolute rapidity separation between the Z boson and the leptonic-side top quark	3L
N_{jets}	Number of selected jets with $p_{\text{T}} > 25\text{GeV}$ and $ \eta < 2.5$	4L
$ \Delta\phi(\ell_t^+, \ell_{\bar{t}}^-) $	Absolute angular separation between the two leptons from the reconstructed $t\bar{t}$ system	4L
$p_{\text{T}}^{t\bar{t}}$	Transverse momentum of the reconstructed $t\bar{t}$ system	4L
$ \Delta\phi(t\bar{t}, Z) $	Absolute angular separation between the Z boson and the reconstructed $t\bar{t}$ system	4L
$ y^Z $	Absolute rapidity of the Z boson	3L+4L
p_{T}^Z	Transverse momentum of the Z boson	3L+4L

7.2 Unfolding tests

The unfolding of the selected differential variables consists in the inversion of the corresponding migration matrices through the iterative Bayesian procedure described in Section 4.2.4. A number of tests are performed to validate the method and are the focus of this section. For simplicity, only

examples related to the two Z kinematic variables in the combination of the 3L and 4L channels, p_T^Z and $|y^Z|$, will be shown.

We start by defining an algorithm to extract the best possible choice of binning for each variable, before fixing the regularisation of this particular unfolding method: the number of iterations. Closure tests are performed to assess possible biases, while MC- and data-driven stress tests gauge the ability of the unfolding procedure to return the correct unfolded spectra. The impact of limited MC statistics is also discussed. Finally, alternative unfolding methods are checked and shown to underperform the current choice of **IBU**.

7.2.1 Binning optimisation

A binning optimisation algorithm has been designed, taking into account two main effects of the investigated choice of binning: the statistical uncertainty in each bin, and the diagonal elements of the migration matrix for each observable. For a given input setting of the maximum desired statistical uncertainty and minimum accepted value of the elements along the diagonal of the migration matrix, the algorithm returns viable configurations between 3 and 10 bins. A scan is performed among several such input requirements: from 30% to 50% (in steps of 10%) for the maximum uncertainty, and from 50% to 90% (in steps of 5%) for the diagonal elements. The final decision of binning is ultimately left to the discretion of the analyser, based on further considerations such as the physical motivation of a given binning solution for a particular observable, the impact on the pull tests (described below) or simply the final number of bins.

The algorithm proceeds as follows: starting with a fine binning of the variable being considered, the bins are merged from left to right (or vice-versa, depending on the shape of the reconstruction-level signal distribution) recursively, until both requirements are satisfied. Once the current coarse bin meets those requirements, its range is fixed and the algorithm proceeds to merge the next series of fine bins into coarse ones. It may happen that the final few fine bins (extreme left or right) are not sufficient to produce a validated coarse bin; nonetheless they are merged together (sub-optimally) for the final result. It is often the case that, in those sub-optimal cases, the analyser takes the decision to merge them into the neighbouring validated bin.

Table 7.2 below reports the final choice of binning for all observables considered in the differential analysis. Although independent bin ranges could be used for the particle- and parton-level measurements, they are here kept the same for simplicity (assuming insignificant differences in the final result).

7.2.2 Number of iterations

To optimise the number of iterations (the regularisation parameter of **IBU**) used in the unfolding for each variable at particle- and parton-level, the entire signal $t\bar{t}Z$ MC sample is used to derive migration matrices and efficiency and acceptance corrections. The reconstruction-level distribution is smeared bin-wise according to Poisson statistics to form a pseudo-experiment; 10,000 pseudo-experiments are generated in this way. Each pseudo-experiment is unfolded with up to ten iterations. After each iteration, the unfolded result in each pseudo-experiment is compared to that of the previous iteration (for the first iteration, to the truth distribution) and a χ^2/NDF discriminant is computed. The convergence of this series of χ^2/NDF values, averaged over pseudo-experiments, as well as the relative unfolding uncertainty (the statistical uncertainty on the unfolded result, after error propagation through the **IBU** equations in Section 4.2.4) averaged over bins and pseudo-experiments, is reported in Figure 7.1.

The optimal number of iterations for a given observable (at particle- and parton-level independently) is determined from a combination of low statistical uncertainty and stabilised χ^2/NDF . Table 7.3 summarises the findings of this test. Hereafter, the optimised number of iterations for each variable is used in all further tests, as well as in the final differential results.

Table 7.2: Optimised bin ranges for each observable to be unfolded in the differential measurement of the $t\bar{t}Z$ cross section.

Variable	Binning	
N_{jets}	[3,4,5,10]	3 bins
$p_{\text{T}}^{\ell^{\text{non-Z}}}$	[0,40,65,105,500] GeV	4 bins
$ \Delta\phi(Z, t_{\text{lep}}) $	[0,0.34,0.82,1]	3 bins
$ \Delta y(Z, t_{\text{lep}}) $	[0,0.57,1.8,4.5]	3 bins
N_{jets}	[2,3,4,5,7]	4 bins
$ \Delta\phi(\ell_t^+, \ell_{\bar{t}}^-) $	[0,0.31,0.59,0.80,1]	4 bins
$p_{\text{T}}^{t\bar{t}}$	[0,67,140,236,600] GeV	4 bins
$ \Delta\phi(t\bar{t}, Z) $	[0,0.73,0.93,1]	3 bins
$ y^Z $	[0,0.10,0.25,0.42,0.64,0.84,1.08,1.33,2.50]	8 bins
p_{T}^Z	[0,40,70,110,160,220,290,1000] GeV	7 bins

Table 7.3: Optimal number of iterations derived for each variable using the iterative unfolding method.

Variable	Particle	Parton
N_{jets}	4	–
$p_{\text{T}}^{\ell^{\text{non-Z}}}$	3	3
$ \Delta\phi(Z, t_{\text{lep}}) $	4	5
$ \Delta y(Z, t_{\text{lep}}) $	4	5
N_{jets}	4	–
$ \Delta\phi(\ell_t^+, \ell_{\bar{t}}^-) $	2	3
$p_{\text{T}}^{t\bar{t}}$	3	4
$ \Delta\phi(t\bar{t}, Z) $	5	5
$ y^Z $	3	3
p_{T}^Z	3	3

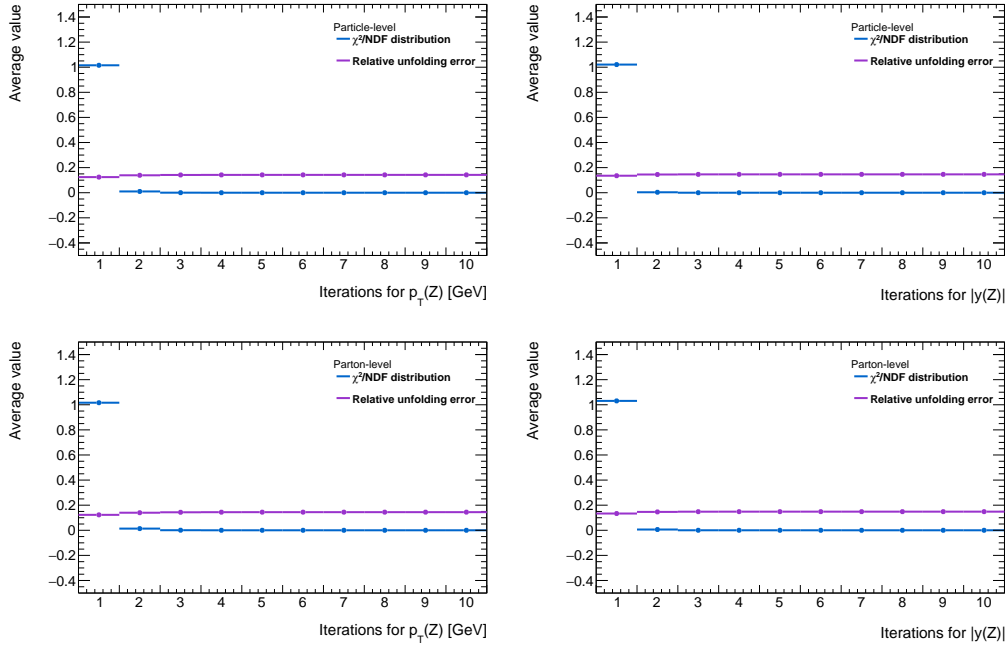


Figure 7.1: Particle-level (top row) and parton-level (bottom row) summary plots for the test of the number of iterations for the observables p_T^Z (left) and $|y^Z|$ (right) in the combined 3L and 4L channels.

7.2.3 Closure tests

The goal of the closure tests is to demonstrate that the **IBU** algorithm is able to correctly unfold data which are fluctuated around their nominal values. Similar pseudo-experiments as described for the test of the number of iterations are used. For each bin i of a given observable and each pseudo-experiment j , the pull p_i^j is computed as

$$p_i^j = \frac{x_i^j - t_i}{\sigma(x_i^j)}, \quad (7.2)$$

where x_i^j denotes the unfolded value in bin i for pseudo-experiment j , t_i the corresponding generator-level bin content and $\sigma(x_i^j)$ the uncertainty on x_i^j . Examples of such pull distributions are shown in Figure 7.2, together with a line of best fit to a Gaussian function. Summary plots are then produced by displaying the fitted pull mean and widths as a function of the bin number, as in Figure 7.3.

In Figure 7.2 it is visible that the Gaussian fit is an imperfect approximation to the pull distribution, which exhibits a more populated tail in the left than in the right. This was found to be caused by limited statistics in the 4L signal regions in particular. Fitting these shapes with a normal Gaussian function results in slightly shifted mean and width values. This is explicitly apparent in Figure 7.3, where the pull mean in each bin is consistently lower than zero. To better understand this non-Gaussianity, we first consider a simple toy MC example.

Towards a modified pull definition

If there are no acceptance and efficiency corrections to apply (assumed to be identically unity), and the migration matrix is diagonal, the unfolding is trivial. The unfolded spectrum should by construction agree with the generator-level distribution. When the reconstructed spectrum is first

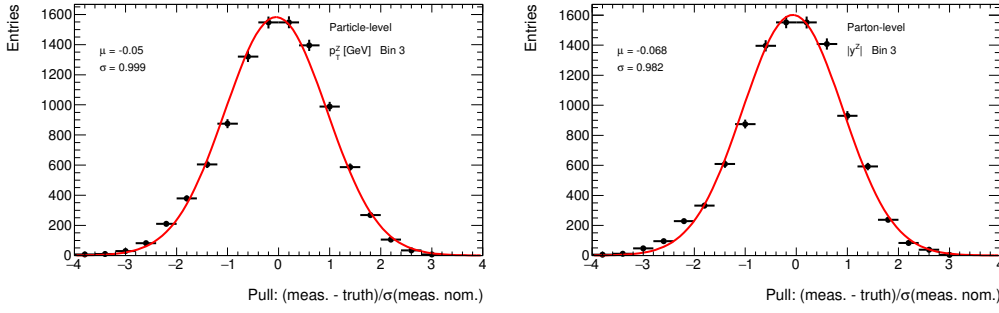


Figure 7.2: Example of pull distributions for the third bin of p_T^Z at particle-level (left) and $|y^Z|$ at parton-level (right). The solid red line corresponds to the fitted Gaussian function.

smearing according to Poisson statistics in a large enough number of pseudo-experiments, the resulting unfolded spectrum for each bin will inherit the same smeared shape as at reconstruction-level. Thus the unfolded spectrum will also follow Poisson statistics.

For a large number of events in each bin, the underlying Poisson distribution converges, to a good approximation, to a Gaussian one. This assumption is however challenged in the 4L channel, where ~ 15 events are expected in each bin. A simple toy MC is thrown, by generating 10^6 random numbers distributed around a Poisson distribution with parameter $\lambda = 15$. This example is shown in Figure 7.4, together with a Gaussian fit. Using the pull definition from (7.2), we first note that subtracting the generator-level component does not affect the shape of this toy distribution but simply shifts it by a constant value across all pseudo-experiments. The source of any shape differences must then lie in the denominator of this pull definition, namely the uncertainty on the unfolded value. For our toy MC, this uncertainty is simply \sqrt{x} , and is indeed the cause of the overpopulated left tail of the pull distributions in Figure 7.2.

This overpopulation effect in the tails is mitigated by large bin contents, as is shown in the bottom right plot of Figure 7.4. To remove this effect altogether, we can substitute the pseudo-experiment-dependent denominator term $\sigma(x_i^j)$ in (7.2) for a comensurate but constant one: the bin-wise uncertainty after unfolding of the nominal (unsmeared) distribution, $\sigma(x_i^{\text{nom}})$. The modified pull definition is then

$$P_i^j = \frac{x_i^j - t_i}{\sigma(x_i^{\text{nom}})}, \quad (7.3)$$

and is applied to our toy MC in Figure 7.5, which demonstrates the expected pull behaviour: a mean close to zero and a width close to one, indicative of no bias and properly estimated uncertainties.

A further complication arises upon transitioning from this toy model to the physical MC samples. For low bin contents, following non-Gaussian Poisson statistics, the discreteness of the resulting pseudo-experiments would yield highly binning-dependent pull fit results. The off-diagonal elements of the migration matrix, together with the acceptance and efficiency corrections, cause additional smearing in the unfolded spectrum, ultimately producing spikes in the pull distribution, that broaden with degrading migration matrix. This is clearly shown in Figure 7.6 for the variable $|y^Z|$, which enjoys a highly diagonal migration matrix. The variable N_{jets} is also shown to illustrate a substantially less diagonal migration matrix.

To avoid an extraction of inappropriate values of the pull mean and width from a Gaussian fit, these values are rather calculated as the arithmetic mean μ and root mean square error σ from the set of all pull values, following standard definitions:

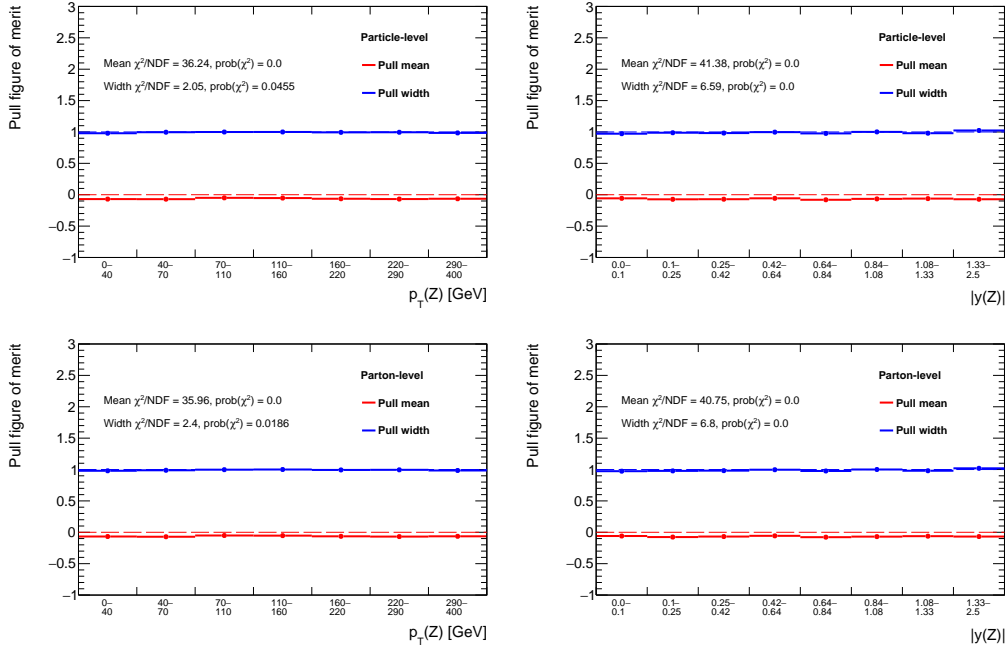


Figure 7.3: Particle-level (top row) and parton-level (bottom row) plots summarising the fitted pull mean and width in each bin of the observables p_T^Z (left) and $|y^Z|$ (right) in the combined 3L and 4L channels.

$$\mu = \frac{1}{N} \sum_{i=1}^N x_i \quad (7.4)$$

$$\sigma = \sqrt{\frac{1}{N} \sum_{i=1}^N (x_i - \mu)^2} \quad (7.5)$$

Using the modified pull definition of (7.3) and a direct calculation of its mean and width, the results originally presented in Figure 7.3 are corrected in Figure 7.7, demonstrating that the unfolding procedure is stable with respect to fluctuations in data.

Closure tests using independent datasets

In order to exclude any bias in the unfolding introduced by using the same MC sample for both building the migration matrix and deriving the acceptance and efficiency corrections, as well as for the input reconstruction- and generator-level distributions, the full MC sample is randomly split into two halves (statistically independent subsets). These two statistically independent datasets are then used for the same (updated) closure test described in the previous subsection. The first half of the events, used for constructing the migration matrix and calculating the extrapolation corrections, is referred to as the *training sample*, while the remaining half, from which the reconstruction-level distribution is taken, as the *testing sample*.

Reconstruction-level distributions from the testing sample are smeared according to Poisson statistics and unfolded. The summary pull plots based on this test are depicted in Figure 7.8. These plots exhibit a significant deviation from zero for the pull means, which would typically suggest that the unfolding is biased. However, this was found to be yet another effect of limited MC statistics. Indeed, the ratio of nominal distributions at reconstruction-level, shown in Figure 7.9 seem to be

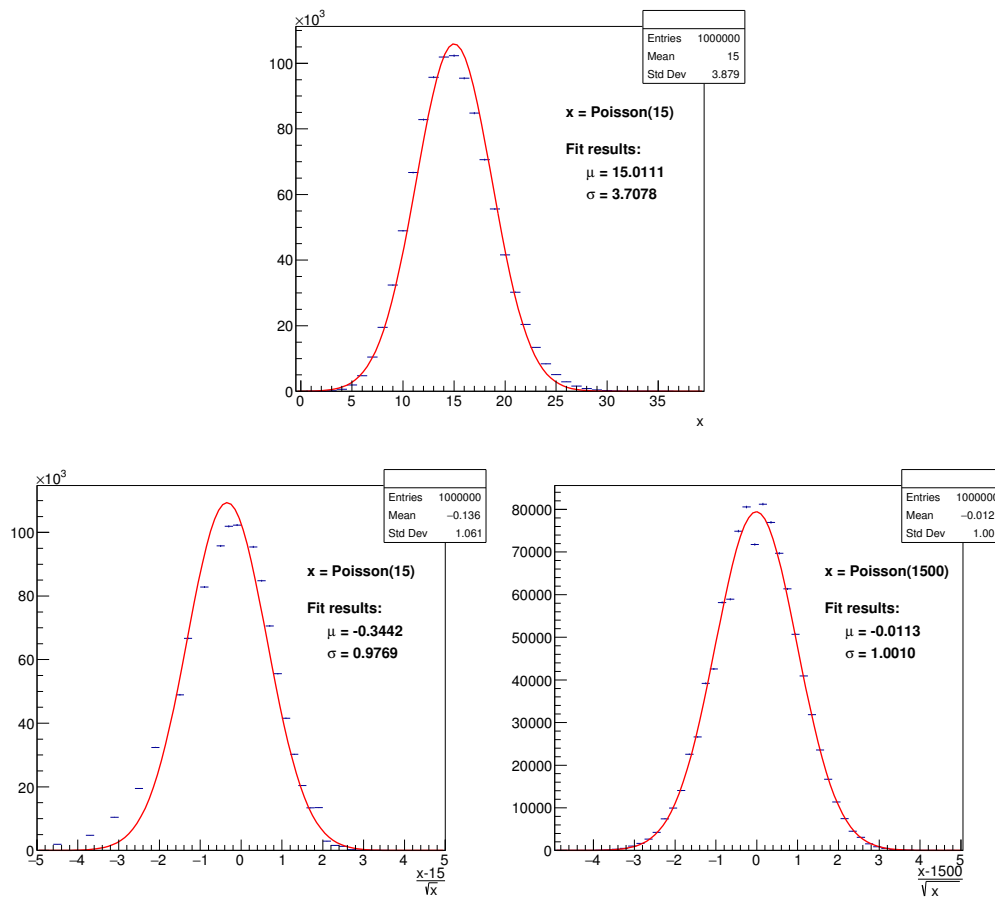


Figure 7.4: 10^6 random numbers are drawn following a Poisson distribution with parameter $\lambda = 15$ (top). The corresponding pull distribution is obtained by subtracting the generator-level contribution and dividing by the uncertainty on the unfolded bin content (bottom left). The procedure is repeated for a different choice of parameter, $\lambda = 1500$ (bottom right). Gaussian fits are displayed as a solid red line.

strongly correlated to these variations in the pull means. This suggests not an inherent bias but an effect of the choice of training and testing samples, and will be studied further in the next section.

7.2.4 Impact of limited MC statistics

Since the signal MC has only a limited number of events, the statistical uncertainty of the MC has to be taken into account. The statistical fluctuations in MC have an effect on migration matrices, efficiency and acceptance corrections, most notably causing the non-closure effects observed in the preceding subsection. In order to estimate this non-closure, the following test is performed.

As in the previous subsection, the MC signal sample is randomly split into two parts of equal size, defining a training and a testing sample. Pseudo-experiments are generated from Poisson smearing of the reconstruction-level testing distribution. The mean value of the relative difference between the unfolded quantity and the underlying generator-level distribution, “(unfolded-truth)/truth”, is computed over a million pseudo-experiments. This entire process for 2,000 random seeds, i.e. 2,000 different random splittings of the signal MC sample.

The RMS of the resulting distribution of means of relative differences described above is an estimate of the expected MC statistical uncertainty for a particular bin and observable. These are summarised in Table 7.4. An example of such distributions is shown in Figure 7.10, specifically in

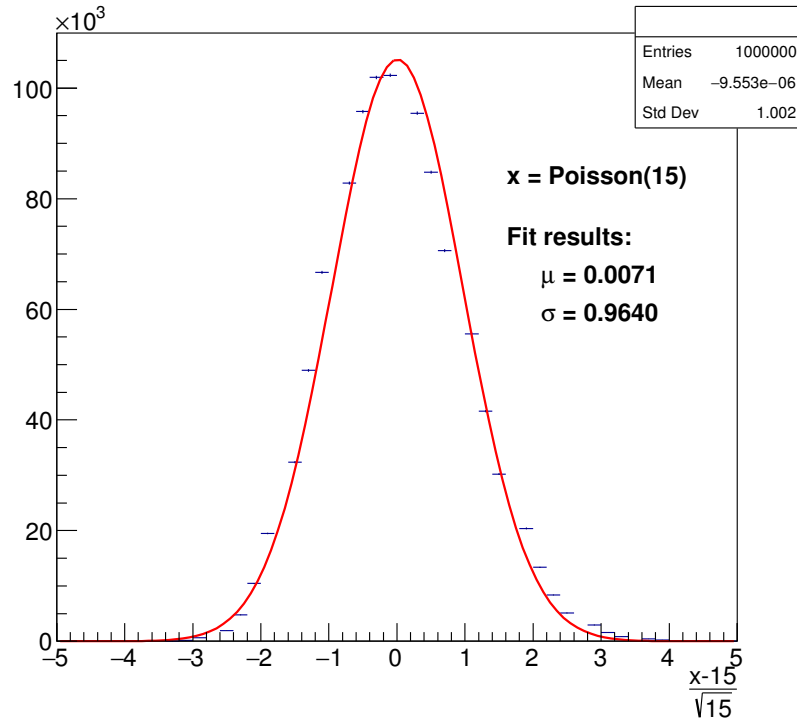


Figure 7.5: 10^6 random numbers are drawn following a Poisson distribution with parameter $\lambda = 15$. The corresponding pull distribution is obtained by subtracting the generator-level contribution and dividing by the uncertainty expected from the nominal value, following the updated definition of (7.3). A Gaussian fit is displayed as a solid red line.

the eighth and final bin of the $|y^Z|$ variable in the combined 3L and 4L channels. The non-closure effect is significantly (factor 10) smaller than the statistical uncertainty of the unfolded result and is therefore not considered further since it cannot have any appreciable effect on the final result of this measurement.

7.2.5 Stress tests

Two different kinds of *stress tests* are performed, which aim at demonstrating the non-closure of the unfolding procedure under significant shape variations of the generator-level distribution. The motivation for this study is clear: if the data were to present very differently from the nominal $t\bar{t}Z$ MC sample, we would expect the output of the unfolding to reflect these discrepancies, rather than be biased towards the MC ground truth. The full signal MC sample is used to extract the migration matrix, and the corresponding reconstruction- and generator-level distributions are reweighted according to the prescriptions below. The resulting unfolded spectrum is then compared to the reweighted generator-level one.

The first set of bin-wise scale factors, S_i , is derived from the observed difference between data and MC at reconstruction-level:

$$S_i = \pm \frac{\text{data}_i - \text{bkgMC}_i}{\text{signalMC}_i}, \quad (7.6)$$

effectively providing two sets of variations to ensure sensitivity to any asymmetric effects. The results of these data-driven stress tests are shown in Figure 7.11 for the differential variables in

Table 7.4: Estimate of the non-closure caused by the limited number of events in the signal Monte Carlo sample for the observables $|y^Z|$ and p_T^Z in the combined 3L and 4L channels. The RMS numbers are given both at particle- and parton-level, and expressed in percent.

Variable	Bin	RMS (particle)	RMS (parton)
$ y^Z $	1	2.2	2.5
	2	1.9	2.1
	3	1.8	2.0
	4	1.6	1.8
	5	1.8	2.0
	6	1.7	1.9
	7	1.9	2.2
	8	1.4	1.6
p_T^Z	1	2.1	2.4
	2	1.8	2.0
	3	1.5	1.6
	4	1.4	1.6
	5	1.6	1.7
	6	2.0	2.2
	7	1.9	2.0

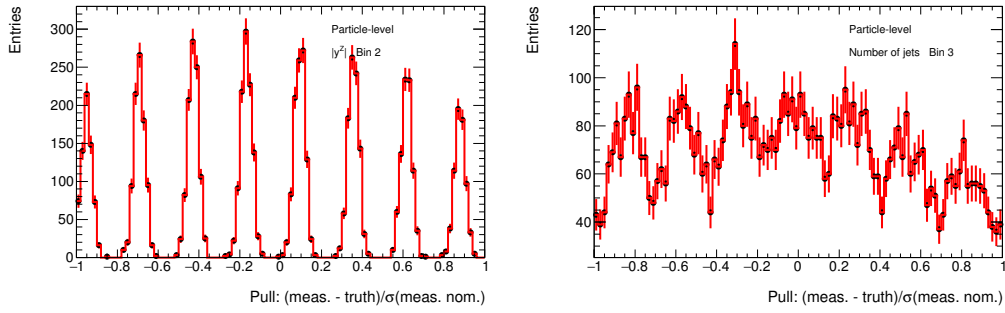


Figure 7.6: Particle-level pull distributions with 10,000 pseudo-experiments for the second bin of the $|y^Z|$ (left) and the third bin of the N_{jets} (right) observables in the 4L channel. The clearly visible spikes correspond to discrete values which become less pronounced after being smeared in the unfolding by the non-diagonal migration matrix.

the combined 3L and 4L channels. They demonstrate a good ability of the unfolding procedure to describe fluctuations of the signal shape in data.

A second set of scale factors is computed so as to provide a linear skewness in the generator-level distribution, with the extreme bins weighted by $\pm 20\%$ or $\pm 40\%$, thereby providing four distinct sets of variations. The results of this second test are displayed in Figure 7.12. As expected, we note a degradation of the ability of the unfolded spectrum to track large enough deviations in the true signal shape.

7.2.6 Alternative unfolding methods

The default unfolding approach to measure the differential $t\bar{t}Z$ cross section is the iterative Bayesian method (IBU) described in Section 4.2.4. Alternative prescriptions exist, such as the bin-by-bin method [268], which doesn't take into account migrations between bins and is only suitable when those are around or below 5%, the singular value decomposition (SVD) scheme [269], another popular regularised unfolding technique, or a simple (unregularised) matrix inversion. A comparison of these three alternatives to the nominal IBU results is shown in Figure 7.13 for the observables pertaining to the combined 3L and 4L channels.

The bin-by-bin and matrix inversion approaches are straightforward and don't employ any regularisation; we however note that the regularisation parameter of the SVD unfolding presented here is not necessarily properly optimised, but has been taken to be half the number of bins in a given observable, a usual choice.

In the case of high-statistics, pure leptonic observables, such as p_T^Z and $|y^Z|$ in the combined 3L and 4L channels, the bin-by-bin algorithm seems almost appropriate in all bins, thanks to the low amount of migration between them. This is however not the case in most other observables, and hence this approach was not selected for global use. The SVD method, although not properly regularised, seems to yield reasonable results in most bins and also benefit from largely reduced uncertainties. Again, this results from the large elements along the diagonals of the migration matrices for these two observables, and doesn't hold in general. It would however be interesting to study the differences between the properly optimised IBU and SVD approaches in future work on measuring the differential cross section of the $t\bar{t}Z$ process. We should also point out that the figure of merit here is matrix inversion, as the only unbiased estimator (by construction). The IBU distributions are indeed able to track the ones obtained by matrix inversion very accurately and offer some improvement in statistical uncertainties while maintaining very low bias.

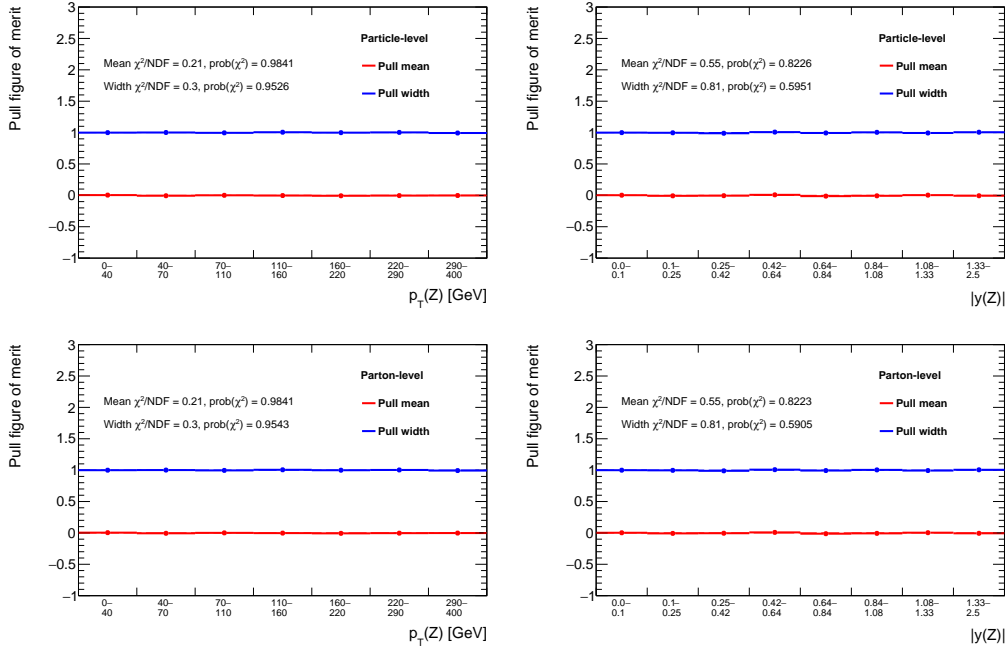


Figure 7.7: Particle-level (top row) and parton-level (bottom row) plots summarising the fitted pull mean and width in each bin of the observables p_T^Z (left) and $|y^Z|$ (right) in the combined 3L and 4L channels, using the modified pull definition of (7.3).

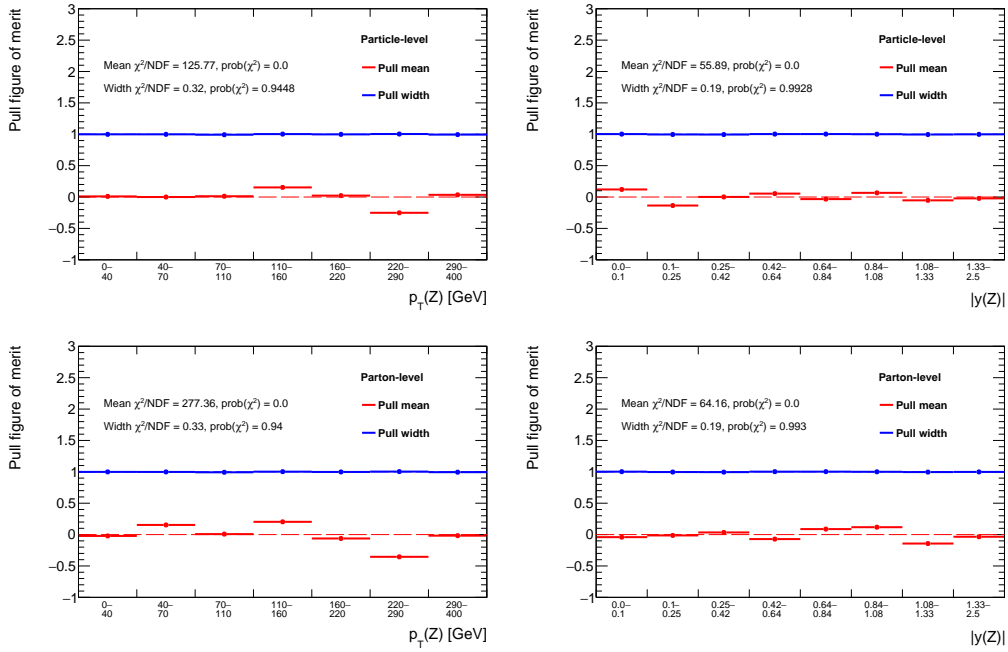


Figure 7.8: Particle-level (top row) and parton-level (bottom row) plots summarising the fitted pull mean and width in each bin of the observables p_T^Z (left) and $|y^Z|$ (right) in the combined 3L and 4L channels, using the modified pull definition of (7.3) and a random splitting of the MC between training and testing samples.

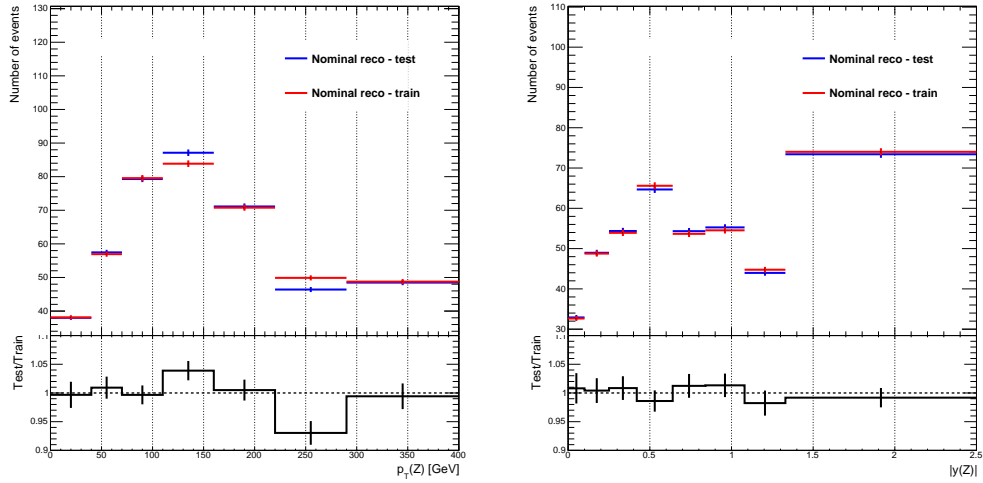


Figure 7.9: Comparison of reconstruction-level distributions in the training and testing samples for the observables p_T^Z (left) and $|y^Z|$ (right) in the combined 3L and 4L channels. The bottom panels show the ratio of these distributions and are to be compared to the means of the pull tests presented in Figure 7.8.

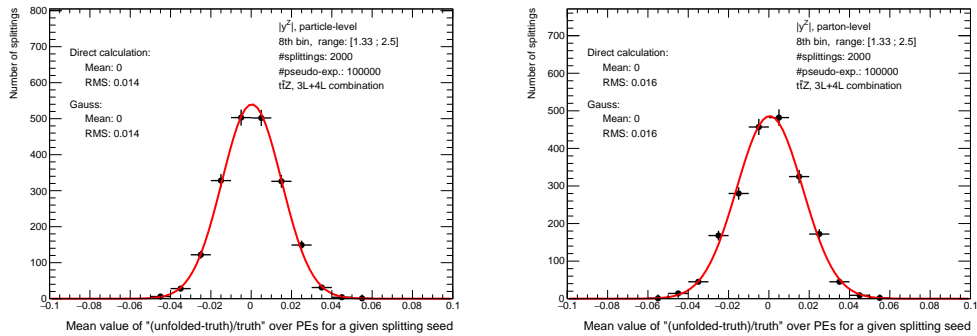


Figure 7.10: Example of distributions of the average relative difference between the unfolded and the underlying generator-level bin contents obtained from 100,000 pseudo-experiments (PEs) for a given splitting seed in the eighth bin of the $|y^Z|$ variable in the combined 3L and 4L channels, at particle- (left) and parton-level (right). The quoted RMS values are taken to represent the amount to which one can expect non-closure in this bin due to the limited MC statistics.

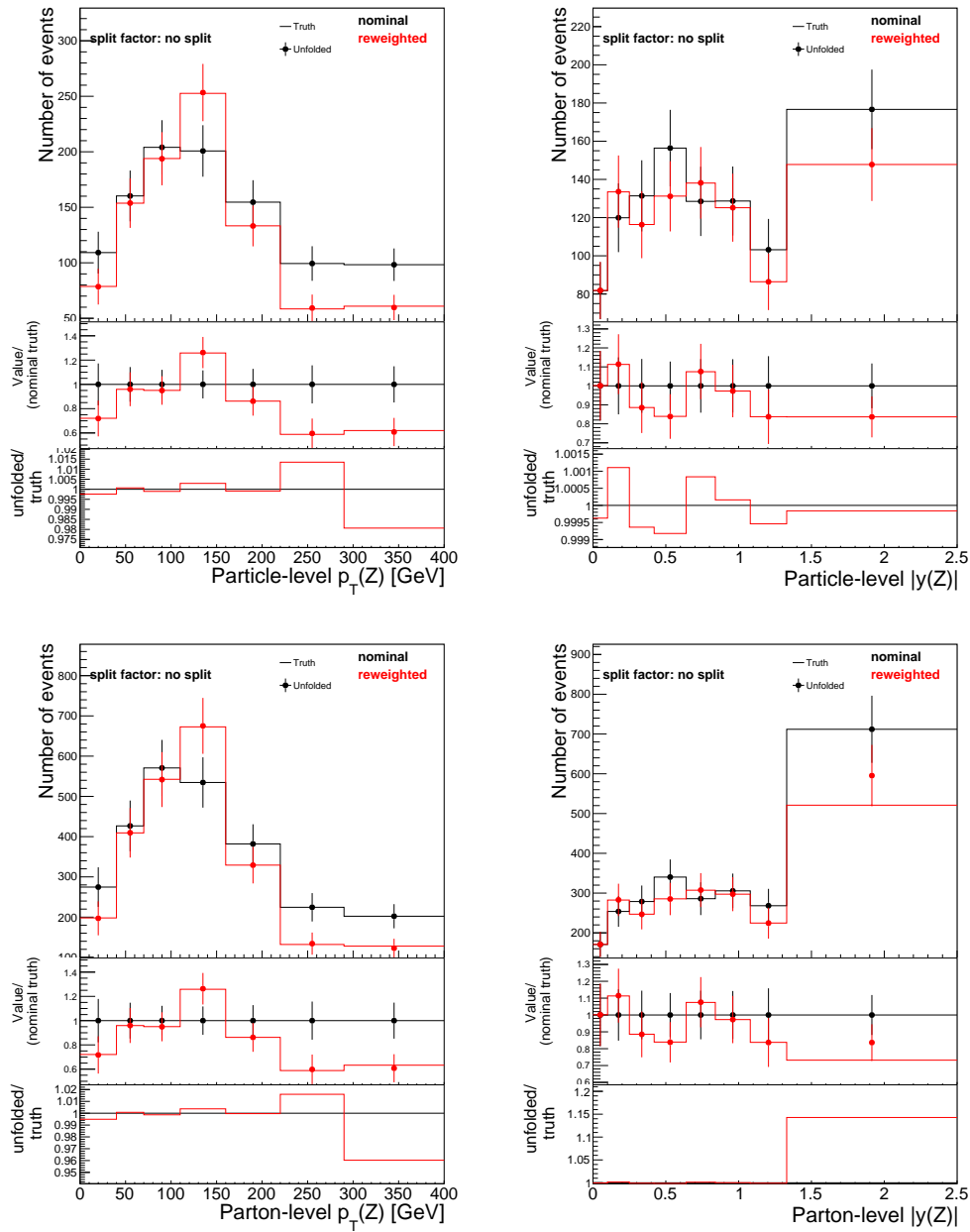


Figure 7.11: Results of the data-driven stress tests for the unfolding to particle- (top) and parton-level (bottom) of the p_T^Z (left) and $|y^Z|$ (right) observables in the combined 3L and 4L channels.

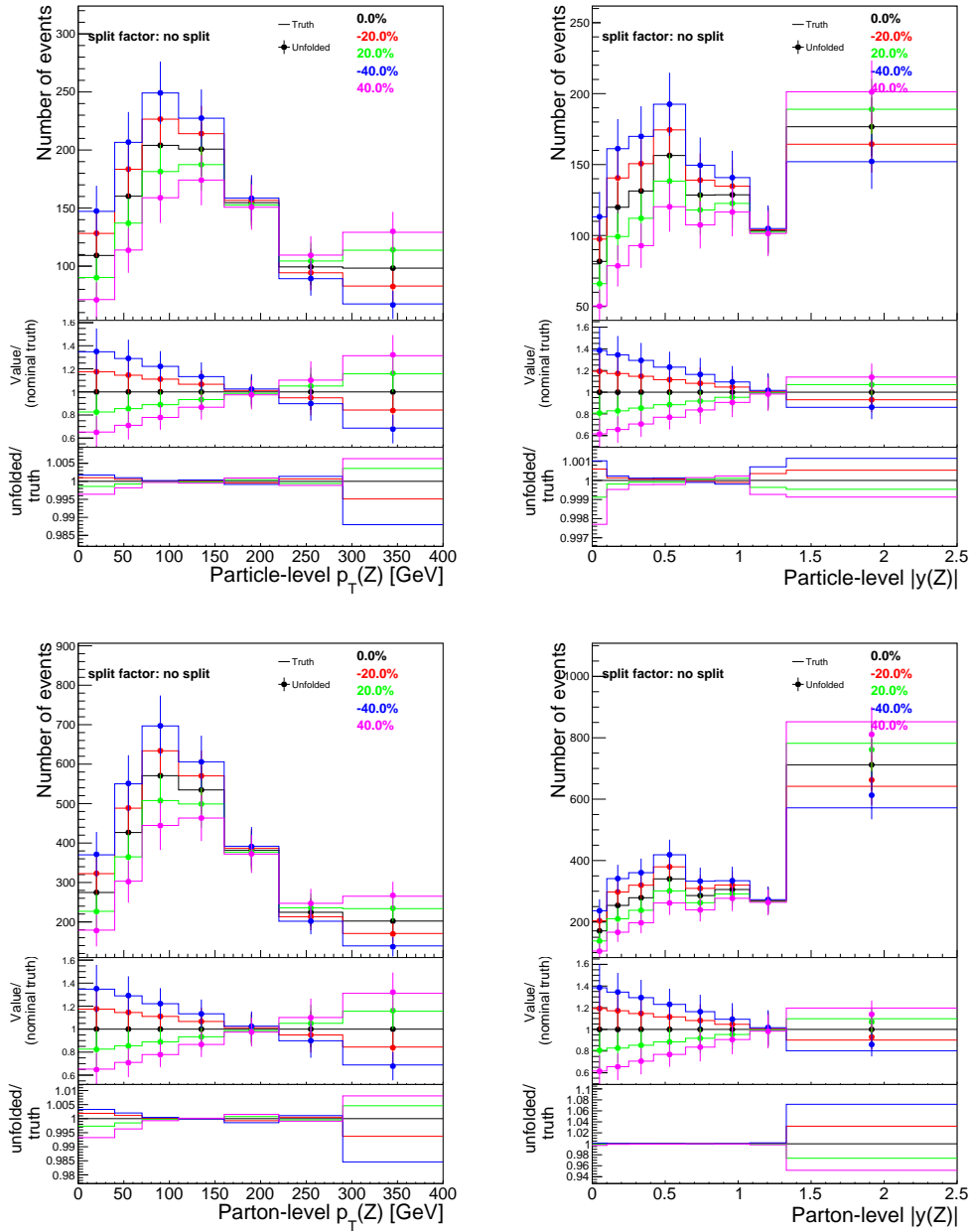


Figure 7.12: Results of the MC-driven stress tests (linear reweighting) for the unfolding to particle-level (top) and parton-level (bottom) of the p_T^Z (left) and $|y^Z|$ (right) observables in the combined 3L and 4L channels.

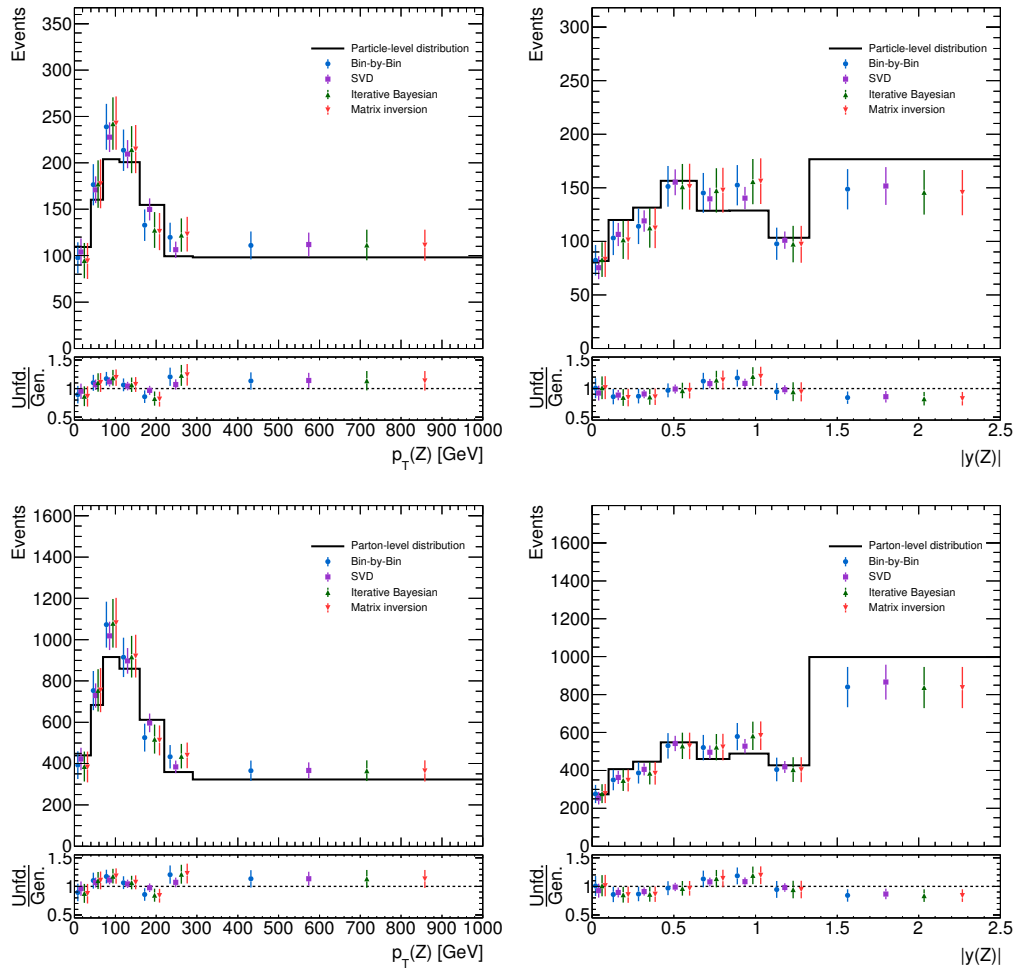


Figure 7.13: Comparison of various techniques in obtaining signal MC spectra unfolded to particle-level (top) and parton-level (bottom) of the p_T^Z (left) and $|y^Z|$ (right) observables in the combined 3L and 4L channels. Uncertainties are statistical only.

7.3 Results

In this section we present the final results of the measurement of the differential $t\bar{t}Z$ cross section in the combined 3L and 4L channels. Reconstruction-level distributions, migration matrices and efficiency and acceptance corrections at particle- and parton-level are shown in Figures 7.14 and 7.15 for the p_T^Z and $|y^Z|$ observables respectively. Figures 7.16 and 7.17 are the corresponding absolute and normalised differential cross sections at particle- and parton-level, while Figures 7.18 and 7.19 give a breakdown of the impact of statistical and systematic uncertainties.

In the differential cross section plots, the unfolded data is compared to the generator-level distributions of various MC signal samples: the nominal $t\bar{t}Z$ MADGRAPH5_aMC@NLO 2.3.3 +PYTHIA 8 used to perform the unfolding, as well as the SHERPA 2.2.1 NLO (“inclusive”) and NLO+LO (“multi-leg”) samples described in Section 6.6.

The results corresponding to the other variables listed in Table 7.1 are given in Appendix A.

7.3.1 Compatibility between observation and prediction

In order to quantify the overall compatibility between the unfolded measurements and the nominal MADGRAPH5_aMC@NLO + PYTHIA 8 predictions, a χ^2/NDF (together with corresponding p -value) is evaluated for each of the differential variables. All uncertainties are considered to be Gaussian in nature. The χ^2 is defined as:

$$\chi^2 = \sum_{i=1}^{N_{\text{bins}}} \sum_{j=1}^{N_{\text{bins}}} (n_i - \mu_i) (n_j - \mu_j) C_{ij}^{-1}, \quad (7.7)$$

where n_i and μ_i correspond to the content in bin i of the distributions from the unfolded data and the prediction, respectively, and C_{ij}^{-1} to the element in row i and column j of the inverse of the covariance matrix for the particular variable.

The covariance matrix is constructed as the linear sum of $N_{\text{bins}} \times N_{\text{bins}}$ matrices corresponding to the N_{sys} individual systematic source of uncertainty, as well as that for the unfolded data:

$$C_{ij} = C_{ij}^{\text{data,unfolded}} + \sum_{k=1}^{N_{\text{sys}}} C_{ij}^k, \quad (7.8)$$

Sources of theoretical uncertainty on the $t\bar{t}Z$ signal are not included in the sum. In general each of the matrices in the linear sum will contain off-diagonal terms, including the matrix associated with the unfolded data, where non-diagonal contributions are introduced during the unfolding process. The bin-to-bin correlations for the nominal signal are evaluated using a bootstrap technique and shown in Figure 7.20 for the combined 3L and 4L channels. These correlations are applied to all systematic sources as well as the unfolded data, such that the elements of the covariance matrix for systematic source k are given by

$$C_{ij}^k = \rho_{ij}^{\text{nominal}} \cdot \sigma_i^k \cdot \sigma_j^k \quad (7.9)$$

In the above σ_i^k and σ_j^k are the uncertainties evaluated for bin i and j , and $\rho_{ij}^{\text{nominal}}$ the corresponding correlation coefficient from the nominal signal $t\bar{t}Z$ sample. Only small differences were observed when the bin-to-bin correlations are set to unity for all systematic sources.

Table 7.5 summarises the χ^2/NDF and p -values based on comparisons to the nominal signal sample. The overall level of compatibility between the spectra from measured unfolded data and the nominal predictions is seen to be good for all variables considered. The poorest p -values are obtained for both the particle- and parton-level normalised cross-section measurements for the $|\Delta\phi(Z, t_{\text{lep}})|$ variable in the trilepton channel.

Region	Variable	Particle-level				Parton-level			
		Absolute cross section		Normalised cross section		Absolute cross section		Normalised cross section	
		χ^2/NDF	p -value	χ^2/NDF	p -value	χ^2/NDF	p -value	χ^2/NDF	p -value
3L	N_{jets}	0.50/3	0.918	0.76/2	0.684	—	—	—	—
	$p_{\text{T}}^{\ell, \text{non-Z}}$	0.06/4	>0.999	0.80/3	0.849	0.06/4	>0.999	0.60/3	0.897
	$ \Delta\phi(Z, t_{\text{lep}}) $	1.00/3	0.801	3.92/2	0.141	1.04/3	0.792	4.12/2	0.128
	$ \Delta y(Z, t_{\text{lep}}) $	0.47/3	0.925	0.32/2	0.851	0.49/3	0.922	0.41/2	0.813
4L	N_{jets}	0.06/4	>0.999	0.33/3	0.955	—	—	—	—
	$ \Delta\phi(\ell_t^+, \ell_{\bar{t}}^-) $	<0.01/4	>0.999	0.63/3	0.890	<0.01/4	>0.999	0.68/3	0.879
	$ \Delta\phi(t\bar{t}, Z) $	0.01/3	>0.999	0.47/2	0.790	0.03/3	0.999	0.76/2	0.684
	$p_{\text{T}}^{t\bar{t}}$	0.69/4	0.953	0.08/3	0.994	0.59/4	0.964	0.08/3	0.994
3L+4L	p_{T}^Z	1.42/7	0.985	1.87/6	0.931	1.46/7	0.984	2.06/6	0.914
	$ y^Z $	<0.01/8	>0.999	0.13/7	>0.999	<0.01/8	>0.999	0.19/7	>0.999

Table 7.5: Summary of the compatibility tests between the measured differential $t\bar{t}Z$ spectra and the nominal MADGRAPH5_aMC@NLO + PYTHIA 8 prediction. Quoted are the χ^2/NDF and corresponding p -values incorporating all bins for the given variable and based on the assumption that all sources of statistical or systematic uncertainty are Gaussian in nature.

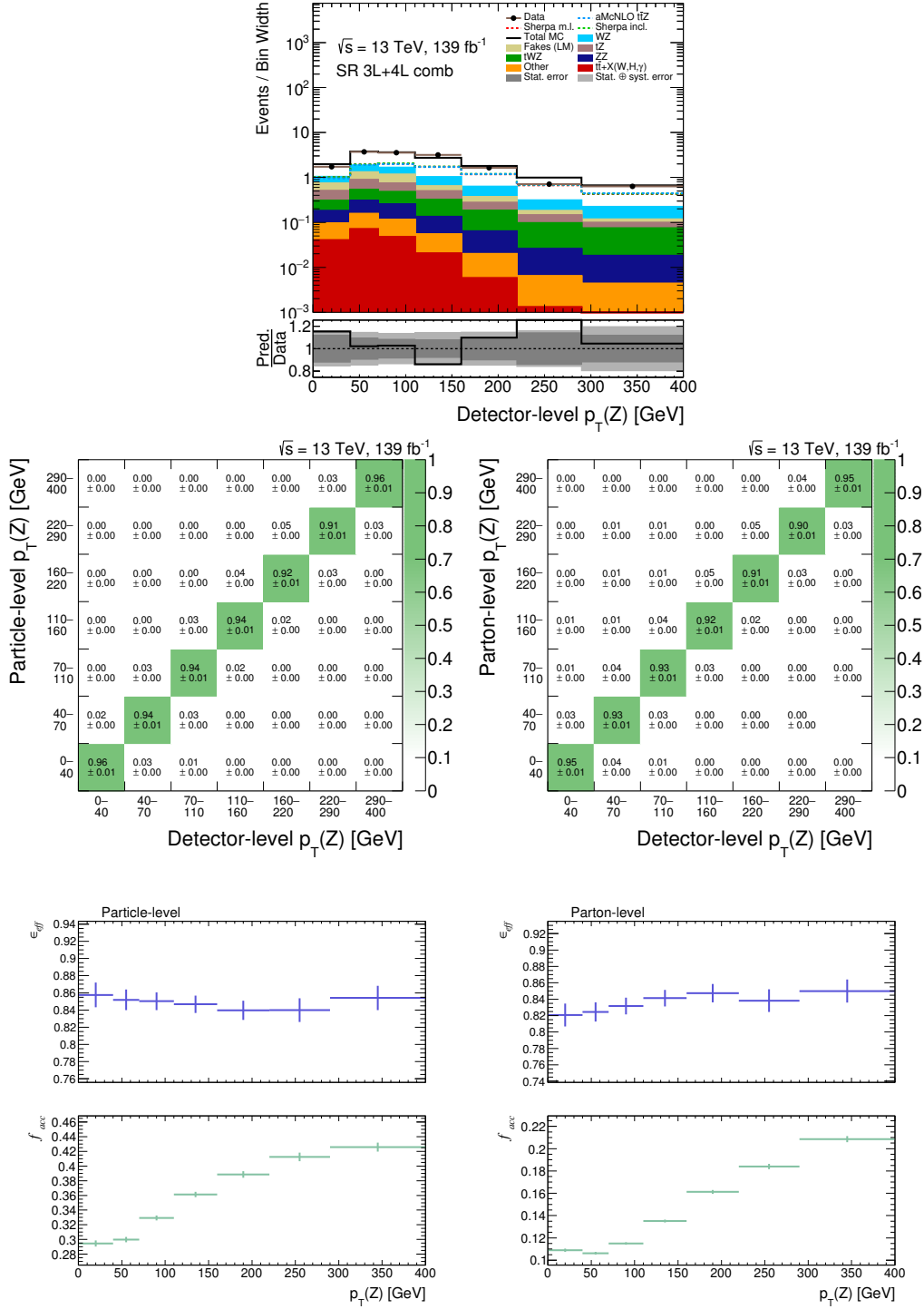


Figure 7.14: Reconstruction-level distribution (top), migration matrices (middle) and efficiency and acceptance corrections (bottom) at particle- (left) and parton-level (right), for the p_T^Z variable in the combined 3L and 4L channels. In the top figure, the solid black line corresponds to the sum of the contributions from background processes (coloured filled areas) and the nominal $t\bar{t}Z$ MADGRAPH5_aMC@NLO sample (white filled area). This $t\bar{t}Z$ contribution is further represented (unstacked) as a dashed blue line, to allow comparison with the alternative generator setups: SHERPA inclusive (dashed green line) and SHERPA multi-leg (dashed red line).

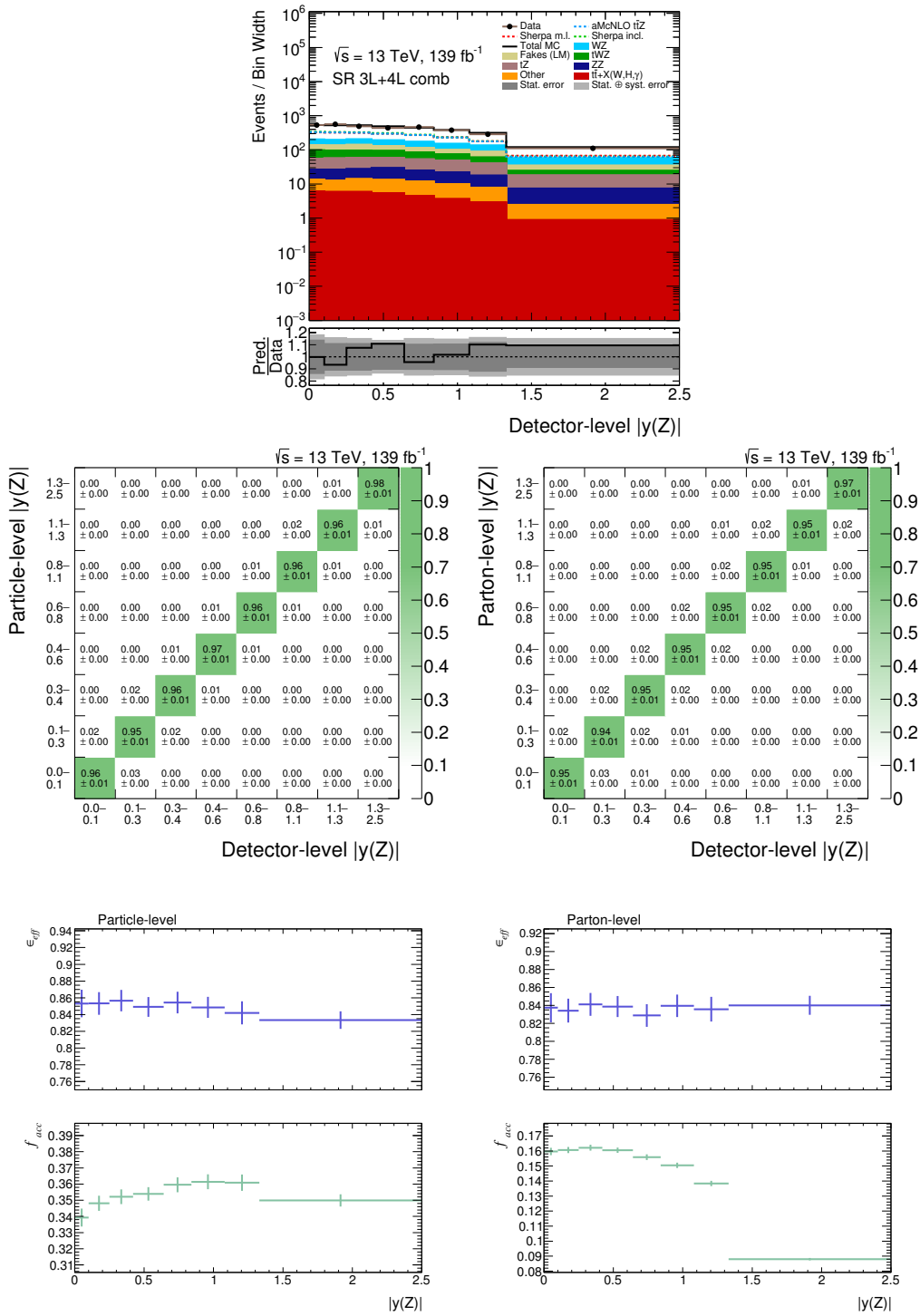


Figure 7.15: Reconstruction-level distribution (top), migration matrices (middle) and efficiency and acceptance corrections (bottom) at particle- (left) and parton-level (right), for the $|y^Z|$ variable in the combined 3L and 4L channels.

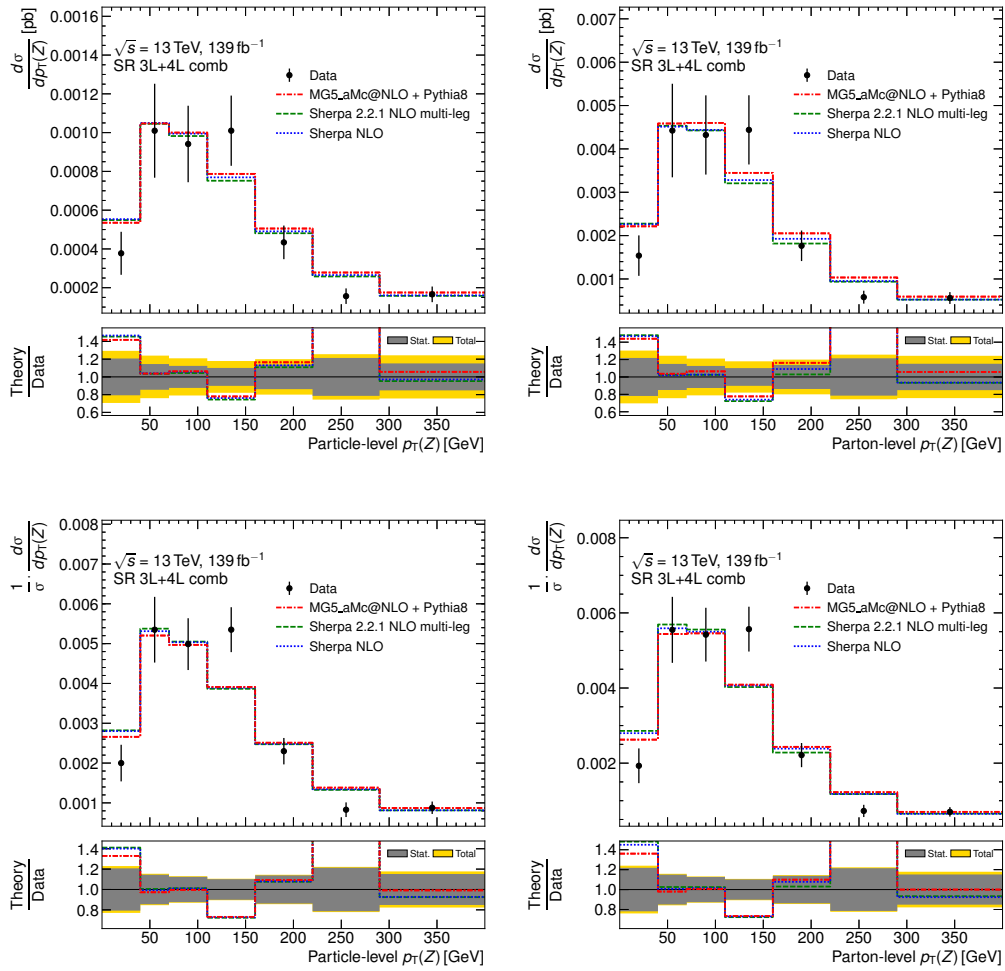


Figure 7.16: Data distributions for the p_T^Z variable in the combined 3L and 4L channels, unfolded to particle- (left) and parton-level (right), absolute (top) and normalised (bottom).

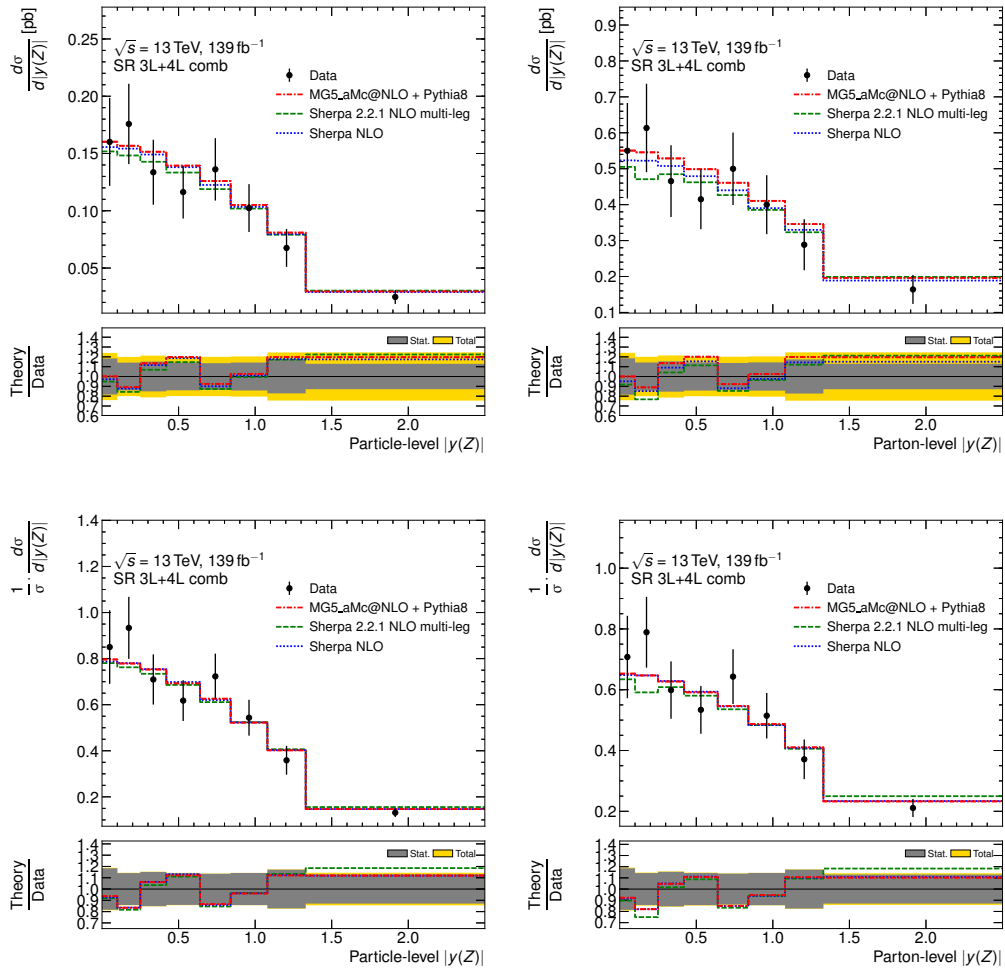


Figure 7.17: Data distributions for the $|y^Z|$ variable in the combined 3L and 4L channels, unfolded to particle- (left) and parton-level (right), absolute (top) and normalised (bottom).

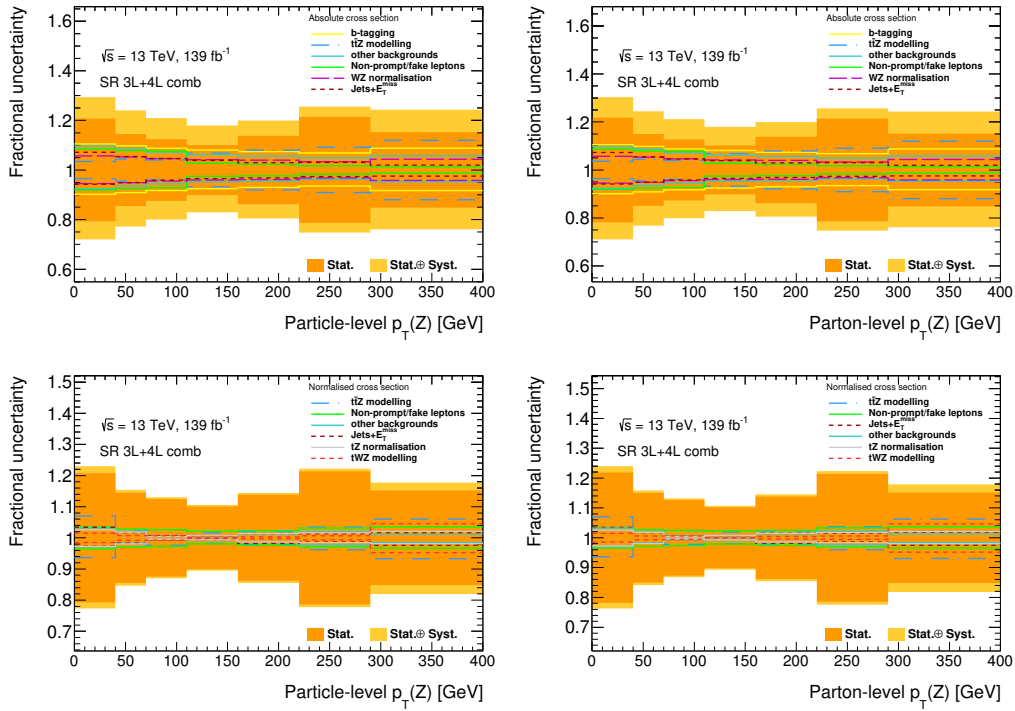


Figure 7.18: Fractional decomposition of statistical and systematic uncertainties for the p_T^Z variable in the combined 3L and 4L channels, unfolded to particle- (left) and parton-level (right), absolute (top) and normalised (bottom).

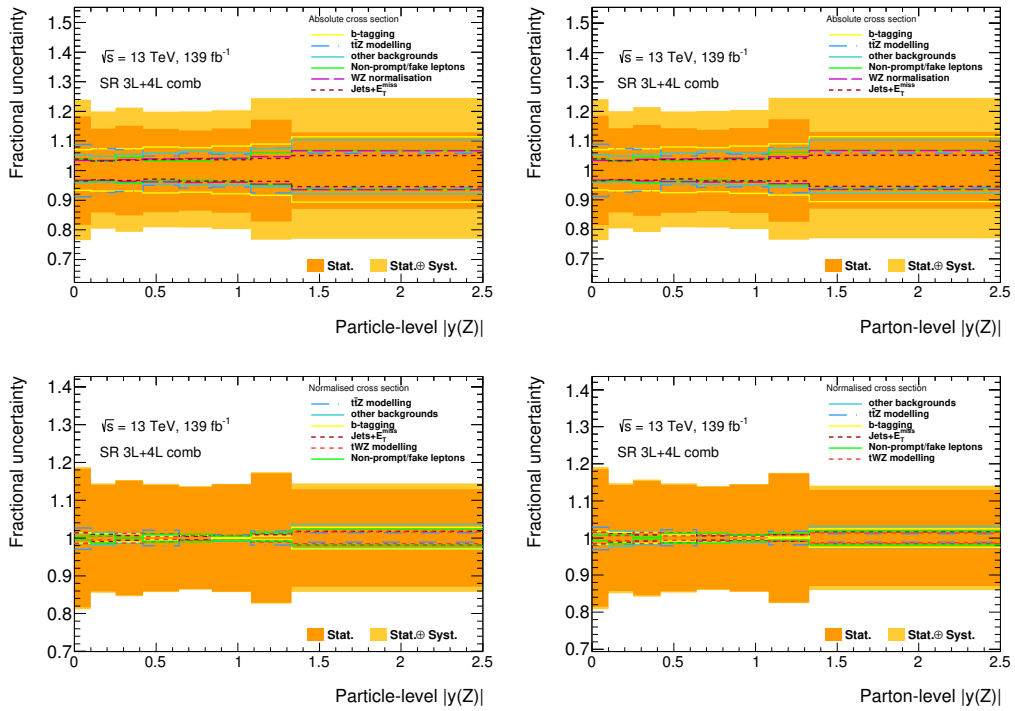


Figure 7.19: Fractional decomposition of statistical and systematic uncertainties for the $|y^Z|$ variable in the combined 3L and 4L channels, unfolded to particle- (left) and parton-level (right), absolute (top) and normalised (bottom).

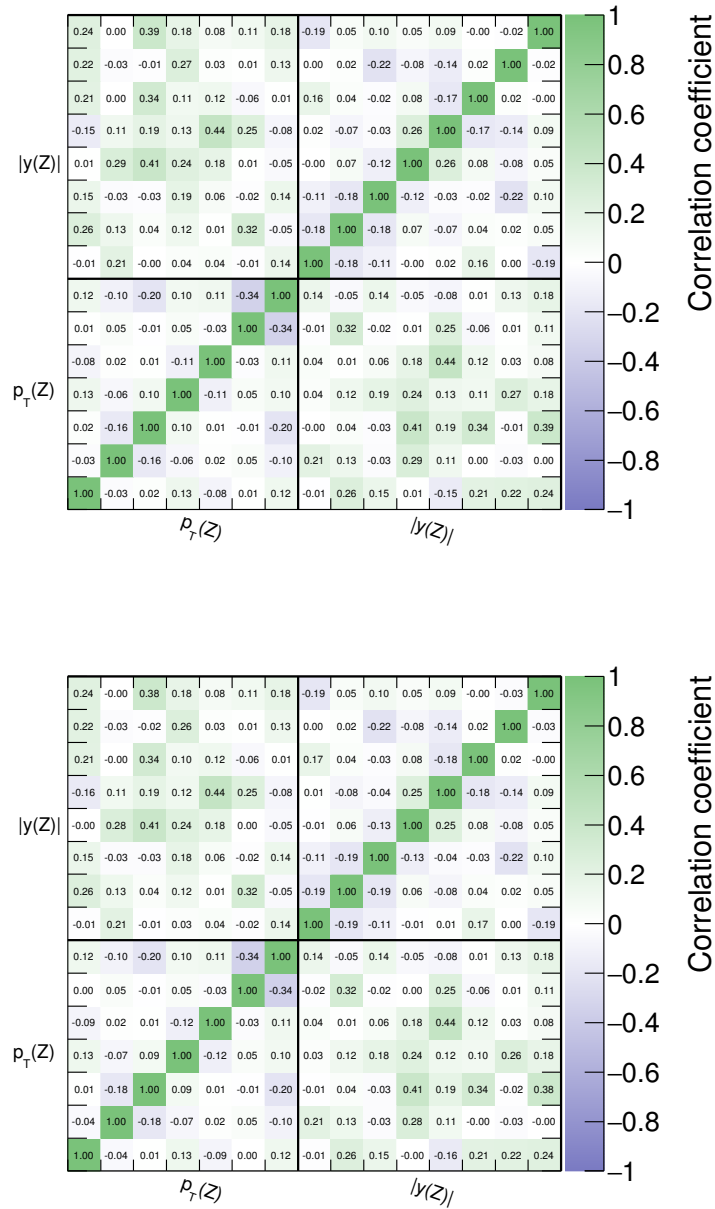
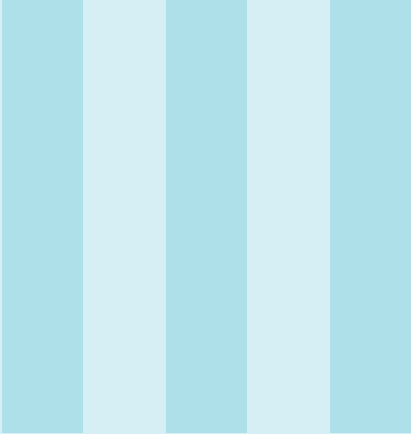


Figure 7.20: Bin-wise correlation factors between variables unfolded to particle- (top) and parton-level (bottom) in the combined 3L and 4L channels.



Search for the supersymmetric partner to the top quark in all-hadronic final states

8 Analysis strategy

- 8.1 Signal processes
- 8.2 Object definitions
- 8.3 Event selection
- 8.4 Signal regions
- 8.5 Prediction of the Standard Model backgrounds

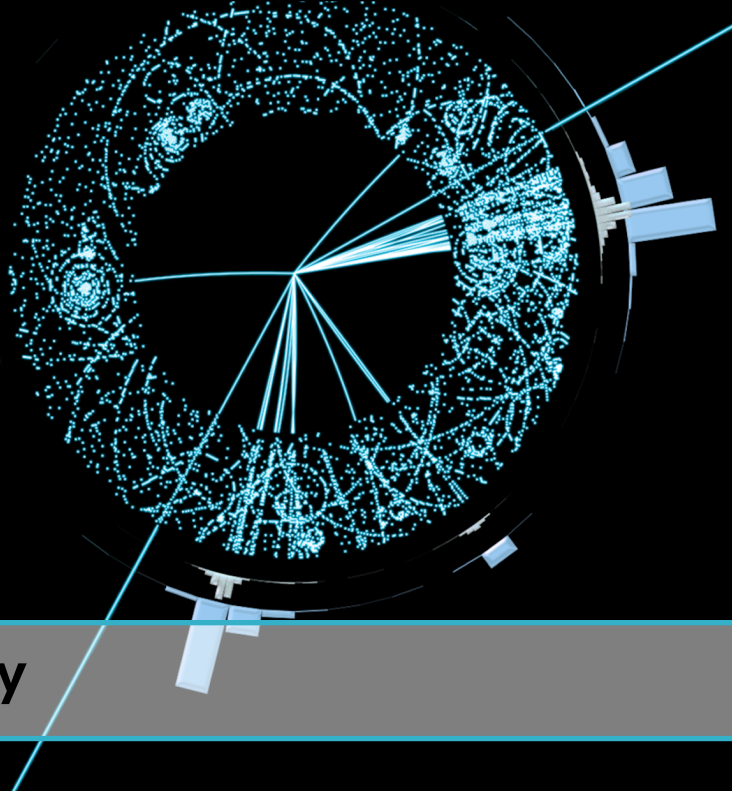
9 Estimation of the irreducible $t\bar{t}Z$ background

- 9.1 Boson replacement
- 9.2 Multi-lepton approach

10 Statistical analysis and search results

- 10.1 Systematic uncertainties
- 10.2 Results

Conclusion



8. Analysis strategy

In this chapter we review the analysis strategy and optimisation in the search for direct pair-production of the supersymmetric partner to the top quark, in all-hadronic final states. Background estimation techniques and final results, using the intermediate Run 2 dataset of $36.1 \text{ fb}^{-1} pp$ collisions at $\sqrt{s} = 13 \text{ TeV}$, will be discussed in Chapters 9 and 10 respectively. The search and its signal process topologies are described in Section 8.1, and reconstructed physics objects and event selection in Sections 8.2 and 8.3. In Section 8.4, search regions for the SUSY signals are constructed, and in Section 8.5 the estimates of various background processes (except $t\bar{t}Z$, the subject of Chapter 9) are outlined. The author's contributions to the work presented in this chapter, part of the paper published by the ATLAS Collaboration in Ref. [3], are modest, covering only part of the optimisation of the signal regions and background estimations.

8.1 Signal processes

The search is performed in the direct $pp \rightarrow t\bar{t}^* + X$ channel, i.e. direct pair-production (in contrast with e.g. gluino cascade decay), where only two decay modes of the top squark are considered: $\tilde{t} \rightarrow t + \tilde{\chi}_1^0$ or $\tilde{t} \rightarrow b + \tilde{\chi}_1^\pm \rightarrow b + W^\pm + \tilde{\chi}_1^0$. In both cases, the hadronic decay of the W is considered, making this analysis orthogonal to concomitant leptonic or photonic searches.

The high number of jets (at least four considered, but nominally six) makes this channel challenging, particularly where top quark reconstruction is concerned. On the other hand, the only intrinsic source of E_T^{miss} is from the $\tilde{\chi}_1^0$'s, thanks to the absence of neutrinos in the final state. Therefore the experimental signature is multiple jets and high E_T^{miss} , where the dominant background sources are:

- $Z(\rightarrow \nu\bar{\nu})$ +jets with additional b -jets,
- semi-leptonic $t\bar{t}$ events, with a lost or mis-identified W lepton and E_T^{miss} from the neutrino,
- $W \rightarrow \ell\bar{\nu}$ plus additional b -jets,
- $t\bar{t}Z$, where both top quarks decay hadronically and $Z \rightarrow \nu\bar{\nu}$, and

“Simulated SUSY event”. Image credits: ATLAS Experiment. © 2014 CERN.

- Wt -channel single top quark decays, where one W decays hadronically and one leptonically (same effect as second point above).

The top squark signals considered are generated using simplified models [101–103], whereby only the \tilde{t} , the $\tilde{\chi}_1^0$ and the $\tilde{\chi}_1^\pm$ are accessible SUSY particles, with the $\tilde{\chi}_1^0$ as the LSP. Pseudo-Feynman diagrams of the following various production modes are shown in Figure 8.1:

- $\tilde{t} \rightarrow t + \tilde{\chi}_1^0$ twice (one-step decay),
- $\tilde{t} \rightarrow b + \tilde{\chi}_1^\pm \rightarrow b + W + \tilde{\chi}_1^0$ twice (two-step decay),
- $\tilde{t}\tilde{t}^* \rightarrow t + \tilde{\chi}_1^0 + b + \tilde{\chi}_1^\pm$ (mixed decay),
- $\tilde{t} \rightarrow b + W + \tilde{\chi}_1^0$ twice (three-body decay), where $m(b) + m(W) < m(\tilde{t}) - m(\tilde{\chi}_1^0) < m(t)$.

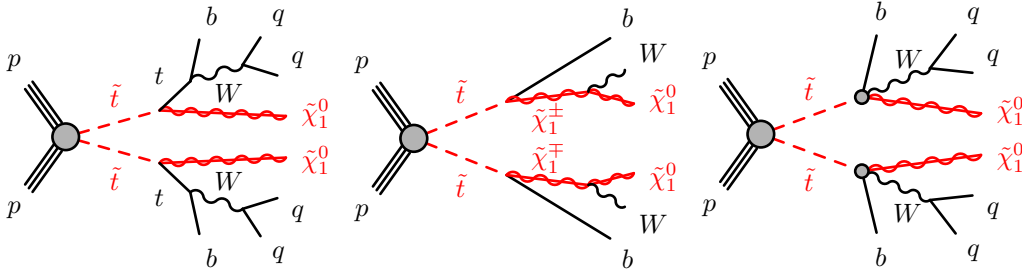


Figure 8.1: Decay topologies of the signal models considered. From left to right: one-step, two-step and three-body decays.

In cases where the NLSP-LSP mass splitting, $\Delta m(\tilde{\chi}_1^\pm, \tilde{\chi}_1^0)$, is assumed to be 1 GeV (leading to a prompt decay of the $\tilde{\chi}_1^\pm$ into a virtual W), we will refer to a natural-SUSY-inspired scenario. This particular configuration also requires the $\tilde{\chi}_1^0$ to be a pure bino state. Additional pMSSM models, with a wino NLSP [86] or a well-tempered neutralino [87], motivate a different choice of the NLSP-LSP mass splitting, usually taken to be $m(\tilde{\chi}_1^\pm) = 2 \cdot m(\tilde{\chi}_1^0)$.

Along the $(m(\tilde{t}_1), m(\tilde{\chi}_1^0))$ plane, a grid of signal points is created with a 50 GeV spacing; at each point a different model is generated, using MADGRAPH5_aMC@NLO 2.2-2.4 interfaced to PYTHIA 8 for the PS and hadronisation, with up to two additional partons beyond the tree-level ME calculation. The decays of heavy-flavour hadrons are simulated with EVTGEN v.1.2.0 [270], while NNPDF2.3LO [237] provides the PDF set and A14 [238] the UE tune for the generation of the \tilde{t} samples. The CKKW prescription is used for ME-PS matching. Signal cross sections are calculated to next-to-leading order in the strong coupling constant, adding the resummation of soft gluon emission at next-to-leading-logarithmic accuracy (NLO+NNLL).

8.2 Object definitions

Physics objects, as introduced in Section 3.2, are first defined as baseline objects, following a loose selection. Ambiguities, such as mis-identification of leptons as jets, are removed at this stage through an Overlap Removal (OR) procedure. The selection on remaining objects is then tightened.

Electrons baseline electrons are required to have $|\eta| < 2.47$ and $p_T > 7$ GeV, as well as pass the VeryLooseLH likelihood-based identification and Gradient Loose isolation [240, 246]. Signal electrons have $p_T > 20$ GeV and pass the TightLLH identification.

Muons baseline muons are required to have $|\eta| < 2.47$ and $p_T > 6$ GeV, as well as pass the Loose quality selection and Gradient Loose isolation [207]. Signal muons have $p_T > 20$ GeV and pass the Medium quality selection.

Jets they are reconstructed using the anti- k_r algorithm [216] with a distance parameter $R = 0.4$. Baseline jets are required to have $|\eta| < 4.8$ and $p_T > 20$ GeV. Signal jets have $|\eta| < 2.8$ and pass the **JVT** requirement. Out of these signal jets, those that are positively identified by the MV2c10 algorithm (using a 77% b-tagging efficiency) and fall within $|\eta| < 2.5$ are considered b -jets.

Missing Transverse Energy overlap-removed baseline electrons, muons and jets are used in the recalculation of the object-based E_T^{miss} [241]. An extra term takes into account soft energy not originating from any of the selected objects. An additional $E_T^{\text{miss,track}}$ quantity is derived from the sum of the transverse momenta of the tracks associated with objects in the event. The azimuthal angle between this and the calorimeter-based E_T^{miss} provides an effective discriminant against events with fake E_T^{miss} .

Photons baseline photons are required to have $|\eta| < 2.37$ and $p_T > 25$ GeV, as well as pass the Tight cut-based identification and FixedCutLoose isolation. Signal photons have $p_T > 130$ GeV.

τ identification for veto a jet is identified as a τ candidate if the jet is the closest jet to the E_T^{miss} with $|\Delta\phi(E_T^{\text{miss}}, \text{jet})| < \pi/5$ and four or fewer tracks are associated with the jet.

Overlap Removal in the case of candidate objects overlapping with each other, all but one object must be removed from the event. The distance metric used to define overlapping objects is $\Delta R = \sqrt{(\Delta\eta)^2 + (\Delta\phi)^2}$:

1. If an electron and jet are located within $\Delta R < 0.2$, consider the object an electron and remove the jet, unless the jet is b-tagged in which case the jet is kept and the electron is removed.
2. If a muon and jet are located within $\Delta R < 0.4$, consider the object a jet and remove the muon, unless the object has fewer than three tracks in which case the jet is removed and the muon is kept.
3. If an electron and jet are located within $0.2 \leq \Delta R < 0.4$, consider the object a jet and remove the electron.

8.3 Event selection

8.3.1 Triggers

In order to collect events with no leptons, multiple jets and E_T^{miss} in the signal regions, an E_T^{miss} trigger is used. Similarly, a single-lepton (or single-photon) trigger is used to select background events for the one-lepton (or one-photon) control regions. The requirements applied by the various triggers are summarised in Table 8.1 below.

Table 8.1: Summary of triggers used in the analysis. Commas in the individual p_T selections denote a logical OR of multiple cuts. Different identification and isolation requirements are used in each trigger, such that their combination is not trivially equivalent to only the first one listed.

Trigger	Data 2015	Data 2016
Electron	$p_T > 24, 60, 120$ GeV	$p_T > 26, 60, 120$ GeV
Muon	$p_T > 20, 50$ GeV	$p_T > 26, 50$ GeV
Photon	$p_T > 120$ GeV	$p_T > 140$ GeV
E_T^{miss}	$E_T^{\text{miss}} > 70$ GeV	$E_T^{\text{miss}} > 90, 100, 110$ GeV

Once events selected by the various triggers have been selected, further offline cuts are applied to ensure the relevant objects are in the plateau region, where the trigger is fully efficient (see Figures 3.6, 3.8, 3.10 and 3.14). This is done by requiring slightly higher-than-threshold transverse momenta, i.e. $p_T(e, \mu) > 27$ GeV, $E_T^{\text{miss}} > 250$ GeV or $p_T(\gamma) > 150$ GeV.

8.3.2 Event cleaning

A number of offline cuts are applied to trigger-selected events. These aim at removing events recorded during a detector fault (by checking the status of the ECAL and HCAL), non-HS events (by reconstructing a primary vertex with at least two tracks above the $p_T > 400$ MeV threshold), events with potential cosmic muons or poorly reconstructed jets (sensitive to large fake-jet contamination).

8.3.3 Discriminating variables

The physics objects previously described, after overlap removal and passing their respective tight selections, are further used to define a number of discriminating variables on which the signal region definitions are based.

$\min|\Delta\phi(\mathbf{E}_T^{\text{miss}}, \text{jet}^{0,1})|$ The minimum difference in ϕ between one of the two leading jets (in p_T) and the E_T^{miss} . This variable rejects events with fake E_T^{miss} from QCD, hadronic $t\bar{t}$ and detector effects.

H_T The scalar sum of the p_T of all signal jets.

m_T^i The transverse mass (m_T) between the i th jet and the E_T^{miss} in the event. The massless approximation is used for this and all following m_T variables:

$$m_T^i = \sqrt{2p_T^{\text{jet},i} E_T^{\text{miss}} (1 - \cos \Delta\phi(E_T^{\text{miss}}, \text{jet}^i))}, \quad (8.1)$$

where $p_T^{\text{jet},i}$ is the transverse momentum of the i th jet.

$m_T^{\text{b,min}}$ The transverse mass between the b -jet closest to the E_T^{miss} and the E_T^{miss} .

$m_T^{\text{b,max}}$ The transverse mass between the b -jet farthest to the E_T^{miss} and the E_T^{miss} . Both $m_T^{\text{b,min}}$ and $m_T^{\text{b,max}}$ provide very good discrimination between the signal and the semileptonic $t\bar{t}$ background.

$\Delta\mathbf{R}(\mathbf{b}, \mathbf{b})$ The angular separation between the two jets with the highest MV2c10 score. This variable is useful in discriminating against the $Z(\rightarrow \nu\bar{\nu}) + b\bar{b}$ +jets background.

m_{T2} The transverse mass is defined as [271, 272]

$$m_{T2}^2(\mathbf{p}_T^{t_1}, \mathbf{p}_T^{t_2}, E_T^{\text{miss}}) = \min_{\mathbf{q}_1 + \mathbf{q}_2 = E_T^{\text{miss}}} \left[\max \left[m_T^2(\mathbf{p}_T^{t_1}, \mathbf{q}_1), m_T^2(\mathbf{p}_T^{t_2}, \mathbf{q}_2) \right] \right], \quad (8.2)$$

where $\mathbf{p}_T^{t_1}$ and $\mathbf{p}_T^{t_2}$ are the transverse momenta of two top quark candidates and \mathbf{q}_1 and \mathbf{q}_2 are the vectors that satisfy $\mathbf{q}_1 + \mathbf{q}_2 = E_T^{\text{miss}}$. The minimisation is performed over all possible decompositions of E_T^{miss} . Each top quark candidate corresponds to the combination of a b -jet and one or two light jets. The minimisation objective is expressed as a χ^2 reduction of invariant masses:

$$\chi^2 = \sum_{i \in \{W_1, W_2, t_1, t_2\}} \frac{(M_{\text{cand}}^i - M_{\text{true}}^i)^2}{M_{\text{true}}^i} \quad (8.3)$$

where M_{cand} is the candidate mass and M_{true} is set to 80.4 GeV and 173.2 GeV for the W boson and top quark, respectively, while the invisible particles are assumed to be massless. The variable m_{T2} therefore provides a lower bound on the square of the transverse mass of the pair of sparticles decaying to the $t\bar{t} + E_{\text{T}}^{\text{miss}}$ system, whilst having a (computable) kinematic endpoint in the case of the $t\bar{t}$ background.

8.3.4 Top quark reconstruction

While the m_{T2} variable defined above provides adequate resolution on the hadronic top quark mass (through the implicit χ^2 reconstruction) at lower momenta, as well as potential kinematic information about the decaying sparticles in the case of a discovery (through a study of endpoints and kinks), it needs to be complemented by other approaches more sensitive at high momenta.

As the $t\bar{t}$ system gets boosted, one expects the anti- k_t $R = 0.4$ jets corresponding to the hadronic W bosons to start overlapping, possibly to the point of also merging with the b -jets. It is however possible to circumvent this problem altogether by running the anti- k_t algorithm again, with a larger radius parameter. The values $R = 1.2$ and $R = 0.8$, yielding large-radius jets to which one associates top quark or W boson (respectively) candidates, were found to be optimal. Four additional discriminating variables are then accessible, corresponding to the invariant masses of the two leading $R = 1.2$ and $R = 0.8$ large- R jets. These are particularly useful in rejecting background events from QCD, W +jets and Z +jets.

Since m_{T2} is by construction correlated with $E_{\text{T}}^{\text{miss}}$, they can be used together in the signal region selection to enhance the rejection of the all-hadronic $t\bar{t}$ background, from which one expects no $E_{\text{T}}^{\text{miss}}$. Such correlation maps are shown in Figure 8.2.

The semileptonic $t\bar{t}$ background can be suppressed by application of the τ -veto mentioned above, as well as through cuts on $m_{\text{T}}^{b,\text{min}}$, where it presents an endpoint at the top quark mass as shown in Figure 8.3.

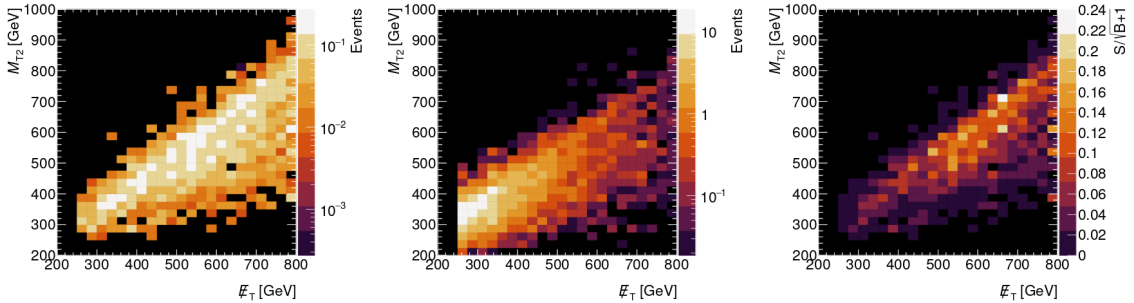


Figure 8.2: From left to right: m_{T2} vs $E_{\text{T}}^{\text{miss}}$ for signal events ($m_{\tilde{t}} = 1000$ GeV and $m_{\tilde{\chi}^0} = 1$ GeV) S , background events B and significance $S/\sqrt{B+1}$. Pre-selection cuts are applied.

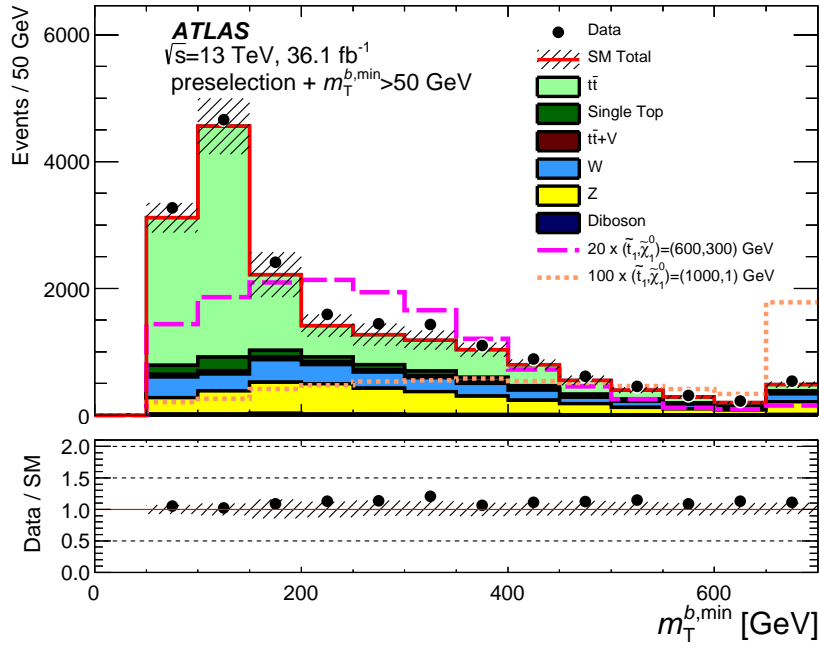


Figure 8.3: Distribution of the discriminating variable $m_T^{b,\min}$ after preselection cuts and an additional $m_T^{b,\min} > 50 \text{ GeV}$ requirement. The rightmost bin includes overflow events.

8.4 Signal regions

The generic signature of the various signal scenarios under study is characterised by multiple jets, including two b -jets, no lepton and a significant amount of E_T^{miss} . The two signal regions to which the author contributed are the so-called SRA and SRB, targeting high- and medium-mass splittings ($\Delta m(\tilde{t}, \tilde{\chi}_1^0)$) and optimised around $(m_{\tilde{t}}, m_{\tilde{\chi}_1^0})$ benchmarks of (1000, 1) and (600, 300) GeV respectively. Further SR, not discussed here any further, target the compressed regime [273, 274], where $\Delta m(\tilde{t}, \tilde{\chi}_1^0) \sim m_t$ (SRC), the $\tilde{t} \rightarrow b + \tilde{\chi}_1^\pm$ two-step decay at lower stop masses (SRD), and gluino-mediated top squark production (SRE).

A common pre-selection is applied to all SR and is described in Table 8.2. In addition to these preliminary requirements, SRA and SRB rely on a number of the discriminating variables we've previously outlined to become sensitive to high stop masses and light neutralinos. The events are further classified into three categories, depending on the reconstructed top quark candidate mass (using $R = 1.2$ re-clustered jets) shown in Figure 8.4. The TT category includes events with two well-reconstructed top quark candidates, the TW category contains events with a well-reconstructed leading p_T top quark candidate and a well-reconstructed subleading W candidate, while the T0 category represents events with only a leading top quark candidate. These are shown graphically in Figure 8.5.

For the benchmark point (1000, 1) GeV, after the common pre-selection $\sim 91\%$ of events fall into one of these three categories (38% in TT, 22% in TW and 31% in T0). Similarly for the point (600, 300) GeV, used for the SRB optimisation, $\sim 69\%$ of events survive the large- R jet requirements (14% in TT, 20% in TW and 35% in T0). In SRA, where the mass splitting is well above the top quark mass, further cuts are applied on m_{T2} as well as on the mass of the leading $R = 0.8$ re-clustered jet (taken as a proxy to the leading hadronic W boson candidate). The final six SR are described in Table 8.3 and statistically combined in the discovery and exclusion fits.

Table 8.2: Pre-selection criteria common to all signal regions, after event cleaning.

Object	Selection
Trigger	E_T^{miss}
E_T^{miss}	$> 250 \text{ GeV}$
N_{lep}	0
anti- k_t , $R = 0.4$ jets	≥ 4 , $p_T > 80, 80, 40, 40 \text{ GeV}$
b -jets	≥ 1
$\min \Delta\phi(E_T^{\text{miss}}, \text{jet}^{0,1}) $	> 0.4
$E_T^{\text{miss,track}}$	$> 30 \text{ GeV}$
$ \Delta\phi(E_T^{\text{miss}}, E_T^{\text{miss,track}}) $	$< \pi/3$

Table 8.3: Selection criteria for SRA and SRB, after pre-selection.

Signal Region	Object	TT	TW	T0
A and B	$m_{\text{jet}, R=1.2}^0$		$> 120 \text{ GeV}$	
	$m_{\text{jet}, R=1.2}^1$	$> 120 \text{ GeV}$	$60 - 120 \text{ GeV}$	$< 60 \text{ GeV}$
	$m_T^{b, \text{min}}$		$> 200 \text{ GeV}$	
	b -jets		≥ 2	
	τ -veto		yes	
	$\min \Delta\phi(E_T^{\text{miss}}, \text{jet}^{0,1,2}) $			> 0.4
A	$m_{\text{jet}, R=0.8}^0$		$> 60 \text{ GeV}$	
	$\Delta R(b, b)$	> 1		
	m_{T2}	$> 400 \text{ GeV}$	$> 400 \text{ GeV}$	$> 500 \text{ GeV}$
	E_T^{miss}	$> 400 \text{ GeV}$	$> 500 \text{ GeV}$	$> 550 \text{ GeV}$
B	$m_T^{b, \text{max}}$		$> 200 \text{ GeV}$	
	$\Delta R(b, b)$		> 1.2	

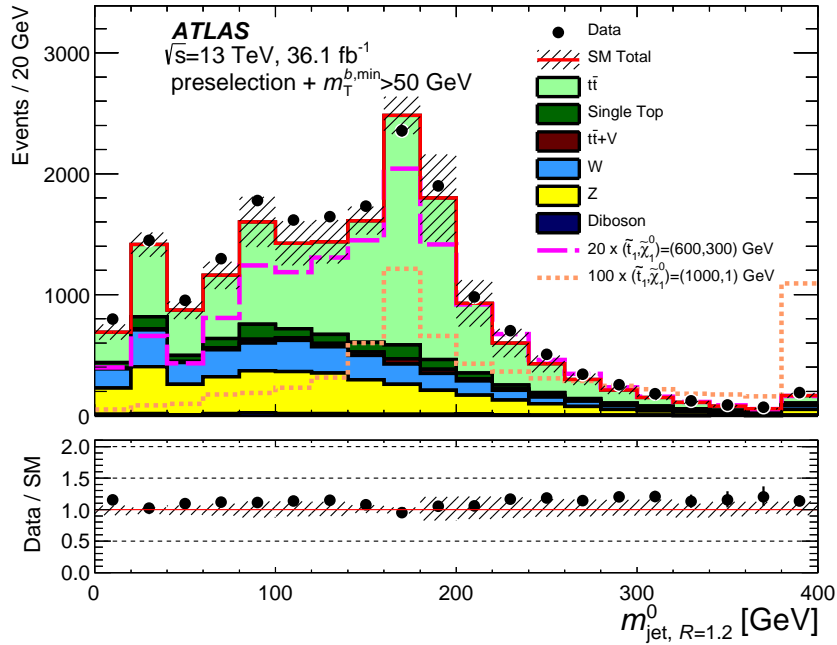


Figure 8.4: Distribution of the discriminating variable $m_{\text{jet}, R=1.2}^0$ after pre-selection cuts and an additional $m_T^{b, \text{min}} > 50$ GeV requirement. The rightmost bin includes overflow events.

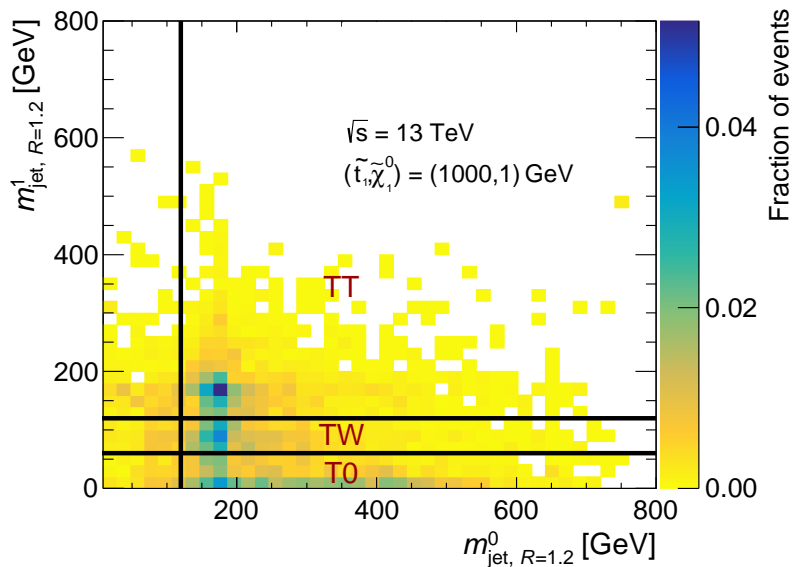


Figure 8.5: Illustration of top quark category definitions (TT, TW and T0) for SRA and SRB, based on $R = 1.2$ re-clustered top quark candidate masses for simulated direct top squark pair production with $(m_{\tilde{t}}, m_{\tilde{\chi}_1^0}) = (1000, 1)$ GeV after pre-selection cuts.

8.5 Prediction of the Standard Model backgrounds

The following processes yield final states that mimic, completely or in part, the sought-after signal signature of jets+ E_T^{miss} and no lepton. In order to estimate their contribution to the various SR, a number of techniques can be employed: a pure MC-based estimation, a semi-data-driven approach with control regions (CR) or fully-data-driven methods (see below, Jet Smearing and $t\bar{t}\gamma$).

Z+jets The $Z(\rightarrow \nu\bar{\nu})$ +jets process is a significant background to this search as it becomes more relevant as the E_T^{miss} requirements are increased. The $(Z \rightarrow q\bar{q})$ +jets process, on the other hand, although benefiting from a much higher branching ratio, is largely subleading behind the multijet background (described below). The $Z(\rightarrow \nu\bar{\nu})$ +jets background is estimated by using a $Z(\rightarrow \ell^+\ell^-)$ +jets control sample, described in the next subsection. The two lepton channel offers the advantage of an easier selection of pure samples in terms of non- Z background, but is statistically limited at high $Z p_T$.

W+jets The hadronic W +jets process is similarly subdominant with respect to the multijet background, but the $W \rightarrow \ell\nu$ decay channel, where the lepton is either lost or mis-identified as a jet, provides a relevant background to the all-hadronic channel. It is estimated from a one-lepton CR.

$t\bar{t}$ The pair production of top quarks produces a rich final state with two b -jets, a large number of light jets and possibly leptons and real E_T^{miss} from neutrinos. As such, it is obviously one of the leading backgrounds to this search. As previously mentioned, complex kinematic variables such as $m_T^{b,\text{min}}$ or m_{T2} can help reducing it. A one-lepton CR is designed for its estimation.

Single top Single top quark production is most relevant in the so-called Wt channel, which produces an additional W and brings the final state very close to that of $t\bar{t}$ production. A one-lepton CR is similarly employed, although the purity is much less than that of $t\bar{t}$, making this a challenging process to constrain.

Multi-jet The multi-jet (or QCD) background is produced abundantly at the LHC, enjoying a cross section much higher than those of the above processes. Even though it can be largely reduced using angular variables such as $\min|\Delta\phi(E_T^{\text{miss}}, \text{jet}^{0,1,2})|$, the combined amount of jet mis-measurement leading to its presence in the signal region can not be reliably modelled from MC, and thus a fully data-driven method is used (see Jet Smearing below).

$t\bar{t}Z$ Out of all the above processes, $t\bar{t}Z(\rightarrow \nu\bar{\nu})$ is the only irreducible background, as it presents with both a fully reconstructed hadronic $t\bar{t}$ system and a high p_T Z able to produce sufficient E_T^{miss} . The treatment of this irreducible background will be studied extensively in the Chapter 9. Similar processes involving the production of $t\bar{t}$ in association with a vector boson, i.e. $t\bar{t}Z(\rightarrow q\bar{q})$, $t\bar{t}W$, $t\bar{t}H$ and $t\bar{t}\gamma$, are rare SM backgrounds and can be estimated directly from MC modelling.

8.5.1 One-lepton control regions

As described above, a number of processes are estimated in one-lepton CRs: the W +jets (CRW), $t\bar{t}$ (CRTopX, a set of regions to match SRA-B and the distinction between top quark categories) and single top quark production (CRST). These backgrounds contribute to the signal regions due to the lepton originating from the decay of a W boson: either out-of-acceptance, mis-identified as a jet, or a hadronically decaying τ -lepton (the dominant effect). The normalisation of these processes in data is therefore straightforwardly done by exploiting a one-lepton selection.

The base selection for the three regions is summarised in Table 8.4. In these regions, the lepton is counted as a jet for the p_T requirements and the jet reclustering (in order to get as close as possible to the SR requirements), but not for the QCD cleaning selection. The top quark control region, CRTopX, is further divided as made explicit in Table 8.5.

The three sets of CRs are mutually exclusive. Furthermore, the requirements on the number of b -jets and on $m_{\text{jet},R=1.2}^0$ ensures that CRW is orthogonal to CRTopX and CRST. The selection on $\Delta R(b_{0,1}, \ell)_{\text{min}}$, defined as the minimum ΔR between the two jets with the highest b -tag weight and the selected lepton, ensures the orthogonality of CRTopX and CRST. In CRST, the requirement on the ΔR of the two leading-weight b -jets is necessary to reject a large part of the remaining $t\bar{t}$ background and reach a single top quark purity of $\sim 50\%$. The distributions of a couple of key variables for CRST and CRW are shown in Figure 8.6.

Table 8.4: Summary of the selection criteria for the one-lepton control regions for single top quark and W +jets, and the common top quark control regions. The signal lepton is treated as a jet for the jet counting and p_T ordering as well as for the top quark reconstruction.

Object	CRTopX	CRST	CRW
N_{lep}		1	
N_{jets}		≥ 4	
p_T of jets		(80, 80, 40, 40) GeV	
$\min \Delta\phi(E_T^{\text{miss}}, \text{jet}^{0,1}) $		> 0.4	
E_T^{miss}		> 250 GeV	
$m_T(\ell, E_T^{\text{miss}})$		30 – 100 GeV	
b -jets		≥ 2	= 1
$m_{\text{jet},R=1.2}^0$		> 120 GeV	< 60 GeV
$m_T^{b,\text{min}}$	> 100 GeV	> 200 GeV	—
$\Delta R(b_{0,1}, \ell)_{\text{min}}$	< 1.5	> 2.0	
$\Delta R(b, b)$	—	> 1.5	—

Table 8.5: Summary of the selection criteria for the one-lepton top quark control regions, after applying the the CRTopX cuts from Table 8.4.

CRTop	Object	TT	TW	T0
A and B	$m_{\text{jet},R=1.2}^1$	> 120 GeV	60 – 120 GeV	< 60 GeV
A	$m_{\text{jet},R=0.8}^0$		> 60 GeV	
	$\Delta R(b, b)$	> 1	—	
	E_T^{miss}	> 250 GeV	> 300 GeV	> 350 GeV
B	$m_T^{b,\text{max}}$		> 200 GeV	
	$\Delta R(b, b)$		> 1.2	

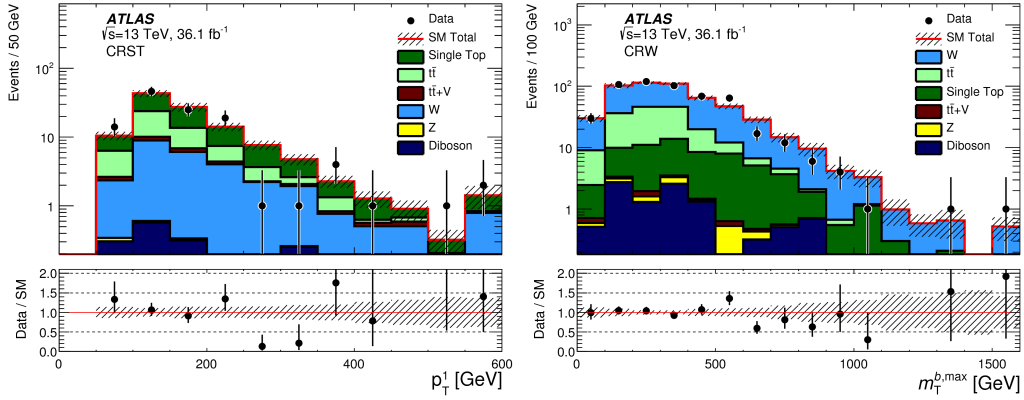


Figure 8.6: Distributions of the sub-leading jet p_T in CRST (left) and $m_T^{b,\max}$ in CRW (right), after normalisation of SM processes in a simultaneous fit of all backgrounds to data. The rightmost bin includes overflow events.

8.5.2 Two-lepton control regions

The $Z(\rightarrow \nu\bar{\nu})$ +jets background is estimated in a set of two-lepton CRs by using a $Z(\rightarrow \ell^+\ell^-)$ +jets control sample. In order to build a CR close to the SRs, the same jet requirements are applied to ensure as little extrapolation as possible. The usual E_T^{miss} trigger is swapped here for a logical OR of the single-electron and single-muon triggers, as detailed in Table 8.1. To reduce contamination from top quark backgrounds, a Z mass window cut is applied and the E_T^{miss} is bounded from above. The transverse momentum of the selected leptons are then removed from the E_T^{miss} , to mimic the neutrinos one expects in the all-hadronic SRs. This results in a modified quantity denoted $E_T^{\text{miss}'}$, which can this time be bounded from below to approximate the E_T^{miss} requirements from the SRs.

Table 8.6 presents the various selection criteria used in defining two CRs for the Z +jets background, one for the mixed TT and TW categories and one for T0 individually. The distribution of m_{T2} in this latter region is shown in Figure 8.7.

Table 8.6: Summary of the selection criteria for the two-lepton Z +jets control regions.

Object	CRZAB-TT-TW	CRZAB-T0
Trigger	single lepton (e or μ)	
N_{lep}	2 (OSSF)	
N_{jets}	≥ 4	
p_T of jets	(80, 80, 40, 40) GeV	
E_T^{miss}	< 50 GeV	
$E_T^{\text{miss}'}$	> 100 GeV	
b -jets	≥ 2	
$m_{\text{jet},R=1,2}^0$	> 120 GeV	
$m_{\text{jet},R=1,2}^1$	> 60 GeV	< 60 GeV

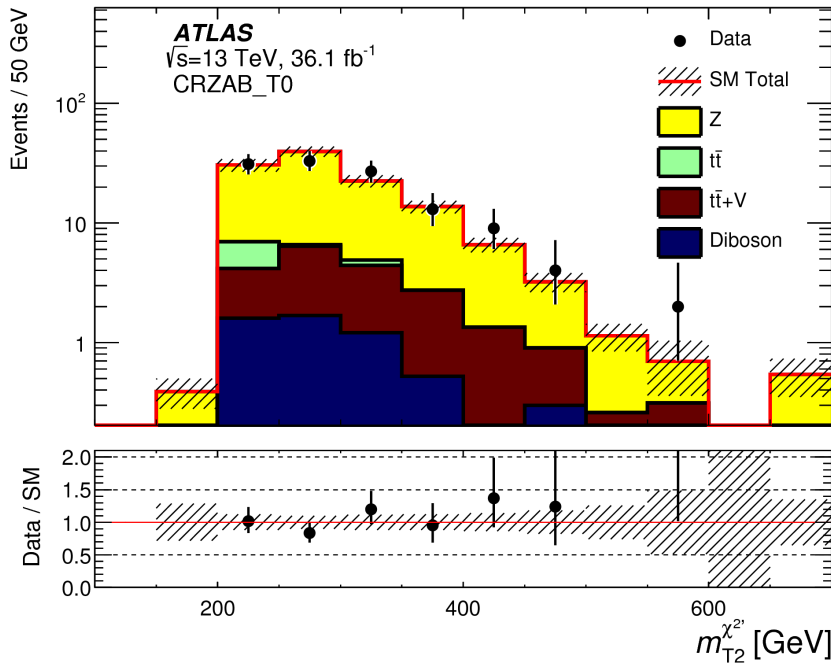


Figure 8.7: Distribution of the variable m_{T2} in CRZAB-T0, after normalisation of SM processes in a simultaneous fit of all backgrounds to data. The rightmost bin includes overflow events.

8.5.3 Jet Smearing

The background arising from the production of multijet events and all-hadronic $t\bar{t}$ events is estimated with the Jet Smearing method [275], relying on the assumption that the QCD background is dominated by the mis-measurement of multiple jets. The term mis-measurement refers to cases in which the hadronisation of partons is not fully reconstructed by ATLAS and cases in which the hadronisation (particularly of heavy-flavour quarks) produces real E_T^{miss} in the form of neutrinos:

- Hadronic calorimeters are not perfect and have limited granularity, leading to errors in the measurement of energies of all particles.
- Since jets are defined as clusters of showering particles according to some algorithm (e.g. anti- k_r), it is possible that some particles are left outside out the jet radius. Additionally, particles interacting with non-detector material won't be taken into account. Overlap removal is also arbitrary and may not completely remove jet particles originating from other sources.
- Not all jets are fully contained within the calorimeter systems: high-energy jets can punch through to the muon systems, leading to an underestimation of their energies. This effect is corrected by the non-Gaussian part of the jet response (see below).
- Jets that are close to areas of large amounts of dead material are vetoed; however there are still regions with small amounts of dead material in the calorimeters which can cause particles to deposit their energy. Damaged or inactive parts of the detector, non-instrumented supports and services for running electronics are examples of such regions.
- In decays of heavy-flavour quarks, real E_T^{miss} arises from the presence of neutrinos. Around 24% of b-quark decays will lead to electron and muon neutrinos, which carry a fraction of the jet energy with them. This gives rise to a larger non-Gaussian tail in the jet response.

The Jet Smearing method relies on repeated smearing of the Lorentz vectors of jets originating from well-measured data events (with small E_T^{miss}), creating artificial samples of pseudo-data with potentially large E_T^{miss} arising from the unbalanced smearing. The algorithm proceeds in three

steps:

1. Data events containing ≥ 4 jets, of which two are b -tagged, are used to select well-measured “seed” events that populate low values of the so-called “missing transverse energy significance”:

$$E_T^{\text{miss sig.}} = \frac{E_T^{\text{miss}} - 8 \text{ GeV}}{\sum E_T} \quad (8.4)$$

where the ad-hoc offset of 8 GeV was optimised to remove any bias in the leading jet p_T distribution of the pseudo-data. Specifically, the requirement is

$$E_T^{\text{miss sig.}} < 0.3 + 0.1 \cdot N_{b\text{-jets}} \quad (8.5)$$

2. The `JetSmearing` tool is then used to smear the four-momenta of jets in the seed events. For each jet, the Lorentz vector is multiplied by a random number derived from pre-determined jet response maps, defined as the ratio of parton-generated to reconstructed jet p_T and binned in ϕ .
3. Point 2 above is repeated 5000 times for each jet in the seed event to randomly generate configurations where the E_T^{miss} comes from multiple fluctuating jets.

The multijet contribution is estimated in a set of CRs close to the SR definitions, loosening the E_T^{miss} requirement and inverting the cut on $\min |\Delta\phi(E_T^{\text{miss}}, \text{jet}^{0,1})|$. The selections are summarised in Table 8.7 and some key variables are shown in Figure 8.8.

Table 8.7: Summary of the selection criteria for the all-hadronic QCD control regions.

Region	Object	CRQ
A and B	Trigger	E_T^{miss}
	N_{lep}	0
	N_{jets}	≥ 4
	b -jets	≥ 2
	τ -veto	yes
	E_T^{miss}	$> 200 \text{ GeV}$
	$\min \Delta\phi(E_T^{\text{miss}}, \text{jet}^{0,1}) $	< 0.1
	$m_{\text{jet}, R=1.2}^0$	$> 120 \text{ GeV}$
	$m_T^{b, \text{min}}$	$> 100 \text{ GeV}$
A	$m_{\text{jet}, R=0.8}^0$	$> 60 \text{ GeV}$
	E_T^{miss}	$> 300 \text{ GeV}$
B	$m_T^{b, \text{max}}$	$> 200 \text{ GeV}$
	$\Delta R(b, b)$	> 1.2

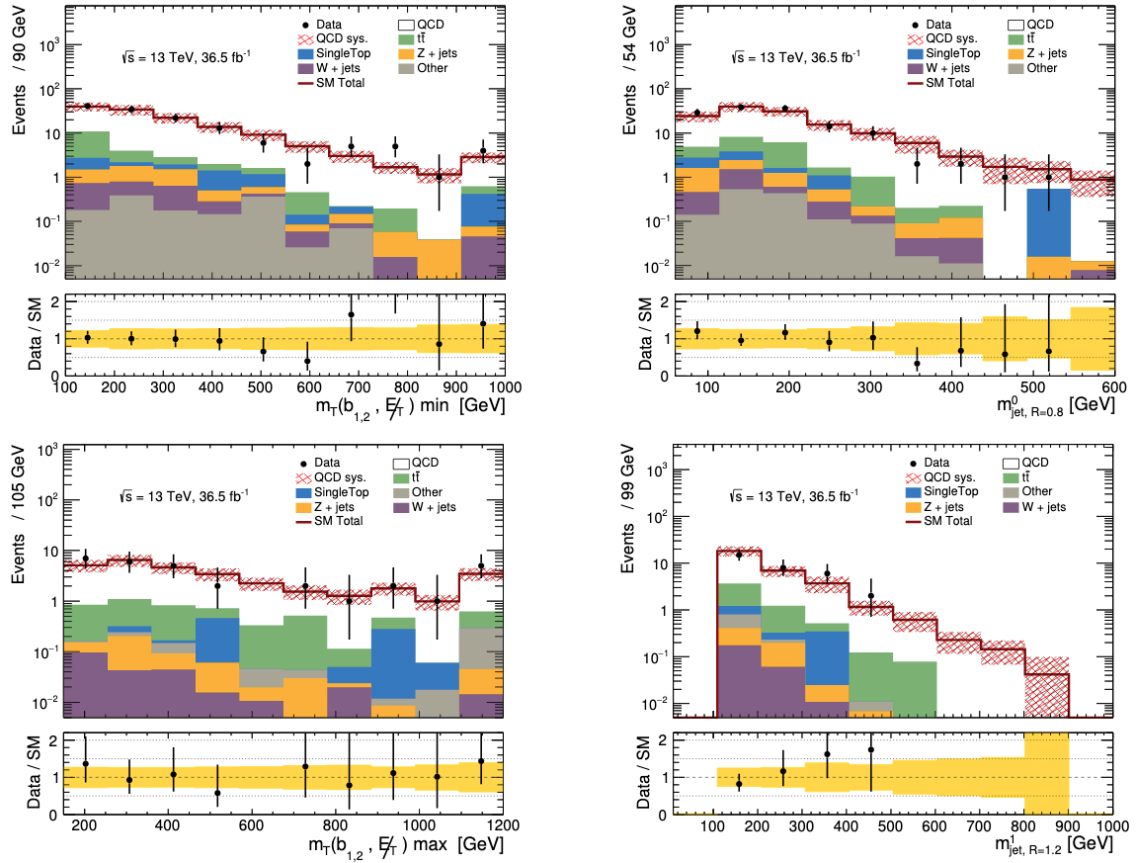
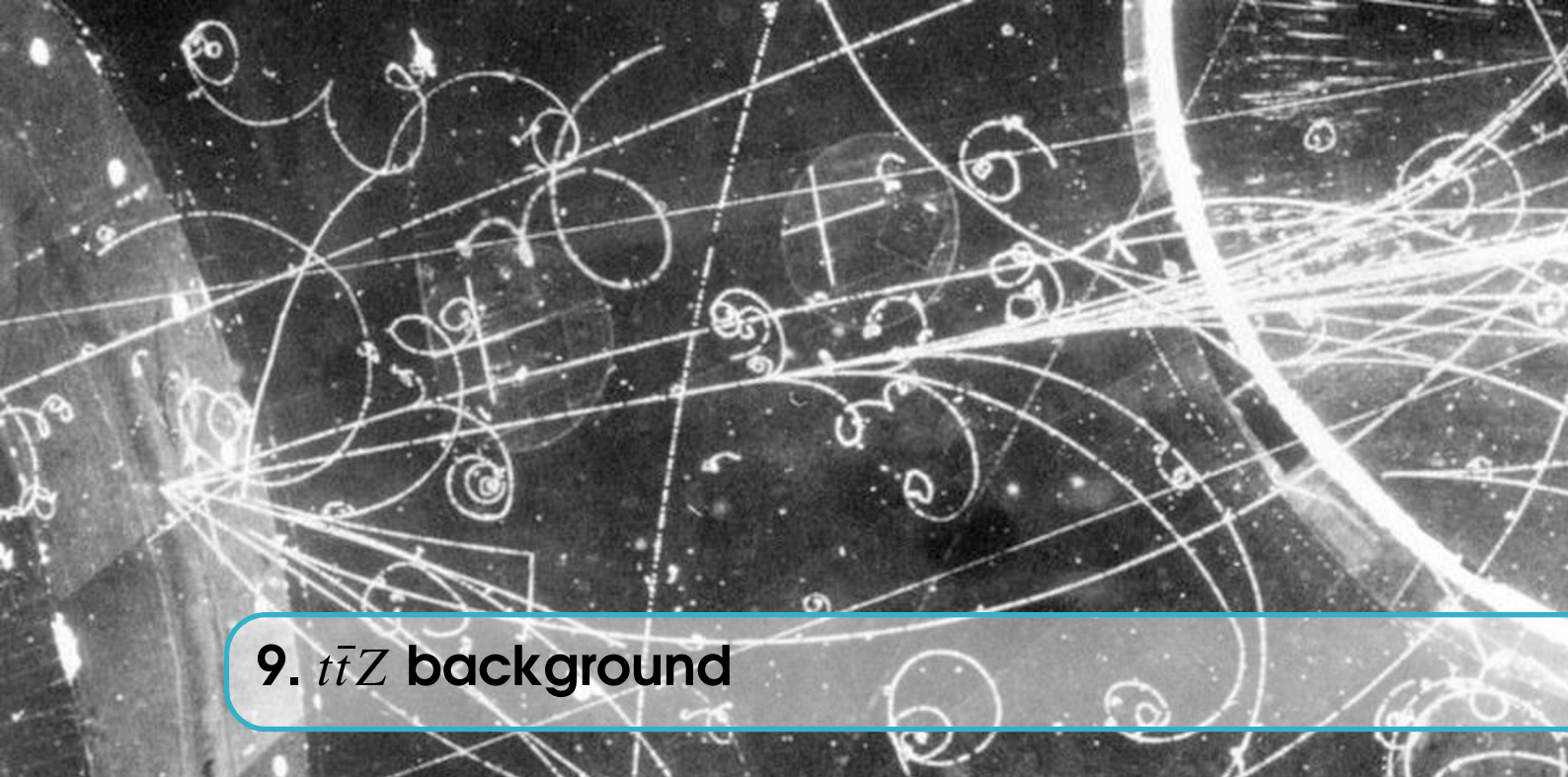


Figure 8.8: Distribution of the variables $m_T^{b,\min}$ (top left) and $m_{\text{jet},R=0.8}^0$ (top right) in CRQA, and $m_T^{b,\max}$ (bottom left) and $m_{\text{jet},R=1.2}^1$ (bottom right) in CRQB. Only the MC statistical uncertainty and the systematic uncertainty from the Jet Smearing method are shown in the yellow (bottom) and red (top) error bands.



9. $t\bar{t}Z$ background

We dedicate this chapter to the presentation of two strategies in the estimation of the irreducible $t\bar{t}Z$ background to the search for direct pair-production of the supersymmetric partner to the top quark in all-hadronic final states. The first one, used in the intermediate Run 2 measurement at 36.1 fb^{-1} [3], relies on boson replacement, considering the $t\bar{t}\gamma$ process instead (Section 9.1). The second (Section 9.2) builds on the measurement of the inclusive $t\bar{t}Z$ cross section in the multi-lepton channel (presented in Chapter 6) to provide a tripleton control region for the follow-up top squark search with the full Run 2 dataset [4], and represents the author’s main contribution to that analysis. This new approach was also implemented in direct top squark searches with one lepton in the final state [276], as well as Z/h mediated top squark decays [277].

9.1 Boson replacement

As described in the previous chapter, the process $t\bar{t}Z(\rightarrow \nu\bar{\nu})$ is a leading irreducible background in the search regions SRA and SRB. Due to the challenging phase-space and unconstrained Z reconstruction, it has never been directly measured by ATLAS. Since it mimics the signal signature of $t\bar{t} + E_{\text{T}}^{\text{miss}}$, one cannot rely only on MC simulation without running the risk of new physics potentially hiding in any mis-modelling of the $Z p_{\text{T}}$ shape.

The use of a multi-lepton CR, targetting $t\bar{t}Z(\rightarrow \ell^+\ell^-)$ would be ideal. However, due to the limited statistics available and the reduced branching fraction of $Z \rightarrow \ell^+\ell^-$, in this and previous all-hadronic top squark searches another approach has to be employed. We will however see in the next section that with the full Run 2 dataset, this multi-lepton CR becomes viable.

9.1.1 Description of the method

The data-driven technique described in what follows relies on the kinematic similarities between the Z boson and the photon as spin-1 bosons, with similar Feynman production diagrams. Despite slightly different cross sections, it can be checked that, given the appropriate choice of phase-space,

“Tracks in a bubble chamber”. © Fermilab.

there are no major shape differences in the p_T distributions of either boson, as is shown in Figure 9.1. We note that boson replacement in the context of the Z +jets background is a fairly well established method [278–281], but its application to the $t\bar{t}Z$ process is very recent.

The selection criteria for a $t\bar{t}\gamma$ CR are found in Table 9.1. It was found that an all-hadronic final state wasn't adequate to reach sufficient $t\bar{t}\gamma$ purity, as this channel is dominated by γ +jets. Instead, a requirement of one lepton is applied. Furthermore, an isolated photon is required, with large enough p_T to both be on plateau of the photon trigger (see Figure 3.10), thereby enjoying full efficiency, and mimic the high E_T^{miss} requirements of the signal regions, since the strategy is based on the approximation $p_T(\gamma) \sim E_T^{\text{miss}}$.

Table 9.1: Selection criteria for the $t\bar{t}\gamma$ one-lepton CR.

Object	Selection
Trigger	single lepton (e or μ)
N_{lep}	1
p_T of lepton	> 28 GeV
N_γ	1
p_T of photon	> 150 GeV
N_{jets}	≥ 4
p_T of jets	(80, 80, 40, 40) GeV
b -jets	≥ 2

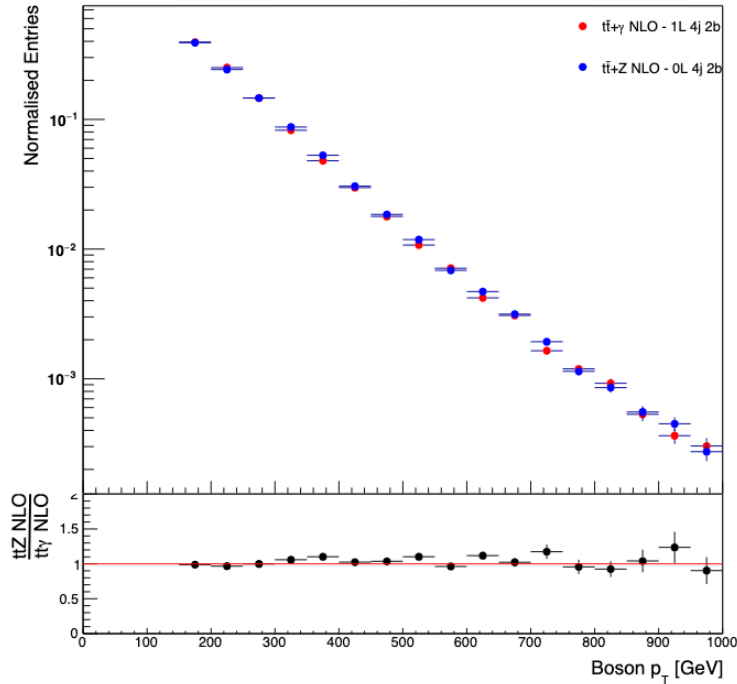


Figure 9.1: Comparison of the truth-level p_T distributions of the relevant bosons for $t\bar{t}Z(\rightarrow \nu\bar{\nu})$ in an SR-like selection and $t\bar{t}\gamma$ in a CR-like selection.

9.1.2 Results

The normalisation of the $t\bar{t}Z(\rightarrow \nu\bar{\nu})$ yields in the signal regions proceeds by means of a simple transfer factor, denoted T_f and taken to be the ratio of $t\bar{t}Z$ to $t\bar{t}\gamma$ in MC. An equivalent formulation compares the yields in data and MC of the $t\bar{t}\gamma$ process in its CR, the $t\bar{t}\gamma$ signal strength parameter or scale factor $\mu_{t\bar{t}\gamma}$. These are related by:

$$N_{t\bar{t}Z}^{\text{exp,SR}} \simeq N_{t\bar{t}\gamma}^{\text{data,CR}} \cdot \frac{N_{t\bar{t}Z}^{\text{MC,SR}}}{N_{t\bar{t}\gamma}^{\text{MC,CR}}} = N_{t\bar{t}\gamma}^{\text{data,CR}} \cdot T_f = N_{t\bar{t}Z}^{\text{MC,SR}} \cdot \mu_{t\bar{t}\gamma}, \quad (9.1)$$

where $N_{t\bar{t}\gamma}^{\text{data,CR}}$ corresponds to the number of $t\bar{t}\gamma$ events observed in data in the CR (subtracting all non- $t\bar{t}\gamma$ events from MC), $N_{t\bar{t}\gamma}^{\text{MC,CR}}$ is the equivalent prediction from pure MC, $N_{t\bar{t}Z}^{\text{MC,SR}}$ the MC prediction for $t\bar{t}Z$ in the signal region and $N_{t\bar{t}Z}^{\text{exp,SR}}$ the final expected yields using this data-driven method.

The approximate equality above becomes exact in the limit of total CR purity: since in practice the CR is contaminated by non- $t\bar{t}\gamma$ processes, the implicit background subtraction from MC in $N_{t\bar{t}\gamma}^{\text{data,CR}}$ is biased. As is shown in Table 9.2, an adequate $t\bar{t}\gamma$ purity of 87% is obtained using the CR definition from Table 9.1 and a $\mu_{t\bar{t}\gamma}$ scale factor (SF) of 1.29 ± 0.12 (stat.) is derived. The scaled distribution of the key variable of interest, $p_T(\gamma)$, is shown in Figure 9.2.

Table 9.2: Background composition of the $t\bar{t}\gamma$ one-lepton CR. Yields are obtained pre-fit, with statistical uncertainties only. The scale factor $\mu_{t\bar{t}\gamma}$ is obtained as the ratio of background-subtracted data to predicted $t\bar{t}\gamma$ and quoted on the last line.

CRTGamma (87% purity)	
$t\bar{t}\gamma$	110 ± 1.5
$V + \gamma$	6.3 ± 0.63
$t\bar{t}$	5.1 ± 1.2
$t\bar{t} + V$	2.3 ± 0.25
single top	2.1 ± 0.80
Z+jets	0.66 ± 0.17
W+jets	0.040 ± 0.020
Total SM	130 ± 2.2
Data	161
SF	1.29 ± 0.12

9.1.3 Limitations

One limitation of using a transfer factor involving not only two different regions, but in this case also two different processes,

$$T_f = \frac{N_{t\bar{t}Z}^{\text{MC,SR}}}{N_{t\bar{t}\gamma}^{\text{MC,CR}}} \quad (9.2)$$

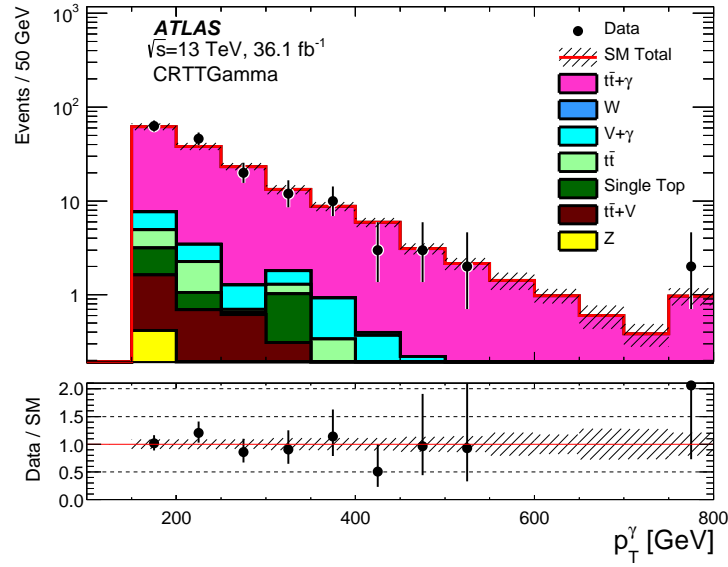


Figure 9.2: Distribution of the transverse momentum of the photon in the $t\bar{t}\gamma$ one-lepton CR, after normalisation of SM processes in a simultaneous fit of all backgrounds to data. The rightmost bin includes overflow events.

is that it leads to only a partial cancellation of the associated theoretical uncertainties, such as scale, PDF and generator variations. When added in quadrature to those theoretical uncertainties on $t\bar{t}Z(\rightarrow \nu\bar{\nu})$ in the signal regions, the uncertainty on T_f itself turns out to be leading. Table 9.3 shows the breakdown of this uncertainty for each signal region. As will be discussed in the next chapter however, the total impact of uncertainties related to the $t\bar{t}Z$ background in the final fit is largely sub-leading.

Table 9.3: Summary of the symmetrised theory uncertainties (in percent) on $t\bar{t}Z$ production obtained on the transfer factor in the signal regions.

Region	Uncertainty (%)
SRA-TT	15.1
SRA-TW	9.9
SRA-T0	13.7
SRB-TT	7.3
SRB-TW	5.7
SRB-T0	3.5

As mentioned in the previous section, one of the underlying assumptions in using this boson replacement method is the similarity between the $t\bar{t}Z$ and $t\bar{t}\gamma$ Feynman production diagrams at leading order. It is worth noting a few caveats to this approximation. Even though both can proceed via FSR or ISR, $t\bar{t}\gamma$ production via FSR raises questions about *bremsstrahlung* and contamination from the electromagnetic radiation of the top quark decay products. At NLO, there also exist $t\bar{t}Z$ diagrams involving neutrino loops, which are completely absent in the case of $t\bar{t}\gamma$ since the photon doesn't couple to neutrinos. This effect is however highly suppressed, being proportional to α_W^5

[282].

The effect of the Z mass could also prove a difficulty. Thankfully, due to the high- p_T phase-space considered, the approximation $p_T(Z) \sim p_T(\gamma)$ holds reasonably well. At low- p_T , one would expect a significant enhancement of the relative photon production (through *bremsstrahlung*), due to the Sudakov suppression of the Z cross-section where the inverse Z mass enters in a logarithmic term [282].

Whereas the interaction of photons with quarks proceeds straightforwardly through the electromagnetic force, with a coupling eQ_q where we recall that Q_q is $\frac{2}{3}$ for up-type quarks and $-\frac{1}{3}$ for down-type quarks, the Z boson interacts with quarks through the weak force, which distinguishes left- and right-handed states with a coupling

$$e \frac{T^3 - \sin^2 \theta_W Q_q}{\cos \theta_W \sin \theta_W}, \quad (9.3)$$

where T^3 is the weak isospin. While the photon couples more strongly to the up-type quarks, the situation is reversed for the Z boson as we have (in the numerator)

$$\begin{cases} \frac{1}{2} - \frac{2}{3} \sin^2 \theta_W & \text{(left),} \\ -\frac{2}{3} \sin^2 \theta_W & \text{(right)} \end{cases} \quad (9.4)$$

for up-type quarks and

$$\begin{cases} -\frac{1}{2} + \frac{1}{3} \sin^2 \theta_W & \text{(left),} \\ \frac{1}{3} \sin^2 \theta_W & \text{(right)} \end{cases} \quad (9.5)$$

for down-type quarks. We can then study the behaviour of the ratio [279, 282]

$$R_q = \frac{\sigma_{t\bar{t}Z}^q}{\sigma_{t\bar{t}\gamma}^q} = \frac{\frac{1}{2} (\sigma_{t\bar{t}Z}^{q,\text{left}} + \sigma_{t\bar{t}Z}^{q,\text{right}})}{\sigma_{t\bar{t}\gamma}^q} \simeq \frac{\left(\frac{1}{2} - |Q_q| \sin^2 \theta_W\right)^2 + \left(Q_q \sin^2 \theta_W\right)^2}{2Q_q^2 \cos^2 \theta_W \sin^2 \theta_W} \quad (9.6)$$

Plugging in the Weinberg angle $\cos \theta_W = \frac{m_W}{m_Z}$, one gets $R_u \approx 0.945$ and $R_d \approx 4.851$. In the limit of pure FSR production (at very high- $p_T(Z, \gamma)$), we would expect the ratio of cross sections to approach R_u since the top quark is an up-type quark. For pure ISR production, there would be a mixture of R_u and R_d .

A simple back-of-the-envelope calculation could be set up as follows. Over N quark-initiated collisions, we expect roughly $\frac{N}{3}$ down quarks and $\frac{2N}{3}$ up quarks. Since $R_u \sim 1$ and $R_d \sim 5$, there are equal numbers of Z and γ events from up partons, but 5 times more Z events than γ events from down partons. Therefore

$$\frac{\sigma_{t\bar{t}Z}}{\sigma_{t\bar{t}\gamma}} \propto \frac{\frac{2N}{3} + \frac{N}{3} \cdot \frac{5}{6}}{\frac{2N}{3} + \frac{N}{3} \cdot \frac{1}{6}} \approx 1.3 \quad (9.7)$$

More subtleties arise, as the valence up quark dominates at high- p_T , driving the ratio closer to $R_u \sim 1$. These cross section ratios, under various production scenarios, are shown in Figure 9.3.

Several observations are to be made from this plot. First of all, as was claimed above, the kinematic differences between $t\bar{t}Z$ and $t\bar{t}\gamma$ are almost p_T -independent above 200–300 GeV, where the Z mass is no longer relevant. The ratio of **ISR** cross sections, plotted in red, is indeed around 1.3 as we have just derived; the slight decrease at high- p_T is the consequence of the argument we have just made about valence up quarks.

More striking is the obvious disagreement between the ratio of **FSR**-initiated cross sections, which we claimed to be around $R_u \sim 1$ but seems to settle at twice that value. The resolution of this problem lies in the polarisation states of the Z : indeed, Z bosons produced from $t\bar{t}$ tend to be polarised longitudinally ($\sim 50\%$), while the massless photon is pure-transverse. The green distribution in Figure 9.3 removes this longitudinal component from the available Z polarisation states, and the ratio is observed to converge to values slightly lower than 1, as expected [282].

The shape uncertainty at **LO** in the key kinematic distributions of $t\bar{t}Z$ and $t\bar{t}\gamma$, estimated by the ratio of a coherent variation of factorisation and renormalisation scales, was previously found to be $\sim 10\%$. As discussed above, it is also more or less completely independent of p_T above 300 GeV. At **NLO**, the uncertainty from additional corrections is $\sim 5\%$ from scale variations, with an additional $\sim 5\%$ coming from the choice of generator and $\sim 2\%$ from the choice of **PDF**. These add up to a maximum theoretical uncertainty on the transfer factor T_f of $\sim 15\%$, as is detailed in Table 9.3.

As we hinted at several times in the previous two sections, the selection cut on $p_T(\gamma) > 150$ GeV serves a double purposes: it ensures full efficiency by placing the selected photon on plateau of the trigger, and reduces the probability of it originating from the decay products of the top quark. This is made more explicit in Figure 9.4, where we see that, with more statistics, a selection of harder photons would make our control sample even more pure in signal $t\bar{t}\gamma$.

Finally, let us note that the selection process of the photon itself, at reconstruction-level, implies a number of factors (trigger efficiency, identification, energy reconstruction, isolation) that could smear the true p_T spectrum of the Z to emulate. Indeed, the neutrinos treated as E_T^{miss} do not suffer from this problem, and could end up anywhere inside the detector. It might then be an improvement to consider the differential yield of the estimated $t\bar{t}Z(\rightarrow \nu\bar{\nu})$ process in a one-lepton selection as a function of boson p_T :

$$dN_{t\bar{t}Z(\rightarrow\nu\bar{\nu})}^{1\ell} = dN_{t\bar{t}\gamma}^{1\ell} \cdot \frac{d\sigma_{t\bar{t}Z}^{\text{NNLO}}}{d\sigma_{t\bar{t}\gamma}^{\text{NNLO}}} \cdot \frac{1}{d\epsilon_\gamma}, \quad (9.8)$$

where $d\epsilon_\gamma$ is the p_T -dependent photon reconstruction efficiency.

Let us end this section by reflecting on the back-of-the-envelope calculations we presented above. At the LHC, $t\bar{t}$ production is dominated by gluon fusion (around 80–90%) and therefore is the main mode of production for both $t\bar{t}Z$ and $t\bar{t}\gamma$ (via **FSR**). We only considered above the differences arising from the coupling of these two vector bosons to quarks. In the case of gluon-initiated processes, the ratio of cross sections has to become equal to R_u (since the top quark is an up-type quark) which is calculated to be $R_u \sim 1$. In the case of quark-initiated processes, the ratio is rather a mixture of R_u and R_d in the pure **ISR** regime, and again only R_u in the pure **FSR** regime. These are therefore only asymptotic behaviours (pure **ISR**, pure **FSR**, gluon- or quark-initiated only), when the actual behaviour of such a ratio would more accurately described by a weighted sum of all these **LO** contributions, plus **NLO** corrections, efficiency and acceptance effects, mass differences, etc. Figure 9.1 shows such a computation (using **NLO+PS** generated events), and the ratio of cross sections at high enough p_T is indeed close to 1.

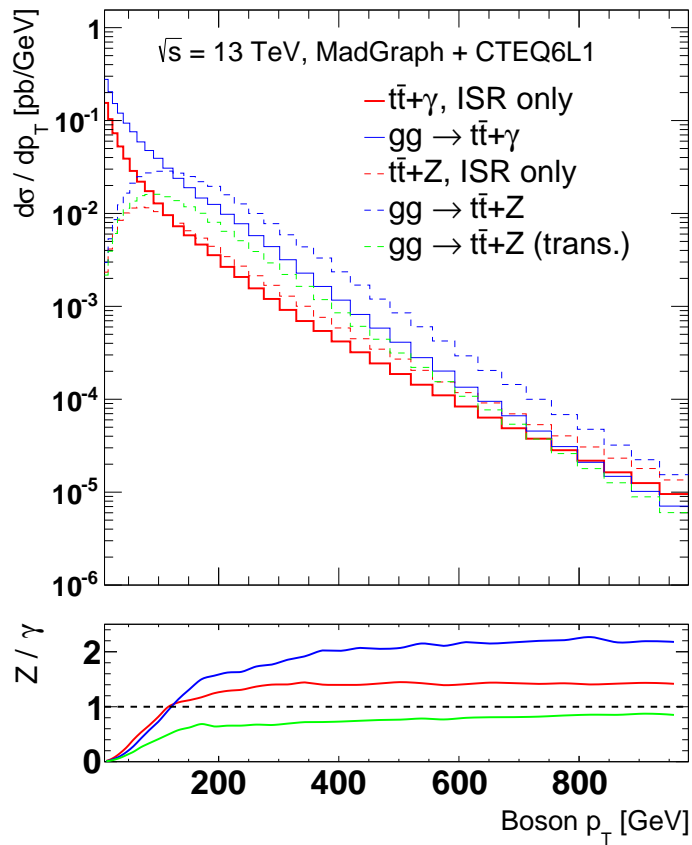


Figure 9.3: Comparison of the boson p_T distributions of $t\bar{t}Z$ and $t\bar{t}\gamma$ at truth-level. Photon radiation from top quark decay products is not included. From [282].

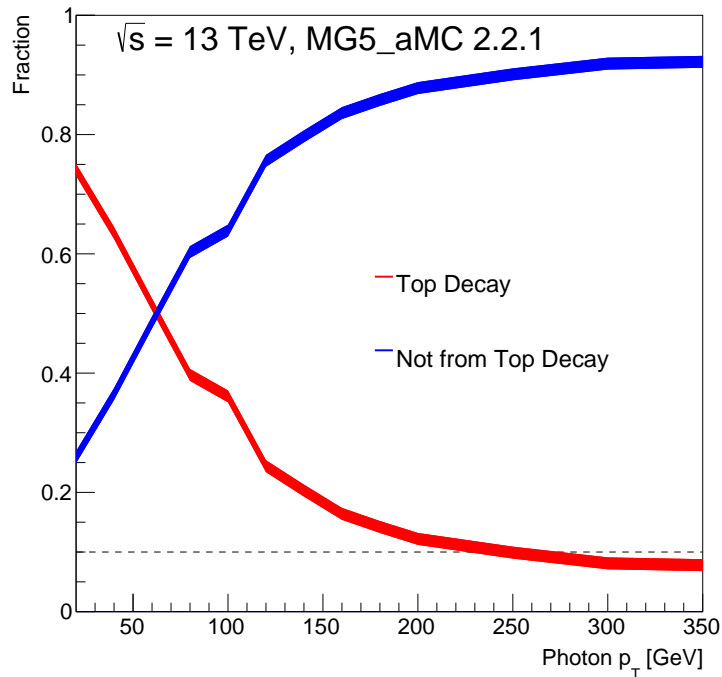


Figure 9.4: Comparison of the fraction of photons radiated from the decay products of the top quark (red) and radiated either directly from the top quark or as ISR (blue). From [282].

9.2 Multi-lepton approach

Following the measurement of the inclusive $t\bar{t}Z$ cross section at 36.1 fb^{-1} by ATLAS in the multi-lepton final state and the availability of almost four times as much statistics with the full Run 2 dataset as with the 2015–2016 one, an estimation of $t\bar{t}Z(\rightarrow \nu\bar{\nu})$ through $t\bar{t}Z(\rightarrow \ell^+\ell^-)$ becomes a viable and attractive prospect. It solves all the problems highlighted in the previous section by simply getting rid of the need for boson replacement and ensures a reduced theoretical uncertainty on the transfer factor from the CR to the SR.

Based on the results of the inclusive $t\bar{t}Z$ analysis, it is clear that a three-lepton control region, described in what follows, is the most promising choice. Indeed, the 2LOS channel is still dominated by the $t\bar{t}$ and Z +jets backgrounds and would introduce unwanted correlations in the systematics (beyond the obvious problem of signal discrimination, as is shown in Figure 9.5), while the 4L channel, although of high purity, is still statistically limited.

It is worth noting that this section refers to the extended search for the supersymmetric partner to the top quark in the all-hadronic final state. It is however very similar in its approach to the 2015–2016 analysis we’ve described so far, up to minor differences in object definitions. We will therefore not introduce the complete analysis again, and wish only to point out the improvement in the $t\bar{t}Z$ estimation. Other searches for supersymmetry, such as for direct top squark pair production in the one- and two-lepton channels, as well as with Z/h mediation, also use the same method.

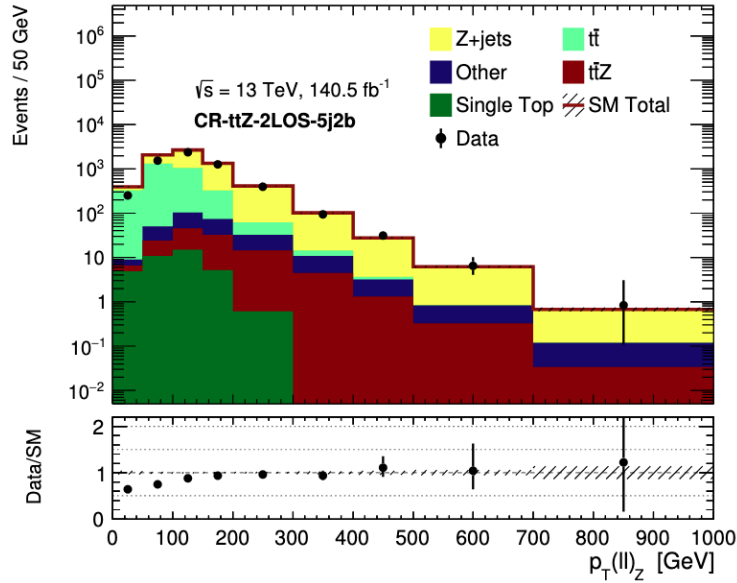


Figure 9.5: Attempt at a definition of a suitable CR for $t\bar{t}Z$ in the 2LOS channel, with simple kinematic cuts requiring a Z candidate, at least two b -jets and exactly 5 jets. The signal $t\bar{t}Z$ contribution is found to be largely sub-leading.

9.2.1 Three-lepton control region

The control region designed for $t\bar{t}Z$ in the three-lepton channel is very similar to the 3L-Z-2b4j region of the inclusive $t\bar{t}Z$ analysis, with additional tightening cuts to bring it closer to the A and B signal regions. Specifically, in order to mimic more closely the jet kinematics of the all-hadronic final state, both the lepton identified as not originating from the decay of the Z and its accompanying neutrino (taken as the full event E_T^{miss}) are treated as jets when applying requirements on the p_T of jets in the event. The transverse momentum of the reconstructed Z boson, used to model E_T^{miss} in the SR, is bounded from below at 200 GeV. The full selection criteria are outlined in Table 9.4 below.

Table 9.4: Selection criteria for the $t\bar{t}Z$ three-lepton CR.

Object	Selection
Trigger	single lepton (e or μ)
N_{lep}	3
p_{T} of leptons	(27, 20, 20) GeV
Z-like OSSF pair	yes
Sum of charges	± 1
N_{jets}	≥ 4
p_{T} of jets	(80, 80, 40, 40) GeV
b -jets	≥ 2
$p_{\text{T}}(Z)$	> 200 GeV

9.2.2 Results

As is shown in Table 9.5, a high purity of 80% is obtained using the CR definition from Table 9.4 and a $\mu_{t\bar{t}Z}$ scale factor (SF) of 0.85 ± 0.12 (stat.) is derived. The distribution of the key variable of interest, $p_{\text{T}}(Z)$, is shown in Figure 9.6. The breakdown of the theoretical uncertainties on T_f is presented in Table 9.6. A significant improvement (up to 10 percentage points) is noted, with respect to the equivalent numbers from the $t\bar{t}\gamma$ method in Table 9.3. This is a direct result of the more complete cancellation of theoretical uncertainties in the transfer from CR to SR, as promised at the beginning of this section.

Table 9.5: Background composition of the $t\bar{t}Z$ three-lepton CR. Yields are obtained pre-fit, with statistical uncertainties only. The scale factor $\mu_{t\bar{t}Z}$ is obtained as the ratio of background-subtracted data to predicted $t\bar{t}Z$ and quoted on the last line. ‘‘Other’’ processes include rare top quark and multi-boson processes as well as tWZ and tZ production.

CRRTZ (80% purity)	
$t\bar{t}Z$	53 ± 0.58
WZ+jets	4.7 ± 0.16
Fakes (MC)	0.55 ± 0.17
Other	8.4 ± 0.32
Total SM	67 ± 0.70
Data	59
SF	0.85 ± 0.12

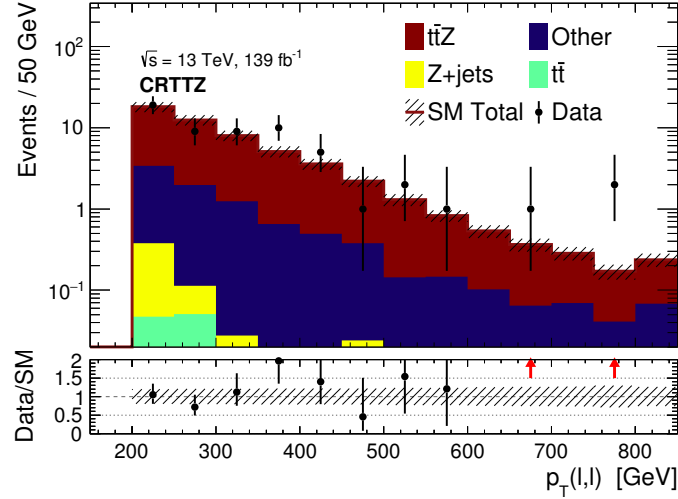
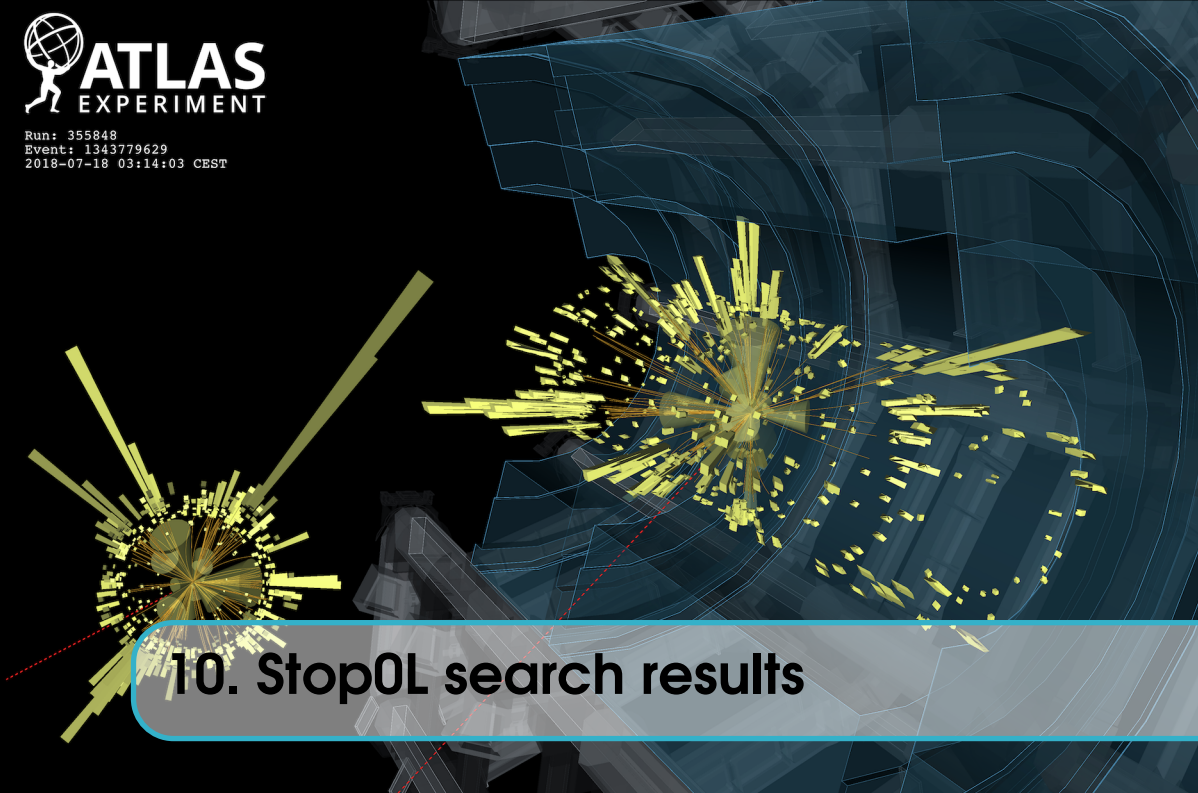


Figure 9.6: Distribution of the transverse momentum of the Z in the $t\bar{t}Z$ three-lepton CR, after normalisation of SM processes in a simultaneous fit of all backgrounds to data. “Other” processes include rare top quark and multi-boson processes as well as tWZ and tZ production. The rightmost bin includes overflow events.

Table 9.6: Summary of the theory uncertainties (in percent, rounded up to the nearest integer) on $t\bar{t}Z$ production obtained on the transfer factor in the signal regions.

Region	Uncertainty (%)
SRA-TT	10
SRA-TW	5
SRA-T0	3
SRB-TT	3
SRB-TW	5
SRB-T0	4



10. Stop0L search results

In this chapter we finish the review of the search for direct pair-production of the supersymmetric partner to the top quark in the all-hadronic final state at 36.1 fb^{-1} of pp collisions at $\sqrt{s} = 13 \text{ TeV}$, introduced in Chapter 8. In Section 10.1, we discuss the treatment of systematic uncertainties; those related to the estimate of the irreducible $t\bar{t}Z$ background were extensively discussed in Chapter 9. Finally, in Section 10.2, we present the results of three types of statistical fits: background-only, discovery and exclusion; as previously defined in Section 4.1. These results were published by the ATLAS Collaboration in Ref. [3].

10.1 Systematic uncertainties

In what follows, we distinguish between two types of systematic uncertainties: those related to detector effects and the reconstruction and calibration of physics objects on one hand, and to the modelling of the various background processes from theoretical calculations on the other.

10.1.1 Experimental uncertainties

Luminosity The luminosity estimate for the data-taking years 2015 and 2016 has an uncertainty of 2.1% in $\sqrt{s} = 13 \text{ TeV}$ analyses, using a method similar to that in Ref. [244]. The luminosity measurement and its uncertainty are based on calibrations performed in low-luminosity runs of the LHC by the LUCID-2 detector [245] (van der Meer scans) and transferred to the high-luminosity range. This uncertainty is applied to all processes determined from Monte Carlo simulations.

Jet Energy Scale (JES) and Jet Energy Resolution (JER) These are the two main uncertainties affecting the reconstructed momentum of jets; schematically: $E_{\text{reco}} = \text{JES} \cdot E_{\text{measured}} + \text{JER}$. The JES correction relates the response of the calorimeter to the true jet energy at parton-level from MC. It is derived in bins of p_T and η , and also includes uncertainties related to flavour composition and pile-up [213]. A reduced set of only 4 nuisance parameters is employed. The JER uncertainty

“High jet multiplicity event”. Image credits: ATLAS Experiment. © 2020 CERN.

is derived as a one-sided variation by comparing data to MC simulation in-situ [283]. Both JES and JER variations are propagated to the calculation of the E_T^{miss} .

b-tagging The b -tagging uncertainty is a large contribution in both signal and background due to the two b -jets requirement of this analysis. Scale factor uncertainties are derived as a function of kinematics and jet flavour. Three kinds of uncertainties on the b -jet weight, up and down, are calculated, propagating the estimated uncertainties on the scale factors for b -jets as well as a mis-tagging correction to c -jets and light-flavour jets.

E_T^{miss} Soft-term Resolution and Scale The scale and resolution uncertainties of individual objects need to be propagated to the E_T^{miss} . Specific systematic uncertainties on the scale and resolution of E_T^{miss} soft term have been derived by two different in-situ methods using $Z \rightarrow \mu\bar{\mu}$ events [241].

Lepton efficiencies Lepton reconstruction and identification efficiencies have contributions to the background estimates. For electrons, the uncertainties originate from the e/γ resolution and scale, as well as from the reconstruction efficiency. Similarly, for muons the uncertainties originate from the muon resolution and reconstruction efficiencies, the isolation and the momentum scale. The lepton trigger scale factors are also included.

Pile-up The uncertainty due to pile-up re-weighting is considered as a two-sided variation in the event weights.

10.1.2 Theoretical uncertainties

Theoretical uncertainties affect both the background normalisation and the shape of kinematic distributions, impacting the background prediction in the signal regions. Statistical uncertainties in the evaluation of systematics are neglected in general, thanks to the large number of available MC events. The theoretical uncertainties listed below are evaluated from the signal regions by considering variations with respect to the default settings and choices for the event generation. For each variation of a background normalised in a control region, the associated systematic is taken on the corresponding transfer factor.

Z+jets The nominal SHERPA 2.2.2 generator is used, with the renormalisation and factorisation scales varied in a seven-point envelope. The theory uncertainty on the normalisation of the Z production is obtained by comparing the SHERPA prediction on the transfer factor between the CR and the SR with and without these variations applied. The uncertainty on the transfer factor is computed according to

$$\Delta_X = \frac{T_f^{\text{up}} - T_f^{\text{down}}}{T_f^{\text{up}} + T_f^{\text{down}}}, \quad (10.1)$$

where X denotes a single variation. The largest uncertainty is 5.5% in SRA-T0.

W+jets A similar approach is performed to assess the W +jets theory uncertainties, also using the nominal SHERPA generator with internal weight variations. The largest uncertainty on the transfer factor is found to be 9.5% in SRA-TT.

$t\bar{t}$ The uncertainty related to hard scatter generation is computed by comparing the nominal POWHEG+PYTHIA sample to MADGRAPH5_aMC@NLO +PYTHIA. Similarly, the parton shower component is estimated by comparing the nominal sample to a Herwig++ generated one. For both these uncertainties, the relevant uncertainty on the transfer factor is given by

$$\Delta_X = \frac{T_f^{\text{nom}} - T_f^{\text{var}}}{T_f^{\text{nom}}}. \quad (10.2)$$

The **ISR/FSR** uncertainties, covering the emission of additional partons in the initial or final state, are evaluated from dedicated POWHEG+PYTHIA samples where the value of α_S is varied up and down. The final uncertainties on the transfer factor typically range from a few percents to 30% and are largely dominated by the generator comparison.

Single top The single top quark background, mainly the Wt sub-process, is evaluated in a similar fashion for the parton shower and ISR/FSR components, but no alternative generator to the nominal POWHEG+PYTHIA one was available. The interference with $t\bar{t}$ is taken into account and conservatively capped at 30%, from comparisons between $WWbb$ events and the sum of $t\bar{t}$ and Wtb . This method is used as an alternative to the usual **DS** vs **DR** approach, since in this case it yields unphysically large results. The ISR/FSR uncertainty on the transfer factor is found to be largely dominant for single top quark production, up to 26%.

$t\bar{t} + W/Z/\gamma$ Scale and NNPDF3.0NLO set variations are used to estimate the modelling uncertainties on the $t\bar{t}W$, $t\bar{t}Z$ and $t\bar{t}\gamma$ processes. To cover the differences at NLO between $t\bar{t}\gamma$ and $t\bar{t}Z$, a comparison is performed between the nominal MADGRAPH5_aMC@NLO +PYTHIA samples and SHERPA +OPENLOOPS. The relative difference between cross section ratios is added in quadrature to the scale and **PDF** uncertainties. The final theoretical uncertainties on the $t\bar{t}Z$ transfer factor were previously shown in Table 9.3.

Diboson A conservative 50% uncertainty is placed on the cross section normalisation of the diboson background, largely sub-dominant and for which no dedicated **CR** was designed.

Signal component The uncertainties in the **MC** modelling of the **SUSY** signal processes are evaluated by varying the parameters of the nominal MADGRAPH +PYTHIA 8 simulation, specifically: α_S , the **QCD** scales, the **CKKW** matching scale and parameters of the A14 **UE** tune. The final uncertainty typically ranges from 10% to 30%.

Table 10.1 presents the impact of the combined experimental and theoretical systematics in the signal regions after the background-only fit (described in the next section). The modelling of the $t\bar{t}$ background is a significant uncertainty across most regions (around 10%), together with the **JER/JES** uncertainties and pile-up modelling (3 – 10%). The relative uncertainties on the background normalisation are largest for the Z +jets process, although $t\bar{t}Z$ has a similar impact in SRA-TT.

Table 10.1: Dominant systematic uncertainties (greater than 1% for at least one SR) for SRA and SRB in percent relative to the total background estimates. The uncertainties due to the normalization from a control region for a given signal region and background are indicated by μ_X . The theory uncertainties are the total uncertainties for a given background.

	SRA-TT	SRA-TW	SRA-T0	SRB-TT	SRB-TW	SRB-T0
Total syst. unc.	24	23	15	19	14	15
$t\bar{t}$ theory	10	6	3	10	11	12
$t\bar{t} + V$ theory	2	< 1	< 1	1	< 1	< 1
Z theory	1	3	2	< 1	1	< 1
Single top theory	6	3	5	3	4	5
Diboson theory	< 1	2	< 1	< 1	< 1	< 1
$\mu_{t\bar{t}}$	< 1	< 1	< 1	2	2	1
$\mu_{t\bar{t}Z}$	6	3	2	4	3	2
μ_Z	6	10	7	5	6	4
μ_W	1	1	1	2	1	2
$\mu_{\text{single top}}$	5	3	5	4	4	5
JER	10	12	4	3	4	3
JES	4	7	1	7	4	< 1
b-tagging	1	3	2	5	4	4
E_T^{miss} soft term	2	2	< 1	1	< 1	< 1
Multijet estimate	1	< 1	< 1	2	2	< 1
Pile-up	10	5	5	8	1	3

10.2 Results

We present in this section the results of the likelihood fits to data in the relevant signal and control regions, including discovery p -values and limits on various signal models.

10.2.1 Description of fits

Three different likelihood fits are performed, following the statistical description given in Section 4.1:

Background-only fit Only the CR are used to constrain the fit parameters (background strengths μ_b). Potential signal contamination is neglected and the number of observed events in the SR is not taken into account.

Discovery fit Both CRs and SRs are used to constrain the fit parameters (including the signal strength μ_s). A potential signal contamination is considered in the SRs but neglected in the CRs, which leads to a conservative estimate of the background contribution in the SRs. This fit configuration is further used to produce model-independent upper limits on the visible signal cross-sections and quote discovery p -values in the case of significant data excesses.

Exclusion fit Similar to the discovery fit, except the signal contribution is also fitted in the CRs using an additional free parameter in the likelihood that is constrained to be non-negative. In this case, the background estimates might differ from the previous two fits. This exclusion fit is used to derive all the model-dependents limits.

10.2.2 Background-only fit

The yields in the control regions, including experimental and theoretical systematic uncertainties, are detailed in Tables 10.2-10.5. The resulting scale factors are summarised in Table 10.6. Key distributions in the W , Z and single top quark control regions, with the appropriate background normalisations, were previously shown in Figures 8.6 and 8.7, and for $t\bar{t}$ in Figure 9.2.

Table 10.2: Results of the background-only fit in CRTopA. The expected (“exp.”) and fitted (“fit.”) total SM contributions are indicated separately. The uncertainties are statistical and systematic.

Yields	CRTopA-TT	CRTopA-TW	CRTopA-T0
Observed events	89	143	76
Total SM (fit.)	89 ± 9.4	140 ± 12	76 ± 8.7
$t\bar{t}$	80 ± 9.6	130 ± 13	67 ± 8.9
W +jets	3.3 ± 0.60	2.0 ± 0.86	3.1 ± 0.99
Z +jets	0.020 ± 0.010	0.010 ± 0.010	$0. \pm 0.020$
$t\bar{t} + V$	1.7 ± 0.46	1.9 ± 0.38	1.2 ± 0.26
Single top	4.1 ± 1.5	5.0 ± 2.0	4.5 ± 1.7
Diboson	—	1.7 ± 1.7	—
Multi-jet	—	—	—
Total SM (exp.)	76 ± 2.5	130 ± 4.3	82 ± 2.0

Table 10.3: Results of the background-only fit in CRTopB. The expected (“exp.”) and fitted (“fit.”) total SM contributions are indicated separately. The uncertainties are statistical and systematic.

Yields	CRTopB-TT	CRTopB-TW	CRTopB-T0
Observed events	86	275	417
Total SM (fit.)	86 ± 9.3	280 ± 17	420 ± 20
$t\bar{t}$	76 ± 9.3	250 ± 17	390 ± 21
W +jets	4.1 ± 0.81	4.6 ± 1.2	5.5 ± 1.1
Z +jets	0.030 ± 0.010	0.010 ± 0.010	0.20 ± 0.11
$t\bar{t} + V$	1.5 ± 0.48	3.6 ± 0.73	3.9 ± 0.82
Single top	4.5 ± 1.7	11 ± 3.7	16 ± 5.3
Diboson	—	1.6 ± 1.6	0.46 ± 0.25
Multi-jet	—	—	—
Total SM (exp.)	71 ± 2.6	280 ± 6.0	450 ± 6.1

Table 10.4: Results of the background-only fit in CRW and CRST. The expected (“exp.”) and fitted (“fit.”) total SM contributions are indicated separately. The uncertainties are statistical and systematic.

Yields	CRW	CRST
Observed events	533	114
Total SM (fit.)	530 ± 23	110 ± 11
$t\bar{t}$	120 ± 19	30 ± 11
W +jets	350 ± 39	26 ± 6.1
Z +jets	1.9 ± 0.62	0.10 ± 0.060
$t\bar{t} + V$	1.2 ± 0.43	3.1 ± 0.59
Single top	55 ± 20	53 ± 18
Diboson	10 ± 2.4	1.6 ± 0.79
Multi-jet	—	—
Total SM (exp.)	460 ± 21	100 ± 12

Table 10.5: Results of the background-only fit in CRZAB. The expected (“exp.”) and fitted (“fit.”) total SM contributions are indicated separately. The uncertainties are statistical and systematic.

Yields	CRZAB-TT	CRZAB-TW
Observed events	68	119
Total SM (fit.)	68 ± 8.3	120 ± 11
$t\bar{t}$	1.5 ± 1.5	3.5 ± 1.9
W+jets	—	—
Z+jets	48 ± 9.2	95 ± 11
$t\bar{t} + V$	15 ± 1.8	15 ± 2.1
Single top	—	—
Diboson	3.9 ± 1.9	5.7 ± 1.4
Multi-jet	—	—
Total SM (exp.)	58 ± 4.3	110 ± 4.2

Table 10.6: Fitted scale factors obtained after the background-only fit, presented for each targeted signal region and top quark category. Uncertainties are experimental and systematic.

Fitted SF	SRA-TT	SRA-TW	SRA-T0	SRB-TT	SRB-TW	SRB-T0
$t\bar{t}$	1.17 ± 0.15	1.14 ± 0.11	0.90 ± 0.12	1.20 ± 0.16	0.97 ± 0.07	0.92 ± 0.05
W+jets			1.27 ± 0.15			
Z+jets	1.17 ± 0.24		1.13 ± 0.14	1.17 ± 0.24		1.13 ± 0.14
Single top			1.17 ± 0.39			
$t\bar{t}\gamma$ ($t\bar{t}Z$)			1.29 ± 0.20			

10.2.3 Discovery fit

The unblinded yields in the signal regions, including experimental and theoretical systematic uncertainties, are detailed in Tables 10.7 and 10.8, and further summarised (along with the additional signal regions not covered in this thesis) in Figure 10.1. Key distributions are shown in Figure 10.2.

No significant excess over the fitted SM predictions is observed in any of the SR. The corresponding p -values are reported in Table 10.9, along with the 95% CL upper limits on the number of signal events (S_{obs}^{95}) and model-independent upper limits on the visible BSM cross-section, defined as S_{obs}^{95} normalised by the integrated luminosity and weighed by efficiency (ϵ) and acceptance (A) corrections terms. The values of $A \cdot \epsilon$ are evaluated separately for each signal region from their respective benchmark points, and are found to be $\sim 9\%$ in SRA and $\sim 1.5\%$ in SRB.

Table 10.7: Results of the likelihood fit in SRA. The expected (“exp.”) and fitted (“fit.”) total SM contributions are indicated separately. The uncertainties are statistical and systematic.

Yields	SRA-TT	SRA-TW	SRA-T0
Observed events	11	9	18
Total SM (fit.)	8.6 ± 2.1	9.4 ± 2.2	19 ± 2.7
$t\bar{t}$	0.71 ± 0.71	0.51 ± 0.51	1.3 ± 0.64
W +jets	0.82 ± 0.15	0.89 ± 0.56	2.0 ± 0.83
Z +jets	2.5 ± 1.3	4.9 ± 1.9	9.8 ± 1.6
$t\bar{t} + V$	3.2 ± 0.66	1.8 ± 0.39	2.6 ± 0.53
Single top	1.2 ± 0.81	0.70 ± 0.42	2.9 ± 1.5
Diboson	—	0.35 ± 0.26	—
Multi-jet	0.21 ± 0.10	0.14 ± 0.090	0.12 ± 0.070
Total SM (exp.)	7.1 ± 1.6	7.9 ± 1.5	16 ± 2.1

10.2.4 Exclusion fit

Model-dependent limits are further set by combining the orthogonal signal sub-regions (top quark categories) and computing CL_s for each model point in the \tilde{t}_1 - $\tilde{\chi}_1^0$ signal grid. The expected limits are obtained from the background expectation values, with a corresponding error band of $\pm 1\sigma_{\text{exp}}$. The observed limits are determined from the observed event yields in each SR and carry a $\pm 1\sigma_{\text{theory}}^{\text{SUSY}}$ uncertainty on the signal cross-sections. These exclusion contours in the $m(\tilde{t}_1, \tilde{\chi}_1^0)$ plane are shown in Figure 10.3. Limits on the \tilde{t}_1 mass from the previous Run 1 analysis are extended by more than 250 GeV for a $\tilde{\chi}_1^0$ mass below 200 GeV. Improvement is also noticeable along the diagonal band, defined by $m_{\tilde{t}_1} = m_t + m_{\tilde{\chi}_1^0}$.

For signal models also considering top squark decays into $b + \tilde{\chi}_1^\pm$ or into additional massive neutralinos, four interpretations are considered:

Natural SUSY-inspired mixed grid A simplified model where $m_{\tilde{\chi}_1^\pm} = m_{\tilde{\chi}_1^0} + 1$ GeV with only two decay modes, $\tilde{t}_1 \rightarrow b + \tilde{\chi}_1^\pm$ and $\tilde{t}_1 \rightarrow t + \tilde{\chi}_1^0$, and only on-shell top quark decays are considered. The same maximal mixing between the partners of the left- and right-handed top quarks and nature of the $\tilde{\chi}_1^0$ (pure bino) as for the $B(\tilde{t}_1 \rightarrow t + \tilde{\chi}_1^0) = 100\%$ case is assumed. The branching ratio to

Table 10.8: Results of the likelihood fit in SRB. The expected (“exp.”) and fitted (“fit.”) total SM contributions are indicated separately. The uncertainties are statistical and systematic.

Yields	SRB-TT	SRB-TW	SRB-T0
Observed events	38	53	206
Total SM (fit.)	39 ± 7.6	52 ± 7.4	180 ± 26
$t\bar{t}$	7.4 ± 4.4	12 ± 5.9	44 ± 22
W +jets	7.8 ± 2.8	4.8 ± 1.2	26 ± 8.8
Z +jets	9.0 ± 2.8	17 ± 4.1	61 ± 9.6
$t\bar{t} + V$	9.3 ± 1.7	11 ± 1.6	20 ± 3.2
Single top	4.2 ± 2.2	5.9 ± 2.8	26 ± 13
Diboson	0.13 ± 0.070	0.60 ± 0.43	1.0 ± 0.73
Multi-jet	1.5 ± 0.64	1.0 ± 0.88	1.8 ± 1.5
Total SM (exp.)	32 ± 6.0	46 ± 7.1	160 ± 26

Table 10.9: Left to right: 95% CL upper limits on the visible cross section ($\langle A \cdot \epsilon \rangle_{\text{obs}}^{95}$) and on the number of signal events (S_{obs}^{95}). The third column (S_{exp}^{95}) shows the 95% CL upper limit on the number of signal events, given the expected number (and $\pm 1\sigma$ excursions on the expectation) of background events. The last two columns indicate the CL_b value, i.e. the confidence level observed for the background-only hypothesis, and the discovery p -value (significance).

Signal region	$\langle A \cdot \epsilon \rangle_{\text{obs}}^{95}$ [fb]	S_{obs}^{95}	S_{exp}^{95}	CL_b	p -value (Z)
SRA-TT	0.30	11.0	$8.7^{+3.0}_{-1.4}$	0.78	0.23 (0.74)
SRA-TW	0.27	9.0	$9.6^{+2.8}_{-2.1}$	0.50	0.50 (0.00)
SRA-T0	0.31	11.2	$11.5^{+3.8}_{-2.0}$	0.46	0.50 (0.00)
SRB-TT	0.54	19.6	$20.0^{+6.5}_{-4.9}$	0.46	0.50 (0.00)
SRB-TW	0.60	21.7	$21.0^{+7.3}_{-4.3}$	0.54	0.37 (0.33)
SRB-T0	2.19	79.1	$57.9^{+22.5}_{-16.7}$	0.83	0.13 (1.15)

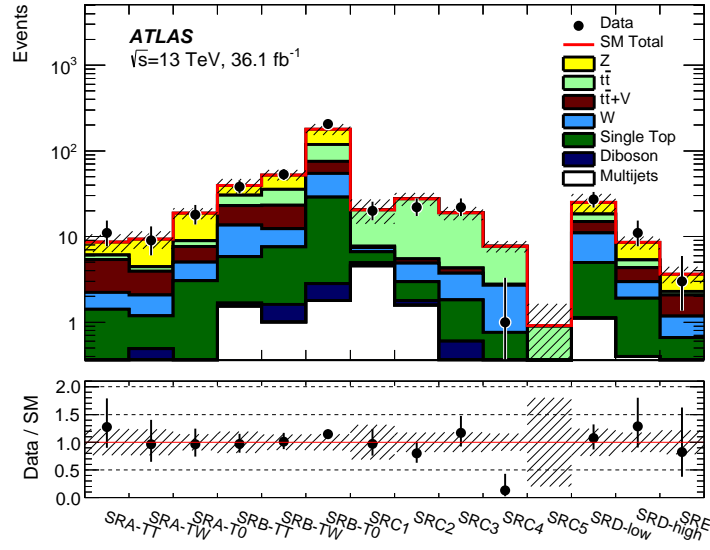


Figure 10.1: Yields for all signal regions after the likelihood fit. The stacked histograms show the SM prediction and the hatched uncertainty band around the SM prediction shows total uncertainty, which consists of the MC statistical uncertainties, detector-related systematic uncertainties, and theoretical uncertainties in the extrapolation from CR to SR.

$\tilde{t}_1 \rightarrow t + \tilde{\chi}_1^0$ is set to 0%, 25%, 50% and 75% and yield the limits shown in Figure 10.4.

Non-asymptotic higgsino A pMSSM-inspired simplified model with a higgsino LSP, $m_{\tilde{\chi}_1^\pm} = m_{\tilde{\chi}_1^0} + 5 \text{ GeV}$, and $m_{\tilde{\chi}_2^0} = m_{\tilde{\chi}_1^0} + 10 \text{ GeV}$, assumes three sets of branching ratios for the considered decays of $\tilde{t} \rightarrow t\tilde{\chi}_2^0$, $\tilde{t} \rightarrow t + \tilde{\chi}_1^0$, $\tilde{t} \rightarrow b\tilde{\chi}_1^\pm$. A set of branching ratios with $B(\tilde{t} \rightarrow t\tilde{\chi}_2^0, \tilde{t} \rightarrow t + \tilde{\chi}_1^0, \tilde{t} \rightarrow b\tilde{\chi}_1^\pm) = 33\%, 33\%, 33\%$ is considered, which is equivalent to a pMSSM model with the lightest stop mostly consisting of the superpartner of the left-handed top quark and $\tan\beta = 60$ (ratio of vacuum expectation values of the two Higgs doublets). Additionally, $B(\tilde{t} \rightarrow t\tilde{\chi}_2^0, \tilde{t} \rightarrow t + \tilde{\chi}_1^0, \tilde{t} \rightarrow b\tilde{\chi}_1^\pm) = 45\%, 10\%, 45\%$ and $B(\tilde{t} \rightarrow t\tilde{\chi}_2^0, \tilde{t} \rightarrow t + \tilde{\chi}_1^0, \tilde{t} \rightarrow b\tilde{\chi}_1^\pm) = 25\%, 50\%, 25\%$ are assumed, which correspond to scenarios with $m_{\tilde{q}L3} < m_{\tilde{t}R}$ (regardless of the choice of $\tan\beta$) and $m_{\tilde{t}R} < m_{\tilde{q}L3}$ with $\tan\beta = 20$, respectively. Here $m_{\tilde{q}L3}$ represents the left-handed third-generation mass parameter and $m_{\tilde{t}R}$ is the mass parameter of the superpartner to the right-handed top quark. Limits in the $m(\tilde{t}_1, \tilde{\chi}_1^0)$ plane are shown in Figure 10.5.

Wino-NLSP pMSSM A pMSSM model where the LSP is bino-like and has mass M_1 and where the NLSP is wino-like with mass M_2 , while $M_2 = 2M_1$ and $m_{\tilde{t}_1} > M_1$. Limits are set for both positive and negative μ (the higgsino mass parameter) as a function of the \tilde{t} and $\tilde{\chi}_1^0$ masses which can be translated to different M_1 and $m_{\tilde{q}L3}$, and are shown in Figure 10.6. Only bottom and top squark production are considered in this interpretation. Allowed decays in the top squark production scenario are $\tilde{t} \rightarrow t\tilde{\chi}_2^0 \rightarrow h/Z\tilde{\chi}_1^0$, at a maximum branching ratio of 33%, and $\tilde{t} \rightarrow b\tilde{\chi}_1^\pm$. Whether the $\tilde{\chi}_2^0$ dominantly decays into a h or Z is determined by the sign of μ . Along the diagonal region, the $\tilde{t} \rightarrow t + \tilde{\chi}_1^0$ decay with 100% branching ratio is also considered. The equivalent decays in bottom-squark production are $\tilde{b} \rightarrow t\tilde{\chi}_1^\pm$ and $\tilde{b} \rightarrow b\tilde{\chi}_2^0$. The remaining pMSSM parameters have the following values: $M_3 = 2.2 \text{ TeV}$ (gluino mass parameter), $M_S = \sqrt{m_{\tilde{t}_1} m_{\tilde{t}_2}} = 1.2 \text{ TeV}$ (geometric mean of stop masses), $X_t/M_S = \sqrt{6}$ (mixing parameter between the superpartners of left- and

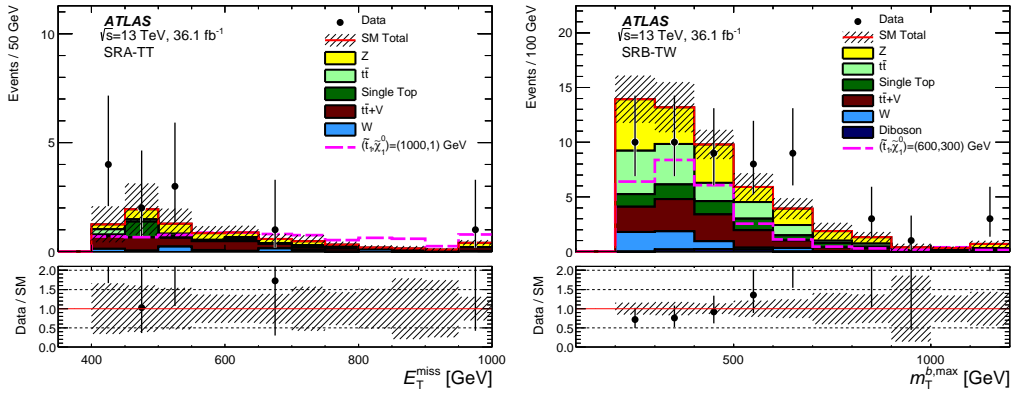


Figure 10.2: Distributions of E_T^{miss} in SRA-TT (left) and $m_T^{b,\text{max}}$ in SRB-TW (right) after the likelihood fit. The stacked histograms show the SM prediction and the hatched uncertainty band around the SM prediction shows the MC statistical and detector-related systematic uncertainties. For each variable, the distribution for a representative signal point is shown.

right-handed states, where $X_t = A_t - \mu/\tan\beta$ and A_t is the trilinear coupling parameter in the top squark sector), and $\tan\beta = 20$. All other pMSSM masses are set to > 3 TeV and effectively decoupled.

Well-tempered neutralino pMSSM A pMSSM model in which three light neutralinos and a light chargino, which are mixtures of bino and higgsino states, are considered with masses within 50 GeV of the lightest state. The model is designed to satisfy the SM Higgs boson mass and the dark-matter relic density ($0.10 < \Omega h^2 < 0.12$, where Ω is the energy density parameter and h is the Planck constant) with pMSSM parameters: $M_1 = -(\mu + \delta)$ where $\delta = 20\text{--}50$ GeV, $M_2 = 2.0$ TeV, $M_3 = 1.8$ TeV, $M_S = 0.8\text{--}1.2$ TeV, $X_t/M_S \sim \sqrt{6}$, and $\tan\beta = 20$. For this model, limits are shown in Figure 10.7. Only bottom- and top squark production are considered in this interpretation. The signal grid points were produced in two planes, μ vs $m_{\tilde{t}R}$ and μ vs $m_{\tilde{q}L3}$, and then projected to the corresponding \tilde{t} and $\tilde{\chi}_1^0$ masses. All other pMSSM masses are set to > 3 TeV and effectively decoupled.

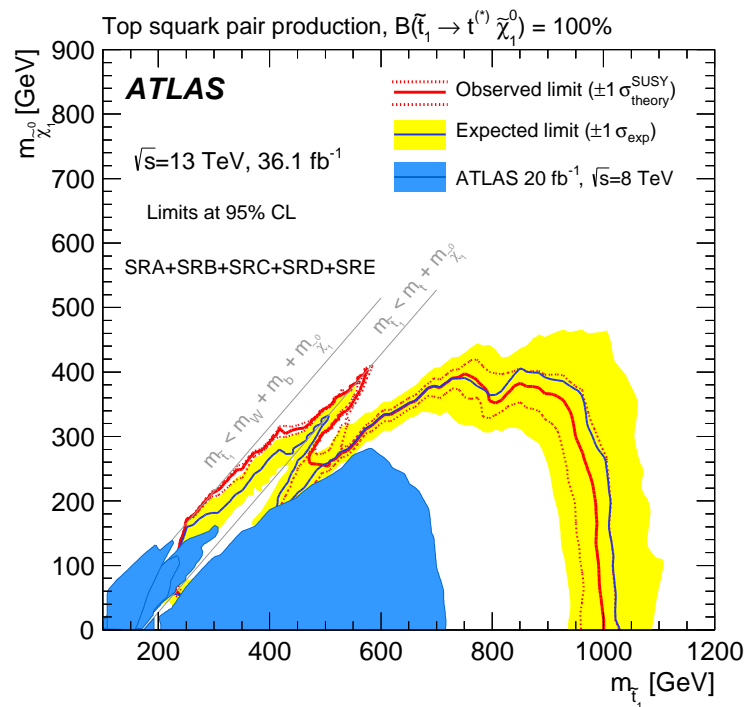


Figure 10.3: Observed (red solid line) and expected (blue solid line) exclusion contours at 95% CL as a function of \tilde{t} and $\tilde{\chi}_1^0$ masses in the scenario where both top squarks decay via $\tilde{t} \rightarrow t^{(*)} + \tilde{\chi}_1^0$. Masses that are within the contours are excluded. Uncertainty bands corresponding to the $\pm 1\sigma$ variation of the expected limit (yellow band) and the sensitivity of the observed limit to $\pm 1\sigma$ variations of the signal theoretical uncertainties (red dotted lines) are also indicated. Observed limits from all third-generation Run-1 searches at $\sqrt{s} = 8 \text{ TeV}$ overlaid for comparison in blue.

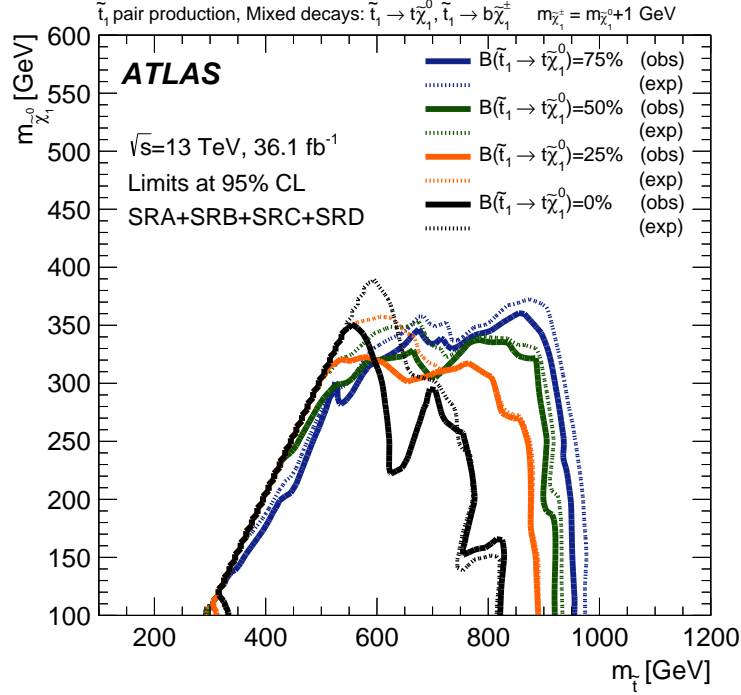


Figure 10.4: Observed (solid line) and expected (dashed line) exclusion contours at 95% CL as a function of \tilde{t} and $\tilde{\chi}_1^0$ masses and branching ratio to $\tilde{t} \rightarrow t\tilde{\chi}_1^0$ in the natural SUSY-inspired mixed grid scenario where $m_{\tilde{\chi}_1^\pm} = m_{\tilde{\chi}_1^0} + 1$ GeV

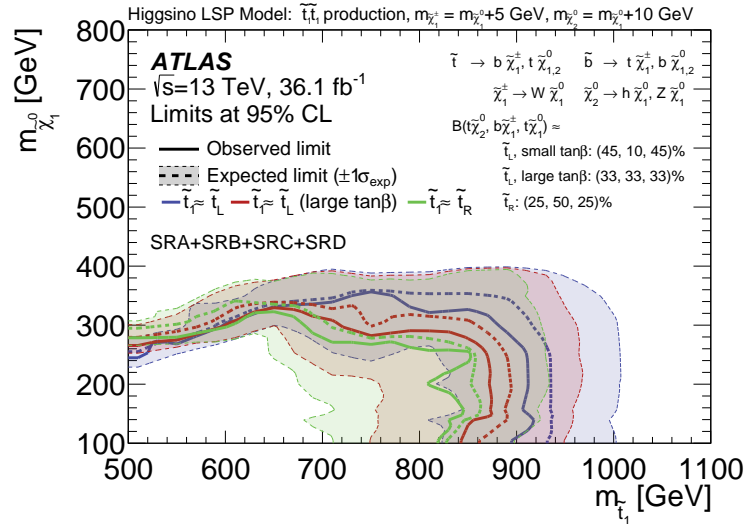


Figure 10.5: Observed (solid line) and expected (dashed line) exclusion contours at 95% CL as a function of $m_{\tilde{t}_1}$ and $m_{\tilde{\chi}_1^0}$ for the pMSSM-inspired non-asymptotic higgsino simplified model for a small $\tan\beta$ with $B(\tilde{t} \rightarrow t\tilde{\chi}_2^0, \tilde{t} \rightarrow t + \tilde{\chi}_1^0, \tilde{t} \rightarrow b\tilde{\chi}_1^\pm) = 45\%, 10\%, 45\%$ (blue), a large $\tan\beta$ with $B(\tilde{t} \rightarrow t\tilde{\chi}_2^0, \tilde{t} \rightarrow t + \tilde{\chi}_1^0, \tilde{t} \rightarrow b\tilde{\chi}_1^\pm) = 33\%, 33\%, 33\%$ (red), and a light \tilde{t}_R with $B(\tilde{t} \rightarrow t\tilde{\chi}_2^0, \tilde{t} \rightarrow t + \tilde{\chi}_1^0, \tilde{t} \rightarrow b\tilde{\chi}_1^\pm) = 25\%, 50\%, 25\%$ (green) assumption. The uncertainty bands correspond to the $\pm 1\sigma$ variation of the expected limit.

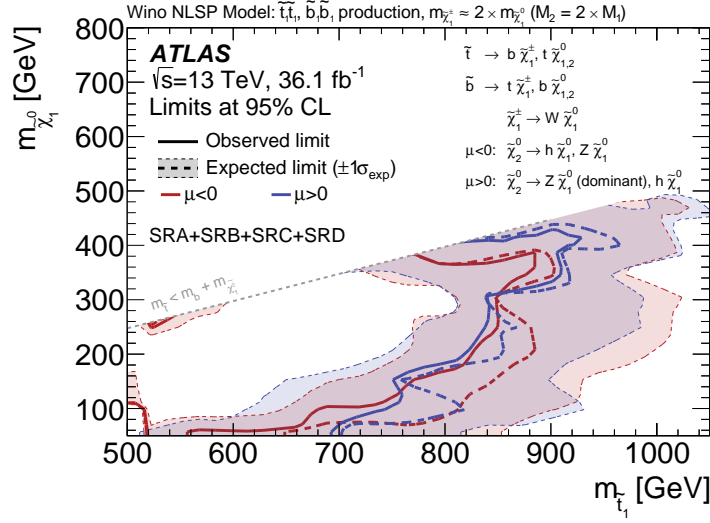


Figure 10.6: Observed (solid line) and expected (dashed line) exclusion contours at 95% CL as a function of \tilde{t} and $\tilde{\chi}_1^0$ masses for the Wino NLSP pMSSM model for both positive (blue) and negative (red) values of μ . The uncertainty bands correspond to the $\pm 1\sigma$ variation of the expected limit.

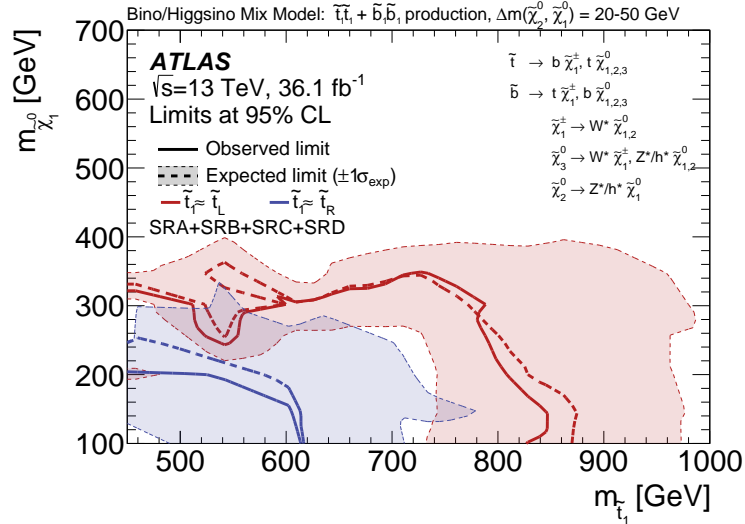
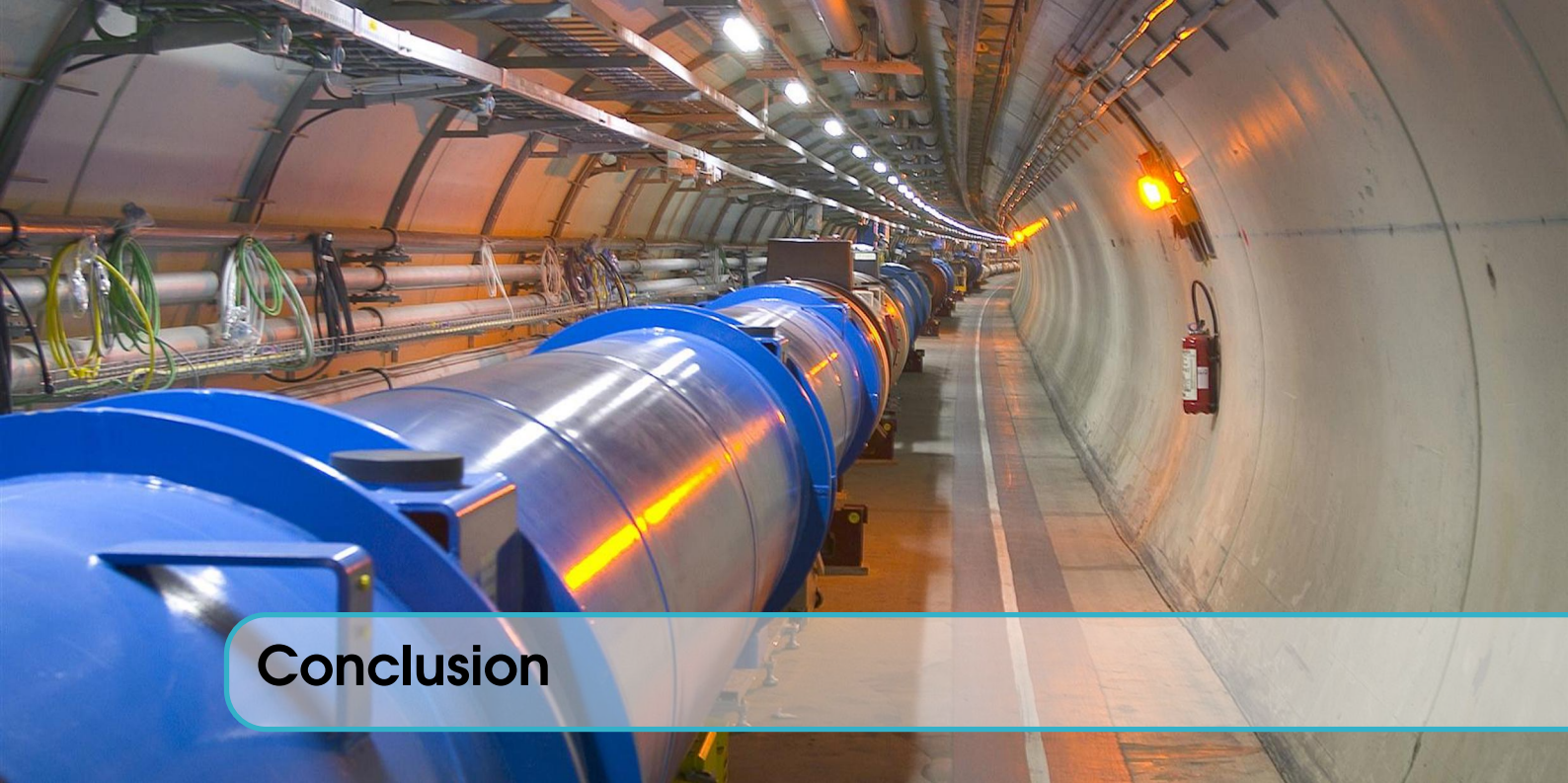


Figure 10.7: Observed (solid line) and expected (dashed line) exclusion contours at 95% CL as a function of \tilde{t} and $\tilde{\chi}_1^0$ masses for the \tilde{t}_L scan (red) as well as for the \tilde{t}_R scan (blue) in the well-tempered pMSSM model. The uncertainty bands correspond to the $\pm 1\sigma$ variation of the expected limit.



Conclusion

Summary

The successful operation of the [LHC](#) during Run 2 allowed the [ATLAS](#) experiment to collect 139 fb^{-1} of data from pp collisions at a centre-of-mass energy of $\sqrt{s} = 13 \text{ TeV}$ between the years 2015 and 2018. The analysis of this data resulted in a rich physics programme for the ATLAS collaboration, and notable achievements in the Higgs sector. In this thesis, four major analyses were discussed, using part or all of the available data. They established an important connection between the Standard Model process of pair production of top quarks in association with a Z boson and the search for a supersymmetric partner to the top quark.

In Chapter 5, a joint measurement of the inclusive $t\bar{t}Z$ and $t\bar{t}W$ cross sections was performed using the 2015–2016 dataset (36.1 fb^{-1}). Using the multi-lepton (two to four electrons and/or muons) final states and including both on-shell and off-shell Z boson contributions, the $t\bar{t}Z$ cross section was found to be $\sigma_{t\bar{t}Z} = 0.95 \pm 0.13 \text{ pb}$, in agreement with the Standard Model prediction of $\sigma_{t\bar{t}Z}^{\text{theory}} = 0.863^{+0.09}_{-0.10}(\text{scale}) \pm 0.03(\text{PDF}+\alpha_s) \text{ pb}$ [35]. Exclusion limits were set on relevant dimension-6 effective field theory operators affecting the top- Z coupling. For the first time in ATLAS, the dominant uncertainties on the measurement were systematic rather than statistical.

In Chapter 6, this measurement was repeated with the full Run 2 dataset, focusing only on the trilepton and tetralepton final states sensitive to the $t\bar{t}Z$ process. Its cross section was measured to be $\sigma_{t\bar{t}Z} = 1.09 \pm 0.10 \text{ pb}$, still in agreement with the Standard Model prediction quoted above. Improvements were made to the modelling of both signal and background processes, allowing a reduction in the systematic uncertainty.

Chapter 7 presented the very first differential measurement of the $t\bar{t}Z$ cross section at ATLAS, also using the full Run 2 dataset, and relied partly on the results of its associated inclusive measurement. The unfolding process and the challenges of dealing with statistical effects of MC were extensively discussed, and differential distributions of two kinematic variables associated to

the Z boson were shown. Further variables used in the differential measurement are available in Appendix A.

Part III of this thesis focused on the search for a scalar partner to the top quark in the all-hadronic final state. Chapter 8 described the design of such a search, using the 2015–2016 ATLAS dataset, and explored various background modelling strategies.

In Chapter 9, a detailed study showed the merits and limitations of a boson replacement strategy in estimating the $t\bar{t}Z(Z \rightarrow \nu\bar{\nu})$ irreducible background. An approach based on multi-lepton signatures was then put forward to overcome these limitations, largely based on the results established in Part II. This method was successfully employed in a similar search using the full Run 2 dataset; only the systematic uncertainties related to the modelling of the $t\bar{t}Z$ background were shown here, and compared to those of the boson replacement approach, noting an improvement in the background estimation strategy.

Finally, Chapter 10 concluded on the search presented in Chapter 8 by discussing its result using the 2015–2016 dataset. No significant excess over the expected Standard Model background was observed. Assuming a 100% branching ratio of $\tilde{t}_1 \rightarrow t + \tilde{\chi}_1^0$, stop masses were excluded up to 1 TeV for neutralino masses smaller than 350 GeV. Various other scenarios were considered, and exclusion limits set correspondingly.

Future work

The ATLAS 2015–2018 dataset remains to be fully explored. No conclusive sign of SUSY has been observed yet, but analysis techniques are constantly being refined and detector performance made more precise, both on the hardware and software levels. The recent surge in machine learning applications to high energy particle physics promises the emergence of new and efficient tools in the scrutiny of this impressive amount of data.

Two axes of future research seem particularly interesting at this point, following the results presented in this thesis. First, further measurements of the $t\bar{t}Z$ cross section can be made using the same full Run 2 dataset, using new and better calibrated approaches. The comparison of the inclusive measurements using 36.1 fb^{-1} and 139 fb^{-1} of ATLAS data, presented in Part II, indeed indicate that this is a viable and promising avenue towards reducing systematic uncertainties. Using multivariate techniques, additional final states can be studied, further enhancing the statistical power of the analysis. The full inclusion of top quark reconstruction algorithms will enable better separation between signal and background events, and allow to probe more relevant effective field theory operators through the differential measurement of the $t\bar{t}Z$ cross section in terms of top- and $t\bar{t}$ -related observables.

Secondly, the absence of any statistically significant excess in the signal regions used in Chapter 8 to search for a supersymmetric partner to the top quark in the all-hadronic channel could effectively make the search interpretable as an inclusive measurement of the $t\bar{t}Z(\rightarrow \nu\bar{\nu})$ cross section. This process has never before been directly measured at the LHC. A challenging task, it could be performed with dedicated machine learning approaches and by combining the all-hadronic channel with the one- and two-lepton channels used in searching for similar supersymmetric processes (and also sensitive to this irreducible background). This first measurement would be particularly helpful if conducted in the extreme kinematic phase-space commonly associated with such searches for new phenomena.

And here we are. Nowhere land.
— That seems hardly a fitting name for a
place so full. Can't you see it?
Perhaps you're not looking hard enough.

Abbreviations

ALICE A Large Ion Collider Experiment	IBL Insertable B-Layer
ATLAS A Toroidal LHC ApparatuS	IBU Iterative Bayesian Unfolding
BDT Boosted Decision Tree	ID Inner Detector
BSM Beyond the Standard Model	ISF Integrated Simulation Framework
CB Combined Muon	ISR Initial State Radiation
CDF Collider Detector at Fermilab	JER Jet Energy Resolution
CDM Cold Dark Matter	JES Jet Energy Scale
CERN Conseil Européen pour la Recherche Nucléaire	JVF Jet Vertex Fraction
CKKW Catani-Krauss-Kuhn-Webber	JVT Jet Vertex Tagger
CKM Cabibbo-Kobayashi-Maskawa	LI Level 1 Trigger
CL Confidence Level	LAr Liquid Argon
CMS Compact Muon Solenoid	LEP Large Electron Positron collider
CP Charge-Parity	LHC Large Hadron Collider
CPU Central Processing Unit	LHCb Large Hadron Collider beauty
CR Control Region	LINAC2 LINear ACcelerator 2
CSC Cathode Strip Chamber	LO Leading Order
CT Calorimeter-Tagged	LSP Lightest Supersymmetric Particle
DIGI DIGItisation	LUCID LUminosity Cherenkov Integrating Detector
DIS Deep Inelastic Scattering	MC Monte Carlo
DM Dark Matter	MDT Monitored Drift Tube
DR Diagram Removal	ME Muon Extrapolation / Extrapolated Muon
DS Diagram Subtraction	ME Matrix Element
ECAL Electromagnetic CALorimeter	MLE Maximum Likelihood Estimator
ECIDS Electron Charge IDentification Selection	MPI Multi-Parton Interaction
EFT Effective Field Theory	MS Muon Spectrometer
EMB ElectroMagnetic Barrel	MSSM Minimal Supersymmetric Standard Model
EMEC ElectroMagnetic End-Cap	NDF Number of Degrees of Freedom
EVGEN EVent GENeration	NLO Next-to-Leading Order
EWK ElectroWeaK	NLSP Next-to-Lightest Supersymmetric Particle
FATRAS FAst TRAck Simulation	NNLL Next-to-Next-to-Logarithmic
FBU Fully Bayesian Unfolding	NNLO Next-to-Next-to-Leading Order
FCAL Forward CALorimeter	NP Nuisance Parameter
FSR Final State Radiation	OR Overlap Removal
GAN Generative Adversarial Network	OS Opposite-Sign
HCAL Hadronic CALorimeter	OSSF Opposite-Sign Same Flavour
HEC Hadronic End-Cap	PCBT Pseudo-Continuous B-Tagging
HL-LHC High-Luminosity LHC	PDF Parton Distribution Function
HLT High-Level Trigger	PDF Probability Density Function
HS Hard Scatter	pMSSM Phenomenological Minimal Supersymmetric Standard Model
i.i.d. independent and identically distributed	PS Proton Synchrotron

PS Parton Shower	SPS Super Proton Synchrotron
PSB Proton Synchrotron Booster	SR Signal Region
PU Pile-Up	ST Segment-Tagged
PV Primary Vertex	SUSY Supersymmetry
QCD Quantum Chromo-Dynamics	SVD Singular Value Decomposition
QFT Quantum Field Theory	TGC Thin-Gap Chamber
RECO RECOstruction	TileCAL Tile CALorimeter
RMS Root Mean Square	TRT Transition Radiation Tracker
RPC Resistive-Plate Chamber	UA1 Underground Area 1
SCT Semi-Conductor Tracker	UA2 Underground Area 2
SF Scale Factor	UE Underlying Event
SIM SIMulation	WIMP Weakly Interacting Massive Particle
SM Standard Model	

List of Tables

1.1	Fermion content of the SM	16
1.2	Boson content of the SM	16
1.3	Main decays of the W boson	18
1.4	Main decays of the $t\bar{t}$ system	18
1.5	Main decays of the Z boson	19
1.6	Chiral supermultiplet content of the MSSM	26
1.7	Gauge supermultiplet content of the MSSM	27
2.1	LHC beam parameters in Run 2	37
3.1	Isolation criteria for leptons and photons	62
5.1	Summary of triggers used	87
5.2	Selection criteria for the three-lepton signal regions	88
5.3	Selection criteria for the four-lepton signal regions	88
5.4	Selection criteria for the three-lepton control region	90
5.5	Selection criteria for the four-lepton control regions	91
5.6	Selection criteria for the fake-factor control region	94
5.7	Yields for all three-lepton regions after the fit to the 3L channel	97
5.8	Yields for all four-lepton regions after the fit to the 4L channel	99
5.9	Signal significance in the various fits	99
5.10	Dominant systematic uncertainties after the fit to $t\bar{t}Z$ and $t\bar{t}W$	101
5.11	Definition of effective field theory operators	105
5.12	Exclusion intervals on the effective field theory operators	106
6.1	Summary of triggers used	108
6.2	Selection criteria for the three-lepton signal regions	109
6.3	Selection criteria for the four-lepton signal regions	110
6.4	Selection criteria for the three-lepton control region	111
6.5	Selection criteria for the four-lepton control region	111
6.6	Theory uncertainties on $t\bar{t}Z$	114
6.7	Yields for all three-lepton regions after the fit to the 3L channel	115
6.8	Yields for all four-lepton regions after the fit to the 4L channel	117
6.9	Dominant systematic uncertainties after the combined $t\bar{t}Z$ fit	118
7.1	Definition of differential observables	126
7.2	Optimised bin ranges for the differential observables	128
7.3	Optimised number of iterations for the differential variables	128
7.4	Estimate of the non-closure from the splitting of the MC sample	134
7.5	Compatibility tests between the unfolded data and the signal MC samples	142
8.1	Summary of triggers used	153
8.2	Pre-selection criteria for all signal regions	157
8.3	Selection criteria for all signal regions	157
8.4	Selection criteria for the one-lepton control regions	160
8.5	Selection criteria for the one-lepton control regions	160

8.6	Selection criteria for the two-lepton control regions	161
8.7	Summary of the selection criteria for the all-hadronic QCD control regions.	163
9.1	Selection criteria for the one-lepton $t\bar{t}\gamma$ control region	166
9.2	Background composition of the one-lepton $t\bar{t}\gamma$ control region	167
9.3	Theory uncertainties on the $t\bar{t}Z$ estimation	168
9.4	Selection criteria for the three-lepton $t\bar{t}Z$ control region	173
9.5	Background composition of the three-lepton $t\bar{t}Z$ control region	173
9.6	Theory uncertainties on the $t\bar{t}Z$ estimate	174
10.1	Dominant systematic uncertainties after the background-only fit	178
10.2	Results of the background-only fit in CRTopA	179
10.3	Results of the background-only fit in CRTopB	180
10.4	Results of the background-only fit in CRW and CRST	180
10.5	Results of the background-only fit in CRZAB	181
10.6	Scale factors after the background-only fit	181
10.7	Results of the discovery fit in SRA	182
10.8	Results of the discovery fit in SRB	183
10.9	Upper limits and discovery p -values	183

List of Figures

1.1	Cross section of $t\bar{t}$ production at the LHC and Tevatron	17
1.2	Example leading-order Feynman diagram for $t\bar{t}Z$ production	19
1.3	CMS scan of the anomalous t - Z couplings	21
1.4	Grand unification in the MSSM	27
1.5	Example of a Feynman diagram for proton decay	28
1.6	Excluded \tilde{t}_1 and $\tilde{\chi}_1^0$ masses from the ATLAS search at $\sqrt{s} = 8$ TeV	31
1.7	Excluded \tilde{t}_1 and $\tilde{\chi}_1^0$ masses from the CMS search at $\sqrt{s} = 13$ TeV	32
2.1	The LHC complex	34
2.2	Parton distribution functions for the proton	35
2.3	Cross sections of various Standard Model processes	36
2.4	The ATLAS detector	38
2.5	The ATLAS magnet systems	39
2.6	The ATLAS inner detector	40
2.7	The ATLAS calorimeters	41
2.8	The ATLAS muon spectrometer	42
2.9	L1 and HLT trigger rates	44
2.10	Event generation	45
2.11	CPU consumption of the Grid	46
2.12	Time taken in the digitisation step per event	47
2.13	The Integrated Simulation Framework	47
2.14	The ATLFASSTII simulator configuration	48
2.15	Comparison of simulators	49
2.16	Comparison of fast and full digitisation time performances	49
2.17	Estimated CPU resources needed by the LHC after Run 2	50
3.1	Luminosity delivered by the LHC and recorded by ATLAS	52
3.2	Mean number of interactions per crossing	52
3.3	Interactions of SM particles with the ATLAS detector	53
3.4	Cartoon of the supercluster electron/photon reconstruction	55
3.5	Electron identification efficiency	56
3.6	Electron trigger efficiency	57
3.7	Muon reconstruction efficiency	58
3.8	Muon trigger efficiency	59
3.9	Photon identification efficiency	60
3.10	Photon trigger efficiency	61
3.11	Jet energy scale	62
3.12	Performance of the MV2c10 b -tagging algorithm	63
3.13	Uncertainty on the E_T^{miss} reconstruction	64
3.14	E_T^{miss} trigger efficiency	65
5.1	Example Feynman diagram for $t\bar{t}Z$ production with decay in the 3L channel	87
5.2	Distributions of kinematic variables in the three-lepton signal regions	89
5.3	Distributions of kinematic variables in the four-lepton signal region	89

5.4	Distributions of kinematic variables in the three-lepton control region	91
5.5	Distributions of kinematic variables in the four-lepton control region	92
5.6	Distribution of kinematic variables in the validation regions for fake leptons	93
5.7	Ranking plot after the fit to the 3L channel	98
5.8	Ranking plot after the fit to the 4L channel	100
5.9	Ranking plot after the combined $t\bar{t}Z$ fit	102
5.10	Result of the simultaneous fit to $t\bar{t}Z$ and $t\bar{t}W$	103
5.11	Yields in all regions after the combined fit to $t\bar{t}Z$ and $t\bar{t}W$	104
5.12	Profile likelihood test statistic for the $C_{\phi t}$ coupling	106
6.1	Distribution of a kinematic variable in the three-lepton control region	112
6.2	Distribution of a kinematic variable for the four-lepton control region	112
6.3	Ranking plot after the fit to the 3L channel	116
6.4	Ranking plot after the fit to the 4L channel	119
6.5	Ranking plot after the combined $t\bar{t}Z$ fit	120
6.6	Yields in all regions after the combined $t\bar{t}Z$ fit	121
6.7	Distributions of kinematic variables in the three-lepton signal regions	121
6.8	Distributions of kinematic variables in the four-lepton signal region	121
7.1	Test of the number of iterations	129
7.2	Example of a pull distribution	130
7.3	Pull means and widths under the standard pull definition	131
7.4	Comparison of pull definitions	132
7.5	Corrected pull definition	133
7.6	Pull distributions showing discrete structure	135
7.7	Pull means and widths under the corrected pull definition	136
7.8	Pull means and widths after splitting the MC sample	136
7.9	Comparison of the training and testing samples	137
7.10	Non-closure expected from the splitting of the MC sample	137
7.11	Data-driven stress tests	138
7.12	MC-driven stress tests	139
7.13	Comparison of unfolding techniques	140
7.14	Unfolding of p_T^Z at particle- and parton-level in the combined channel	143
7.15	Unfolding of $ y^Z $ at particle- and parton-level in the combined channel	144
7.16	Differential distributions for p_T^Z at particle- and parton-level in the combined channel	145
7.17	Differential distributions for $ y^Z $ at particle- and parton-level in the combined channel	146
7.18	Unfolded uncertainties for p_T^Z at particle- and parton-level in the combined channel	147
7.19	Unfolded uncertainties for $ y^Z $ at particle- and parton-level in the combined channel	147
7.20	Correlation factors at particle- and parton-level	148
8.1	SUSY signal decay topology	152
8.2	Correlation between the m_{T2} and E_T^{miss} variables	155
8.3	Distribution of the $m_T^{b,\text{min}}$ variable	156
8.4	Distribution of the $m_{\text{jet},R=1,2}^0$ variable	158
8.5	Definition of top quark categories	158
8.6	Distributions of kinematic variables in the control regions	161
8.7	Distribution of the m_{T2} variable	162

8.8	Distributions of kinematic variables in the control regions	164
9.1	Ratio of the transverse momenta of $t\bar{t}\gamma$ and $t\bar{t}Z$	166
9.2	Distribution of a kinematic variable in the $t\bar{t}\gamma$ control region	168
9.3	Further ratios of the transverse momenta of $t\bar{t}\gamma$ and $t\bar{t}Z$	171
9.4	Origin of radiated photons	171
9.5	Distribution of p_T^Z in a two-lepton control region	172
9.6	Distribution of p_T^Z in the three-lepton control region	174
10.1	Yields for all signal regions after the discovery fit	184
10.2	Distributions of kinematic variables in the signal regions after the discovery fit	185
10.3	Exclusion contours in the $\tilde{t} \rightarrow t^{(*)} + \tilde{\chi}_1^0$ scenario	186
10.4	Exclusion contours in the natural SUSY scenario	187
10.5	Exclusion contours in the pMSSM scenario	187
10.6	Exclusion contours in the Wino NLSP scenario	188
10.7	Exclusion contours in the well-tempered pMSSM scenario	188
A.1	Unfolding of N_{jets} at particle-level in the 3L channel	224
A.2	Differential distributions for N_{jets} at particle-level in the 3L channel	225
A.3	Unfolded uncertainties for N_{jets} at particle-level in the 3L channel	226
A.4	Unfolding of $p_T^{\ell\text{non-Z}}$ at particle- and parton-level in the 3L channel	227
A.5	Differential distributions for $p_T^{\ell\text{non-Z}}$ at particle- and parton-level in the 3L channel	228
A.6	Unfolded uncertainties for $p_T^{\ell\text{non-Z}}$ at particle- and parton-level in the 3L channel	229
A.7	Unfolding of $ \Delta\phi(Z, t_{\text{lep}}) $ at particle- and parton-level in the 3L channel	230
A.8	Differential distributions for $ \Delta\phi(Z, t_{\text{lep}}) $ at particle- and parton-level in the 3L channel	231
A.9	Unfolded uncertainties for $ \Delta\phi(Z, t_{\text{lep}}) $ at particle- and parton-level in the 3L channel	232
A.10	Unfolding of $ \Delta y(Z, t_{\text{lep}}) $ at particle- and parton-level in the 3L channel	233
A.11	Differential distributions for $ \Delta y(Z, t_{\text{lep}}) $ at particle- and parton-level in the 3L channel	234
A.12	Unfolded uncertainties for $ \Delta y(Z, t_{\text{lep}}) $ at particle- and parton-level in the 3L channel	235
A.13	Unfolding of N_{jets} at particle-level in the 4L channel	237
A.14	Differential distributions for N_{jets} at particle-level in the 4L channel	238
A.15	Unfolded uncertainties for N_{jets} at particle-level in the 4L channel	239
A.16	Unfolding of $ \Delta\phi(\ell_t^+, \ell_{\bar{t}}^-) $ at particle- and parton-level in the 4L channel	240
A.17	Differential distributions for $ \Delta\phi(\ell_t^+, \ell_{\bar{t}}^-) $ at particle- and parton-level in the 4L channel	241
A.18	Unfolded uncertainties for $ \Delta\phi(\ell_t^+, \ell_{\bar{t}}^-) $ at particle- and parton-level in the 4L channel	242
A.19	Unfolding of $p_T^{t\bar{t}}$ at particle- and parton-level in the 4L channel	243
A.20	Differential distributions for $p_T^{t\bar{t}}$ at particle- and parton-level in the 4L channel	244
A.21	Unfolded uncertainties for $p_T^{t\bar{t}}$ at particle- and parton-level in the 4L channel	245
A.22	Unfolding of $ \Delta\phi(t\bar{t}, Z) $ at particle- and parton-level in the 4L channel	246
A.23	Differential distributions for $ \Delta\phi(t\bar{t}, Z) $ at particle- and parton-level in the 4L channel	247
A.24	Unfolded uncertainties for $ \Delta\phi(t\bar{t}, Z) $ at particle- and parton-level in the 4L channel	248

References

- [1] ATLAS Collaboration. “Measurement of the $t\bar{t}Z$ and $t\bar{t}W$ cross sections in proton-proton collisions at $\sqrt{s} = 13$ TeV with the ATLAS detector”. In: *Phys. Rev. D* 99.7 (2019), page 072009. DOI: [10.1103/PhysRevD.99.072009](https://doi.org/10.1103/PhysRevD.99.072009). arXiv: [1901.03584 \[hep-ex\]](https://arxiv.org/abs/1901.03584) (cited on pages [5](#), [85](#), [107](#)).
- [2] ATLAS Collaboration. *Measurements of the inclusive and differential production cross sections of a top-quark-antiquark pair in association with a Z boson at $\sqrt{s} = 13$ TeV with the ATLAS detector*. Technical report ATLAS-CONF-2020-028. CERN, Aug. 2020. URL: <http://cds.cern.ch/record/2725734> (cited on pages [5](#), [107](#), [123](#)).
- [3] ATLAS Collaboration. “Search for a scalar partner of the top quark in the jets plus missing transverse momentum final state at $\sqrt{s} = 13$ TeV with the ATLAS detector”. In: *JHEP* 12 (2017), page 085. DOI: [10.1007/JHEP12\(2017\)085](https://doi.org/10.1007/JHEP12(2017)085). arXiv: [1709.04183 \[hep-ex\]](https://arxiv.org/abs/1709.04183) (cited on pages [5](#), [151](#), [165](#), [175](#)).
- [4] ATLAS Collaboration. “Search for a scalar partner of the top quark in the all-hadronic $t\bar{t}$ plus missing transverse momentum final state at $\sqrt{s} = 13$ TeV with the ATLAS detector”. In: *Eur. Phys. J. C* 80.8 (2020), page 737. DOI: [10.1140/epjc/s10052-020-8102-8](https://doi.org/10.1140/epjc/s10052-020-8102-8). arXiv: [2004.14060 \[hep-ex\]](https://arxiv.org/abs/2004.14060) (cited on pages [5](#), [165](#)).
- [5] L. Evans and P. Bryant. “LHC Machine”. In: *JINST* 3 (2008), S08001. DOI: [10.1088/1748-0221/3/08/S08001](https://doi.org/10.1088/1748-0221/3/08/S08001) (cited on pages [12](#), [33](#)).
- [6] ATLAS Collaboration. “The ATLAS Experiment at the CERN Large Hadron Collider”. In: *JINST* 3 (2008), S08003. DOI: [10.1088/1748-0221/3/08/S08003](https://doi.org/10.1088/1748-0221/3/08/S08003) (cited on pages [12](#), [33](#), [34](#), [37](#)).
- [7] ATLAS Collaboration. “Observation of a new particle in the search for the Standard Model Higgs boson with the ATLAS detector at the LHC”. In: *Physics Letters B* 716.1 (2012), pages 1–29. ISSN: 0370-2693. DOI: <http://dx.doi.org/10.1016/j.physletb.2012.08.020> (cited on pages [12](#), [16](#)).

- [8] CMS Collaboration. “Observation of a new boson at a mass of 125 GeV with the CMS experiment at the LHC”. In: *Physics Letters B* 716.1 (2012), pages 30–61. ISSN: 0370-2693. DOI: <http://dx.doi.org/10.1016/j.physletb.2012.08.021> (cited on pages 12, 16).
- [9] J. McFayden. *Third generation SUSY and $t\bar{t} + Z$ production*. Springer International Publishing, 2014. DOI: [10.1007/978-3-319-07191-6](https://doi.org/10.1007/978-3-319-07191-6). URL: <https://doi.org/10.1007/978-3-319-07191-6> (cited on page 12).
- [10] S. L. Glashow. “Partial-symmetries of weak interactions”. In: *Nuclear Physics* 22.4 (Feb. 1961), pages 579–588. DOI: [10.1016/0029-5582\(61\)90469-2](https://doi.org/10.1016/0029-5582(61)90469-2). URL: [https://doi.org/10.1016/0029-5582\(61\)90469-2](https://doi.org/10.1016/0029-5582(61)90469-2) (cited on page 15).
- [11] S. Weinberg. “A Model of Leptons”. In: *Physical Review Letters* 19.21 (Nov. 1967), pages 1264–1266. DOI: [10.1103/physrevlett.19.1264](https://doi.org/10.1103/physrevlett.19.1264). URL: <https://doi.org/10.1103/physrevlett.19.1264> (cited on page 15).
- [12] A. Salam and J. C. Ward. “Electromagnetic and weak interactions”. In: *Phys. Lett.* 13 (1964), pages 168–171. DOI: [10.1016/0031-9163\(64\)90711-5](https://doi.org/10.1016/0031-9163(64)90711-5) (cited on page 15).
- [13] M. Gell-Mann. *The Eightfold Way: A Theory of Strong Interaction Symmetry*. Technical report. Mar. 1961. DOI: [10.2172/4008239](https://doi.org/10.2172/4008239). URL: <https://doi.org/10.2172/4008239> (cited on page 15).
- [14] D. J. Gross and F. Wilczek. “Ultraviolet Behavior of Non-Abelian Gauge Theories”. In: *Physical Review Letters* 30.26 (June 1973), pages 1343–1346. DOI: [10.1103/physrevlett.30.1343](https://doi.org/10.1103/physrevlett.30.1343). URL: <https://doi.org/10.1103/physrevlett.30.1343> (cited on page 15).
- [15] H. D. Politzer. “Reliable Perturbative Results for Strong Interactions”. In: *Physical Review Letters* 30.26 (June 1973), pages 1346–1349. DOI: [10.1103/physrevlett.30.1346](https://doi.org/10.1103/physrevlett.30.1346). URL: <https://doi.org/10.1103/physrevlett.30.1346> (cited on page 15).
- [16] F. Wilczek. “Quantum Chromodynamics: The Modern Theory of the Strong Interaction”. In: *Annual Review of Nuclear and Particle Science* 32.1 (Dec. 1982), pages 177–209. DOI: [10.1146/annurev.ns.32.120182.001141](https://doi.org/10.1146/annurev.ns.32.120182.001141). URL: <https://doi.org/10.1146/annurev.ns.32.120182.001141> (cited on page 15).
- [17] P. W. Higgs. “Broken Symmetries and the Masses of Gauge Bosons”. In: *Physical Review Letters* 13 (Oct. 1964), pages 508–509. DOI: [10.1103/PhysRevLett.13.508](https://doi.org/10.1103/PhysRevLett.13.508) (cited on page 16).
- [18] F. Englert and R. Brout. “Broken Symmetry and the Mass of Gauge Vector Mesons”. In: *Physical Review Letters* 13 (Aug. 1964), pages 321–323. DOI: [10.1103/PhysRevLett.13.321](https://doi.org/10.1103/PhysRevLett.13.321) (cited on page 16).
- [19] G. S. Guralnik, C. R. Hagen, and T. W. Kibble. “Global Conservation Laws and Massless Particles”. In: *Physical Review Letters* 13 (Nov. 1964), pages 585–587. DOI: [10.1103/PhysRevLett.13.585](https://doi.org/10.1103/PhysRevLett.13.585) (cited on page 16).
- [20] Particle Data Group. “Review of Particle Physics”. In: *Phys. Rev. D* 98 (3 Aug. 2018), page 030001. DOI: [10.1103/PhysRevD.98.030001](https://doi.org/10.1103/PhysRevD.98.030001). URL: <https://link.aps.org/doi/10.1103/PhysRevD.98.030001> (cited on pages 16–18, 23, 34, 123, 125).
- [21] CDF Collaboration. “Observation of Top Quark Production in $p\bar{p}$ collisions with the Collider Detector at Fermilab”. In: *Physical Review Letters* 74.14 (Apr. 1995), pages 2626–2631. DOI: [10.1103/physrevlett.74.2626](https://doi.org/10.1103/physrevlett.74.2626). URL: <https://doi.org/10.1103/physrevlett.74.2626> (cited on page 17).

- [22] D0 Collaboration. “Observation of the Top Quark”. In: *Physical Review Letters* 74.14 (Apr. 1995), pages 2632–2637. DOI: [10.1103/physrevlett.74.2632](https://doi.org/10.1103/physrevlett.74.2632). URL: <https://doi.org/10.1103/physrevlett.74.2632> (cited on page 17).
- [23] J. Gao, C. S. Li, and H. X. Zhu. “Top-Quark Decay at Next-to-Next-to-Leading Order in QCD”. In: *Physical Review Letters* 110.4 (Jan. 2013). DOI: [10.1103/physrevlett.110.042001](https://doi.org/10.1103/physrevlett.110.042001). URL: <https://doi.org/10.1103/physrevlett.110.042001> (cited on page 17).
- [24] ATLAS Collaboration. “Measurement of the $t\bar{t}$ production cross-section using $e\mu$ events with b -tagged jets in pp collisions at $\sqrt{s} = 13$ TeV with the ATLAS detector”. In: *Physics Letters B* 761 (Oct. 2016), pages 136–157. DOI: [10.1016/j.physletb.2016.08.019](https://doi.org/10.1016/j.physletb.2016.08.019). URL: <https://doi.org/10.1016/j.physletb.2016.08.019> (cited on page 17).
- [25] ATLAS Collaboration. *Top working group cross-section summary plots*. Technical report ATL-PHYS-PUB-2019-035. Geneva: CERN, Sept. 2019. URL: <http://cds.cern.ch/record/2690525> (cited on page 17).
- [26] ATLAS Collaboration. “Search for top-quark decays $t \rightarrow Hq$ with 36 fb^{-1} of pp collision data at $\sqrt{s} = 13$ TeV with the ATLAS detector”. In: *JHEP* 05 (Dec. 2018), 123. 68 p. DOI: [10.1007/JHEP05\(2019\)123](https://doi.org/10.1007/JHEP05(2019)123). URL: <http://cds.cern.ch/record/2652764> (cited on page 17).
- [27] ATLAS Collaboration. “Search for flavour-changing neutral current top-quark decays to qZ in pp collision data collected with the ATLAS detector at $\sqrt{s} = 8$ TeV.” In: *Eur. Phys. J. C* 76 (Aug. 2015), 12. 35 p. DOI: [10.1140/epjc/s10052-015-3851-5](https://doi.org/10.1140/epjc/s10052-015-3851-5). URL: <http://cds.cern.ch/record/2046583> (cited on page 17).
- [28] ATLAS Collaboration. *Search for charged lepton-flavour violation in top-quark decays at the LHC with the ATLAS detector*. Technical report ATLAS-CONF-2018-044. Geneva: CERN, Sept. 2018. URL: <http://cds.cern.ch/record/2638305> (cited on page 17).
- [29] CMS Collaboration. “Search for the flavor-changing neutral current interactions of the top quark and the Higgs boson which decays into a pair of b quarks at $\sqrt{s} = 13$ TeV”. In: *JHEP* 06 (Dec. 2017), 102. 37 p. DOI: [10.1007/JHEP06\(2018\)102](https://doi.org/10.1007/JHEP06(2018)102). URL: <https://cds.cern.ch/record/2296416> (cited on page 17).
- [30] CMS Collaboration. “Search for associated production of a Z boson with a single top quark and for tZ flavour-changing interactions in pp collisions at $\sqrt{s} = 8$ TeV”. In: *JHEP* 07 (Feb. 2017), 003. 43 p. DOI: [10.1007/JHEP07\(2017\)003](https://doi.org/10.1007/JHEP07(2017)003). URL: <https://cds.cern.ch/record/2244396> (cited on page 17).
- [31] UA1 Collaboration. “Experimental Observation of Lepton Pairs of Invariant Mass Around $95 \text{ GeV}/c^2$ at the CERN SPS Collider”. In: *Phys. Lett.* 126B (1983), pages 398–410. DOI: [10.1016/0370-2693\(83\)90188-0](https://doi.org/10.1016/0370-2693(83)90188-0) (cited on page 18).
- [32] UA2 Collaboration. “Evidence for $Z^0 \rightarrow e^+e^-$ at the CERN $p\bar{p}$ collider”. In: *Physics Letters B* 129.1-2 (Sept. 1983), pages 130–140. DOI: [10.1016/0370-2693\(83\)90744-x](https://doi.org/10.1016/0370-2693(83)90744-x). URL: [https://doi.org/10.1016/0370-2693\(83\)90744-x](https://doi.org/10.1016/0370-2693(83)90744-x) (cited on page 18).
- [33] Gargamelle Collaboration. “Search for Elastic ν_μ Electron Scattering”. In: *Phys. Lett.* 46B (1973), pages 121–124. DOI: [10.1016/0370-2693\(73\)90494-2](https://doi.org/10.1016/0370-2693(73)90494-2) (cited on page 18).
- [34] Gargamelle Collaboration. “Observation of Neutrino Like Interactions Without Muon Or Electron in the Gargamelle Neutrino Experiment”. In: *Phys. Lett.* 46B (1973), pages 138–140. DOI: [10.1016/0370-2693\(73\)90499-1](https://doi.org/10.1016/0370-2693(73)90499-1) (cited on page 18).

- [35] A. Kulesza et al. “Associated production of a top quark pair with a heavy electroweak gauge boson at NLO+NNLL accuracy”. In: *The European Physical Journal C* 79.3 (Mar. 2019). DOI: [10.1140/epjc/s10052-019-6746-z](https://doi.org/10.1140/epjc/s10052-019-6746-z). URL: <https://doi.org/10.1140/epjc/s10052-019-6746-z> (cited on pages 19, 117, 189).
- [36] U. Baur et al. “Probing electroweak top quark couplings at hadron colliders”. In: *Phys. Rev. D* 71 (2005), page 054013. DOI: [10.1103/PhysRevD.71.054013](https://doi.org/10.1103/PhysRevD.71.054013). arXiv: [hep-ph/0412021](https://arxiv.org/abs/hep-ph/0412021) [[hep-ph](#)] (cited on page 20).
- [37] R. Röntsch and M. Schulze. “Constraining couplings of top quarks to the Z boson in $t\bar{t} + Z$ production at the LHC”. In: *JHEP* 07 (2014). [Erratum: *JHEP*09,132(2015)], page 091. DOI: [10.1007/JHEP09\(2015\)132](https://doi.org/10.1007/JHEP09(2015)132), [10.1007/JHEP07\(2014\)091](https://doi.org/10.1007/JHEP07(2014)091). arXiv: [1404.1005](https://arxiv.org/abs/1404.1005) [[hep-ph](#)] (cited on page 20).
- [38] J. Adelman et al. “Top Couplings: pre-Snowmass Energy Frontier 2013 Overview”. In: *Proceedings, Community Summer Study 2013: Snowmass on the Mississippi (CSS2013): Minneapolis, MN, USA, July 29-August 6, 2013*. 2013. arXiv: [1309.1947](https://arxiv.org/abs/1309.1947) [[hep-ex](#)]. URL: <https://inspirehep.net/record/1253365/files/arXiv:1309.1947.pdf> (cited on page 20).
- [39] E. L. Berger, Q.-H. Cao, and I. Low. “Model Independent Constraints Among the Wtb , Zb anti- b , and Zt anti- t Couplings”. In: *Phys. Rev. D* 80 (2009), page 074020. DOI: [10.1103/PhysRevD.80.074020](https://doi.org/10.1103/PhysRevD.80.074020). arXiv: [0907.2191](https://arxiv.org/abs/0907.2191) [[hep-ph](#)] (cited on page 20).
- [40] O. Bessidskaia Bylund et al. “Probing top quark neutral couplings in the Standard Model Effective Field Theory at NLO in QCD”. In: *JHEP* 05 (2016), page 052. DOI: [10.1007/JHEP05\(2016\)052](https://doi.org/10.1007/JHEP05(2016)052). arXiv: [1601.08193](https://arxiv.org/abs/1601.08193) [[hep-ph](#)] (cited on page 20).
- [41] R. Röntsch and M. Schulze. “Constraining the top-Z coupling through $t\bar{t}Z$ production at the LHC”. In: *Nuclear and Particle Physics Proceedings* 273-275 (Apr. 2016), pages 2311–2316. DOI: [10.1016/j.nuclphysbps.2015.09.377](https://doi.org/10.1016/j.nuclphysbps.2015.09.377). URL: <https://doi.org/10.1016/j.nuclphysbps.2015.09.377> (cited on page 20).
- [42] CMS Collaboration. “Measurement of associated production of vector bosons and $t\bar{t}$ at $\sqrt{s} = 7\text{TeV}$ ”. In: *Phys. Rev. Lett.* 110 (Mar. 2013), 172002. 27 p. DOI: [10.1103/PhysRevLett.110.172002](https://doi.org/10.1103/PhysRevLett.110.172002). URL: <https://cds.cern.ch/record/1528157> (cited on page 20).
- [43] M. V. Garzelli et al. “ $t\bar{t}W$ and $t\bar{t}Z$ Hadroproduction at NLO accuracy in QCD with Parton Shower and Hadronization effects”. In: *JHEP* 11 (2012), page 056. DOI: [10.1007/JHEP11\(2012\)056](https://doi.org/10.1007/JHEP11(2012)056). arXiv: [1208.2665](https://arxiv.org/abs/1208.2665) [[hep-ph](#)] (cited on pages 20, 21).
- [44] CMS Collaboration. “Measurement of top quark-antiquark pair production in association with a W or Z boson in pp collisions at $\sqrt{s} = 8\text{TeV}$ ”. In: *Eur. Phys. J. C* 74 (June 2014), 3060. 26 p. DOI: [10.1140/epjc/s10052-014-3060-7](https://doi.org/10.1140/epjc/s10052-014-3060-7). URL: <https://cds.cern.ch/record/1712680> (cited on page 21).
- [45] CMS Collaboration. “Observation of top quark pairs produced in association with a vector boson in pp collisions at $\sqrt{s} = 8\text{TeV}$ ”. In: *JHEP* 01 (Oct. 2015), 096. 52 p. DOI: [10.1007/JHEP01\(2016\)096](https://doi.org/10.1007/JHEP01(2016)096). URL: <https://cds.cern.ch/record/2057196> (cited on page 21).
- [46] ATLAS Collaboration. “Measurement of the $t\bar{t}W$ and $t\bar{t}Z$ production cross sections in pp collisions at $\sqrt{s} = 8\text{TeV}$ with the ATLAS detector”. In: *JHEP* 11 (2015), page 172. DOI: [10.1007/JHEP11\(2015\)172](https://doi.org/10.1007/JHEP11(2015)172). arXiv: [1509.05276](https://arxiv.org/abs/1509.05276) [[hep-ex](#)] (cited on page 21).

- [47] ATLAS Collaboration. “Measurement of the $t\bar{t}Z$ and $t\bar{t}W$ production cross sections in multilepton final states using 3.2 fb^{-1} of pp collisions at $\sqrt{s} = 13 \text{ TeV}$ with the ATLAS detector.” In: *Eur. Phys. J. C* 77 (Sept. 2016), 40. 22 p. DOI: [10.1140/epjc/s10052-016-4574-y](https://doi.org/10.1140/epjc/s10052-016-4574-y). URL: <https://cds.cern.ch/record/2213556> (cited on page 21).
- [48] G. 't Hooft. “Symmetry Breaking through Bell-Jackiw Anomalies”. In: *Phys. Rev. Lett.* 37 (1 July 1976), pages 8–11. DOI: [10.1103/PhysRevLett.37.8](https://doi.org/10.1103/PhysRevLett.37.8). URL: <https://link.aps.org/doi/10.1103/PhysRevLett.37.8> (cited on page 22).
- [49] R. D. Peccei and H. R. Quinn. “CP Conservation in the Presence of Pseudoparticles”. In: *Phys. Rev. Lett.* 38 (25 June 1977), pages 1440–1443. DOI: [10.1103/PhysRevLett.38.1440](https://doi.org/10.1103/PhysRevLett.38.1440). URL: <https://link.aps.org/doi/10.1103/PhysRevLett.38.1440> (cited on page 22).
- [50] R. D. Peccei and H. R. Quinn. “Constraints imposed by CP conservation in the presence of pseudoparticles”. In: *Phys. Rev. D* 16 (6 Sept. 1977), pages 1791–1797. DOI: [10.1103/PhysRevD.16.1791](https://doi.org/10.1103/PhysRevD.16.1791). URL: <https://link.aps.org/doi/10.1103/PhysRevD.16.1791> (cited on page 22).
- [51] A. Buras et al. “Aspects of the grand unification of strong, weak and electromagnetic interactions”. In: *Nuclear Physics B* 135.1 (Mar. 1978), pages 66–92. DOI: [10.1016/0550-3213\(78\)90214-6](https://doi.org/10.1016/0550-3213(78)90214-6). URL: [https://doi.org/10.1016/0550-3213\(78\)90214-6](https://doi.org/10.1016/0550-3213(78)90214-6) (cited on page 22).
- [52] H. Georgi and S. L. Glashow. “Unity of All Elementary-Particle Forces”. In: *Phys. Rev. Lett.* 32 (8 Feb. 1974), pages 438–441. DOI: [10.1103/PhysRevLett.32.438](https://doi.org/10.1103/PhysRevLett.32.438). URL: <https://link.aps.org/doi/10.1103/PhysRevLett.32.438> (cited on page 22).
- [53] J. Ellis. “Physics gets physical”. In: *Nature* 415.6875 (Feb. 2002), pages 957–957. DOI: [10.1038/415957b](https://doi.org/10.1038/415957b). URL: <https://doi.org/10.1038/415957b> (cited on page 22).
- [54] P. Nath and P. F. Pérez. “Proton stability in grand unified theories, in strings and in branes”. In: *Physics Reports* 441.5-6 (Apr. 2007), pages 191–317. DOI: [10.1016/j.physrep.2007.02.010](https://doi.org/10.1016/j.physrep.2007.02.010). URL: <https://doi.org/10.1016/j.physrep.2007.02.010> (cited on page 22).
- [55] K. Garrett and G. Duda. “Dark Matter: A Primer”. In: *Advances in Astronomy* 2011 (2011), pages 1–22. DOI: [10.1155/2011/968283](https://doi.org/10.1155/2011/968283). URL: <https://doi.org/10.1155/2011/968283> (cited on page 22).
- [56] G. Bertone and D. Hooper. “History of dark matter”. In: *Reviews of Modern Physics* 90.4 (Oct. 2018). DOI: [10.1103/revmodphys.90.045002](https://doi.org/10.1103/revmodphys.90.045002). URL: <https://doi.org/10.1103/revmodphys.90.045002> (cited on page 22).
- [57] J. H. Oort. “The force exerted by the stellar system in the direction perpendicular to the galactic plane and some related problems”. In: *Bull. Astron. Inst. Netherlands* 6 (1932), pages 249–287. URL: <https://cds.cern.ch/record/436532> (cited on page 22).
- [58] F. Zwicky. “Die Rotverschiebung von extragalaktischen Nebeln”. In: *Helv. Phys. Acta* 6 (1933). [Gen. Rel. Grav.41,207(2009)], pages 110–127. DOI: [10.1007/s10714-008-0707-4](https://doi.org/10.1007/s10714-008-0707-4) (cited on page 22).
- [59] V. C. Rubin and J. F. W. Kent. “Rotation of the Andromeda Nebula from a Spectroscopic Survey of Emission Regions”. In: *The Astrophysical Journal* 159 (Feb. 1970), page 379. DOI: [10.1086/150317](https://doi.org/10.1086/150317). URL: <https://doi.org/10.1086/150317> (cited on page 22).

- [60] V. C. Rubin et al. “Motion of the Galaxy and the local group determined from the velocity anisotropy of distant SC I galaxies. I - The data”. In: *The Astronomical Journal* 81 (Sept. 1976), page 687. DOI: [10.1086/111942](https://doi.org/10.1086/111942). URL: <https://doi.org/10.1086/111942> (cited on page 22).
- [61] V. C. Rubin et al. “Motion of the Galaxy and the local group determined from the velocity anisotropy of distant SC I galaxies. II - The analysis for the motion”. In: *The Astronomical Journal* 81 (Sept. 1976), page 719. DOI: [10.1086/111943](https://doi.org/10.1086/111943). URL: <https://doi.org/10.1086/111943> (cited on page 22).
- [62] V. C. Rubin. “Dark Matter in Spiral Galaxies”. In: *Scientific American* 248.6 (June 1983), pages 96–108. DOI: [10.1038/scientificamerican0683-96](https://doi.org/10.1038/scientificamerican0683-96). URL: <https://doi.org/10.1038/scientificamerican0683-96> (cited on page 22).
- [63] D. Walsh, R. F. Carswell, and R. J. Weymann. “0957 + 561 A,B: twin quasistellar objects or gravitational lens?” In: *Nature* 279.5712 (May 1979), pages 381–384. DOI: [10.1038/279381a0](https://doi.org/10.1038/279381a0). URL: <https://doi.org/10.1038/279381a0> (cited on page 22).
- [64] A. G. Bergmann, V. Petrosian, and R. Lynds. “Gravitational lens models of arcs in clusters”. In: *The Astrophysical Journal* 350 (Feb. 1990), page 23. DOI: [10.1086/168359](https://doi.org/10.1086/168359). URL: <https://doi.org/10.1086/168359> (cited on page 22).
- [65] V. Mukhanov. *Physical Foundations of Cosmology*. Cambridge University Press, Nov. 2005. DOI: [10.1017/cbo9780511790553](https://doi.org/10.1017/cbo9780511790553). URL: <https://doi.org/10.1017/cbo9780511790553> (cited on page 22).
- [66] G. Ellis, R. Maartens, and M. MacCallum. *Relativistic Cosmology*. Cambridge University Press, 2009. DOI: [10.1017/cbo9781139014403](https://doi.org/10.1017/cbo9781139014403). URL: <https://doi.org/10.1017/cbo9781139014403> (cited on page 22).
- [67] Planck Collaboration. “Planck2015 results”. In: *Astronomy & Astrophysics* 594 (Sept. 2016), A13. DOI: [10.1051/0004-6361/201525830](https://doi.org/10.1051/0004-6361/201525830). URL: <https://doi.org/10.1051/0004-6361/201525830> (cited on page 22).
- [68] L. Roszkowski, E. M. Sessolo, and S. Trojanowski. “WIMP dark matter candidates and searches—current status and future prospects”. In: *Reports on Progress in Physics* 81.6 (May 2018), page 066201. DOI: [10.1088/1361-6633/aab913](https://doi.org/10.1088/1361-6633/aab913). URL: <https://doi.org/10.1088/1361-6633/aab913> (cited on page 23).
- [69] N. Sakai. “Naturalness in Supersymmetric Guts”. In: *Z. Phys. C* 11 (1981), page 153. DOI: [10.1007/BF01573998](https://doi.org/10.1007/BF01573998) (cited on pages 23, 27).
- [70] S. Dimopoulos, S. Raby, and F. Wilczek. “Supersymmetry and the Scale of Unification”. In: *Phys. Rev. D* 24 (1981), pages 1681–1683. DOI: [10.1103/PhysRevD.24.1681](https://doi.org/10.1103/PhysRevD.24.1681) (cited on pages 23, 27).
- [71] L. E. Ibanez and G. G. Ross. “Low-Energy Predictions in Supersymmetric Grand Unified Theories”. In: *Phys. Lett. B* 105 (1981), page 439. DOI: [10.1016/0370-2693\(81\)91200-4](https://doi.org/10.1016/0370-2693(81)91200-4) (cited on pages 23, 27).
- [72] W. D. Boer. “Grand unified theories and supersymmetry in particle physics and cosmology”. In: *Progress in Particle and Nuclear Physics* 33 (Jan. 1994), pages 201–301. DOI: [10.1016/0146-6410\(94\)90045-0](https://doi.org/10.1016/0146-6410(94)90045-0). URL: [https://doi.org/10.1016/0146-6410\(94\)90045-0](https://doi.org/10.1016/0146-6410(94)90045-0) (cited on page 23).
- [73] G. Senjanović et al. “Proton decay and grand unification”. In: AIP, 2010. DOI: [10.1063/1.3327552](https://doi.org/10.1063/1.3327552). URL: <https://doi.org/10.1063/1.3327552> (cited on page 23).

- [74] S. P. Martin. “A Supersymmetry primer”. In: *Adv. Ser. Direct. High Energy Phys.* 18 (1998), page 1. DOI: [10.1142/9789812839657_0001](https://doi.org/10.1142/9789812839657_0001), [10.1142/9789814307505_0001](https://doi.org/10.1142/9789814307505_0001). arXiv: [hep-ph/9709356](https://arxiv.org/abs/hep-ph/9709356) [[hep-ph](#)] (cited on page 23).
- [75] Yu. A. Golfand and E. P. Likhtman. “Extension of the Algebra of Poincare Group Generators and Violation of p Invariance”. In: *JETP Lett.* 13 (1971), pages 323–326 (cited on pages 23, 24).
- [76] D. V. Volkov and V. P. Akulov. “Is the Neutrino a Goldstone Particle?” In: *Phys. Lett. B* 46 (1973), pages 109–110. DOI: [10.1016/0370-2693\(73\)90490-5](https://doi.org/10.1016/0370-2693(73)90490-5) (cited on pages 23, 24).
- [77] J. Wess and B. Zumino. “Supergauge Transformations in Four-Dimensions”. In: *Nucl. Phys. B* 70 (1974), pages 39–50. DOI: [10.1016/0550-3213\(74\)90355-1](https://doi.org/10.1016/0550-3213(74)90355-1) (cited on pages 23, 26).
- [78] J. Wess and B. Zumino. “Supergauge Invariant Extension of Quantum Electrodynamics”. In: *Nucl. Phys. B* 78 (1974), page 1. DOI: [10.1016/0550-3213\(74\)90112-6](https://doi.org/10.1016/0550-3213(74)90112-6) (cited on pages 23, 26).
- [79] S. Ferrara and B. Zumino. “Supergauge Invariant Yang-Mills Theories”. In: *Nucl. Phys. B* 79 (1974), page 413. DOI: [10.1016/0550-3213\(74\)90559-8](https://doi.org/10.1016/0550-3213(74)90559-8) (cited on page 23).
- [80] A. Salam and J. A. Strathdee. “Supersymmetry and Nonabelian Gauges”. In: *Phys. Lett. B* 51 (1974), pages 353–355. DOI: [10.1016/0370-2693\(74\)90226-3](https://doi.org/10.1016/0370-2693(74)90226-3) (cited on page 23).
- [81] S. Coleman and J. Mandula. “All Possible Symmetries of the S-Matrix”. In: *Physical Review* 159.5 (July 1967), pages 1251–1256. DOI: [10.1103/physrev.159.1251](https://doi.org/10.1103/physrev.159.1251). URL: <https://doi.org/10.1103/physrev.159.1251> (cited on page 24).
- [82] O. Pelc and L. P. Horwitz. “Generalization of the Coleman-Mandula theorem to higher dimension”. In: *Journal of Mathematical Physics* 38.1 (Jan. 1997), pages 139–172. DOI: [10.1063/1.531846](https://doi.org/10.1063/1.531846). URL: <https://doi.org/10.1063/1.531846> (cited on page 24).
- [83] R. Haag, J. T. Lopuszański, and M. Sohnius. “All possible generators of supersymmetries of the S-matrix”. In: *Nuclear Physics B* 88.2 (Mar. 1975), pages 257–274. DOI: [10.1016/0550-3213\(75\)90279-5](https://doi.org/10.1016/0550-3213(75)90279-5). URL: [https://doi.org/10.1016/0550-3213\(75\)90279-5](https://doi.org/10.1016/0550-3213(75)90279-5) (cited on page 24).
- [84] P. Fayet. “Supersymmetry and Weak, Electromagnetic and Strong Interactions”. In: *Phys. Lett. B* 64 (1976), page 159. DOI: [10.1016/0370-2693\(76\)90319-1](https://doi.org/10.1016/0370-2693(76)90319-1) (cited on page 26).
- [85] P. Fayet. “Spontaneously Broken Supersymmetric Theories of Weak, Electromagnetic and Strong Interactions”. In: *Phys. Lett. B* 69 (1977), page 489. DOI: [10.1016/0370-2693\(77\)90852-8](https://doi.org/10.1016/0370-2693(77)90852-8) (cited on page 26).
- [86] A. Djouadi et al. “The Minimal supersymmetric standard model: Group summary report”. In: *GDR (Groupement De Recherche) - Supersymetrie Montpellier, France, April 15-17, 1998*. 1998. arXiv: [hep-ph/9901246](https://arxiv.org/abs/hep-ph/9901246) [[hep-ph](#)] (cited on pages 26, 152).
- [87] C. F. Berger et al. “Supersymmetry Without Prejudice”. In: *JHEP* 02 (2009), page 023. DOI: [10.1088/1126-6708/2009/02/023](https://doi.org/10.1088/1126-6708/2009/02/023). arXiv: [0812.0980](https://arxiv.org/abs/0812.0980) [[hep-ph](#)] (cited on pages 26, 152).
- [88] H. Murayama. “Supersymmetry phenomenology”. In: *Proceedings, Summer School in Particle Physics: Trieste, Italy, June 21-July 9, 1999*. 2000, pages 296–335. arXiv: [hep-ph/0002232](https://arxiv.org/abs/hep-ph/0002232) [[hep-ph](#)]. URL: <http://alice.cern.ch/format/showfull?sysnb=2177492> (cited on page 26).
- [89] L. Girardello and M. T. Grisaru. “Soft Breaking of Supersymmetry”. In: *Nucl. Phys. B* 194 (1982), page 65. DOI: [10.1016/0550-3213\(82\)90512-0](https://doi.org/10.1016/0550-3213(82)90512-0) (cited on page 27).

- [90] P. Fayet and J. Iliopoulos. “Spontaneously Broken Supergauge Symmetries and Goldstone Spinors”. In: *Phys. Lett. B* 51 (1974), pages 461–464. DOI: [10.1016/0370-2693\(74\)90310-4](https://doi.org/10.1016/0370-2693(74)90310-4) (cited on page 27).
- [91] L. O’Raifeartaigh. “Spontaneous Symmetry Breaking for Chiral Scalar Superfields”. In: *Nucl. Phys. B* 96 (1975), page 331. DOI: [10.1016/0550-3213\(75\)90585-4](https://doi.org/10.1016/0550-3213(75)90585-4) (cited on page 27).
- [92] S. Dimopoulos and H. Georgi. “Softly Broken Supersymmetry and SU(5)”. In: *Nucl. Phys. B* 193 (1981), page 150. DOI: [10.1016/0550-3213\(81\)90522-8](https://doi.org/10.1016/0550-3213(81)90522-8) (cited on page 27).
- [93] Super-Kamiokande Collaboration. “Search for proton decay via $p \rightarrow e^+\pi^0$ and $p \rightarrow \mu^+\pi^0$ in 0.31 megaton-years exposure of the Super-Kamiokande Water Cherenkov Detector”. In: *Physical Review D* 95.1 (Jan. 2017). DOI: [10.1103/physrevd.95.012004](https://doi.org/10.1103/physrevd.95.012004). URL: <https://doi.org/10.1103/physrevd.95.012004> (cited on page 28).
- [94] R. Barbieri and G. F. Giudice. “Upper Bounds on Supersymmetric Particle Masses”. In: *Nucl. Phys. B* 306 (1988), page 63. DOI: [10.1016/0550-3213\(88\)90171-X](https://doi.org/10.1016/0550-3213(88)90171-X) (cited on page 28).
- [95] B. de Carlos and J. A. Casas. “One loop analysis of the electroweak breaking in supersymmetric models and the fine tuning problem”. In: *Phys. Lett. B* 309 (1993), pages 320–328. DOI: [10.1016/0370-2693\(93\)90940-J](https://doi.org/10.1016/0370-2693(93)90940-J). arXiv: [hep-ph/9303291](https://arxiv.org/abs/hep-ph/9303291) [[hep-ph](#)] (cited on page 28).
- [96] G. R. Farrar and P. Fayet. “Phenomenology of the Production, Decay, and Detection of New Hadronic States Associated with Supersymmetry”. In: *Phys. Lett. B* 76 (1978), pages 575–579. DOI: [10.1016/0370-2693\(78\)90858-4](https://doi.org/10.1016/0370-2693(78)90858-4) (cited on page 28).
- [97] H. Goldberg. “Constraint on the Photino Mass from Cosmology”. In: *Phys. Rev. Lett.* 50 (1983). [Erratum: *Phys. Rev. Lett.* 103,099905(2009)], page 1419. DOI: [10.1103/PhysRevLett.50.1419](https://doi.org/10.1103/PhysRevLett.50.1419) (cited on page 29).
- [98] J. R. Ellis et al. “Supersymmetric Relics from the Big Bang”. In: *Nucl. Phys. B* 238 (1984), pages 453–476. DOI: [10.1016/0550-3213\(84\)90461-9](https://doi.org/10.1016/0550-3213(84)90461-9) (cited on page 29).
- [99] K. Inoue et al. “Aspects of Grand Unified Models with Softly Broken Supersymmetry”. In: *Prog. Theor. Phys.* 68 (1982). [Erratum: *Prog. Theor. Phys.* 70,330(1983)], page 927. DOI: [10.1143/PTP.68.927](https://doi.org/10.1143/PTP.68.927) (cited on page 30).
- [100] J. R. Ellis and S. Rudaz. “Search for Supersymmetry in Toponium Decays”. In: *Phys. Lett. B* 128 (1983), page 248. DOI: [10.1016/0370-2693\(83\)90402-1](https://doi.org/10.1016/0370-2693(83)90402-1) (cited on page 30).
- [101] J. Alwall et al. “Searching for Directly Decaying Gluinos at the Tevatron”. In: *Phys. Lett. B* 666 (2008), pages 34–37. DOI: [10.1016/j.physletb.2008.06.065](https://doi.org/10.1016/j.physletb.2008.06.065). arXiv: [0803.0019](https://arxiv.org/abs/0803.0019) [[hep-ph](#)] (cited on pages 30, 152).
- [102] J. Alwall, P. Schuster, and N. Toro. “Simplified Models for a First Characterization of New Physics at the LHC”. In: *Phys. Rev. D* 79 (2009), page 075020. DOI: [10.1103/PhysRevD.79.075020](https://doi.org/10.1103/PhysRevD.79.075020). arXiv: [0810.3921](https://arxiv.org/abs/0810.3921) [[hep-ph](#)] (cited on pages 30, 152).
- [103] D. Alves. “Simplified Models for LHC New Physics Searches”. In: *J. Phys. G* 39 (2012). Edited by N. Arkani-Hamed et al., page 105005. DOI: [10.1088/0954-3899/39/10/105005](https://doi.org/10.1088/0954-3899/39/10/105005). arXiv: [1105.2838](https://arxiv.org/abs/1105.2838) [[hep-ph](#)] (cited on pages 30, 152).
- [104] M. Papucci, J. T. Ruderman, and A. Weiler. “Natural SUSY Endures”. In: *JHEP* 09 (2012), page 035. DOI: [10.1007/JHEP09\(2012\)035](https://doi.org/10.1007/JHEP09(2012)035). arXiv: [1110.6926](https://arxiv.org/abs/1110.6926) [[hep-ph](#)] (cited on page 30).

- [105] ATLAS Collaboration. “Search for a supersymmetric partner to the top quark in final states with jets and missing transverse momentum at $\sqrt{s} = 7$ TeV with the ATLAS detector”. In: *Phys. Rev. Lett.* 109 (2012), page 211802. DOI: [10.1103/PhysRevLett.109.211802](https://doi.org/10.1103/PhysRevLett.109.211802). arXiv: [1208.1447](https://arxiv.org/abs/1208.1447) [[hep-ex](#)] (cited on page [31](#)).
- [106] ATLAS Collaboration. “Search for direct pair production of the top squark in all-hadronic final states in proton-proton collisions at $\sqrt{s} = 8$ TeV with the ATLAS detector”. In: *JHEP* 09 (2014), page 015. DOI: [10.1007/JHEP09\(2014\)015](https://doi.org/10.1007/JHEP09(2014)015). arXiv: [1406.1122](https://arxiv.org/abs/1406.1122) [[hep-ex](#)] (cited on page [31](#)).
- [107] CMS Collaboration. “Search for direct pair production of supersymmetric top quarks decaying to all-hadronic final states in pp collisions at $\sqrt{s} = 8$ TeV”. In: *Eur. Phys. J. C* 76.8 (2016), page 460. DOI: [10.1140/epjc/s10052-016-4292-5](https://doi.org/10.1140/epjc/s10052-016-4292-5). arXiv: [1603.00765](https://arxiv.org/abs/1603.00765) [[hep-ex](#)] (cited on page [31](#)).
- [108] CMS Collaboration. “Search for supersymmetry in the all-hadronic final state using top quark tagging in pp collisions at $\sqrt{s} = 13$ TeV”. In: *Phys. Rev. D* 96 (Jan. 2017), 012004. 32 p. DOI: [10.1103/PhysRevD.96.012004](https://doi.org/10.1103/PhysRevD.96.012004). URL: <https://cds.cern.ch/record/2240708> (cited on pages [31](#), [32](#)).
- [109] R. Jansky. “The ATLAS Fast Monte Carlo Production Chain Project”. In: *Journal of Physics: Conference Series* 664.7 (Dec. 2015), page 072024. DOI: [10.1088/1742-6596/664/7/072024](https://doi.org/10.1088/1742-6596/664/7/072024). URL: <https://doi.org/10.1088/1742-6596/664/7/072024> (cited on pages [33](#), [46](#), [48](#)).
- [110] S. Myers. *The LEP Collider, from design to approval and commissioning*. John Adams’ Lecture. Delivered at CERN, 26 Nov 1990. Geneva: CERN, 1991. DOI: [10.5170/CERN-1991-008](https://doi.org/10.5170/CERN-1991-008). URL: <https://cds.cern.ch/record/226776> (cited on page [33](#)).
- [111] E. Boltezar et al. “PERFORMANCE OF THE NEW CERN 50-MeV LINAC.” In: *IEEE Trans. Nucl. Sci.* 26 (1979), pages 3674–3676. DOI: [10.1109/TNS.1979.4330576](https://doi.org/10.1109/TNS.1979.4330576) (cited on page [33](#)).
- [112] D. J. Warner. *Project study for a new 50 MeV linear accelerator for the C. P. S.* Technical report CERN-MPS-LINP-73-1. Geneva: CERN, Oct. 1973. URL: <https://cds.cern.ch/record/414071> (cited on page [33](#)).
- [113] *The second stage CPS improvement study: 800 MeV booster synchrotron*. Geneva: CERN, 1967. URL: <https://cds.cern.ch/record/109292> (cited on page [33](#)).
- [114] *CERN Rapport annuel 1988*. Technical report. Geneva: CERN, 1989. URL: <https://cds.cern.ch/record/1516883> (cited on page [33](#)).
- [115] *CERN’s 25 GeV proton synchrotron*. Geneva: CERN, 1960. URL: <https://cds.cern.ch/record/445034> (cited on page [33](#)).
- [116] *The 300 GeV programme*. Geneva: CERN, 1972. URL: <https://cds.cern.ch/record/104068> (cited on page [33](#)).
- [117] ALICE Collaboration. “The ALICE experiment at the CERN LHC”. In: *JINST* 3 (2008), S08002. DOI: [10.1088/1748-0221/3/08/S08002](https://doi.org/10.1088/1748-0221/3/08/S08002) (cited on page [34](#)).
- [118] CMS Collaboration. “The CMS Experiment at the CERN LHC”. In: *JINST* 3 (2008), S08004. DOI: [10.1088/1748-0221/3/08/S08004](https://doi.org/10.1088/1748-0221/3/08/S08004) (cited on page [34](#)).
- [119] LHCb Collaboration. “The LHCb Detector at the LHC”. In: *JINST* 3 (2008), S08005. DOI: [10.1088/1748-0221/3/08/S08005](https://doi.org/10.1088/1748-0221/3/08/S08005) (cited on page [34](#)).

- [120] E. Mobs. “The CERN accelerator complex - 2019. Complexe des accélérateurs du CERN - 2019”. In: (July 2019). General Photo. URL: <https://cds.cern.ch/record/2684277> (cited on page 34).
- [121] J. C. Collins and D. E. Soper. “Parton distribution and decay functions”. In: *Nuclear Physics B* 194.3 (Jan. 1982), pages 445–492. DOI: [10.1016/0550-3213\(82\)90021-9](https://doi.org/10.1016/0550-3213(82)90021-9). URL: [https://doi.org/10.1016/0550-3213\(82\)90021-9](https://doi.org/10.1016/0550-3213(82)90021-9) (cited on page 34).
- [122] R. D. Ball et al. “Parton distributions from high-precision collider data”. In: *The European Physical Journal C* 77.10 (Oct. 2017). DOI: [10.1140/epjc/s10052-017-5199-5](https://doi.org/10.1140/epjc/s10052-017-5199-5). URL: <https://doi.org/10.1140/epjc/s10052-017-5199-5> (cited on page 35).
- [123] J. Collins. *Foundations of Perturbative QCD*. Cambridge University Press, 2009. DOI: [10.1017/cbo9780511975592](https://doi.org/10.1017/cbo9780511975592). URL: <https://doi.org/10.1017/cbo9780511975592> (cited on page 34).
- [124] ATLAS Collaboration. *Standard Model Summary Plots Summer 2019*. Technical report ATL-PHYS-PUB-2019-024. Geneva: CERN, July 2019. URL: <http://cds.cern.ch/record/2682186> (cited on page 36).
- [125] ATLAS Collaboration. “Performance of pile-up mitigation techniques for jets in pp collisions at $\sqrt{s} = 8\text{TeV}$ using the ATLAS detector”. In: *The European Physical Journal C* 76.11 (Oct. 2016). DOI: [10.1140/epjc/s10052-016-4395-z](https://doi.org/10.1140/epjc/s10052-016-4395-z). URL: <https://doi.org/10.1140/epjc/s10052-016-4395-z> (cited on pages 35, 59).
- [126] W. Herr and B. Muratori. “Concept of luminosity”. In: (2006). DOI: [10.5170/CERN-2006-002.361](https://cds.cern.ch/record/941318). URL: <https://cds.cern.ch/record/941318> (cited on page 36).
- [127] R. Bruce et al. “LHC Run 2: Results and challenges”. In: *Proceedings, 57th ICFA Advanced Beam Dynamics Workshop on High-Intensity and High-Brightness Hadron Beams (HB2016): Malmö, Sweden, July 3-8, 2016*. 2016, MOAM5P50. DOI: [10.18429/JACoW-HB2016-MOAM5P50](https://doi.org/10.18429/JACoW-HB2016-MOAM5P50) (cited on page 37).
- [128] J. Pequeno. “Computer generated image of the whole ATLAS detector”. Mar. 2008. URL: <https://cds.cern.ch/record/1095924> (cited on page 38).
- [129] ATLAS Collaboration. *ATLAS magnet system: Technical Design Report, 1*. Technical Design Report ATLAS. Geneva: CERN, 1997. URL: <https://cds.cern.ch/record/338080> (cited on page 38).
- [130] J. Goodson. URL: <http://www.jetgoodson.com/images/thesisImages/magnetSystems.png> (cited on page 39).
- [131] ATLAS Collaboration. *ATLAS inner detector: Technical Design Report, 1*. Technical Design Report ATLAS. Geneva: CERN, 1997. URL: <https://cds.cern.ch/record/331063> (cited on page 38).
- [132] G. Ripellino. “The alignment of the ATLAS Inner Detector in Run-2”. In: *Proceedings of Fourth Annual Large Hadron Collider Physics — PoS(LHCP2016)*. Sissa Medialab, Sept. 2016. DOI: [10.22323/1.276.0196](https://doi.org/10.22323/1.276.0196). URL: <https://doi.org/10.22323/1.276.0196> (cited on page 38).
- [133] J. Pequeno. “Computer generated image of the ATLAS inner detector”. Mar. 2008. URL: <https://cds.cern.ch/record/1095926> (cited on page 40).
- [134] N. Wermes and G. Hallewel. *ATLAS pixel detector: Technical Design Report*. Technical Design Report ATLAS. Geneva: CERN, 1998. URL: <https://cds.cern.ch/record/381263> (cited on page 39).

- [135] ATLAS Collaboration. “ATLAS pixel detector electronics and sensors”. In: *JINST* 3 (2008), P07007. DOI: [10.1088/1748-0221/3/07/P07007](https://doi.org/10.1088/1748-0221/3/07/P07007). URL: <https://cds.cern.ch/record/1119279> (cited on page 39).
- [136] M. Capeans et al. *ATLAS Insertable B-Layer Technical Design Report*. Technical report CERN-LHCC-2010-013. ATLAS-TDR-19. Sept. 2010. URL: <https://cds.cern.ch/record/1291633> (cited on page 39).
- [137] ATLAS Collaboration. “Production and integration of the ATLAS Insertable B-Layer”. In: *Journal of Instrumentation* 13.05 (May 2018), T05008–T05008. DOI: [10.1088/1748-0221/13/05/t05008](https://doi.org/10.1088/1748-0221/13/05/t05008). URL: <https://doi.org/10.1088/1748-0221/13/05/t05008> (cited on page 39).
- [138] A. Miucci. “The ATLAS Insertable B-Layer project”. In: *Journal of Instrumentation* 9.02 (Feb. 2014), pages C02018–C02018. DOI: [10.1088/1748-0221/9/02/c02018](https://doi.org/10.1088/1748-0221/9/02/c02018). URL: <https://doi.org/10.1088/1748-0221/9/02/c02018> (cited on page 39).
- [139] V. A. Mitsou. *The ATLAS Transition Radiation Tracker*. Technical report ATL-CONF-2003-012. Geneva: CERN, Nov. 2003. DOI: [10.1142/9789812702708_0073](https://doi.org/10.1142/9789812702708_0073). URL: <https://cds.cern.ch/record/686973> (cited on page 39).
- [140] A. Bingül. “The ATLAS TRT and its Performance at LHC”. In: *Journal of Physics: Conference Series* 347 (Feb. 2012), page 012025. DOI: [10.1088/1742-6596/347/1/012025](https://doi.org/10.1088/1742-6596/347/1/012025). URL: <https://doi.org/10.1088/1742-6596/347/1/012025> (cited on page 39).
- [141] A. Vogel. *ATLAS Transition Radiation Tracker (TRT): Straw Tube Gaseous Detectors at High Rates*. Technical report ATL-INDET-PROC-2013-005. Geneva: CERN, Apr. 2013. URL: <https://cds.cern.ch/record/1537991> (cited on page 39).
- [142] ATLAS Collaboration. *ATLAS calorimeter performance: Technical Design Report*. Technical Design Report ATLAS. Geneva: CERN, 1996. URL: <https://cds.cern.ch/record/331059> (cited on page 40).
- [143] F. Teischinger. “Energy Measurement with the ATLAS Electromagnetic Calorimeter at the Per Mill Accuracy Level”. Presented 19 Mar 2014. Feb. 2014. URL: <https://cds.cern.ch/record/1699838> (cited on page 40).
- [144] L. Plazak. *The ATLAS hadronic calorimeter at the LHC and the phase II upgrade program*. Technical report ATL-TILECAL-PROC-2015-022. Geneva: CERN, Nov. 2015. URL: <https://cds.cern.ch/record/2108963> (cited on page 40).
- [145] J. Pequeno. “Computer Generated image of the ATLAS calorimeter”. Mar. 2008. URL: <https://cds.cern.ch/record/1095927> (cited on page 41).
- [146] ATLAS Collaboration. *ATLAS liquid-argon calorimeter: Technical Design Report*. Technical Design Report ATLAS. Geneva: CERN, 1996. URL: <https://cds.cern.ch/record/331061> (cited on page 41).
- [147] M. Aleksa et al. *ATLAS Liquid Argon Calorimeter Phase-I Upgrade Technical Design Report*. Technical report CERN-LHCC-2013-017. Final version presented to December 2013 LHCC. Sept. 2013. URL: <https://cds.cern.ch/record/1602230> (cited on page 41).
- [148] ATLAS Collaboration. “Energy Linearity and Resolution of the ATLAS Electromagnetic Barrel Calorimeter in an Electron Test-Beam”. In: *Nucl. Instrum. Methods Phys. Res., A* 568.2 (Aug. 2006), 601–623. 48 p. DOI: [10.1016/j.nima.2006.07.053](https://doi.org/10.1016/j.nima.2006.07.053). URL: <https://cds.cern.ch/record/976098> (cited on page 41).

- [149] ATLAS Collaboration. “Performance of the ATLAS Electromagnetic Calorimeter End-cap Module 0”. In: *Nucl. Instrum. Methods Phys. Res., A* 500 (Nov. 2002), 178–201r. 31 p. DOI: [10.1016/S0168-9002\(03\)00344-9](https://doi.org/10.1016/S0168-9002(03)00344-9). URL: <https://cds.cern.ch/record/606885> (cited on page 41).
- [150] D. Fortin. “Performance of the ATLAS Hadronic Endcap Calorimeter Modules to Electrons and Pions”. Presented 30 Nov 2000. 2000. URL: <https://cds.cern.ch/record/1324857> (cited on page 41).
- [151] R. S. Orr. *The ATLAS Forward Calorimeter*. Technical report ATL-LARG-SLIDE-2011-592. Sept. 2011. URL: <https://cds.cern.ch/record/1386649> (cited on page 42).
- [152] ATLAS Collaboration. *ATLAS tile calorimeter: Technical Design Report*. Technical Design Report ATLAS. Geneva: CERN, 1996. URL: <https://cds.cern.ch/record/331062> (cited on page 42).
- [153] ATLAS Collaboration. *ATLAS muon spectrometer: Technical Design Report*. Technical Design Report ATLAS. Geneva: CERN, 1997. URL: <https://cds.cern.ch/record/331068> (cited on page 42).
- [154] J. Pequeno. “Computer generated image of the ATLAS Muons subsystem”. Mar. 2008. URL: <https://cds.cern.ch/record/1095929> (cited on page 42).
- [155] M. Livan. *Monitored drift tubes in ATLAS*. Technical report ATL-M-PN-129. Geneva: CERN, Sept. 1996. DOI: [10.1016/S0168-9002\(96\)00851-0](https://doi.org/10.1016/S0168-9002(96)00851-0). URL: <https://cds.cern.ch/record/319197> (cited on page 43).
- [156] T. Argyropoulos et al. “Cathode strip chambers in ATLAS : Installation, commissioning and in situ performance”. In: *2008 IEEE Nuclear Science Symposium Conference Record*. IEEE, Oct. 2008. DOI: [10.1109/nssmic.2008.4774958](https://doi.org/10.1109/nssmic.2008.4774958). URL: <https://doi.org/10.1109/nssmic.2008.4774958> (cited on page 43).
- [157] D. Boscherini. *Performance and operation of the ATLAS Resistive Plate Chamber system in LHC Run-1*. Technical report ATL-MUON-PROC-2014-005. 12. Geneva: CERN, Sept. 2014. DOI: [10.1088/1748-0221/9/12/C12039](https://doi.org/10.1088/1748-0221/9/12/C12039). URL: <https://cds.cern.ch/record/1753173> (cited on page 43).
- [158] K. Nagai. “Thin gap chambers in ATLAS”. In: *Nuclear Instruments and Methods in Physics Research Section A: Accelerators, Spectrometers, Detectors and Associated Equipment* 384.1 (Dec. 1996), pages 219–221. DOI: [10.1016/S0168-9002\(96\)01065-0](https://doi.org/10.1016/S0168-9002(96)01065-0). URL: [https://doi.org/10.1016/S0168-9002\(96\)01065-0](https://doi.org/10.1016/S0168-9002(96)01065-0) (cited on page 43).
- [159] ATLAS Collaboration. *ATLAS high-level trigger, data acquisition and controls: Technical design report*. Technical report CERN-LHCC-2003-022. 2003 (cited on page 43).
- [160] W. Buttinger. *The ATLAS Level-1 Trigger System*. Technical report ATL-DAQ-PROC-2012-024. Geneva: CERN, June 2012. DOI: [10.1088/1742-6596/396/1/012010](https://doi.org/10.1088/1742-6596/396/1/012010). URL: <https://cds.cern.ch/record/1456546> (cited on page 43).
- [161] K. Nagano. “Algorithms, performance, development of the ATLAS High-Level trigger”. In: *Journal of Physics: Conference Series* 513.1 (June 2014), page 012026. DOI: [10.1088/1742-6596/513/1/012026](https://doi.org/10.1088/1742-6596/513/1/012026). URL: <https://doi.org/10.1088/1742-6596/513/1/012026> (cited on page 43).
- [162] ATLAS Collaboration. “Performance of the ATLAS Trigger System in 2015”. In: *Eur. Phys. J. C* 77.CERN-EP-2016-241. 5 (Nov. 2016), 317. 76 p. DOI: [10.1140/epjc/s10052-017-4852-3](https://doi.org/10.1140/epjc/s10052-017-4852-3). URL: <https://cds.cern.ch/record/2235584> (cited on page 44).

- [163] ATLAS Collaboration. “The ATLAS Simulation Infrastructure”. In: *The European Physical Journal C* 70.3 (Sept. 2010), pages 823–874. DOI: [10.1140/epjc/s10052-010-1429-9](https://doi.org/10.1140/epjc/s10052-010-1429-9). URL: <https://doi.org/10.1140/epjc/s10052-010-1429-9> (cited on page 44).
- [164] T. Sjöstrand et al. “An introduction to PYTHIA 8.2”. In: *Computer Physics Communications* 191 (June 2015), pages 159–177. DOI: [10.1016/j.cpc.2015.01.024](https://doi.org/10.1016/j.cpc.2015.01.024). URL: <https://doi.org/10.1016/j.cpc.2015.01.024> (cited on page 44).
- [165] B. Andersson et al. “Parton fragmentation and string dynamics”. In: *Physics Reports* 97.2-3 (July 1983), pages 31–145. DOI: [10.1016/0370-1573\(83\)90080-7](https://doi.org/10.1016/0370-1573(83)90080-7). URL: [https://doi.org/10.1016/0370-1573\(83\)90080-7](https://doi.org/10.1016/0370-1573(83)90080-7) (cited on page 44).
- [166] M. Bähr et al. “Herwig++ physics and manual”. In: *The European Physical Journal C* 58.4 (Nov. 2008), pages 639–707. DOI: [10.1140/epjc/s10052-008-0798-9](https://doi.org/10.1140/epjc/s10052-008-0798-9). URL: <https://doi.org/10.1140/epjc/s10052-008-0798-9> (cited on page 44).
- [167] B. R. Webber. “Hadronization”. In: *Proceedings: Summer School on Hadronic Aspects of Collider Physics, Zuoz, Switzerland, Aug 23-31, 1994*. 1994, pages 49–77. arXiv: [hep-ph/9411384](https://arxiv.org/abs/hep-ph/9411384) [[hep-ph](https://arxiv.org/abs/hep-ph/9411384)] (cited on page 44).
- [168] S. Catani et al. “QCD Matrix Elements + Parton Showers”. In: *Journal of High Energy Physics* 2001.11 (Nov. 2001), pages 063–063. DOI: [10.1088/1126-6708/2001/11/063](https://doi.org/10.1088/1126-6708/2001/11/063). URL: <https://doi.org/10.1088/1126-6708/2001/11/063> (cited on page 45).
- [169] J. Alwall et al. “The automated computation of tree-level and next-to-leading order differential cross sections, and their matching to parton shower simulations”. In: *Journal of High Energy Physics* 2014.7 (July 2014). DOI: [10.1007/jhep07\(2014\)079](https://doi.org/10.1007/jhep07(2014)079). URL: [https://doi.org/10.1007/jhep07\(2014\)079](https://doi.org/10.1007/jhep07(2014)079) (cited on page 45).
- [170] E. Bothmann et al. “Event generation with Sherpa 2.2”. In: *SciPost Physics* 7.3 (Sept. 2019). DOI: [10.21468/scipostphys.7.3.034](https://doi.org/10.21468/scipostphys.7.3.034). URL: <https://doi.org/10.21468/scipostphys.7.3.034> (cited on pages 45, 114).
- [171] F. Buccioni et al. “OpenLoops 2”. In: *The European Physical Journal C* 79.10 (Oct. 2019). DOI: [10.1140/epjc/s10052-019-7306-2](https://doi.org/10.1140/epjc/s10052-019-7306-2). URL: <https://doi.org/10.1140/epjc/s10052-019-7306-2> (cited on page 45).
- [172] S. Höche et al. “QCD matrix elements + parton showers. The NLO case”. In: *Journal of High Energy Physics* 2013.4 (Apr. 2013). DOI: [10.1007/jhep04\(2013\)027](https://doi.org/10.1007/jhep04(2013)027). URL: [https://doi.org/10.1007/jhep04\(2013\)027](https://doi.org/10.1007/jhep04(2013)027) (cited on page 45).
- [173] C. Oleari. “The POWHEG BOX”. In: *Nuclear Physics B - Proceedings Supplements* 205-206 (Aug. 2010), pages 36–41. DOI: [10.1016/j.nuclphysbps.2010.08.016](https://doi.org/10.1016/j.nuclphysbps.2010.08.016). URL: <https://doi.org/10.1016/j.nuclphysbps.2010.08.016> (cited on page 45).
- [174] A. Buckley et al. “General-purpose event generators for LHC physics”. In: *Physics Reports* 504.5 (July 2011), pages 145–233. DOI: [10.1016/j.physrep.2011.03.005](https://doi.org/10.1016/j.physrep.2011.03.005). URL: <https://doi.org/10.1016/j.physrep.2011.03.005> (cited on page 45).
- [175] T. Gleisberg et al. “Event generation with SHERPA 1.1”. In: *Journal of High Energy Physics* 2009.02 (Feb. 2009), pages 007–007. DOI: [10.1088/1126-6708/2009/02/007](https://doi.org/10.1088/1126-6708/2009/02/007). URL: <https://doi.org/10.1088/1126-6708/2009/02/007> (cited on page 45).
- [176] S. Agostinelli et al. “Geant4—a simulation toolkit”. In: *Nuclear Instruments and Methods in Physics Research Section A: Accelerators, Spectrometers, Detectors and Associated Equipment* 506.3 (July 2003), pages 250–303. DOI: [10.1016/s0168-9002\(03\)01368-8](https://doi.org/10.1016/s0168-9002(03)01368-8). URL: [https://doi.org/10.1016/s0168-9002\(03\)01368-8](https://doi.org/10.1016/s0168-9002(03)01368-8) (cited on page 45).

- [177] C. Eck et al. *LHC computing Grid: Technical Design Report. Version 1.06 (20 Jun 2005)*. Technical Design Report LCG. Geneva: CERN, 2005. URL: <https://cds.cern.ch/record/840543> (cited on page 46).
- [178] A. G. et al., editors. *High-Luminosity Large Hadron Collider (HL-LHC): Technical Design Report V. 0.1*. CERN Yellow Reports: Monographs. Geneva: CERN, 2017. DOI: [10.23731/CYRM-2017-004](https://doi.org/10.23731/CYRM-2017-004). URL: <https://cds.cern.ch/record/2284929> (cited on page 46).
- [179] J. Schaarschmidt. *The new ATLAS Fast Calorimeter Simulation*. Technical report ATL-SOFT-PROC-2017-005. Geneva: CERN, Jan. 2017. URL: <https://cds.cern.ch/record/2240206> (cited on pages 46–48).
- [180] ATLAS Collaboration. *The simulation principle and performance of the ATLAS fast calorimeter simulation FastCaloSim*. Technical report ATL-PHYS-PUB-2010-013. Geneva: CERN, Oct. 2010. URL: <https://cds.cern.ch/record/1300517> (cited on pages 46, 47).
- [181] K. Edmonds et al. *The fast ATLAS track simulation (FATRAS)*. Technical report ATL-SOFT-PUB-2008-001, ATL-COM-SOFT-2008-002. 2008 (cited on pages 46, 47).
- [182] ATLAS Collaboration. “ATLAS Computing and Software Public Results”. URL: <https://twiki.cern.ch/twiki/bin/view/AtlasPublic/ComputingandSoftwarePublicResults> (cited on pages 46, 47, 50).
- [183] E. Ritsch et al. “ATLAS Detector Simulation in the Integrated Simulation Framework applied to the W Boson Mass Measurement”. Presented 27 Feb 2015. PhD thesis. Innsbruck U., Dec. 2014. URL: <https://cds.cern.ch/record/2221649> (cited on pages 46, 47).
- [184] R. Jansky. “Truth Seeded Reconstruction for Fast Simulation in the ATLAS Experiment”. Master’s thesis. Innsbruck U., 2013. URL: http://inspirehep.net/record/1296567/files/44446892_CERN-THESIS-2013-194.pdf (cited on page 47).
- [185] ATLAS Collaboration. “ATLAS Simulation CPU Performance”. URL: <https://atlas.web.cern.ch/Atlas/GROUPS/PHYSICS/PLOTS/SIM-2019-002/> (cited on page 49).
- [186] Z. Marshall and the Atlas Collaboration. “Simulation of Pile-up in the ATLAS Experiment”. In: *Journal of Physics: Conference Series* 513.2 (2014), page 022024. URL: <http://stacks.iop.org/1742-6596/513/i=2/a=022024> (cited on page 47).
- [187] R. Davis and P. Savard. *A Study of Pileup Noise in the Barrel and Endcap Calorimetry*. Technical report ATL-CAL-96-084, ATL-AC-PN-84. Geneva: CERN, Mar. 1996. URL: <https://cds.cern.ch/record/685704> (cited on page 47).
- [188] ATLAS Collaboration. “MC+MC Pile-up Overlay Performance Plots”. URL: <https://atlas.web.cern.ch/Atlas/GROUPS/PHYSICS/PLOTS/SIM-2018-002/> (cited on page 49).
- [189] ATLAS Collaboration. *Deep generative models for fast shower simulation in ATLAS*. Technical report ATL-SOFT-PUB-2018-001. Geneva: CERN, July 2018. URL: <http://cds.cern.ch/record/2630433> (cited on page 48).
- [190] ATLAS Collaboration. *Luminosity determination in pp collisions at $\sqrt{s} = 13$ TeV using the ATLAS detector at the LHC*. Technical report ATLAS-CONF-2019-021. Geneva: CERN, June 2019. URL: <https://cds.cern.ch/record/2677054> (cited on pages 51, 113).
- [191] LHC Team. *LHC Report: end of 2016 proton-proton operation*. Technical report. Oct. 2016. URL: <https://cds.cern.ch/record/2229040> (cited on page 51).

- [192] ATLAS Collaboration. “ATLAS Luminosity Public Results”. URL: <https://twiki.cern.ch/twiki/bin/view/AtlasPublic/LuminosityPublicResultsRun2> (cited on page 52).
- [193] J. Pequeno. “Event Cross Section in a computer generated image of the ATLAS detector.” Mar. 2008. URL: <https://cds.cern.ch/record/1096081> (cited on page 53).
- [194] T. Cornelissen et al. *Concepts, Design and Implementation of the ATLAS New Tracking (NEWT)*. Technical report ATL-SOFT-PUB-2007-007. ATL-COM-SOFT-2007-002. Geneva: CERN, Mar. 2007. URL: <https://cds.cern.ch/record/1020106> (cited on page 53).
- [195] R. Frühwirth. “Application of Kalman filtering to track and vertex fitting”. In: *Nuclear Instruments and Methods in Physics Research Section A: Accelerators, Spectrometers, Detectors and Associated Equipment* 262.2-3 (Dec. 1987), pages 444–450. DOI: [10.1016/0168-9002\(87\)90887-4](https://doi.org/10.1016/0168-9002(87)90887-4). URL: [https://doi.org/10.1016/0168-9002\(87\)90887-4](https://doi.org/10.1016/0168-9002(87)90887-4) (cited on page 53).
- [196] ATLAS Collaboration. *Early Inner Detector Tracking Performance in the 2015 data at $\sqrt{s} = 13$ TeV*. Technical report ATL-PHYS-PUB-2015-051. Geneva: CERN, Dec. 2015. URL: <https://cds.cern.ch/record/2110140> (cited on page 53).
- [197] ATLAS Collaboration. *Vertex Reconstruction Performance of the ATLAS Detector at $\sqrt{s} = 13$ TeV*. Technical report ATL-PHYS-PUB-2015-026. Geneva: CERN, July 2015. URL: <https://cds.cern.ch/record/2037717> (cited on page 53).
- [198] ATLAS Collaboration. *Performance of the ATLAS Inner Detector Track and Vertex Reconstruction in the High Pile-Up LHC Environment*. Technical report ATLAS-CONF-2012-042. Geneva: CERN, Mar. 2012. URL: <https://cds.cern.ch/record/1435196> (cited on page 53).
- [199] ATLAS Collaboration. *Optimisation of the ATLAS b-tagging performance for the 2016 LHC Run*. Technical report ATL-PHYS-PUB-2016-012. Geneva: CERN, June 2016. URL: <https://cds.cern.ch/record/2160731> (cited on pages 53, 60, 63).
- [200] ATLAS Collaboration. “Electron reconstruction and identification in the ATLAS experiment using the 2015 and 2016 LHC proton-proton collision data at $\sqrt{s} = 13$ TeV”. In: *The European Physical Journal C* 79.8 (Aug. 2019). DOI: [10.1140/epjc/s10052-019-7140-6](https://doi.org/10.1140/epjc/s10052-019-7140-6). URL: <https://doi.org/10.1140/epjc/s10052-019-7140-6> (cited on page 54).
- [201] ATLAS Collaboration. *Electron efficiency measurements with the ATLAS detector using the 2015 LHC proton-proton collision data*. Technical report ATLAS-CONF-2016-024. Geneva: CERN, June 2016. URL: <https://cds.cern.ch/record/2157687> (cited on page 54).
- [202] ATLAS Collaboration. *Electron and photon energy calibration with the ATLAS detector using data collected in 2015 at $\sqrt{s} = 13$ TeV*. Technical report ATL-PHYS-PUB-2016-015. Geneva: CERN, Aug. 2016. URL: <https://cds.cern.ch/record/2203514> (cited on page 54).
- [203] ATLAS Collaboration. “Electron and photon energy calibration with the ATLAS detector using 2015–2016 LHC proton-proton collision data”. In: *JINST* 14.03 (2019), P03017. DOI: [10.1088/1748-0221/14/03/P03017](https://doi.org/10.1088/1748-0221/14/03/P03017). arXiv: [1812.03848](https://arxiv.org/abs/1812.03848) [hep-ex] (cited on page 54).
- [204] ATLAS Collaboration. *Electron and photon reconstruction and performance in ATLAS using a dynamical, topological cell clustering-based approach*. Technical report ATL-PHYS-PUB-2017-022. Geneva: CERN, Dec. 2017. URL: <http://cds.cern.ch/record/2298955> (cited on pages 54, 55).

- [205] ATLAS Collaboration. “Electron and photon performance measurements with the ATLAS detector using the 2015–2017 LHC proton-proton collision data”. In: *JINST* 14.12 (2019), P12006. DOI: [10.1088/1748-0221/14/12/P12006](https://doi.org/10.1088/1748-0221/14/12/P12006). arXiv: [1908.00005](https://arxiv.org/abs/1908.00005) [hep-ex] (cited on page 56).
- [206] ATLAS Collaboration. *Single electron trigger 2018 performance plots*. Technical report ATL-COM-DAQ-2019-049. Geneva: CERN, Mar. 2019. URL: <https://cds.cern.ch/record/2668252> (cited on page 57).
- [207] ATLAS Collaboration. “Muon reconstruction performance of the ATLAS detector in proton–proton collision data at $\sqrt{s} = 13$ TeV”. In: *Eur. Phys. J. C* 76.5 (2016), page 292. DOI: [10.1140/epjc/s10052-016-4120-y](https://doi.org/10.1140/epjc/s10052-016-4120-y). arXiv: [1603.05598](https://arxiv.org/abs/1603.05598) [hep-ex] (cited on pages 55, 58, 86, 94, 152).
- [208] ATLAS Collaboration. *Muon trigger efficiency in early 2018 data taking*. Technical report ATL-COM-DAQ-2018-047. Geneva: CERN, May 2017. URL: <https://cds.cern.ch/record/2318500> (cited on page 59).
- [209] ATLAS Collaboration. “Measurement of the photon identification efficiencies with the ATLAS detector using LHC Run-1 data”. In: *Eur. Phys. J. C* 76.12 (2016), page 666. DOI: [10.1140/epjc/s10052-016-4507-9](https://doi.org/10.1140/epjc/s10052-016-4507-9). arXiv: [1606.01813](https://arxiv.org/abs/1606.01813) [hep-ex] (cited on pages 56, 60).
- [210] ATLAS Collaboration. “Measurement of the photon identification efficiencies with the ATLAS detector using LHC Run 2 data collected in 2015 and 2016”. In: *The European Physical Journal C* 79.3 (Mar. 2019). DOI: [10.1140/epjc/s10052-019-6650-6](https://doi.org/10.1140/epjc/s10052-019-6650-6). URL: <https://doi.org/10.1140/epjc/s10052-019-6650-6> (cited on page 56).
- [211] ATLAS Collaboration. “Photon identification efficiencies using the full 2015+2016 dataset”. URL: <https://atlas.web.cern.ch/Atlas/GROUPS/PHYSICS/PLOTS/EGAM-2017-004/> (cited on page 60).
- [212] ATLAS Collaboration. *Electron and photon trigger efficiency plots using the full 2016 dataset*. Technical report ATL-COM-DAQ-2017-015. Geneva: CERN, Mar. 2017. URL: <https://cds.cern.ch/record/2254973> (cited on page 61).
- [213] ATLAS Collaboration. “Jet energy scale measurements and their systematic uncertainties in proton-proton collisions at $\sqrt{s} = 13$ TeV with the ATLAS detector”. In: *Phys. Rev. D* 96 (7 Oct. 2017), page 072002. DOI: [10.1103/PhysRevD.96.072002](https://doi.org/10.1103/PhysRevD.96.072002). URL: <https://link.aps.org/doi/10.1103/PhysRevD.96.072002> (cited on pages 58, 62, 95, 175).
- [214] ATLAS Collaboration. “Determination of jet calibration and energy resolution in proton-proton collisions at $\sqrt{s} = 8$ TeV using the ATLAS detector”. In: (2019). arXiv: [1910.04482](https://arxiv.org/abs/1910.04482) [hep-ex] (cited on page 58).
- [215] A. Schwartzman. “Jet energy calibration at the LHC”. In: *International Journal of Modern Physics A* 30.31 (Nov. 2015), page 1546002. DOI: [10.1142/s0217751x15460021](https://doi.org/10.1142/s0217751x15460021). URL: <https://doi.org/10.1142/s0217751x15460021> (cited on page 58).
- [216] M. Cacciari, G. P. Salam, and G. Soyez. “The Anti-k(t) jet clustering algorithm”. In: *JHEP* 04 (2008), page 063. DOI: [10.1088/1126-6708/2008/04/063](https://doi.org/10.1088/1126-6708/2008/04/063). arXiv: [0802.1189](https://arxiv.org/abs/0802.1189) [hep-ph] (cited on pages 58, 86, 153).
- [217] ATLAS Collaboration. *Constituent-level pile-up mitigation techniques in ATLAS*. Technical report ATLAS-CONF-2017-065. Geneva: CERN, Aug. 2017. URL: <https://cds.cern.ch/record/2281055> (cited on page 59).

- [218] ATLAS Collaboration. “Jet energy scale and uncertainties in 2015-2017 data and simulation”. URL: <https://atlas.web.cern.ch/Atlas/GROUPS/PHYSICS/PLOTS/JETM-2018-006/> (cited on page 62).
- [219] M. Lehmacher. *b-Tagging Algorithms and their Performance at ATLAS*. Technical report ATL-PHYS-PROC-2008-052. Geneva: CERN, July 2008. URL: <https://cds.cern.ch/record/1128662> (cited on page 59).
- [220] ATLAS Collaboration. *Expected performance of the ATLAS b-tagging algorithms in Run-2*. Technical report ATL-PHYS-PUB-2015-022. Geneva: CERN, July 2015. URL: <http://cds.cern.ch/record/2037697> (cited on page 59).
- [221] ATLAS Collaboration. “Performance of b-jet identification in the ATLAS experiment”. In: *Journal of Instrumentation* 11.04 (Apr. 2016), P04008–P04008. DOI: 10.1088/1748-0221/11/04/p04008. URL: <https://doi.org/10.1088/1748-0221/11/04/p04008> (cited on page 59).
- [222] ATLAS Collaboration. *Calibration of b-tagging using dileptonic top pair events in a combinatorial likelihood approach with the ATLAS experiment*. Technical report ATLAS-CONF-2014-004. Geneva: CERN, Feb. 2014. URL: <https://cds.cern.ch/record/1664335> (cited on pages 60, 95).
- [223] ATLAS Collaboration. “ATLAS b-jet identification performance and efficiency measurement with $t\bar{t}$ events in pp collisions at $\sqrt{s} = 13$ TeV”. In: *The European Physical Journal C* 79.11 (Nov. 2019). DOI: 10.1140/epjc/s10052-019-7450-8. URL: <https://doi.org/10.1140/epjc/s10052-019-7450-8> (cited on page 60).
- [224] ATLAS Collaboration. “Performance of missing transverse momentum reconstruction with the ATLAS detector using proton–proton collisions at $\sqrt{s} = 13$ TeV”. In: *The European Physical Journal C* 78.11 (Nov. 2018). DOI: 10.1140/epjc/s10052-018-6288-9. URL: <https://doi.org/10.1140/epjc/s10052-018-6288-9> (cited on pages 60, 64).
- [225] ATLAS Collaboration. “ATLAS Missing Energy Trigger Public Results”. URL: <https://twiki.cern.ch/twiki/bin/view/AtlasPublic/MissingEtTriggerPublicResults> (cited on page 65).
- [226] ATLAS Collaboration. “Measurements of top-quark pair differential cross-sections in the lepton+jets channel in pp collisions at $\sqrt{s} = 8$ TeV using the ATLAS detector”. In: *The European Physical Journal C* 76.10 (Oct. 2016). DOI: 10.1140/epjc/s10052-016-4366-4. URL: <https://doi.org/10.1140/epjc/s10052-016-4366-4> (cited on page 66).
- [227] M. Cacciari, G. P. Salam, and G. Soyez. “The catchment area of jets”. In: *Journal of High Energy Physics* 2008.04 (Apr. 2008), pages 005–005. DOI: 10.1088/1126-6708/2008/04/005. URL: <https://doi.org/10.1088/1126-6708/2008/04/005> (cited on pages 66, 124).
- [228] G. Cowan. *Statistical data analysis*. Oxford, UK: Clarendon 197 p, 1998. ISBN: 9780198501565 (cited on pages 71, 74).
- [229] G. Cowan. “Topics in statistical data analysis for high-energy physics”. In: arXiv:1012.3589 (Dec. 2010), 197–218. 22 p. DOI: 10.5170/CERN-2010-002.197. URL: <https://cds.cern.ch/record/1281954> (cited on pages 71, 74).
- [230] L. Lista. “Statistical Methods for Data Analysis in Particle Physics”. In: *Lect. Notes Phys.* 941 (2017), pages 1–257. DOI: 10.1007/978-3-319-62840-0 (cited on pages 71, 74).

- [231] A. L. Read. “Presentation of search results: the CL_s technique”. In: *Journal of Physics G: Nuclear and Particle Physics* 28.10 (Sept. 2002), pages 2693–2704. DOI: [10.1088/0954-3899/28/10/313](https://doi.org/10.1088/0954-3899/28/10/313). URL: <https://doi.org/10.1088/0954-3899/28/10/313> (cited on page 76).
- [232] R. D. Cousins, S. J. May, and Y. Sun. *Should unfolded histograms be used to test hypotheses?* 2016. arXiv: [1607.07038](https://arxiv.org/abs/1607.07038) [[physics.data-an](https://arxiv.org/archive/physics)] (cited on page 78).
- [233] G. D’Agostini. “Improved iterative Bayesian unfolding”. In: *Alliance Workshop on Unfolding and Data Correction Hamburg, Germany, May 27-28, 2010*. 2010. arXiv: [1010.0632](https://arxiv.org/abs/1010.0632) [[physics.data-an](https://arxiv.org/archive/physics)] (cited on page 79).
- [234] G. Choudalakis. *Fully Bayesian Unfolding*. 2012. arXiv: [1201.4612](https://arxiv.org/abs/1201.4612) [[physics.data-an](https://arxiv.org/archive/physics)] (cited on page 80).
- [235] A. P. Dempster, N. M. Laird, and D. B. Rubin. “Maximum Likelihood from Incomplete Data via the EM Algorithm”. In: *Journal of the Royal Statistical Society. Series B (Methodological)* 39.1 (1977), pages 1–38. ISSN: 00359246. URL: <http://www.jstor.org/stable/2984875> (cited on page 80).
- [236] T. Adye. “Unfolding algorithms and tests using RooUnfold”. In: *Proceedings, PHYSTAT 2011 Workshop on Statistical Issues Related to Discovery Claims in Search Experiments and Unfolding, CERN, Geneva, Switzerland 17-20 January 2011*. CERN. Geneva: CERN, 2011, pages 313–318. DOI: [10.5170/CERN-2011-006.313](https://doi.org/10.5170/CERN-2011-006.313). arXiv: [1105.1160](https://arxiv.org/abs/1105.1160) [[physics.data-an](https://arxiv.org/archive/physics)] (cited on page 81).
- [237] R. D. Ball et al. “Parton distributions with LHC data”. In: *Nuclear Physics B* 867.2 (Feb. 2013), pages 244–289. DOI: [10.1016/j.nuclphysb.2012.10.003](https://doi.org/10.1016/j.nuclphysb.2012.10.003). URL: <https://doi.org/10.1016/j.nuclphysb.2012.10.003> (cited on pages 86, 152).
- [238] ATLAS Collaboration. *ATLAS Pythia 8 tunes to 7 TeV datas*. Technical report ATL-PHYS-PUB-2014-021. Geneva: CERN, Nov. 2014. URL: <http://cds.cern.ch/record/1966419> (cited on pages 86, 152).
- [239] D. de Florian et al. “Handbook of LHC Higgs Cross Sections: 4. Deciphering the Nature of the Higgs Sector”. In: (2016). DOI: [10.2172/1345634](https://doi.org/10.2172/1345634), [10.23731/CYRM-2017-002](https://doi.org/10.23731/CYRM-2017-002). arXiv: [1610.07922](https://arxiv.org/abs/1610.07922) [[hep-ph](https://arxiv.org/archive/hep)] (cited on pages 86, 96).
- [240] ATLAS Collaboration. “Electron efficiency measurements with the ATLAS detector using 2012 LHC proton–proton collision data”. In: *Eur. Phys. J. C* 77.3 (2017), page 195. DOI: [10.1140/epjc/s10052-017-4756-2](https://doi.org/10.1140/epjc/s10052-017-4756-2). arXiv: [1612.01456](https://arxiv.org/abs/1612.01456) [[hep-ex](https://arxiv.org/archive/hep)] (cited on pages 86, 94, 152).
- [241] ATLAS Collaboration. “Performance of algorithms that reconstruct missing transverse momentum in $\sqrt{s} = 8$ TeV proton-proton collisions in the ATLAS detector”. In: *Eur. Phys. J. C* 77.4 (2017), page 241. DOI: [10.1140/epjc/s10052-017-4780-2](https://doi.org/10.1140/epjc/s10052-017-4780-2). arXiv: [1609.09324](https://arxiv.org/abs/1609.09324) [[hep-ex](https://arxiv.org/archive/hep)] (cited on pages 86, 153, 176).
- [242] H.-L. Lai et al. “New parton distributions for collider physics”. In: *Phys. Rev. D* 82 (2010), page 074024. DOI: [10.1103/PhysRevD.82.074024](https://doi.org/10.1103/PhysRevD.82.074024). arXiv: [1007.2241](https://arxiv.org/abs/1007.2241) [[hep-ph](https://arxiv.org/archive/hep)] (cited on page 89).
- [243] ATLAS Collaboration. “Measurement of the top quark-pair production cross section with ATLAS in pp collisions at $\sqrt{s} = 7$ TeV”. In: *Eur. Phys. J. C* 71 (2011), page 1577. DOI: [10.1140/epjc/s10052-011-1577-6](https://doi.org/10.1140/epjc/s10052-011-1577-6). arXiv: [1012.1792](https://arxiv.org/abs/1012.1792) [[hep-ex](https://arxiv.org/archive/hep)] (cited on page 92).
- [244] ATLAS Collaboration. “Luminosity determination in pp collisions at $\sqrt{s} = 8$ TeV using the ATLAS detector at the LHC”. In: *Eur. Phys. J. C* 76.12 (2016), page 653. DOI: [10.1140/epjc/s10052-016-4466-1](https://doi.org/10.1140/epjc/s10052-016-4466-1). arXiv: [1608.03953](https://arxiv.org/abs/1608.03953) [[hep-ex](https://arxiv.org/archive/hep)] (cited on pages 94, 175).

- [245] G. Avoni et al. “The new LUCID-2 detector for luminosity measurement and monitoring in ATLAS”. In: *Journal of Instrumentation* 13.07 (July 2018), P07017–P07017. DOI: [10.1088/1748-0221/13/07/p07017](https://doi.org/10.1088/1748-0221/13/07/p07017). URL: <https://doi.org/10.1088/1748-0221/13/07/p07017> (cited on pages 94, 175).
- [246] ATLAS Collaboration. *Electron identification measurements in ATLAS using $\sqrt{s} = 13$ TeV data with 50 ns bunch spacing*. Technical report ATL-PHYS-PUB-2015-041. Geneva: CERN, Sept. 2015. URL: <https://cds.cern.ch/record/2048202> (cited on pages 94, 152).
- [247] ATLAS Collaboration. “Electron reconstruction and identification efficiency measurements with the ATLAS detector using the 2011 LHC proton-proton collision data”. In: *Eur. Phys. J. C* 74.7 (2014), page 2941. DOI: [10.1140/epjc/s10052-014-2941-0](https://doi.org/10.1140/epjc/s10052-014-2941-0). arXiv: [1404.2240](https://arxiv.org/abs/1404.2240) [hep-ex] (cited on page 94).
- [248] ATLAS Collaboration. *Measurement of b-tagging Efficiency of c-jets in $t\bar{t}$ Events Using a Likelihood Approach with the ATLAS Detector*. Technical report ATLAS-CONF-2018-001. Geneva: CERN, Mar. 2018. URL: <https://cds.cern.ch/record/2306649> (cited on page 95).
- [249] ATLAS Collaboration. *Calibration of light-flavour jet b-tagging rates on ATLAS proton-proton collision data at $\sqrt{s} = 13$ TeV*. Technical report ATLAS-CONF-2018-006. Geneva: CERN, Apr. 2018. URL: <https://cds.cern.ch/record/2314418> (cited on page 95).
- [250] ATLAS Collaboration. “Measurements of b-jet tagging efficiency with the ATLAS detector using $t\bar{t}$ events at $\sqrt{s} = 13$ TeV”. In: *JHEP* 08 (2018), page 089. DOI: [10.1007/JHEP08\(2018\)089](https://doi.org/10.1007/JHEP08(2018)089). arXiv: [1805.01845](https://arxiv.org/abs/1805.01845) [hep-ex] (cited on page 95).
- [251] F. Demartin et al. “tWH associated production at the LHC”. In: *Eur. Phys. J. C* 77.1 (2017), page 34. DOI: [10.1140/epjc/s10052-017-4601-7](https://doi.org/10.1140/epjc/s10052-017-4601-7). arXiv: [1607.05862](https://arxiv.org/abs/1607.05862) [hep-ph] (cited on page 96).
- [252] ATLAS Collaboration. “Measurement of the production cross-section of a single top quark in association with a Z boson in proton–proton collisions at 13 TeV with the ATLAS detector”. In: *Phys. Lett. B* 780 (2018), pages 557–577. DOI: [10.1016/j.physletb.2018.03.023](https://doi.org/10.1016/j.physletb.2018.03.023). arXiv: [1710.03659](https://arxiv.org/abs/1710.03659) [hep-ex] (cited on pages 96, 113).
- [253] CMS Collaboration. “Measurement of the associated production of a single top quark and a Z boson in pp collisions at $\sqrt{s} = 13$ TeV”. In: *Phys. Lett. B* 779 (2018), pages 358–384. DOI: [10.1016/j.physletb.2018.02.025](https://doi.org/10.1016/j.physletb.2018.02.025). arXiv: [1712.02825](https://arxiv.org/abs/1712.02825) [hep-ex] (cited on pages 96, 113).
- [254] ATLAS Collaboration. *Modelling of the $t\bar{t}H$ and $t\bar{t}V$ ($V = W, Z$) processes for $\sqrt{s} = 13$ TeV ATLAS analyses*. Technical report ATL-PHYS-PUB-2016-005. Geneva: CERN, Jan. 2016. URL: <https://cds.cern.ch/record/2120826> (cited on page 96).
- [255] S. Frixione et al. “Electroweak and QCD corrections to top-pair hadroproduction in association with heavy bosons”. In: *JHEP* 06 (2015), page 184. DOI: [10.1007/JHEP06\(2015\)184](https://doi.org/10.1007/JHEP06(2015)184). arXiv: [1504.03446](https://arxiv.org/abs/1504.03446) [hep-ph] (cited on pages 100, 103, 105).
- [256] J. A. Aguilar-Saavedra. “A Minimal set of top anomalous couplings”. In: *Nucl. Phys. B* 812 (2009), pages 181–204. DOI: [10.1016/j.nuclphysb.2008.12.012](https://doi.org/10.1016/j.nuclphysb.2008.12.012). arXiv: [0811.3842](https://arxiv.org/abs/0811.3842) [hep-ph] (cited on page 105).
- [257] B. Grzadkowski et al. “Dimension-Six Terms in the Standard Model Lagrangian”. In: *JHEP* 10 (2010), page 085. DOI: [10.1007/JHEP10\(2010\)085](https://doi.org/10.1007/JHEP10(2010)085). arXiv: [1008.4884](https://arxiv.org/abs/1008.4884) [hep-ph] (cited on page 105).

- [258] D. Barducci et al. “Interpreting top-quark LHC measurements in the standard-model effective field theory”. In: (2018). Edited by J. A. Aguilar-Saavedra et al. arXiv: [1802.07237 \[hep-ph\]](#) (cited on page [105](#)).
- [259] C. Zhang, N. Greiner, and S. Willenbrock. “Constraints on Non-standard Top Quark Couplings”. In: *Phys. Rev. D* 86 (2012), page 014024. DOI: [10.1103/PhysRevD.86.014024](#). arXiv: [1201.6670 \[hep-ph\]](#) (cited on page [106](#)).
- [260] CMS Collaboration. “Measurement of the t-channel single-top-quark production cross section and of the $|V_{tb}|$ CKM matrix element in pp collisions at $\sqrt{s} = 8$ TeV”. In: *JHEP* 06 (2014), page 090. DOI: [10.1007/JHEP06\(2014\)090](#). arXiv: [1403.7366 \[hep-ex\]](#) (cited on page [106](#)).
- [261] ATLAS Collaboration. “Measurement of the W boson polarisation in $t\bar{t}$ events from pp collisions at $\sqrt{s} = 8$ TeV in the lepton + jets channel with ATLAS”. In: *Eur. Phys. J. C* 77.4 (2017). [Erratum: *Eur. Phys. J. C* 79, no. 1, 19 (2019)], page 264. DOI: [10.1140/epjc/s10052-018-6520-7](#), [10.1140/epjc/s10052-017-4819-4](#). arXiv: [1612.02577 \[hep-ex\]](#) (cited on page [106](#)).
- [262] A. Buckley et al. “Constraining top quark effective theory in the LHC Run II era”. In: *JHEP* 04 (2016), page 015. DOI: [10.1007/JHEP04\(2016\)015](#). arXiv: [1512.03360 \[hep-ph\]](#) (cited on page [106](#)).
- [263] ATLAS Collaboration. “ATLAS b -jet identification performance and efficiency measurement with $t\bar{t}$ events in pp collisions at $\sqrt{s} = 13$ TeV”. In: *Eur. Phys. J. C* 79 (July 2019), 970. 36 p. DOI: [10.1140/epjc/s10052-019-7450-8](#). URL: <https://cds.cern.ch/record/2682119> (cited on page [108](#)).
- [264] J. Butterworth et al. “PDF4LHC recommendations for LHC Run II”. In: *J. Phys. G* 43 (2016), page 023001. DOI: [10.1088/0954-3899/43/2/023001](#). arXiv: [1510.03865 \[hep-ph\]](#) (cited on page [113](#)).
- [265] S. Dulat et al. “New parton distribution functions from a global analysis of quantum chromodynamics”. In: *Phys. Rev. D* 93.3 (2016), page 033006. DOI: [10.1103/PhysRevD.93.033006](#). arXiv: [1506.07443 \[hep-ph\]](#) (cited on page [113](#)).
- [266] L. A. Harland-Lang et al. “Parton distributions in the LHC era: MMHT 2014 PDFs”. In: *Eur. Phys. J. C* 75.5 (2015), page 204. DOI: [10.1140/epjc/s10052-015-3397-6](#). arXiv: [1412.3989 \[hep-ph\]](#) (cited on page [113](#)).
- [267] ATLAS Collaboration. *Observation of the associated production of a top quark and a Z boson in pp collisions at $\sqrt{s} = 13$ TeV with the ATLAS detector*. 2020. arXiv: [2002.07546 \[hep-ex\]](#) (cited on page [113](#)).
- [268] G. Choudalakis. “Unfolding in ATLAS”. In: *Proceedings, PHYSTAT 2011 Workshop on Statistical Issues Related to Discovery Claims in Search Experiments and Unfolding, CERN, Geneva, Switzerland 17-20 January 2011*. CERN. Geneva: CERN, 2011, pages 297–308. DOI: [10.5170/CERN-2011-006.297](#). arXiv: [1104.2962 \[hep-ex\]](#) (cited on page [135](#)).
- [269] A. Hocker and V. Kartvelishvili. “SVD approach to data unfolding”. In: *Nucl. Instrum. Meth. A* 372 (1996), pages 469–481. DOI: [10.1016/0168-9002\(95\)01478-0](#). arXiv: [hep-ph/9509307 \[hep-ph\]](#) (cited on page [135](#)).

- [270] D. J. Lange. “The EvtGen particle decay simulation package”. In: *Nuclear Instruments and Methods in Physics Research Section A: Accelerators, Spectrometers, Detectors and Associated Equipment* 462.1-2 (Apr. 2001), pages 152–155. DOI: [10.1016/S0168-9002\(01\)00089-4](https://doi.org/10.1016/S0168-9002(01)00089-4). URL: [https://doi.org/10.1016/S0168-9002\(01\)00089-4](https://doi.org/10.1016/S0168-9002(01)00089-4) (cited on page 152).
- [271] C. G. Lester and D. J. Summers. “Measuring masses of semiinvisibly decaying particles pair produced at hadron colliders”. In: *Phys. Lett.* B463 (1999), pages 99–103. DOI: [10.1016/S0370-2693\(99\)00945-4](https://doi.org/10.1016/S0370-2693(99)00945-4). arXiv: [hep-ph/9906349](https://arxiv.org/abs/hep-ph/9906349) [[hep-ph](#)] (cited on page 154).
- [272] A. Barr, C. Lester, and P. Stephens. “m(T2): The Truth behind the glamour”. In: *J. Phys.* G29 (2003), pages 2343–2363. DOI: [10.1088/0954-3899/29/10/304](https://doi.org/10.1088/0954-3899/29/10/304). arXiv: [hep-ph/0304226](https://arxiv.org/abs/hep-ph/0304226) [[hep-ph](#)] (cited on page 154).
- [273] P. Jackson, C. Rogan, and M. Santoni. “Sparticles in motion: Analyzing compressed SUSY scenarios with a new method of event reconstruction”. In: *Phys. Rev.* D95.3 (2017), page 035031. DOI: [10.1103/PhysRevD.95.035031](https://doi.org/10.1103/PhysRevD.95.035031). arXiv: [1607.08307](https://arxiv.org/abs/1607.08307) [[hep-ph](#)] (cited on page 156).
- [274] P. Jackson and C. Rogan. *Recursive Jigsaw Reconstruction: HEP event analysis in the presence of kinematic and combinatoric ambiguities*. 2017. arXiv: [1705.10733](https://arxiv.org/abs/1705.10733) [[hep-ph](#)] (cited on page 156).
- [275] G. T. Fletcher et al. *A data-driven method for measuring the mismeasured jet background for missing transverse energy searches in multijet, Z+jet and γ +jet events*. Technical report ATL-COM-PHYS-2014-1243. Geneva: CERN, Sept. 2014. URL: <https://cds.cern.ch/record/1950335> (cited on page 162).
- [276] ATLAS Collaboration. *Search for new phenomena with top quark pairs in final states with one lepton, jets, and missing transverse momentum in pp collisions at $\sqrt{s} = 13$ TeV with the ATLAS detector*. Technical report ATLAS-CONF-2020-003. Geneva: CERN, Feb. 2020. URL: <http://cds.cern.ch/record/2711489> (cited on page 165).
- [277] ATLAS Collaboration. *Search for top squarks in events with a Z boson using 139 fb^{-1} of pp collision data at $\sqrt{s} = 13$ TeV with the ATLAS detector*. Technical report ATLAS-CONF-2019-016. Geneva: CERN, May 2019. URL: <http://cds.cern.ch/record/2676592> (cited on page 165).
- [278] CMS Collaboration. *Data-Driven Estimation of the Invisible Z Background to the SUSY MET Plus Jets Search*. Technical report CMS-PAS-SUS-08-002. Geneva: CERN, Jan. 2009. URL: <https://cds.cern.ch/record/1194471> (cited on page 166).
- [279] S. Ask et al. “Using γ +jets Production to Calibrate the Standard Model $Z(\nu\bar{\nu})$ +jets Background to New Physics Processes at the LHC”. In: *JHEP* 10 (2011), page 058. DOI: [10.1007/JHEP10\(2011\)058](https://doi.org/10.1007/JHEP10(2011)058). arXiv: [1107.2803](https://arxiv.org/abs/1107.2803) [[hep-ph](#)] (cited on pages 166, 169).
- [280] Z. Bern et al. “Driving Missing Data at Next-to-Leading Order”. In: *Phys. Rev.* D84 (2011), page 114002. DOI: [10.1103/PhysRevD.84.114002](https://doi.org/10.1103/PhysRevD.84.114002). arXiv: [1106.1423](https://arxiv.org/abs/1106.1423) [[hep-ph](#)] (cited on page 166).
- [281] CMS Collaboration. “Comparison of the $Z/\gamma^* +$ jets to $\gamma +$ jets cross sections in pp collisions at $\sqrt{s} = 8$ TeV”. In: *JHEP* 10 (2015), page 128. DOI: [10.1007/JHEP04\(2016\)010](https://doi.org/10.1007/JHEP04(2016)010), [10.1007/JHEP10\(2015\)128](https://doi.org/10.1007/JHEP10(2015)128). arXiv: [1505.06520](https://arxiv.org/abs/1505.06520) [[hep-ex](#)] (cited on page 166).
- [282] B. Nachman. “Investigating the Quantum Properties of Jets and the Search for a Supersymmetric Top Quark Partner with the ATLAS Detector”. PhD thesis. Stanford U., Phys. Dept., 2016. arXiv: [1609.03242](https://arxiv.org/abs/1609.03242) [[hep-ex](#)]. URL: <https://searchworks.stanford.edu/view/11849292> (cited on pages 169–171).

- [283] ATLAS Collaboration. *Jet energy resolution and selection efficiency relative to track jets from in-situ techniques with the ATLAS Detector Using Proton-Proton Collisions at a Center of Mass Energy $\sqrt{s} = 7\text{TeV}$* . Technical report ATLAS-CONF-2010-054. Geneva: CERN, July 2010. URL: <http://cds.cern.ch/record/1281311> (cited on page 176).

Appendices

- A** Further $t\bar{t}Z$ differential results with the full Run 2 dataset
 - A.1 Results in the 3L channel
 - A.2 Results in the 4L channel



A. Further $t\bar{t}Z$ differential results

In this appendix we present the measurement of the differential $t\bar{t}Z$ cross section in the 3L and 4L channels described in Chapter 7, for the observables in Table 7.1. The variables used in the combined 3L and 4L channels were the focus of Chapter 7 and are not repeated here. All observables are unfolded using an iterative bayesian method, described in Section 4.2.4; the regularisation parameter (number of iterations) for each variable is listed in Table 7.1.

A.1 Results in the 3L channel

Reconstruction-level distributions, migration matrices, and efficiency and acceptance corrections for the 3L observables N_{jets} , $p_{\text{T}}^{\ell \text{ non-}Z}$, $|\Delta\phi(Z, t_{\text{lep}})|$ and $|\Delta y(Z, t_{\text{lep}})|$, respectively, are shown in Figures A.1, A.4, A.7 and A.10. The corresponding absolute and normalised data distributions, unfolded to particle- and parton-level, are presented in Figures A.2, A.5, A.8 and A.11. The fractional decomposition of statistical and systematic uncertainties is given in Figures A.3, A.6, A.9 and A.12.

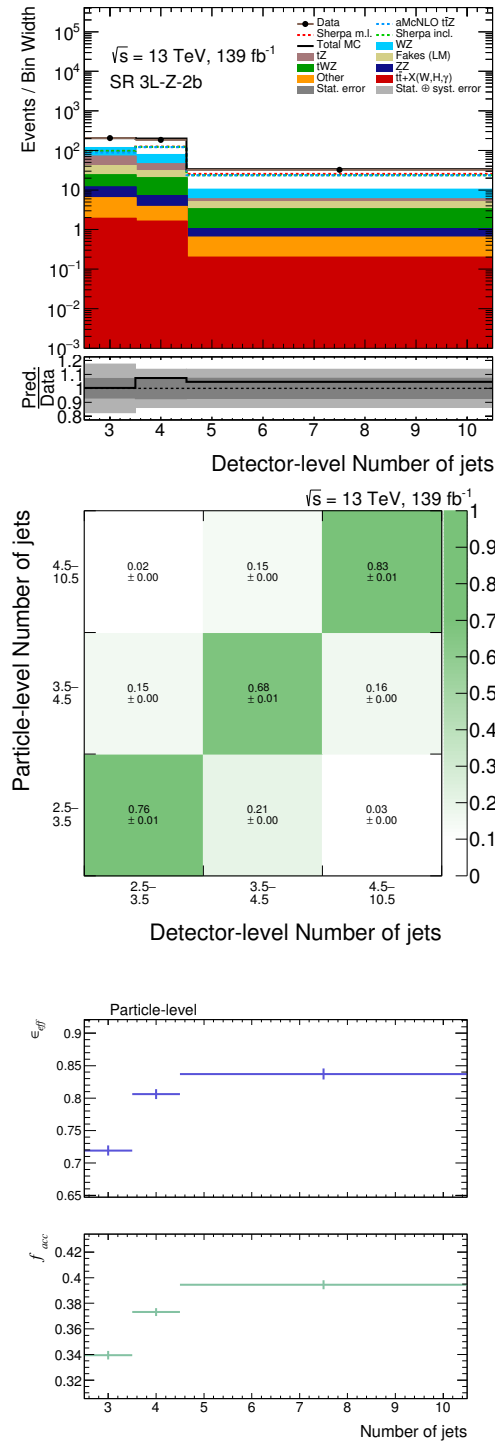


Figure A.1: Reconstruction-level distribution (top), migration matrices (middle) and efficiency and acceptance corrections (bottom) at particle-level, for the N_{jets} variable in the 3L channel. In the top figure, the solid black line corresponds to the sum of the contributions from background processes (coloured filled areas) and the nominal $t\bar{t}Z$ MADGRAPH5_aMC@NLO sample (white filled area). This $t\bar{t}Z$ contribution is further represented (unstacked) as a dashed blue line, to allow comparison with the alternative generator setups: SHERPA inclusive (dashed green line) and SHERPA multi-leg (dashed red line).

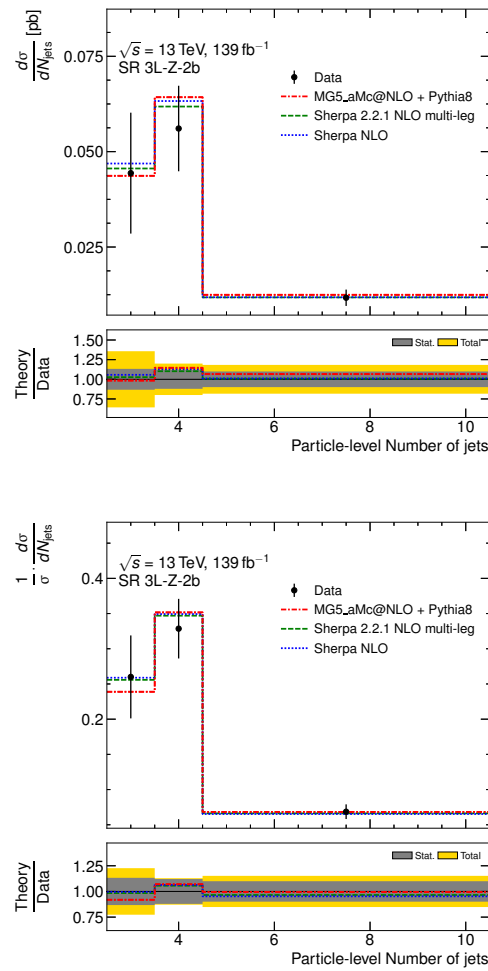


Figure A.2: Data distributions for the N_{jets} variable in the 3L channel, unfolded to particle-level, absolute (top) and normalised (bottom).

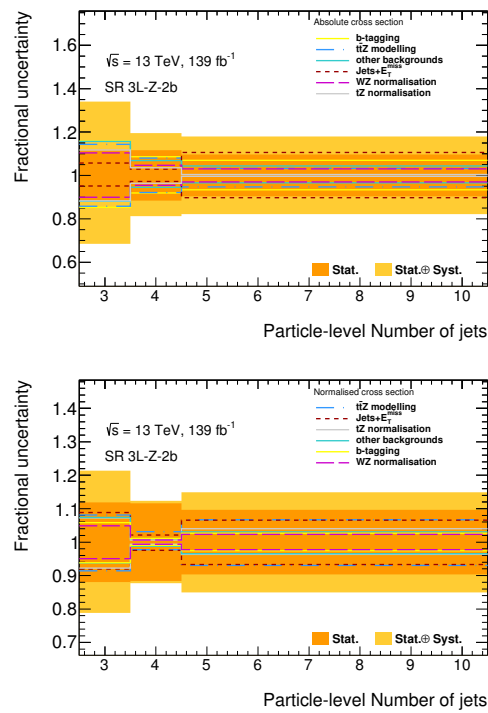


Figure A.3: Fractional decomposition of statistical and systematic uncertainties for the N_{jets} variable in the 3L channel, unfolded to particle-level, absolute (top) and normalised (bottom).

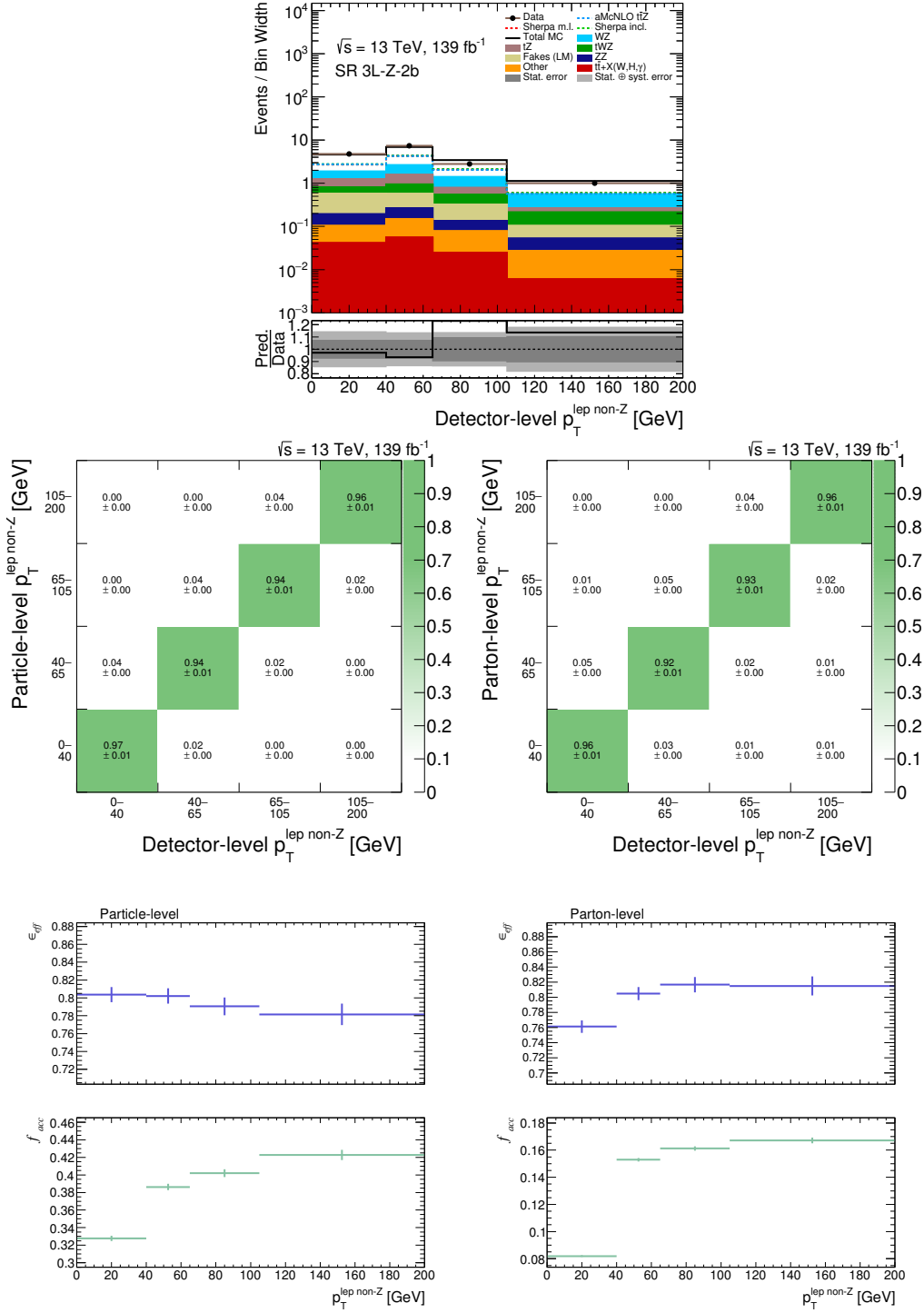


Figure A.4: Reconstruction-level distribution (top), migration matrices (middle) and efficiency and acceptance corrections (bottom) at particle- (left) and parton-level (right), for the $p_T^{\ell \text{ non-Z}}$ variable in the 3L channel. In the top figure, the solid black line corresponds to the sum of the contributions from background processes (coloured filled areas) and the nominal $t\bar{t}Z$ MADGRAPH5_aMC@NLO sample (white filled area). This $t\bar{t}Z$ contribution is further represented (unstacked) as a dashed blue line, to allow comparison with the alternative generator setups: SHERPA inclusive (dashed green line) and SHERPA multi-leg (dashed red line).

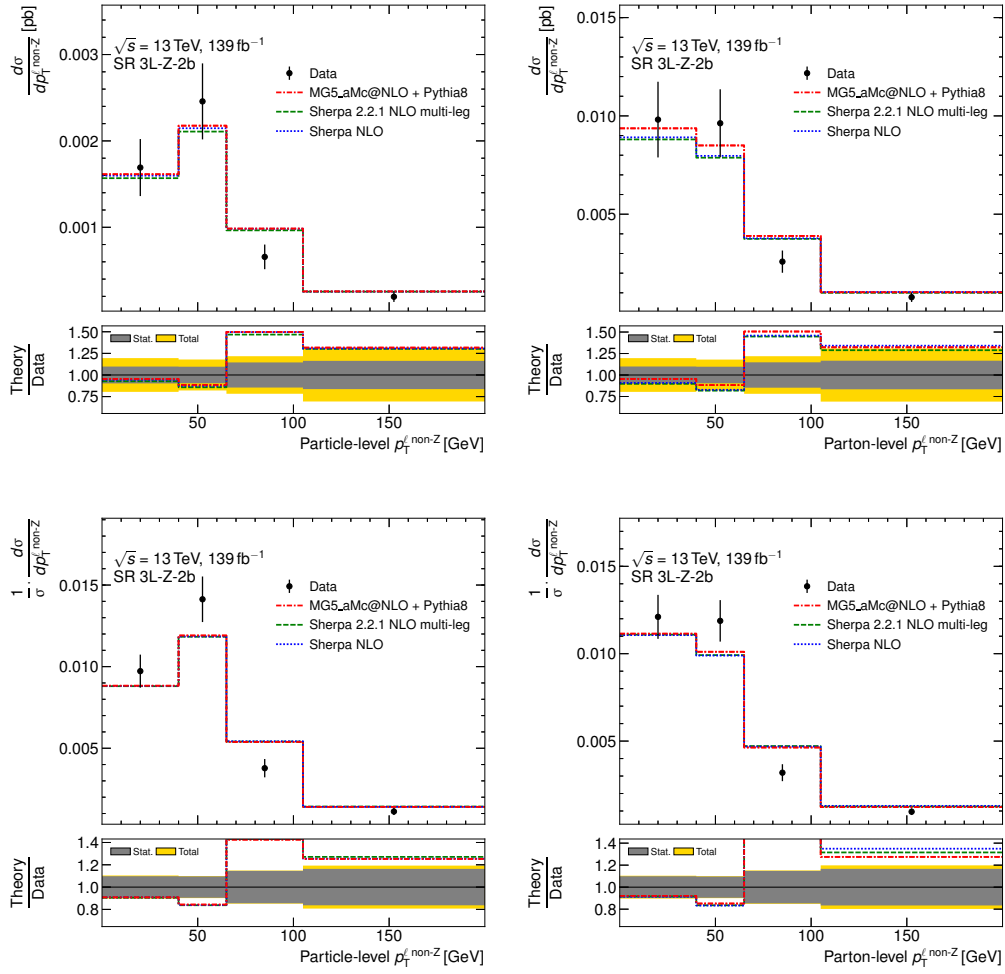


Figure A.5: Data distributions for the $p_T^{\text{non-Z}}$ variable in the 3L channel, unfolded to particle- (left) and parton-level (right), absolute (top) and normalised (bottom).

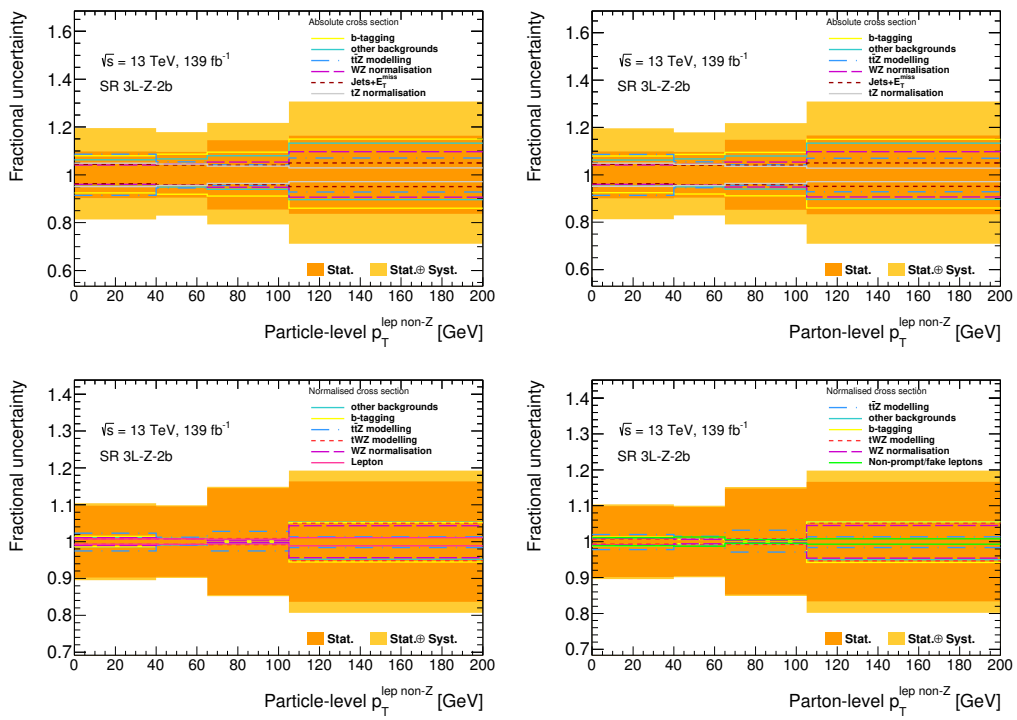


Figure A.6: Fractional decomposition of statistical and systematic uncertainties for the $p_T^{\text{lep non-Z}}$ variable in the 3L channel, unfolded to particle- (left) and parton-level (right), absolute (top) and normalised (bottom).

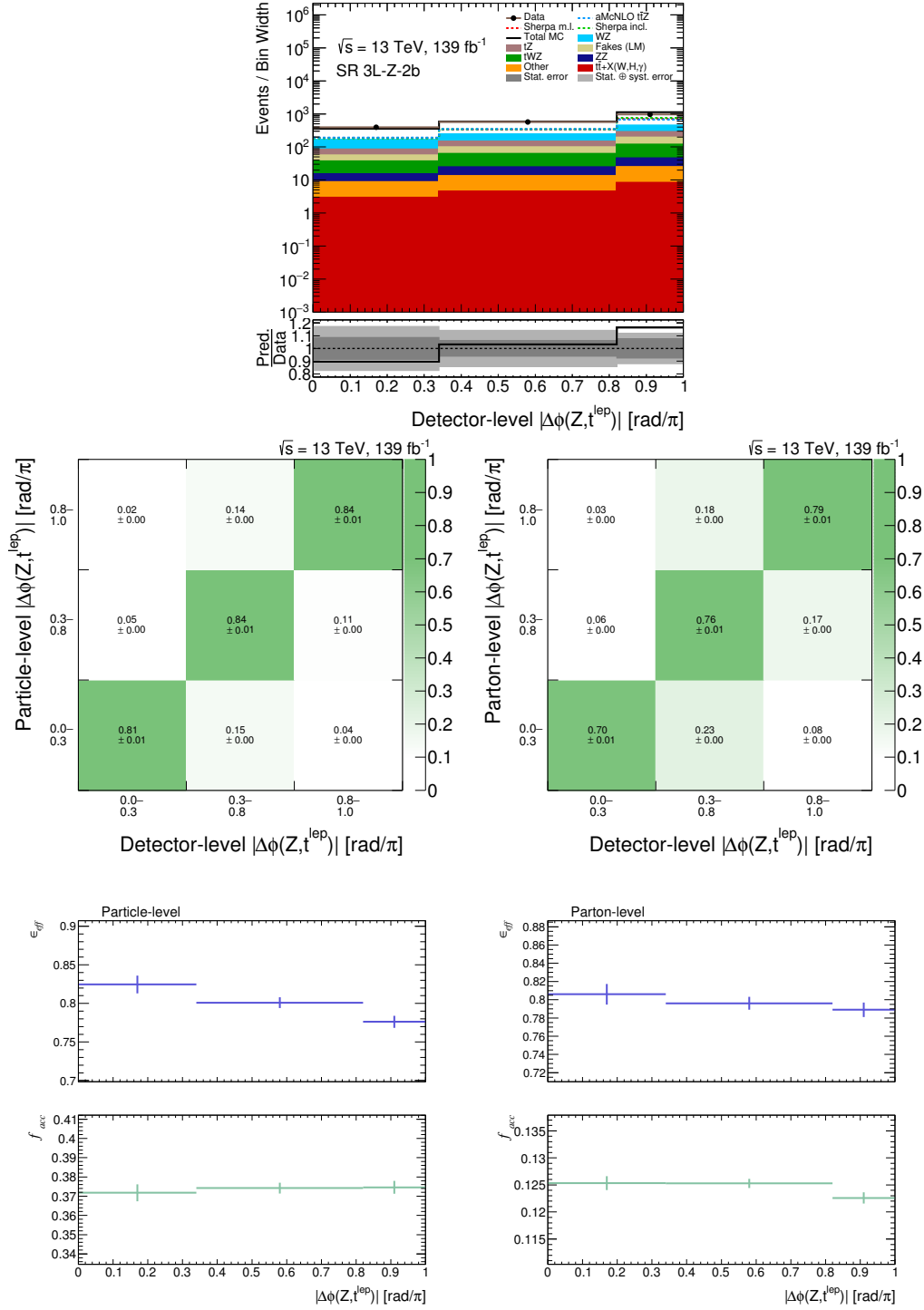


Figure A.7: Reconstruction-level distribution (top), migration matrices (middle) and efficiency and acceptance corrections (bottom) at particle- (left) and parton-level (right), for the $|\Delta\phi(Z, t^{\text{lep}})|$ variable in the 3L channel. In the top figure, the solid black line corresponds to the sum of the contributions from background processes (coloured filled areas) and the nominal $t\bar{t}Z$ MADGRAPH5_aMC@NLO sample (white filled area). This $t\bar{t}Z$ contribution is further represented (unstacked) as a dashed blue line, to allow comparison with the alternative generator setups: SHERPA inclusive (dashed green line) and SHERPA multi-leg (dashed red line).

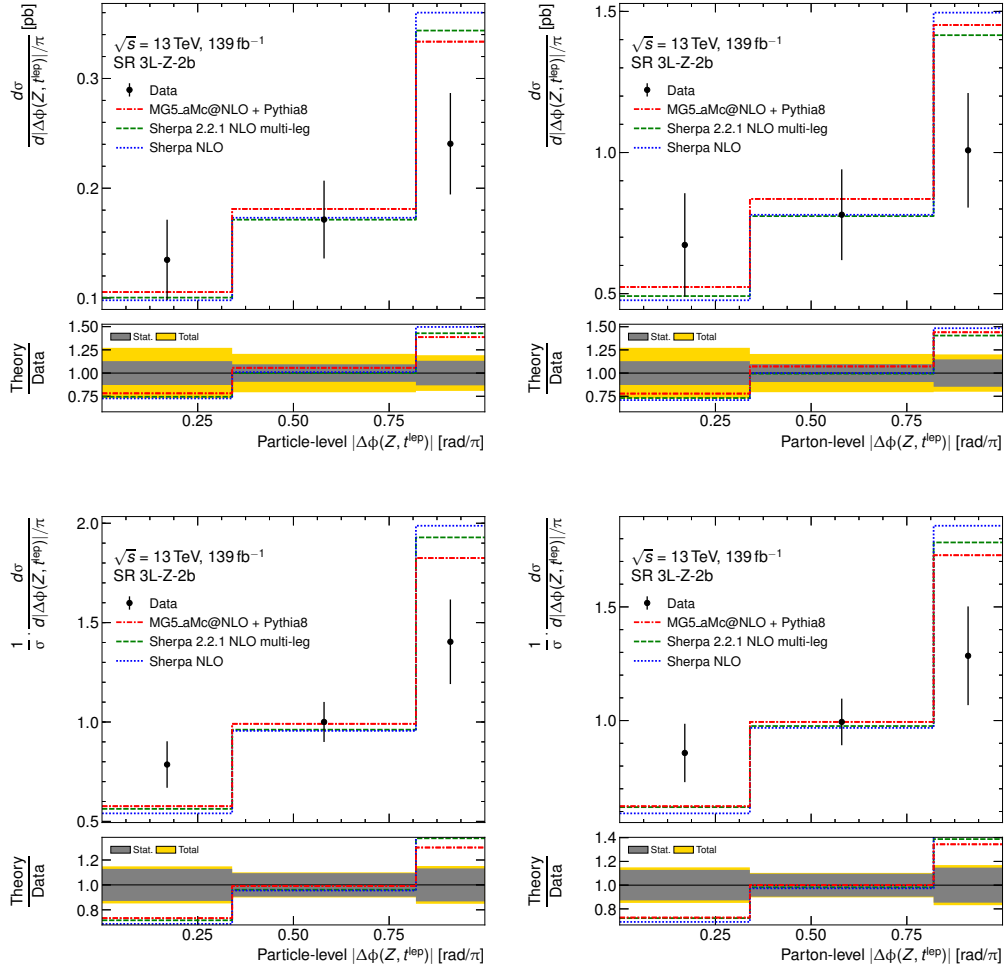


Figure A.8: Data distributions for the $|\Delta\phi(Z, t_{lep})|$ variable in the 3L channel, unfolded to particle-level (left) and parton-level (right), absolute (top) and normalised (bottom).

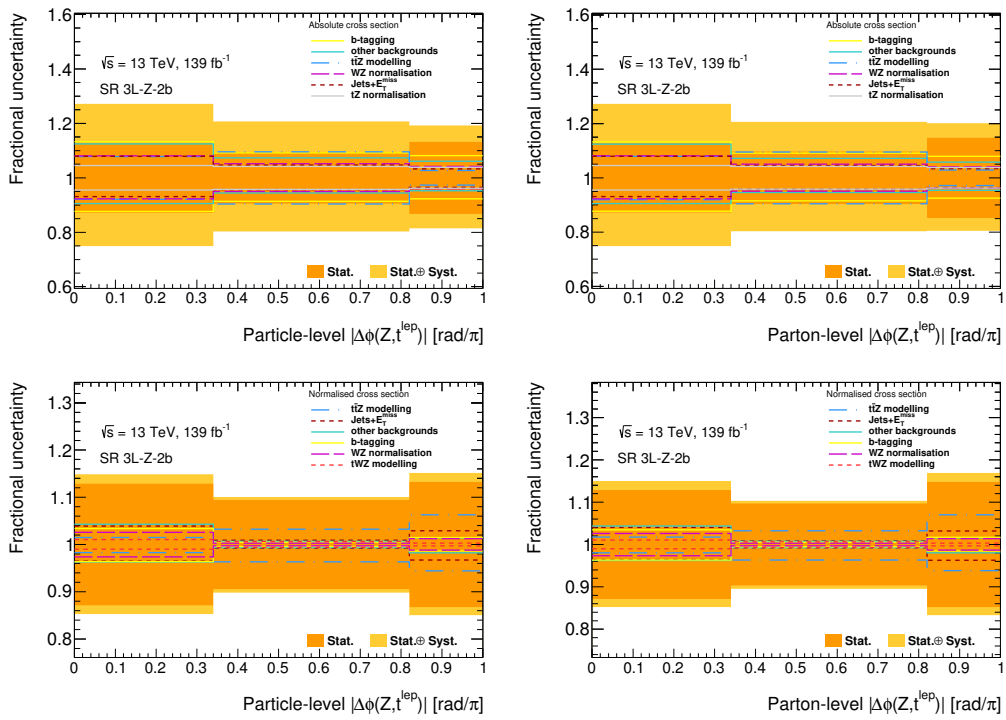


Figure A.9: Fractional decomposition of statistical and systematic uncertainties for the $|\Delta\phi(Z, t_{lep})|$ variable in the 3L channel, unfolded to particle- (left) and parton-level (right), absolute (top) and normalised (bottom).

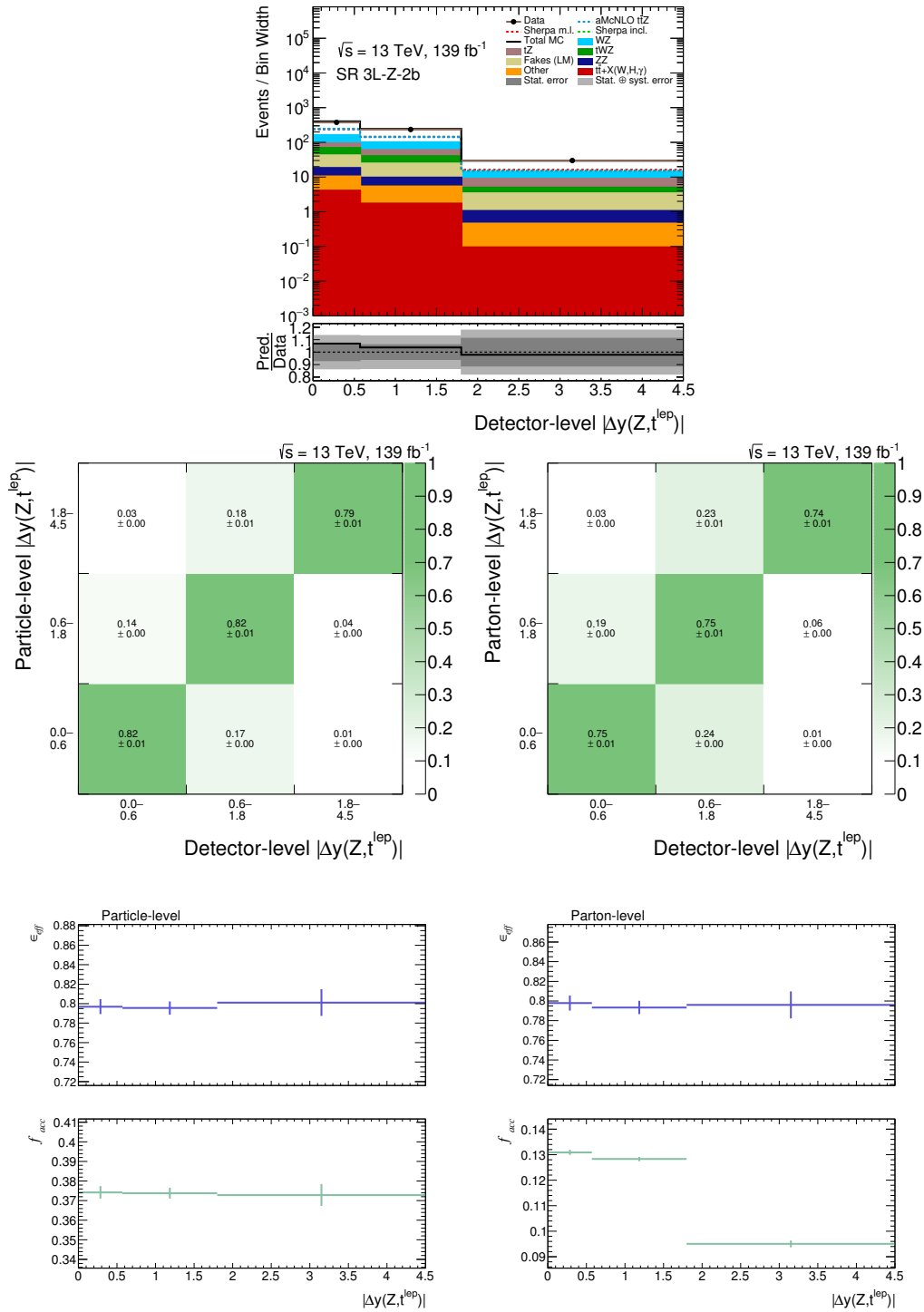


Figure A.10: Reconstruction-level distribution (top), migration matrices (middle) and efficiency and acceptance corrections (bottom) at particle- (left) and parton-level (right), for the $|\Delta y(Z, t^{\text{lep}})|$ variable in the 3L channel. In the top figure, the solid black line corresponds to the sum of the contributions from background processes (coloured filled areas) and the nominal $t\bar{t}Z$ MADGRAPH5_aMC@NLO sample (white filled area). This $t\bar{t}Z$ contribution is further represented (unstacked) as a dashed blue line, to allow comparison with the alternative generator setups: SHERPA inclusive (dashed green line) and SHERPA multi-leg (dashed red line).

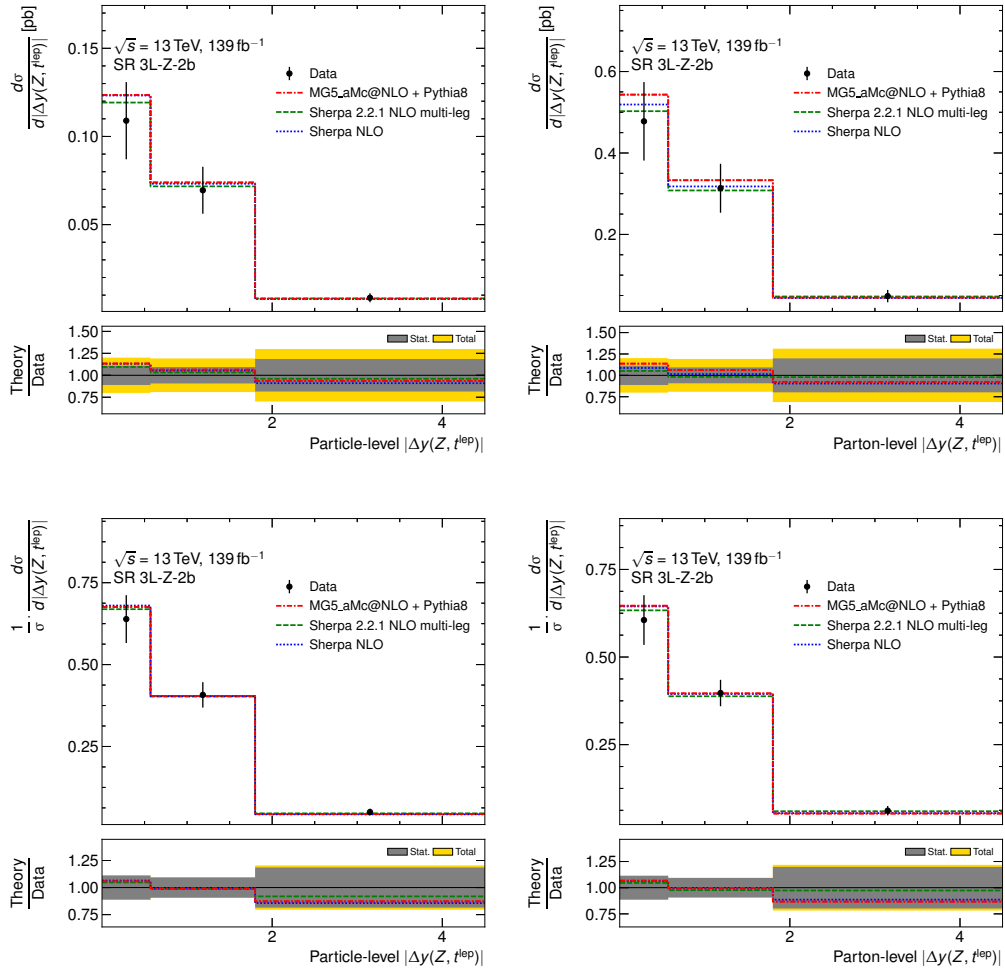


Figure A.11: Data distributions for the $|\Delta y(Z, t_{lep})|$ variable in the 3L channel, unfolded to particle-level (left) and parton-level (right), absolute (top) and normalised (bottom).

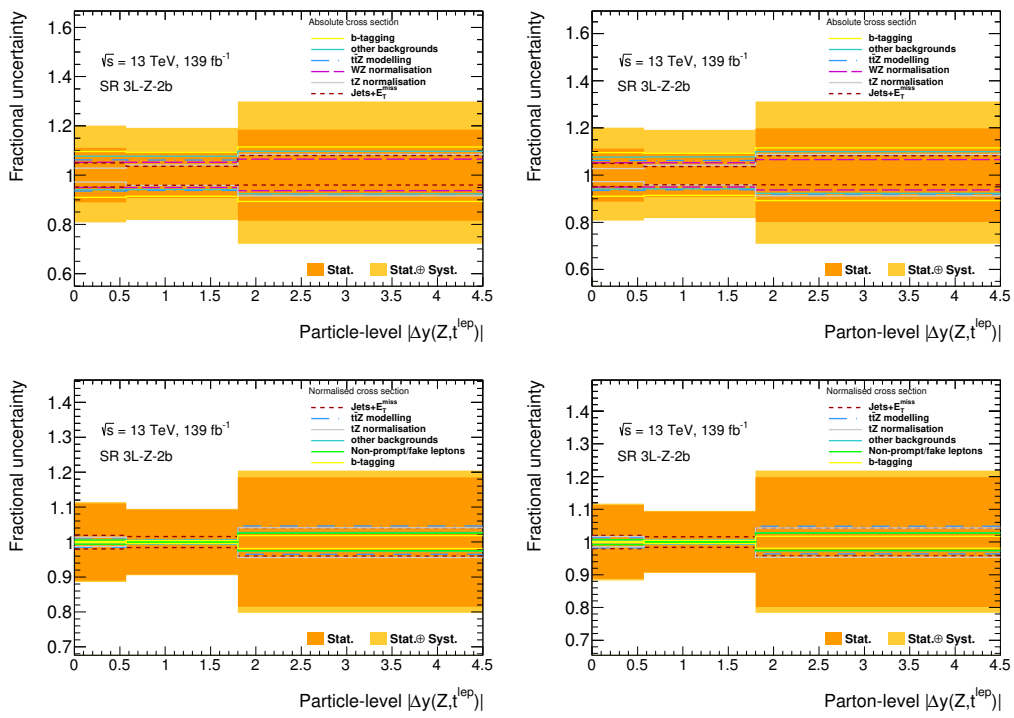


Figure A.12: Fractional decomposition of statistical and systematic uncertainties for the $|\Delta y(Z, t_{lep})|$ variable in the 3L channel, unfolded to particle- (left) and parton-level (right), absolute (top) and normalised (bottom).

A.2 Results in the 4L channel

Reconstruction-level distributions, migration matrices, and efficiency and acceptance corrections for the 4L observables N_{jets} , $|\Delta\phi(\ell_t^+, \ell_{\bar{t}}^-)|$, $p_{\text{T}}^{t\bar{t}}$ and $|\Delta\phi(t\bar{t}, Z)|$, respectively, are shown in Figures A.13, A.16, A.19 and A.22. The corresponding absolute and normalised data distributions, unfolded to particle- and parton-level, are presented in Figures A.14, A.17, A.20 and A.23. The fractional decomposition of statistical and systematic uncertainties is given in Figures A.15, A.18, A.21 and A.24.

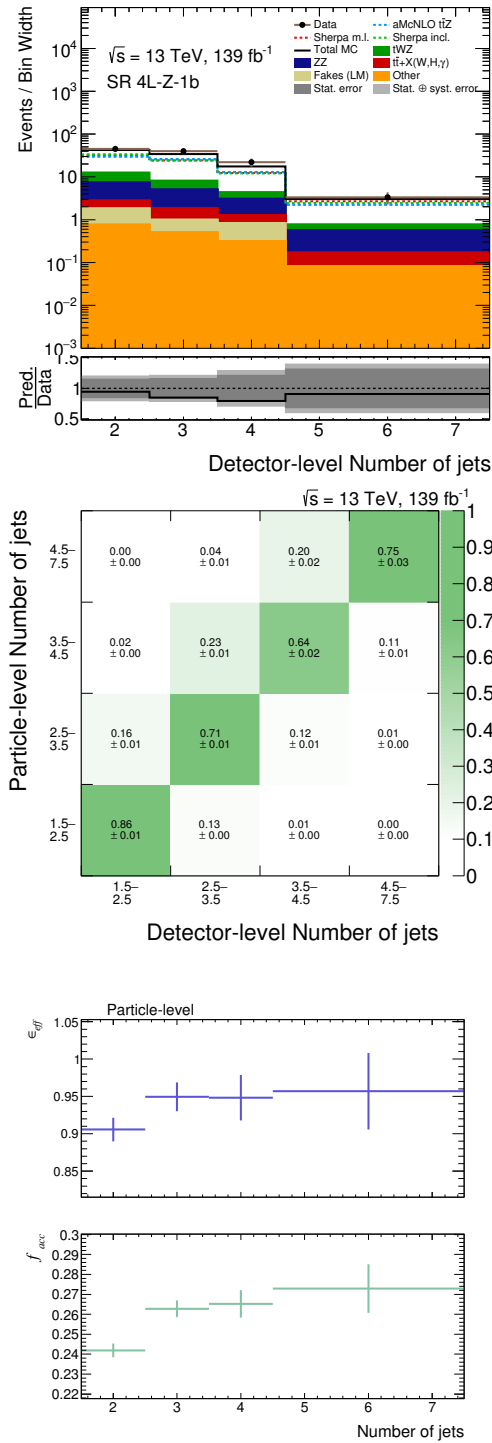


Figure A.13: Reconstruction-level distribution (top), migration matrices (middle) and efficiency and acceptance corrections (bottom) at particle-level, for the N_{jets} variable in the 4L channel. In the top figure, the solid black line corresponds to the sum of the contributions from background processes (coloured filled areas) and the nominal $t\bar{t}Z$ MADGRAPH5_aMC@NLO sample (white filled area). This $t\bar{t}Z$ contribution is further represented (unstacked) as a dashed blue line, to allow comparison with the alternative generator setups: SHERPA inclusive (dashed green line) and SHERPA multi-leg (dashed red line).

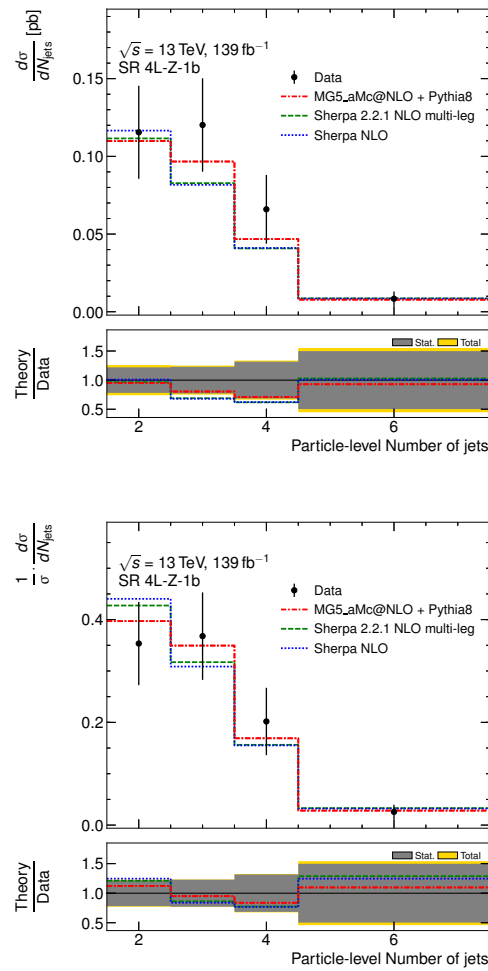


Figure A.14: Data distributions for the N_{jets} variable in the 4L channel, unfolded to particle-level, absolute (top) and normalised (bottom).

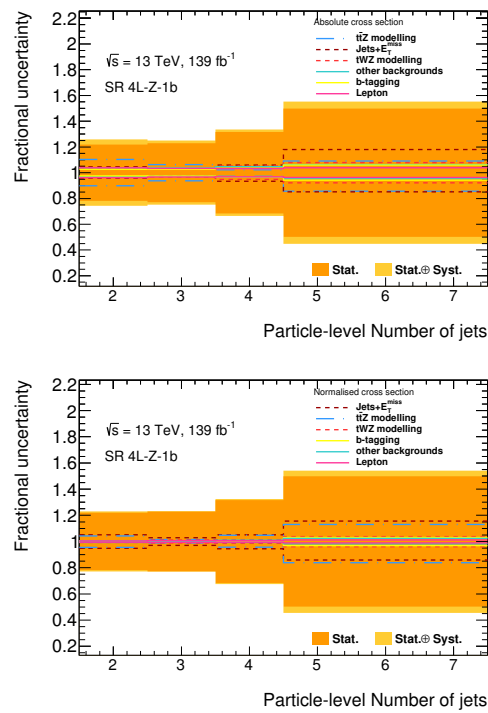


Figure A.15: Fractional decomposition of statistical and systematic uncertainties for the N_{jets} variable in the 4L channel, unfolded to particle-level, absolute (top) and normalised (bottom).

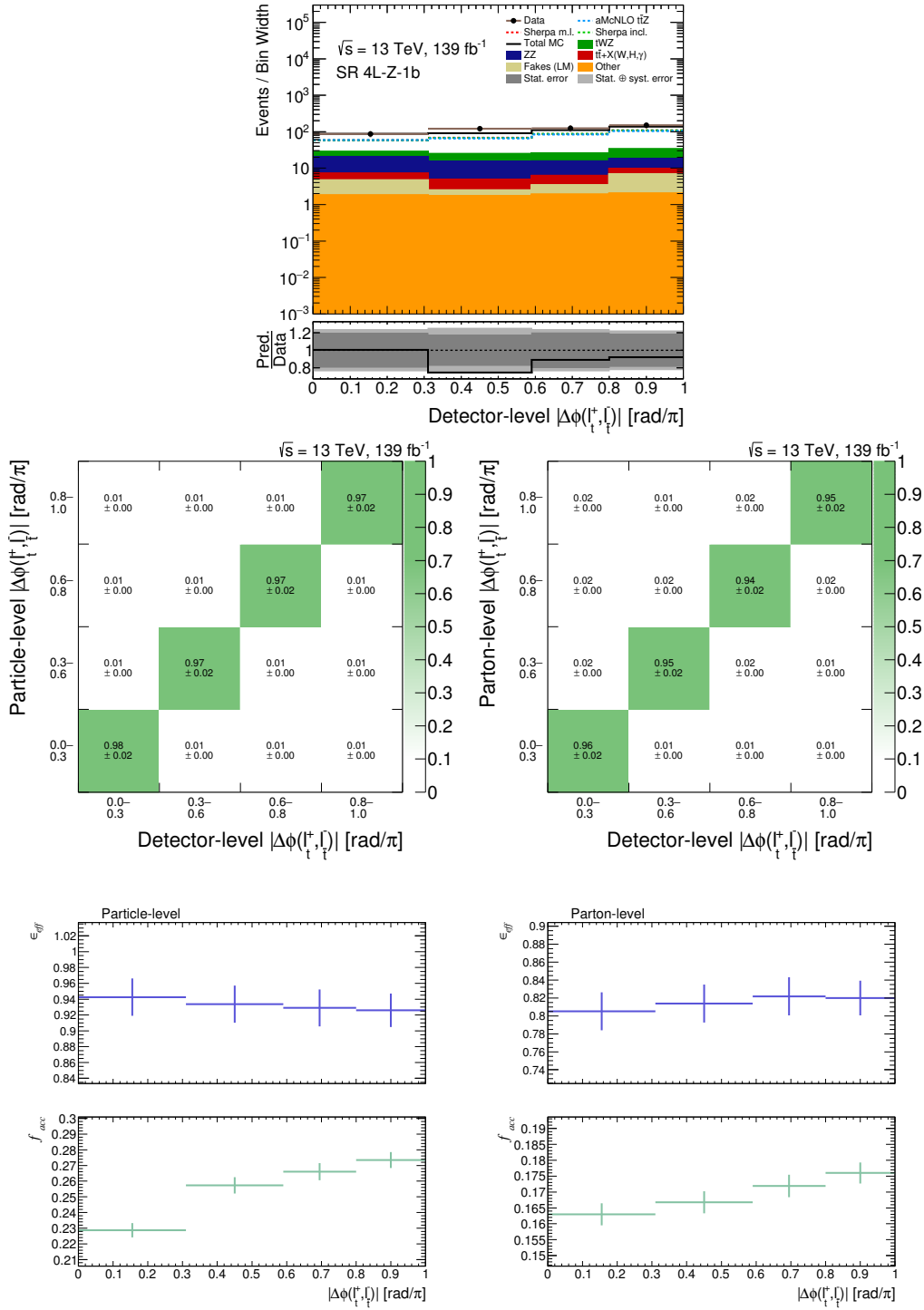


Figure A.16: Reconstruction-level distribution (top), migration matrices (middle) and efficiency and acceptance corrections (bottom) at particle- (left) and parton-level (right), for the $|\Delta\phi(\ell_t^+, \ell_t^-)|$ variable in the 4L channel. In the top figure, the solid black line corresponds to the sum of the contributions from background processes (coloured filled areas) and the nominal $t\bar{t}Z$ MADGRAPH5_aMC@NLO sample (white filled area). This $t\bar{t}Z$ contribution is further represented (unstacked) as a dashed blue line, to allow comparison with the alternative generator setups: SHERPA inclusive (dashed green line) and SHERPA multi-leg (dashed red line).

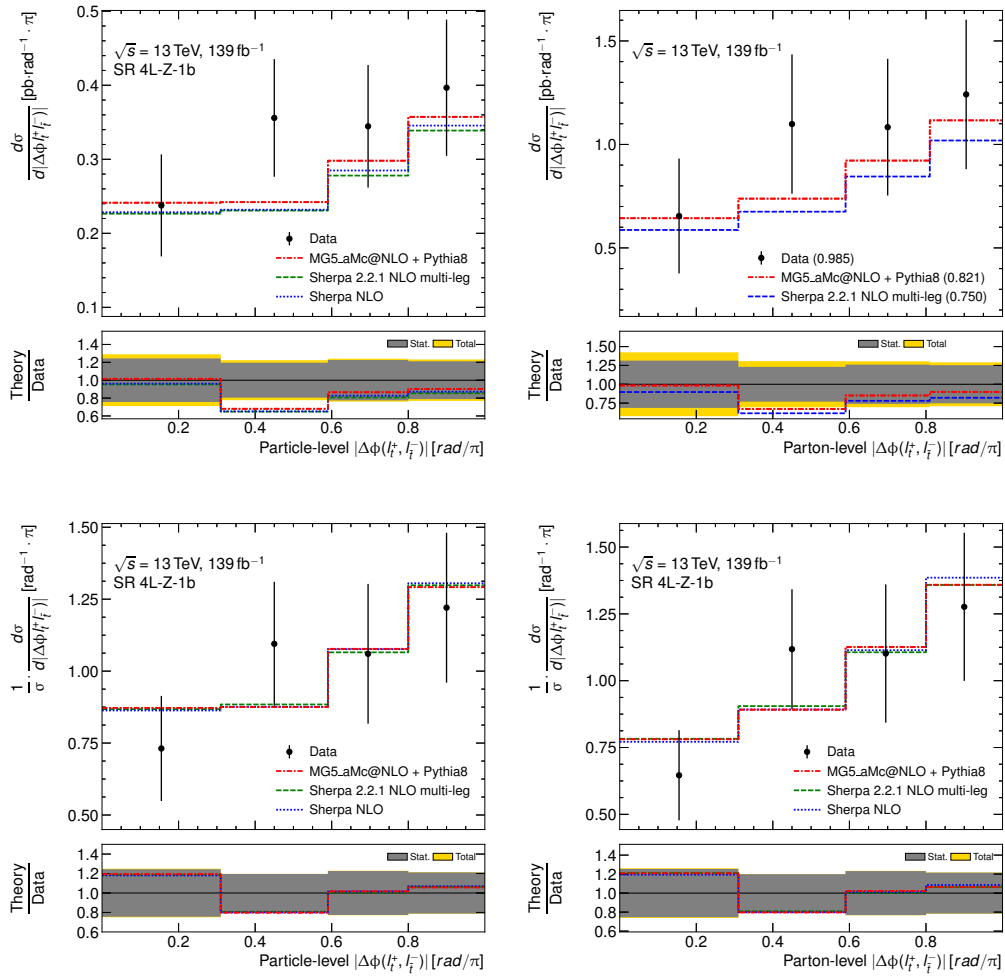


Figure A.17: Data distributions for the $|\Delta\phi(\ell_t^+, \ell_t^-)|$ variable in the 4L channel, unfolded to particle-level (left) and parton-level (right), absolute (top) and normalised (bottom).

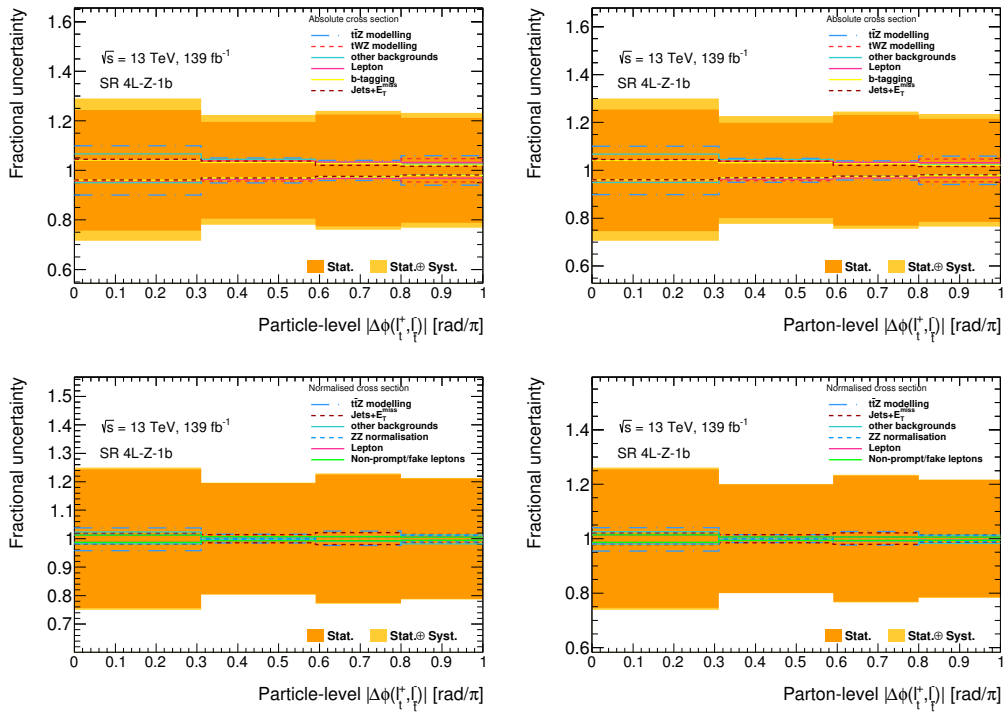


Figure A.18: Fractional decomposition of statistical and systematic uncertainties for the $|\Delta\phi(\ell_i^+, \ell_i^-)|$ variable in the 4L channel, unfolded to particle- (left) and parton-level (right), absolute (top) and normalised (bottom).

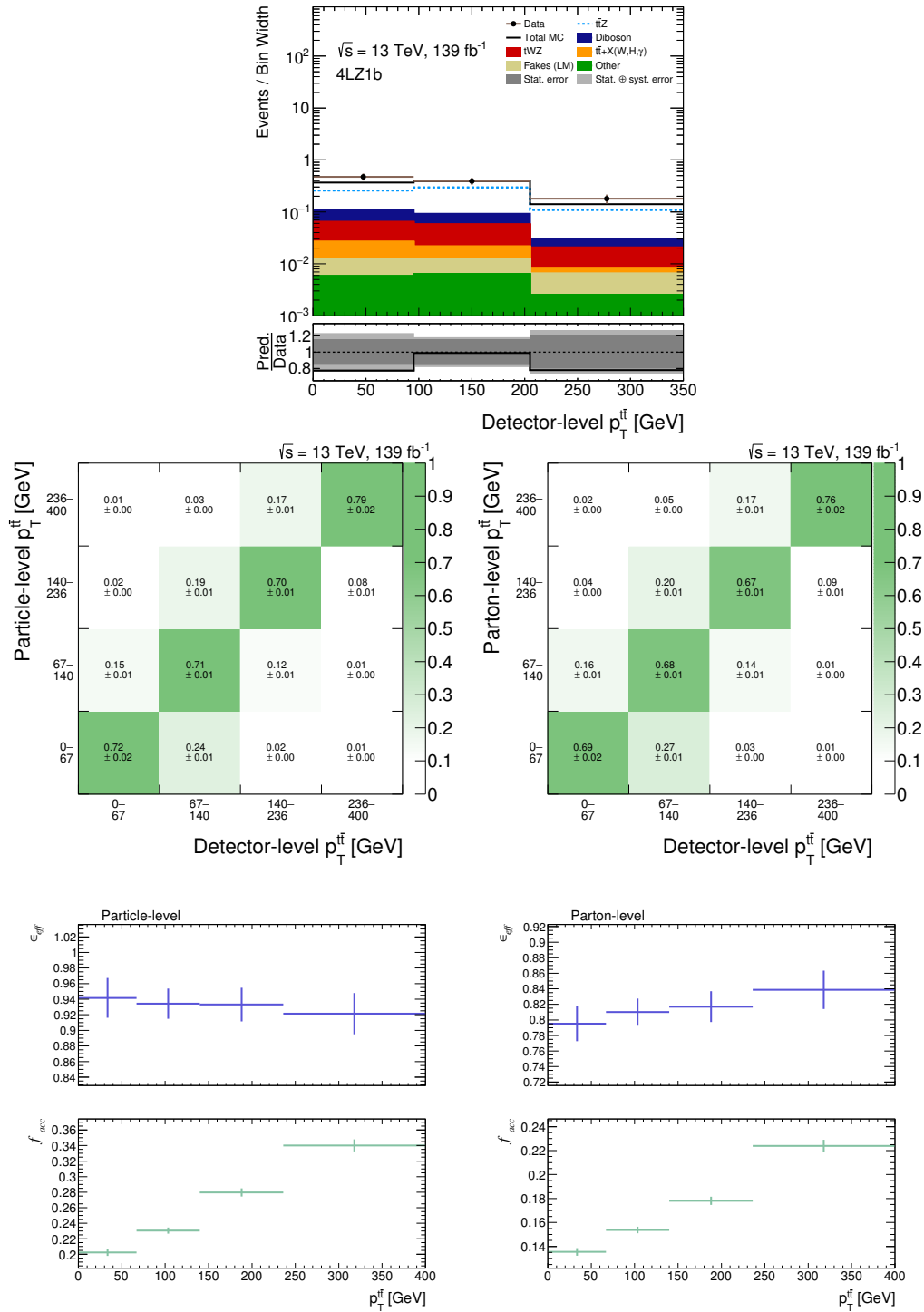


Figure A.19: Reconstruction-level distribution (top), migration matrices (middle) and efficiency and acceptance corrections (bottom) at particle- (left) and parton-level (right), for the $p_T^{t\bar{t}}$ variable in the 4L channel. In the top figure, the solid black line corresponds to the sum of the contributions from background processes (coloured filled areas) and the nominal $t\bar{t}Z$ MADGRAPH5_aMC@NLO sample (white filled area). This $t\bar{t}Z$ contribution is further represented (unstacked) as a dashed blue line, to allow comparison with the alternative generator setups: SHERPA inclusive (dashed green line) and SHERPA multi-leg (dashed red line).

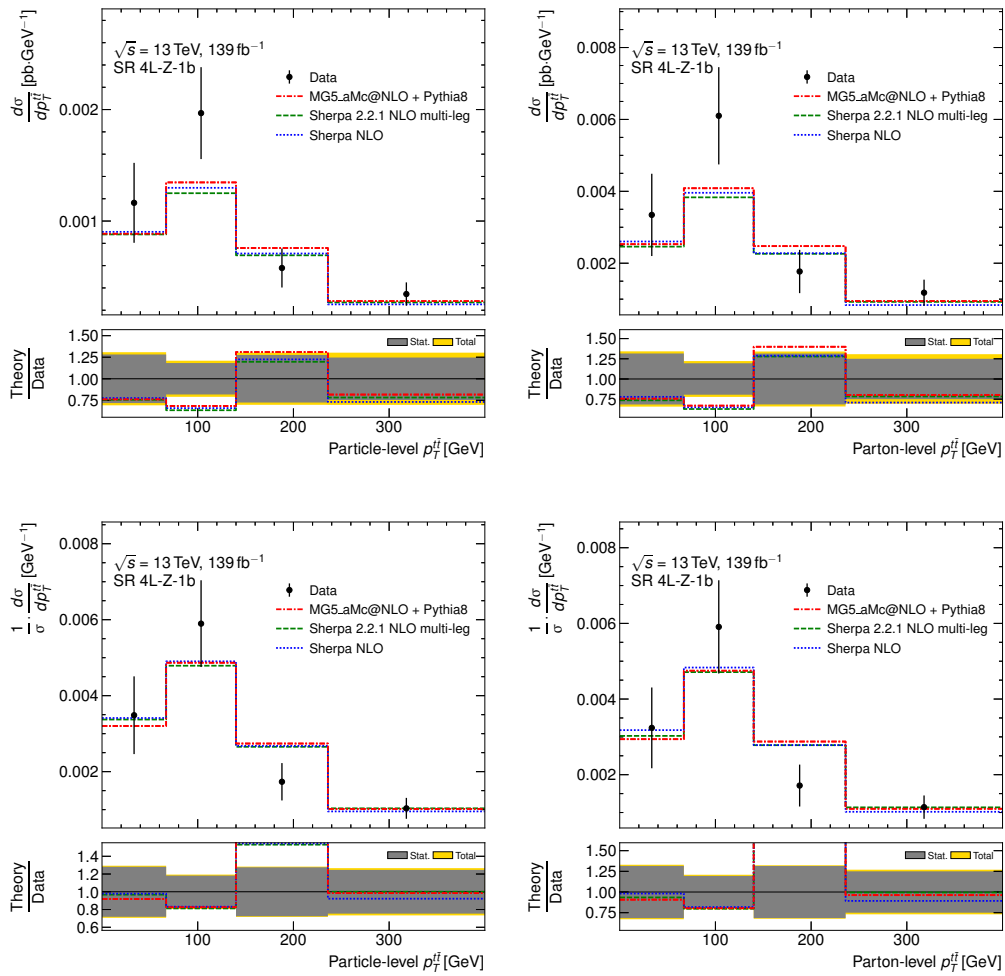


Figure A.20: Data distributions for the $p_T^{t\bar{t}}$ variable in the 4L channel, unfolded to particle- (left) and parton-level (right), absolute (top) and normalised (bottom).

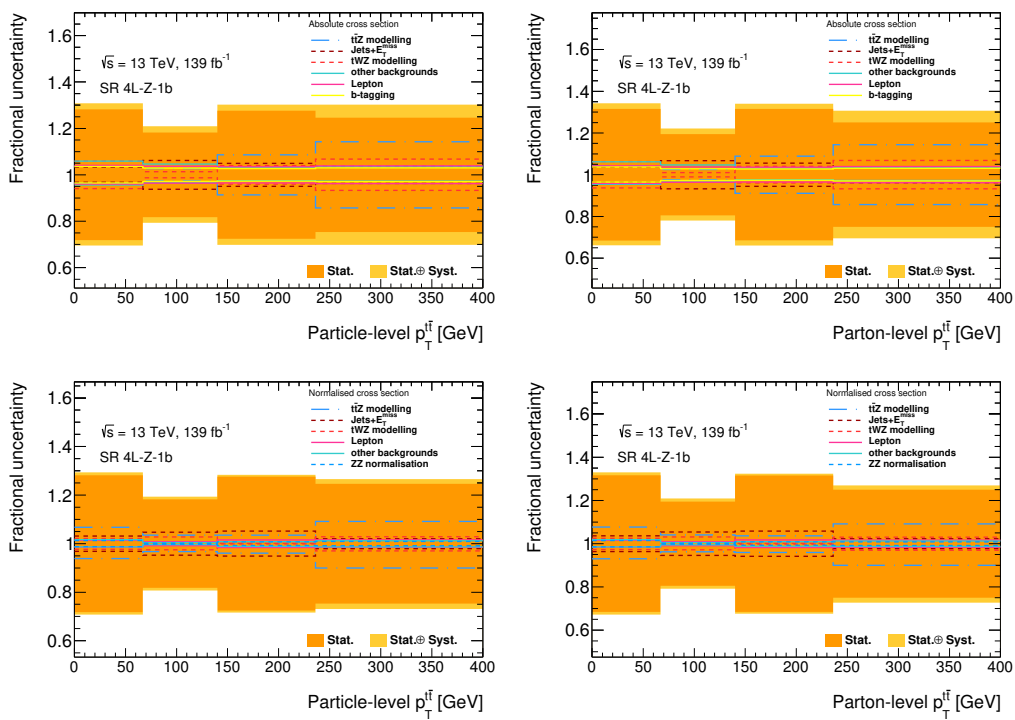


Figure A.21: Fractional decomposition of statistical and systematic uncertainties for the $p_T^{t\bar{t}}$ variable in the 4L channel, unfolded to particle- (left) and parton-level (right), absolute (top) and normalised (bottom).

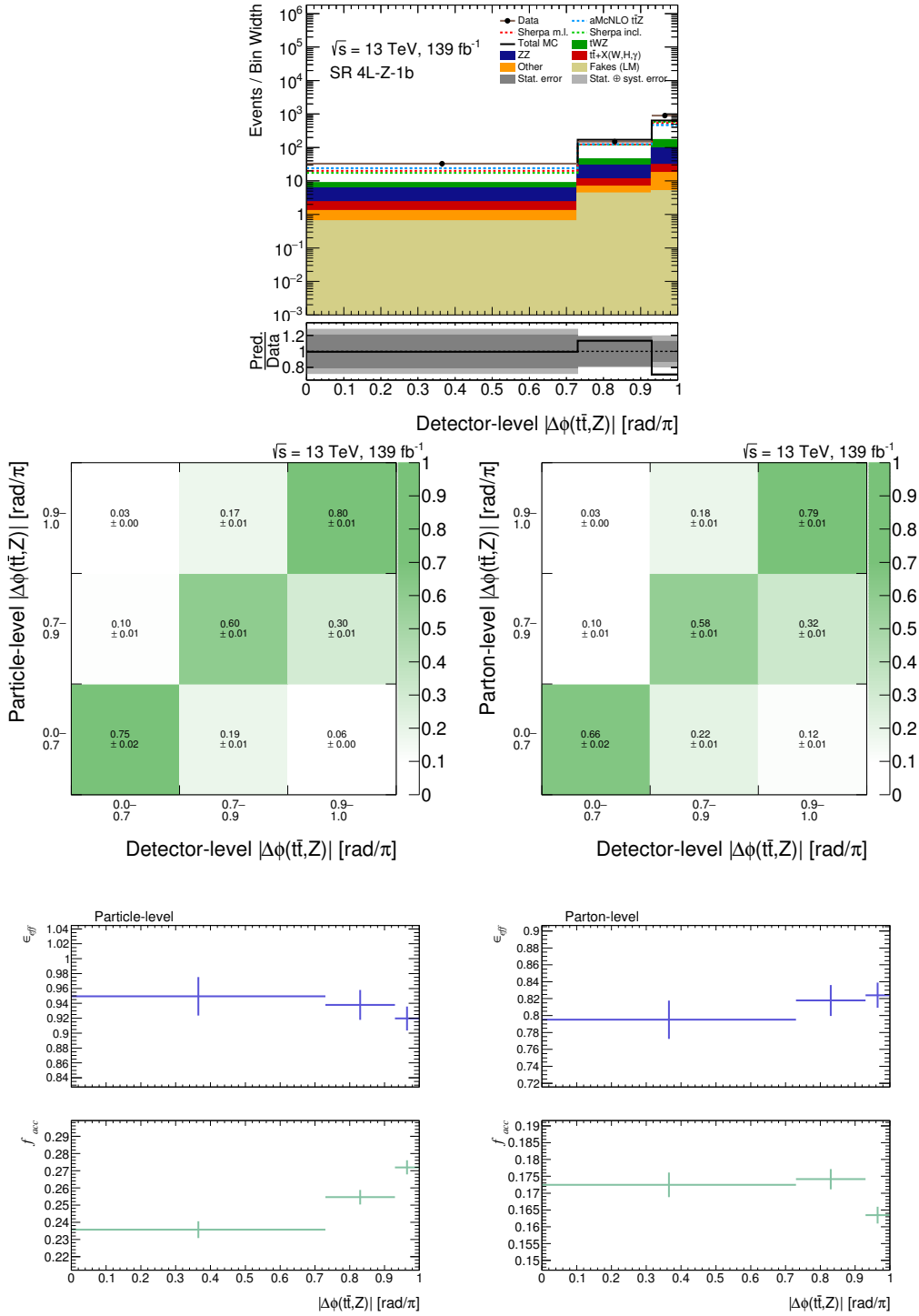


Figure A.22: Reconstruction-level distribution (top), migration matrices (middle) and efficiency and acceptance corrections (bottom) at particle- (left) and parton-level (right), for the $|\Delta\phi(t\bar{t}, Z)|$ variable in the 4L channel. In the top figure, the solid black line corresponds to the sum of the contributions from background processes (coloured filled areas) and the nominal $t\bar{t}Z$ MADGRAPH5_aMC@NLO sample (white filled area). This $t\bar{t}Z$ contribution is further represented (unstacked) as a dashed blue line, to allow comparison with the alternative generator setups: SHERPA inclusive (dashed green line) and SHERPA multi-leg (dashed red line).

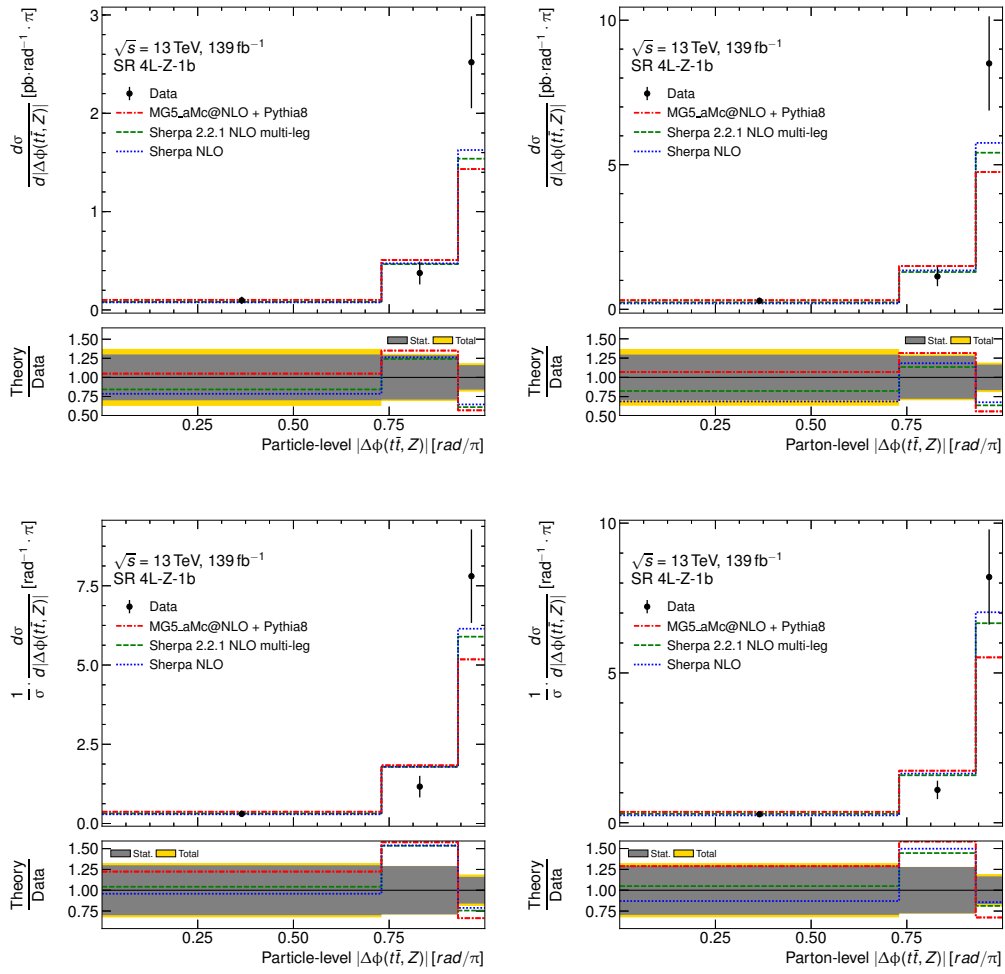


Figure A.23: Data distributions for the $|\Delta\phi(t\bar{t}, Z)|$ variable in the 4L channel, unfolded to particle-level (left) and parton-level (right), absolute (top) and normalised (bottom).

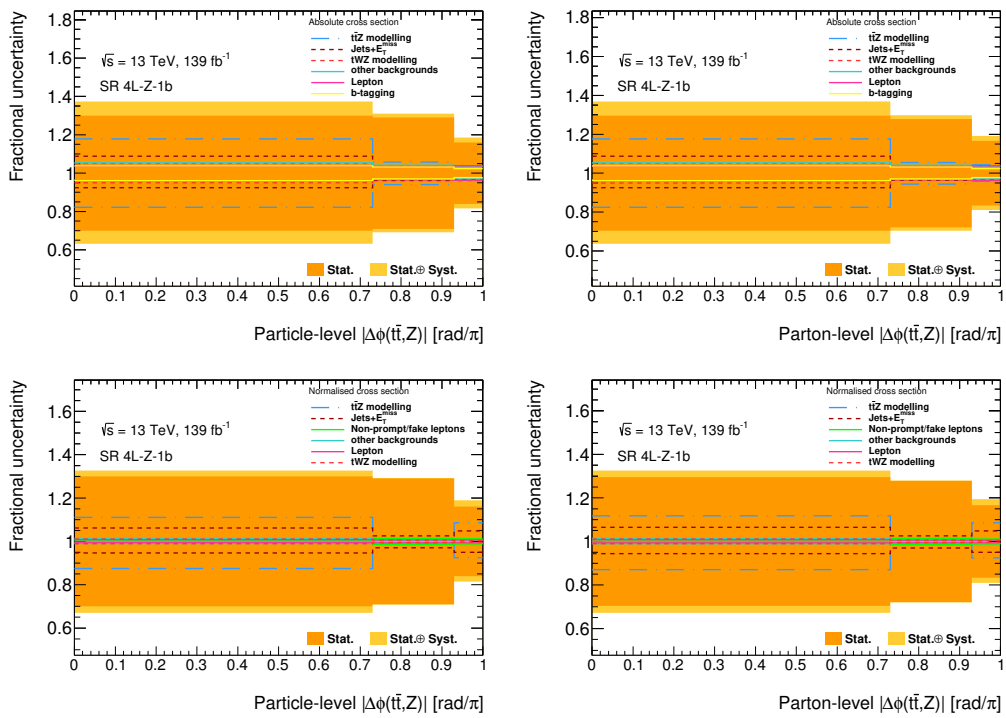


Figure A.24: Fractional decomposition of statistical and systematic uncertainties for the $|\Delta\phi(t\bar{t}, Z)|$ variable in the 4L channel, unfolded to particle- (left) and parton-level (right), absolute (top) and normalised (bottom).